Fine scale observations and modeling of the internal deformation and basal friction of glaciers

Juan Pedro Roldan-Blasco

▶ To cite this version:

Juan Pedro Roldan-Blasco. Fine scale observations and modeling of the internal deformation and basal friction of glaciers. Glaciology. Université Grenoble Alpes, 2023. English. NNT : . tel-04186216

HAL Id: tel-04186216
https://theses.hal.science/tel-04186216

Submitted on 23 Aug 2023

THÈSE

Pour obtenir le grade de

DOCTEUR DE L'UNIVERSITÉ GRENOBLE ALPES

École doctorale : I-MEP2 - Ingénierie - Matériaux, Mécanique, Environnement, Energétique, Procédés, Production
Spécialité : 2MGE : Matériaux, Mécanique, Génie civil, Electrochimie
Unité de recherche : Institut des Géosciences de lEnvironnement

Observations et modélisation aux petites échelles des processus de déformation interne et du frottement à la base des glaciers

Fine-scale observations and modeling of the internal deformation and basal friction of glaciers

Présentée par :

Juan Pedro ROLDÁN BLASCO

Direction de thèse :

Olivier GAGLIARDINI PROFESSEUR DES UNIVERSITES, Université Grenoble Alpes	Directeur de thèse
Christian VINCENT INGENIEUR DE RECHERCHE, CNRS	Co-directeur de thèse
Florent Gimbert CHARGE DE RECHERCHE, CNRS	Co-encadrant de thèse

Rapporteurs :

Ian HEWITT
PROFESSEUR ASSOCIE, University of Oxford
Peter NIENOW
PROFESSEUR, University of Edinburgh

Thèse soutenue publiquement le 16 Mars 2023, devant le jury composé de :

Olivier GAGLIARDINI PROFESSEUR DES UNIVERSITES, Université Grenoble Alpes	Directeur de thèse
Christian VINCENT INGENIEUR DE RECHERCHE, CNRS	Co-directeur de thèse
Ian HEWITT PROFESSEUR ASSOCIE, University of Oxford	Rapporteur
Peter NIENOW PROFESSEUR, University of Edinburgh	Rapporteur
Anne MANGENEY PROFESSEUR DES UNIVERSITES, Université Paris Diderot, IPG	Examinatrice
David AMITRANO PROFESSEUR DES UNIVERSITES, Université Grenoble Alpes	Examinateur

Invités :

Florent Gimbert
CHARGE DE RECHERCHE, CNRS
Adrien Gilbert
CHARGE DE RECHERCHE, CNRS

In recognition of all those who suffered while working on their (finished, or unfinished) PhD thesis.

Résumé

L’étude des glaciers est fondamentale pour évaluer les changements climatiques et ses impacts sur la planète. Néanmoins, les processus important liés à l’écoulement des glaciers ne sont pas tous identifiés et complètement compris. En effet, la rhéologie de la glace qui contrôle la vitesse de déformation est mal contrainte en raison de la rareté des observations et de la forte dépendance de la fluidité de la glace à l’égard de différentes variables telles que la température, la teneur en eau de la glace ou la structure des grains. De même, les processus qui contrôlent la vitesse basale suivant les conditions hydrologiques sous glaciaires restent très mal connus. En particulier, les modèles qui lient la vitesse basale à la friction et le réseau sous-glacier sont basées sur des hypothèses, comme le manque de debris ou l’évolution lente des pressions d’eau, qui sont contesté par des observations à la base des glaciers. Cette thèse apporte des nouveaux éléments pour la compréhension de la dynamique de déformation de la glace grâce aux observations in-situ, et l’amélioration des lois de frictions par des approches théoriques et numérique à l’échelle du processus.

L’étude de la déformation de la glace est faite à partir de mesures in-situ par inclinométrie dans des trous de forages effectués dans la zone d’ablation du Glacier d’Argentière, un glacier alpin tempéré, entre 2019 et 2020. Combinées aux mesures de vitesses en surface, ces observations permettent de déterminer à la fois les vitesses de déformation et les vitesses basales. De plus, en utilisant les résultats d’un modèle d’écoulement, ces observations permettent de calculer les paramètres rhéologiques, tel que le facteur de fluage A. Nous avons montré que nos observations ne peuvent s’expliquer que par une augmentation importante de A avec la profondeur, qui pourrait être liée à une augmentation de la teneur en eau avec la profondeur. Par ailleurs, nous montrons que, localement, la variabilité à court terme (jours à semaines) de la vitesse de surface est dictée par le glissement, alors que la variabilité saisonnière est dictée par la déformation interne de la glace.

Cette thèse contribue à améliorer la loi de friction à l’aide d’un modèle analytique et numérique de glissement pour tenir en compte de l’effet de la contrainte de cisaillement locale (débris) jusqu’à présent négligé dans cette loi. Nous mettons en évidence que la friction causée par les débris diminue le glissement, mais que la viscosité de la glace diminue aussi à cause de l’augmentation de la déformation de la glace. La loi de frottement proposée dans cette thèse, avec une contrainte de cisaillement locale non nulle à la base, conserve la forme des lois de friction classique. Cela permet de généraliser les lois couramment utilisées pour la prise en compte de l’influence des débris.

Dans la dernière partie de cette thèse, nous avons étudié l’impact des pressions d’eau non stationnaires sur la friction à travers le modèle couplé hydro-mécanique non publié de Lliboutry (2005), qui sont en lien avec les travaux récents sur le couplage hydromécanique à la base des glaciers. Il contribue au développement de nouvelles approches théoriques pour prendre en compte les interactions entre l’hydrologie sous-glaciaire et la friction.

Nos résultats permettent ainsi d’améliorer la compréhension de l’écoulement des glaciers tempérés et de proposer quelques pistes pour améliorer les futurs modèles d’écoulement de glaciers. Cette thèse illustre que la modélisation précise des glaciers nécessite de prendre en compte l’hétérogénéité spatiale des conditions basales et de la rhéologie de la glace. Elle montre aussi que la modélisation à l’échelle du processus permet d’améliorer notre représentation des conditions basales dans les modèles à grandes échelles.

Mots clés: Écoulement des glaciers, dynamique des fluides, observations, modélisation numérique.

Abstract

he study of glaciers is fundamental to assessing climate change and its impacts on the planet. However, the important processes related to glacier flow are not all identified and fully understood. In particular, the rheology of the ice that controls the rate of deformation is poorly constrained due to the paucity of observations and the strong dependency of ice flow on different variables such as temperature, ice water content or grain structure. Similarly, the processes that control basal velocity under changing subglacial hydrological conditions remain poorly understood. Furthermore, models that link basal velocity to friction and subglacial hydrology are based on assumptions, such as lack of debris or slow evolution of water pressures, which are challenged by observations at the base of the glaciers. This thesis provides new insights into the dynamics of ice deformation through in-situ observations, and the improvement of friction laws through theoretical and numerical approaches at the process scale.

The study of ice deformation is based on in-situ measurements carried out with tiltmeters in boreholes drilled in the ablation zone of the Argentière Glacier, a temperate alpine glacier, between 2019 and 2020. Combined with surface velocity measurements, these observations allow both deformation and basal velocities to be determined. Using the results of a flow model, these observations allow the calculation of rheological parameters, such as the creep factor A. We have shown that our observations can only be explained if A significantly increases with depth, which could be related to an associated increase in ice water content. Furthermore, we show that, locally, the short-term (days to weeks) variability of the surface velocity is driven by sliding, while the seasonal variability is driven by the internal deformation of the ice.

The contribution of this thesis to the improvement of friction laws is made by using an analytical and numerical model of glacier sliding over rough beds that considers the effect of local shear stress (debris), until now neglected. We show that friction caused by debris decreases sliding velocities, but ice viscosity also decreases due to increased stress concentrations. Our obtained friction law with a non-zero local shear stress at the base retains the form of the classical friction laws, such that they may still apply to the case of debris given proper normalization.

In the last part of this thesis, we studied the impact of non-stationary water pressures on friction through the unpublished coupled hydro-mechanical model of Lliboutry (2005). We show that this work exhibits interesting similarities with more recent work on hydromechanical coupling at the base of glaciers. It contributes to the development of new theoretical approaches representing the interactions between subglacial hydrology and friction.

Our results thus improve the understanding of temperate glacier flow and suggest ways to improve future glacier flow models. This thesis illustrates that accurate glacier modeling requires considering the spatial heterogeneity of basal conditions and ice rheology and that process-scale modeling can improve our representation of basal conditions in large-scale models.

Keywords: Glacier flow, fluid dynamics, observations, numerical modeling.

Acknowledgements

This PhD cannot be understood without all those that have accompanied me over the last four years. I would like to start by thanking those who have guided and supervised my dive into glaciology. Olivier, thank you for your faith in me, your support and your care. You are, in the end, the one responsible for me being in glaciology after all: for advertising the internship back in 2019, for selecting me among the other candidates, and for supporting my PhD application. I would also like to thank Florent, for your honest comments during these years, your contagious excitement for this profession, the passionate discussions about glacier dynamics and your immense patience with my writing. I cannot go on without thanking you, Christian, for your willingness to help me understand the behaviour of "real" glaciers and your critical eye on the results which has pushed me to improve. And I would like to finish by thanking my fourth (unofficial) supervisor, Adrien. Thank you for your interest in what I have been doing, and for your patience with me, especially at the end of the PhD. Your interest during the inclinometry project was especially important during a time when I was a bit lost, and helped me make it through it.

I have also enjoyed the help of all the beautiful people that have shared their time with me in the lab and over many evenings and weekends. Thank you Nate, for being there since literally my first day in this field, always encouraging me and always ready to participate in any evening plan. Thank you as well to my other office mates, to Ugo for receiving my phone calls during times of crisis, to Jordi for your strong spirit of innovation, independence and for the passion you show everytime we talk, and to Anuar for your disponibility to help with the velocities and your chocolate! Thank you as well to those who suffered my unprompted visits: Marco, l'etrusquino bringer of guanciale and pecorino, Anna, who makes a delicious bortsch, Benoît (the first doctor among us) who taught me that there is never enough reblochon in tartiflette, and Eliot, my alpine roadtrip (or traintrip?) companion. Thank you Clara and Samuel for your Slack conversations, the bingoes and the boardgames. Thank you Clara again, and Annah, Étienne and Pyrène for having nicely hosted me in times of need. Thank you Evangelos for, together with Samuel, making the confined Mondays more bearable. Thanks to Guillaume and Romane for sharing with me the responsabilities of the Laboratory Council. Thanks to Anil and Laura who helped me build a strong spicy food tolerance. Thanks to all those that were always ready for discussing anything and everything during coffee time: to the cowboy-looking Cruz, to the hidden urbanist and journalist in Olivier, to the youtuber Mickäel and to Álvaro, who was the first to put on the unique ring. And thanks as well to those with whom I have shared nice moments in the lab, and those that have helped me during these years: Alexis, Astrid, Jai, Jonathan, Julien, Foteini, Luc, both Nicos, Sarah, and all those that I haven't mentioned yet.

And finally, thanks to the people that have been with me in the distance: my lovely friends Esteban and Laura Pinsh, my intermittently employed fellows Christino, Colorado, Miguel Ángel, Migue, Tomás and Tulisio, my dearest friend Julia who brought me to Grenoble, and my travelling lads Uudam, Tulsa and Espisi. I cannot finish without mentioning my family, who have always been there: Mònica, Jan (the youngest proofreader in this beautiful field), Emerano, Amanda, my siblings Antonio, Carmen, Emi and Azu, and my PhD-wielding parents, whose trace I am proudly following here.

Preface

Θάλλατα! Θάλλατα!
Xenophon, *Anabasis*, IV, 7.

Following the defeat at Cunaxa, the Ten Thousand greek mercenaries, formerly employed by the by-then dead Cyrus the Young, had to walk from nowadays Iran to their homeland. After many months of sufferings, a cry of joy was heard when they were traversing mount Theches (Turkey): they saw, for the first time since the start of their return, the sea. The trip was not over but there they saw that its end was near.

This quote has come to my mind several times during this PhD thesis. The sea is finally here, in the 150 pages of this manuscript. The path has been quite less problematic than the one of Xenophon, fortunately, but in any case it has been a sort of intellectual and personal anabasis. It has also ended with a written account of the events that have been witnessed, the discoveries that have been found, and the new friends that have been made during such adventure.

Contents

Chapter 1

Context and introduction

Ice will not stop melting whether we solve the friction of glaciers sooner or later.
Paraphrasing a well known glaciologist.

1.1 What are glaciers, and why do we care about them?

From the high peaks of mountains and other cold areas of the Earth, glaciers flow towards valleys and oceans like frozen rivers, shaping the future and serving as witness of the past. At the highest part of a glacier, in the so-called accumulation zone, snowfall survives summer and slowly compresses into ice. Ice, which at a first glance seems a solid, deforms and flows under the great pressures caused by the tens, hundreds or even thousands of meters of ice that form up the different glaciers, ice caps, ice-sheets and ice shelves of the Earth, and thus the glaciers flow. As a result, ice is transported downwards, entering the ablation zone, i.e. the part of the glacier where mass loss due to melting and other processes is higher than snowfall accumulation, until ablation is so high that ice disappears and the glacier ends. If ice did not deform, ice would not be found on the ablation zone and glaciers would just be still mountains of ice, not rivers of ice.

In their descent, glaciers erode mountains and shape them (see Figure 1.1), becoming part of the landscape. Likewise, they are also incised in the collective memory of those who live close to them, ranging from traditional communities who consider glaciers religious entities (Allison, 2015), to the inhabitants of the European Alps who have witnessed the progressive retreat of glaciers in the last century (Cerdan et al., 2019). By storing air bubbles and surface debris in their ice layers, glaciers have been used as witnesses of the past and studied to answer a wide variety of questions, ranging from the state of the climate in the last millenia (Jouzel et al., 2007), the production of lead in Ancient Europe (McConnell et al., 2018; Preunkert et al., 2019), or even the location of accidents happening at the surface of glaciers (Jouvet and Funk, 2014; Compagno et al., 2019).

Glaciers also play an important environmental role. They provide important natural resources, as they release sediments and meltwater, transporting nutrients and feeding rivers, lakes and aquifers throughout summer and supporting agriculture, see for instance the extremely high contribution of meltwater to stream discharge in the Indus plain (India) in Figure 1.2 (a) (Biemans et al., 2019). Several economical activities actively exploit glaciers, such as the hydroelectrical stations that generate power from subglacial runoff (see the hydropower station at Glacier d'Argentière of Electricité d'Emosson SA), or the different touristic businesses dedicated to skiing, hiking on glaciers, visiting inglacial tunnels and other types of glacier-related outdoor activities. Last, but not least, glaciers are complex geophysical systems, and inspire researchers in their quest for answers and understanding of reality.

Unfortunately, climate change has given motives to be increasingly concerned about glacier evolution in the coming decades. A direct implication of warming is the imbalance of glacier mass: glaciers have been (for the most part) retreating almost continuously since at least the 1950's (WGMS, 2022). We show the expected mass loss of alpine glaciers in Figure 1.2 (b) as given by Zekollari et al. (2019). The prospective future of mountain glaciers are particularly grim, and glacier farewell parties have become a relatively common event in some countries, (e.g. Luckhurst, 2019; Jaquet and l'afp, 2019; Bouhassira, 2020), as the glaciers seen by generations of still-living mountain dwellers are confined to photographs.

A comment on glacier names: Glacier names are usually written in the native language of the country where they are, and typically mean 'Something glacier', or 'The glacier by some town'. For instance, we have Engabreen (Norway), which could be directly translated as Glacier of the meadow, Glacier d'Argentière (France), which is sometimes written Argentière Glacier (in its english form), and means the glacier by (the town of) Argentière, Aletschgletscher (Switzerland) which literally means Aletsch Glacier, and is sometimes called so in the literature, and Hofsjökull (Iceland), 'temple glacier' in icelandic, is sometimes referred as 'Hofsjökull Ice Cap' (therefore, the temple glacier ice cap). Choosing one option over another has advantages and disadvantages, and while it could be understood that we refer to La Mer de Glace (France), meaning 'the sea of ice', by the 'Mer de Glace Glacier', it would make no sense to refer to Glacier d'Argentière as 'Glacier d'Argentière Glacier'. In this PhD thesis we will avoid any type of confusion by always respecting, and referring to, the original name (Engabreen, Glacier d'Argentière, etc). This is a PhD on glaciers, after all, and context is strong enough to suggest that Storglaciarën (Sweden) is anything but a swedish glacier (and a fast flowing one, on a completely unrelated note).

The rapid warming and retreat of mountain glaciers put all those that depend on glaciers in jeopardy. For example, the patterns of water availability will be disrupted, increasing the severity of droughts and affecting agricultural yields (Intergovernmental Panel on Climate Change, 2022). Similarly, while glacier-related catastrophes are found in history (e.g. Vincent et al., 2010), climate change has paved the way for more recent glacier collapses (Kääb et al., 2018), and is expected to increase the likelihood of glacier-related catastrophes in the future (Intergovernmental Panel on Climate Change, 2022). On a global level, glacier mass loss is, and will continue to be, the main contributor to the increase in sea level during the 21st century (WGMS, 2022). Since the 1960's, the sea level has been rising at increasing rates following a combination of heat expansion, glacier mass loss, and ice sheet mass loss (Greenland and Antarctica), with an estimated rise by 2050 between 0.24 m and 0.32 m (see Figure 1.2 (c)), affecting hundreds of million of people living in coastal areas (Intergovernmental Panel on Climate Change, 2022).

Despite the growing interest in understanding glacier evolution, and the increase in the number of observations of glacier dynamics and their increasing accuracy, there are still many unknowns and poorly understood processes that govern the flow of glaciers (e.g. Pattyn, 2010; Brondex et al., 2019; Zeitz et al., 2020). Therefore, there is still plenty of room to improve our knowledge of how glaciers move and how they will affect us.

Figure 1.1: View of Glacier d'Argentière from the moraine on the west side, the perspective is against the flow. The glacier lies on a valley carved through the granite and gneiss of the Mont Blanc range. The ablation zone can be seen on the lower and right side of the picture. The lateral crevasses, typical of glacier margins, can be identified in the lower left. The central dark lines are made of rocks that have fallen from the surrounding mountains and are transported with the flow, resting uncovered as all snow has already melted. The accumulation zone is behind the turn on the left side of the picture. Photographed by Bruno Jourdain in September 2019, and used with permission.

Classification of glaciers

Before continuing with a review on the current knowledge, we will give a brief description of the different types of glaciers. Glaciers can be classified depending on several criteria, of which we list here thermal regime, bed type, and size. Depending of their temperature distribution glaciers are classified into temperate glaciers, if the ice is everywhere at the pressure melting point, in cold glaciers, if they are below it, or polythermal if they are partly temperate (typically at and close to the bed) and partly cold. Glacier beds are classified in two large groups: hard and soft beds. Hard beds are typically made of bedrock, and are considered a hard, solid boundary over which temperate ice slides, while soft beds are made of sediments which may deform due to the drag exerted by the glacier onto them. We can also consider here ice shelves, which are the part of glaciers that have reached the ocean and are floating. Focusing on size, from larger to smaller, we classify glaciers into ice sheets if they cover more than 50000 km^2 (nowadays covering Antarctica and most of Greenland), ice caps if they cover smaller areas such as nowadays in some parts of Iceland or in the past glaciations over mountain ranges such as the Shaluli Shan (China) (Fu et al., 2013), and finally, we usually reserve the actual word 'glaciers' for the smaller glaciers, such as the glaciers that occupy alpine valleys, or the outlet glaciers that drain the ice sheets in Western Antarctica. In this PhD thesis we focus the study on temperate ice sliding over hard beds. The observations carried out during this PhD thesis correspond to an alpine temperate glacier.

In the rest of this introduction we will do an overview on how we model glaciers and some of the open questions that remain opened. We will continue with a brief account of the recent scientific history of Glacier d'Argentière. Finally, we will provide the objectives set up for this PhD thesis and lay out the structure of the document.

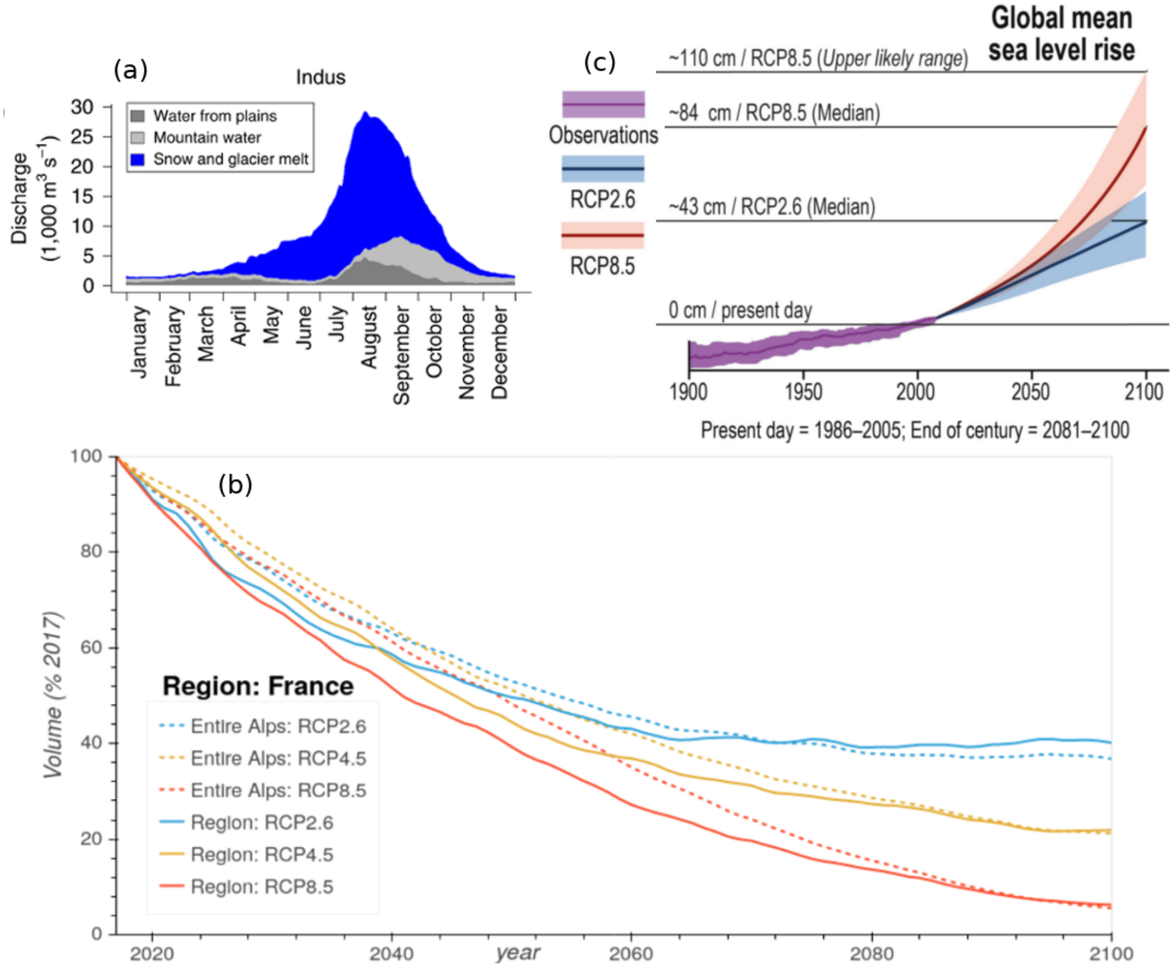

Figure 1.2: Present and future importance of the decrease in glacier volume. Panel (a) shows the extremely high contribution of snow and glacier melt to the discharge in the Indus basin (India), estimated close to the basin's outlet. The figure has been taken from Biemans et al. (2019). Panel (b) shows the expected glacier mass loss in the French Alps (solid lines) and in all the Alps (dashed lines) from 2017 to 2100 under three climatic scenarios. Panel (b) has been obtained from the interactive graphic provided by OGGM - edu (web resource) using data from Zekollari et al. (2019). Panel (c) is adapted from the *Special Report on the Ocean and Cryosphere in a Changing Climate* and shows the projections of sea level rise under different climatic scenarios, as sea water continues to expand and ice (such as the one that feeds the Indus plain) continues to melt.

1.2 Early glaciology

Between the XIVth and the end of the XIXth centuries, Europe experienced an intermittent period of cold temperatures and glacier advance, the so-called 'Little Ice Age'. From the XVIth century onward, glacier advance became more widespread (Francou and Vincent, 2010; Solomina et al., 2016), and glaciers started to get the attention of the public. If at the beginning of this period they were considered dangerous environments that threatened towns with their continuous advance (Rémy and Testut, 2006), such that priests had to be called to make the glaciers stop (as was done with success in the French and Swiss Alps (Francou and Vincent, 2010)), towards the end of the XVIIIth century the Illustration, and later the romanticism, changed the point of view that the general public and naturalists had on glaciers. Naturalists began to ask themselves what glaciers were, and how they moved. The theories, much as glaciers during these centuries, followed a cycle of advance, retreat, and advance again, during which glaciologists combined field observations of increasing accuracy with theories of increasing complexity.

Pioneering among them, the swiss Horace Bénédict de Saussure (1740-1799) expanded on previous ideas and proposed in 1769 that glaciers move by sliding over their beds as a solid block of ice, thanks to the presence of liquid water that lubricates the bed. It would take two centuries to definitively prove some points of Saussure's theory. Meanwhile, another theory based on the solid nature of ice emerged: the dilatation theory. It gained a lot of popularity in the scientific community, with its strongest defender in the Swiss naturalist Louis Agassiz (1807-1873). In this mechanism, glacier movement has its origin in the surface water that falls through crevasses (cracks) and moulins (water-melted shafts) and freezes when reaches the glacier bed. Since water expands upon freezing, the glacier swells and moves forward. A variant of the dilatation theory was the regelation theory, developed later in the XIXth century and whose maximum exponent was John Tyndall (1820-1893). Tyndall proposed that glaciers advance by a combination of melting due to increased pressure and downstream refreeze of the meltwater. The dilatation/regelation theory became immensely popular during the mid XIXth century until well into the XXth century (Rémy and Testut, 2006) thanks to the efforts of Agassiz and Tyndall to refute other competing theories, their wealth of evidence, and the exploitation of their respective scientific reputations and manly exploration feats to promote their ideas and mobilize support for them (Schaer, 2001; Rémy and Testut, 2006; Carey et al., 2016).

In the meantime, another school of glaciologists appeared, those supporting the 'Viscous Theory of Glaciers' as called by its most arduous defender, the scottish James David Forbes (1809-1868). The proponents of this theory recognised the fluid-like behaviour of glaciers, which adapted to the shape of the valleys and moved like 'liquor in a vase'. This mechanical behaviour could explain Forbes' observations that glaciers moved faster at the center and it meant that glaciers moved faster at the surface than at the bed (Forbes, 1859). Forbes also intuitively noticed the role of water in regulating glacier flow, observing that glaciers moved faster when the air temperature was hotter, and when their 'veins' were full of meltwater (as in summer). Unable to explain the solid features of glaciers, such as crevasses, and faced with Tyndall, fluid theory was not supported during Forbes' times.[1].

The last twist of the story arrived in the first half of the XXth century, in which the tide turned again towards the deformation and sliding theories. While theoretical models of glacier flow started to use the Navier-Stokes equations since 1906, more accurate observations of sliding and deformation supported this change of doctrine (Rémy and Testut, 2006). The entry of fluid dynamics into glaciology opened another line of research, whose echoes are found in this PhD thesis: the rheology of ice, i.e. the relationship between force and deformation in a material. If ice is a fluid, is it a newtonian fluid, such as water but much more viscous, as initially assumed by Weinberg, Somigliana and Lagally (Perutz, 1947; Rémy and Testut, 2006), or is it a plastic material, such as metals (Seligman, 1949)? What physical variables control the deformation of ice? What is the relationship between the rheology of ice and the sliding at the base? The answer given to those questions in the 1950's and later decades founded today's physical framework of glacier dynamics.

---

[1] Forbes addressed the small success of the fluid theory as a gentleman, stating "It is often difficult to obtain a calm and full hearing for any new theory or experimental investigation; not because there is any antipathy to novelty, or that experiment is under-valued, but simply because, in an age of bustle and struggle for pre-eminence, each man is so busy with his own reputation, or the means of increasing it, that he has no leisure to attend to the claims of others" (Forbes, 1859).

From the mid XXth century onwards, physicists and mathematicians started to get interested in glaciology, bringing a new dimension to the understanding of glacier dynamics (Clarke, 1987), as depicted in Figure 1.3. The observations of Perutz (1949, 1950) showed that glaciers moved faster at the surface than at their bed, which would be confirmed by even more observations later (e.g. Sharp, 1953; Mathews, 1959). After shearing ice in the laboratory, Glen (1955) showed that glaciers deformed non-linearly under continuously applied stress, setting the basis for modern understanding of glacier flow. Ice, therefore, was indeed a very viscous fluid. Since the seminal work of Glen, great efforts have been carried out to validate his work, determine the values of the parameters that control ice deformation, and establish the control of physical variables such as temperature, water content (Duval, 1977; Adams et al., 2021), or ice crystal size (Schulson and Duval, 2009) in ice deformation. We discuss some of these controls later. It would turn out that the complexity of ice rheology makes it very difficult to properly constrain *in-situ* observations of glacier flow, and laboratory experiments are also not without problems that limit extrapolating experimental results to real conditions. A few examples of these problems are the differences in material properties between artificial ice and natural ice (e.g. Adams et al., 2021; Cohen, 2000), how well can the stress regime studied in the laboratory represent natural conditions, or the small spatial and temporal scale that limit the experiments (e.g. Budd and Jacka, 1989).

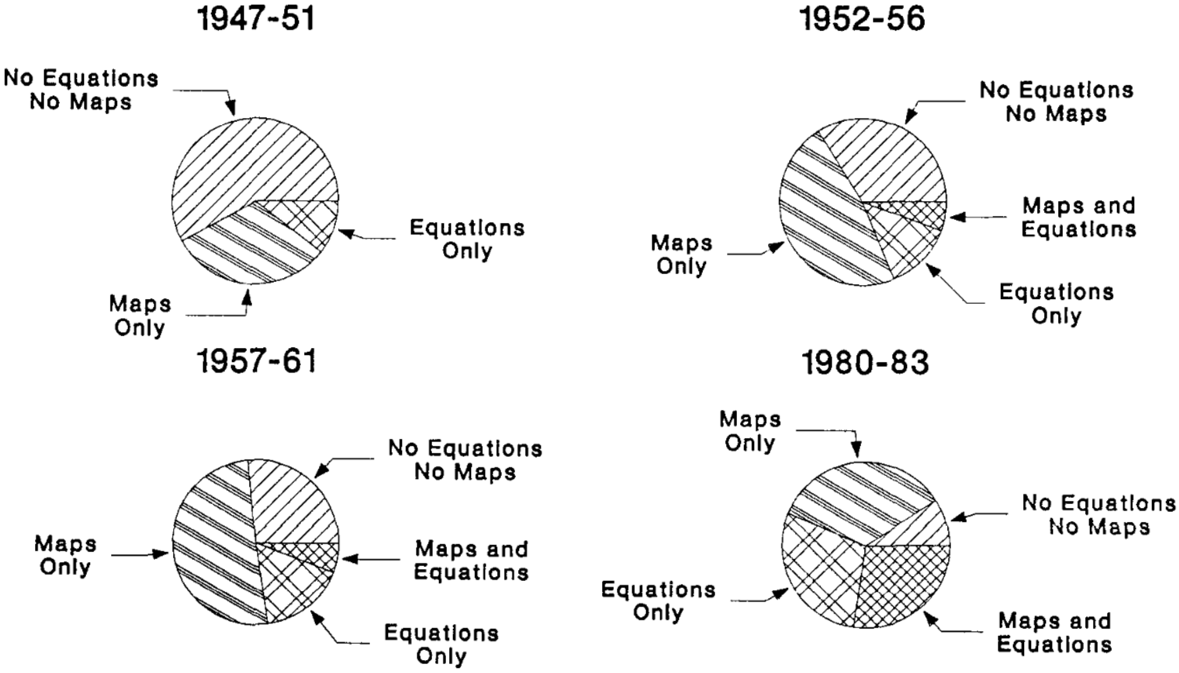

Figure 1.3: Evolution of the content in *Journal of Glaciology* during the 1947 - 1983 period, adapted from Clarke (1987). Equations pass from being present in less than one eighth of the publications in 1947-1951 to being in more than half the publications during the 1980-1983 period. This evolution is a result of the development of physical models in glaciology, i.e. the works of Weertman, Lliboutry, Röthlisberger... Note that the content is not reported for the 1962 - 1979 period.

The development of models and observations of ice deformation allowed glaciologists to put their attention on sliding and develop theories of how glaciers flow over their beds, more or less backed by evidence. This allowed them to relate glacier velocity to glacier thickness, slope, temperature, bed geometry, etc. This type of relationship, called friction laws, saw a period of great discussion during the late 1950's and the 1960's (Fowler, 2011), and during the subsequent decades the proposed models were progressively refined. Work on glacier friction and velocities brought glaciologists to the field of glacial hydrology, particularly subglacial hydrology, i.e. the flow of water at the base of glaciers (e.g. Shreve and Sharp, 1970; Röthlisberger, 1972; Weertman, 1972; Iken, 1981; Iken and Bindschadler, 1986).

Nowadays it is clear that at the scales relevant to most studies regarding glacier dynamics, ice behaves like a viscous fluid. If basal ice is temperate, the glacier slips over its bed in a process that is controlled by how water is spread along the bed. Creep, sliding, and subglacial hydrology are therefore strongly related to one another and it is difficult to explain one without referencing the other. In the next section we will provide an assessment of how we understand the flow of ice nowadays, some of the questions that stay open regarding ice creep, sliding and the flow of water at glaciers, and on a field technique that has been used to observe and understand these components of ice dynamics.

1.3 Glacier dynamics: current knowledge and challenges

1.3.1 Ice deformation

Ice is a polycrystalline material, made of a collection of crystals (also called grains), that present many discontinuities in their crystal structure and at the boundaries between crystals. These defects allow for the atoms that conform the crystals to move through dislocations, facilitating the deformation of the crystalline structure. For a single ice crystal, most of this deformation happens along a plane, called basal plane, whose perpendicular orientation is called c axes. The arrangement of c axes in a group of crystals is called the fabric. If a group of crystals have their c axes uniformly distributed in space, then there is no preferred orientation for deformation, and the ice has an isotropic fabric and an isotropic behaviour at the scale of the polycrystal. Otherwise, it is anisotropic, with one or several preferred directions for deformation. Ice fabric and crystal size evolve as ice deforms, and can be used to study the history of stress of an ice sample (e.g. Raymond, 1971; Vallon et al., 1976; Mangeney et al., 1996).

Ice deviatoric stress and strain rates are expressed with the symmetric tensors $\boldsymbol{\tau}$ and $\dot{\boldsymbol{\varepsilon}}$. Each component ij represents the deviatoric stress (deviatoric force per unit area) or strain rate (rate of change in shape) over a plane of normal i, along the direction j, with i and j the directions of a three dimensional ortonormal reference system. $\boldsymbol{\tau}$ and $\dot{\boldsymbol{\varepsilon}}$ have thus six independent components. We provide in Annex A an introduction to continuum mechanics, where we briefly expand on these concepts. At a macroscopic level, ice behaves as an incompressible fluid, such that when subjected to any deformation regime, its density ($\rho_i = 911$ kg m^{-3} at 0°C) does not change. In terms of strain rate this is equivalent to imposing that the trace of the strain rate tensor is zero,

$$tr(\dot{\boldsymbol{\varepsilon}}) = \dot{\varepsilon}_{11} + \dot{\varepsilon}_{22} + \dot{\varepsilon}_{33} = 0. \tag{1.1}$$

Thus, the number of unknown components of the strain rate tensor is reduced by 1. By definition, $\boldsymbol{\tau}$ is also trace-less. The other 5 must be either known (or *assumed*, as we will do a few times in this thesis) or computed via the stress tensor. To link the deviatoric stress tensor and the strain rate tensor we will use a constitutive law, of the form $\dot{\boldsymbol{\varepsilon}} = f(\boldsymbol{\tau})$.

1.3.1.1 Glen's flow law

The most common constitutive law for ice used in glaciology is the isotropic Glen's flow law (Glen, 1955),

$$\dot{\varepsilon}_{ij} = A\tau_E^{n-1}\tau_{ij}, \tag{1.2}$$

where A and n are material parameters called creep factor (also known as rate factor) and Glen's flow law exponent, respectively, and τ_E is the second invariant of $\boldsymbol{\tau}$ and is called the effective deviatoric stress, a scalar measure of the deviatoric stress, computed at any point with

$$\tau_E = (\tau_{ij}\tau_{ij})^{1/2} = \sqrt{\frac{1}{2}(\tau_{11}^2 + \tau_{22}^2 + \tau_{33}^2) + \tau_{12}^2 + \tau_{13}^2 + \tau_{23}^2}. \tag{1.3}$$

Therefore, we can see that ice deformation in any given direction ij (or, more accurately, strain rate) depends on material parameters (A and n), on the stress acting in said direction (τ_{ij}) and, very importantly, it depends non-linearly on all the other stress components via τ_E. This brings all sorts of problems in modeling glacier dynamics and is one of the reasons why ice, despite being a slow moving fluid, is so difficult to study. In Chapter 3 we will see one implication of this non-linear relation between strain rate and stress.

Glen's flow law was proposed for ice undergoing secondary creep, a creep regime for deviatoric stress roughly between 0.050 and 0.150 MPa (Lliboutry and Duval, 1985; Hooke, 2005; Cuffey and Paterson, 2010). For higher stress, experiments suggest that another type of creep regime, called tertiary creep, develops. Tertiary creep is characterized with softer ice and fabric development (anisotropy). Note that fabric development can happen at lower stresses as well for ice at very low temperatures, as is typically considered for polar ice (Dahl-Jensen, 1989; Mangeney et al., 1996).

Despite the potential inadequacy of Glen's flow law for modeling ice flow in some particular places of a glacier, it is widely considered a good approximation to model the overall ice flow of glaciers (Cuffey and Paterson, 2010), and as such, it should not be surprising that it may need some adjustments when we confront the law to actual field data. For what is left of the overview on ice deformation, we will review with a little bit more detail the material parameters n and A.

1.3.1.2 Glen's flow law exponent

The flow exponent is typically assumed to be $n = 3$, a value that represents well the results of different laboratory experiments and field observations (Cuffey and Paterson, 2010). It is the default value considered when modeling ice dynamics, common in an wide array of ice flow studies, ranging from future glacier evolution (e.g. Bolibar et al., 2022), contribution of glaciers to sea level rise (e.g. Ritz et al., 2015), reconstruction of glaciers during past glaciations (e.g. Eis et al., 2021), study of basal conditions such as melting (e.g. Karlsson et al., 2019), basal velocities (e.g. Vincent and Moreau, 2016), basal drag (e.g. Morlighem et al., 2013), and bed erosion (e.g. Herman et al., 2015), inversion of thickness (e.g. Millan et al., 2022), the list goes on.

Higher n values imply softer ice and increased sensitivity of the ice to the overall stress state. The appropriate value of n is usually related to the magnitude of deviatoric stress of the ice. A multitude of studies suggest values between 2 and 4 (Cuffey and Paterson, 2010), and later studies at the natural scale propose a value that is closer to 4, therefore, that ice is softer than we usually consider (Gillet-Chaulet et al., 2011; Millstein et al., 2022). For low stress ($< 50 - 100$ kPa, depending on the study) it has been observed (e.g. Marshall et al., 2002; Chandler et al., 2008) that ice behaves as a linear fluid as mechanisms other than dislocation creep dominate deformation. Thus, in this scenario $n \approx 1$, and strain rates are directly proportional to the applied stress τ_{ij}. The value of n can vary spatially if the stress conditions are different for different part of the glaciers, as proposed by Marshall et al. (2002) for Worthington Glacier (USA): at the upper part of glaciers deviatoric stress is low and thus $n \approx 1$, while towards the bottom the deviatoric stress increases due to the overlaying ice column becoming thicker, and n is approximately 3 or 4.

1.3.1.3 Glen's flow law creep factor

The typical value of A for temperate ice ($T = 0$°C), common in recent studies of glacier dynamics at the glacier scale (e.g. Vincent et al., 2022b), or ice sheet scale (Morlighem et al., 2013; Maier et al., 2019), is $A = 78$ MPa^{-3} a^{-1} for $n = 3$ (Cuffey and Paterson, 2010). Its value is highly dependent on many, usually unquantified, physical variables, as we will see below, and depends on the flow law exponent. This typical value of A was proposed for $n = 3$ after a review of lab-based experiments and studies at the natural scale (Cuffey and Paterson, 2010)[2], such that it works as a sort of jack of all trades. The review recognises the variable nature of A, and therefore recommend researchers to find the best value when possible for any given glacier. A typical approach for retrieving a sensible value for A is based on inversion methods. In this case, glacier observations (typically surface glacier velocities and ice thickness) are used to infer the value (or values) of A and other parameters that make the glacier behave as closely as possible to said observations. This methodology integrates all dependencies on A into one value, that is sometimes considered uniform for a single glacier (e.g. Vincent et al., 2022b), uniform for a whole set of glaciers of the same region (e.g. Millan et al., 2022), or spatially heterogeneous depending on the zone of the glacier (e.g. Hill et al., 2018).

While determining the value of A is a difficult task, we have a better idea on the dependency on A with respect to different physical variables, such as temperature, interstitial water content, fabric development, and impurity content.

Temperature Temperature plays a key role in ice creep, with A increasing exponentially the closer the temperature gets to the ice melting point. This behaviour is typically modeled with an Arrhenius law,

$$A = A_0 \exp \frac{-Q}{RT_h}. \tag{1.4}$$

In this case, A_0 is called prefactor, Q is an activation energy that depends on the temperature, R the gas constant and T_h is the temperature, adjusted for the melting point depression due to pressure. More complicated expressions of the temperature dependency of A are available in the literature. Since in this PhD thesis we will only consider temperate glaciers, we will not go further into detail regarding the temperature control on A.

Water content The effect of water content on the creep of temperate ice has only been measured in two laboratory experiments, by Duval (1977) and more recently by Adams et al. (2021). Each study focuses on different stress regimes, and as such they are not completely comparable. We will start with Duval (1977), then comment on Adams et al. (2021), and finish with what has been observed in temperate glaciers.

Duval (1977) analyzed the water content in ice samples retrieved in 1971 in La Vallée Blanche (France), a tributary glacier of Mer de Glace (France). The experimental procedure consisted in straining the ice

---

[2] Actually, $A = 78$ MPa^{-3} a^{-1} for $n = 3$ is proposed in the fourth edition of *The Physics of Glaciers* (Cuffey and Paterson, 2010), whereas its third edition proposed $A = 159$ MPa^{-3} a^{-1} for $n = 3$ (Paterson, 1994).

at the lab until it reached tertiary creep and measuring the stress and strain. Without stopping the experiment, they passed a cold wave through the ice samples, and measured the time Δt it took for the cold front to travel through a distance Δx. The speed of the cold front $\Delta x/\Delta t$ allows to determine the amount of water in the sample by solving a Stefan problem. The results of Duval (1977) suggest that ice creep increases linearly with interstitial water content W,

$$A = A_0(1 + 2.34W), \tag{1.5}$$

with A_0 the creep factor when $W = 0$, water content W in %, and for $n = 3$. The W measured at temperatures between 0°C and 0.20°C ranged from 0 to 0.7 ± 0.1 %.

More than 40 years later, Adams et al. (2021) performed similar experiments on deionized lab-made ice, mostly sheared at secondary creep, and extending the range of water content beyond the 0.7% studied by Duval (1977) up to 1.7 ± 0.23 %. For better comparison purposes, they also ran one experiment at tertiary creep, with $W = 0.31 \pm 0.08$ %. While they don't provide a relationship between A and W, they observed the following:

1. A is more sensitive to W in secondary creep, than when deformed in tertiary creep, i.e. at higher stress.
2. For $W > 0.6$ %, ice under secondary creep becomes insensitive to further increments of W.
3. Additionally, for $W > 0.6$ % ice under secondary creep becomes linearly viscous ($n = 1$).
4. The results of the tertiary creep experiment were comparable to Duval (1977). The ice of Adams et al. (2021) was slightly stiffer than that of Duval, but it could be due to Adams et al. (2021) studying deionized water (more details about the role of impurities later).

In view of their observations, Adams et al. (2021) recommend caution when extrapolating the model of Duval (1977) for $W > 0.7\%$. Unfortunately, the differences between both studies do not offer more light on the limits of their observations. In particular, we can ask ourselves if the switch from non-linear to linear rheology for $W > 0.6$ % is a feature only present for secondary creep. If that is not the case, then it is important to determine the threshold value of W at which ice turns into a linear viscous fluid.

This question is very important for mountain glaciers, as several studies carried out in temperate glaciers have found $0 \leq W < 3\%$, well over the 0.6% threshold observed by Adams et al. (2021). Table 1.4 summarizes these studies. The spatial distribution of water content in glaciers is still unclear, although some insight can be obtained from previous studies. Several vertical profiles of water content in temperate glaciers show depth increasing water content (Vallon et al., 1976; Hubbard et al., 2003; Murray et al., 2007), while some studies report an important decrease in W close to the bed (Murray et al., 2000; Benjumea et al., 2003). These observations are accompanied by great uncertainties: calorimetry must be carried out carefully so as to not measure environmentally-related changes in temperature (probably the case for the data of Lliboutry and Duval, 1985, as we comment later), while studies carried out with ground penetrating radar (GPR) may provide an overestimation of W due to integrating interstitial water and small scale veins that would normally be considered part of the hydrology system, and not as water trapped between ice crystals (Murray et al., 2007). Another factor to take into account is the differences between water content in the accumulation and the ablation zone of the glacier: Lliboutry (1971) shows higher W in the ablation zone of La Vallée Blanche (France) than in the accumulation zone. Although we are focused on temperate glaciers, it is worth mentioning that Pettersson et al. (2004) reported lateral variations along a transect located on the ablation zone of Störglaciaren, a polythermal glacier. Their conclusion was that the observed spatial variability in W in the ablation zone was a result of different patterns of water content in the accumulation zone, which were then advected downstream. Differences in water input at the surface, strain heating, or even local melting or refreezing due to changes in the melting point of the ice as a result of gradients of hydrostatic pressure could not explain such changes. We excluded from the review in Table 1.4 the vertical profile of W reported in Lliboutry and Duval (1985) in an ice core obtained in Glacier d'Argentière which have since then appeared in well cited compilations of observations of interstitial water content (e.g. Pettersson et al., 2004; Cuffey and Paterson, 2010). The reason for our disregard is the low trust that the engineers and researchers that performed the measurements give to the water content shown in Lliboutry and Duval (1985) (Paul Duval, personal communication), which is thought to reflect more the temperature at the time each sample was measured than the water content in the ice, except perhaps for the higher values of W retrieved (Michel Vallon, personal communication).

Study	Glacier	Area	Avg. W %	Method	Notes
Joubert (1963)	Vallée Blance (France)	Accum.	0.15 - 0.1	Calorimeter	Only surveyed upper part of the column
Lliboutry (1971)	Vallée Blanche (France)	Accum. Ablat.	0 - 0.6 0 - 1.7	Calorimeter	No details on the spatial distribution
Vallon et al. (1976)	Vallée Blanche (France)	Accum.	0.32 - 1.31	Calorimeter	Depth increasing W, drops at the bed
Zryd (1991)	Findelengletscher (Switzerland)	-	$0.5 – 1.5$	Calorimeter	Basal ice
Cohen (2000)	Engabreen (Norway)	-	1 (bubbly ice) > 2 (sediments)	Calorimeter	Basal ice
Murray et al. (2000)	Falljökull (Iceland)	Ablat.	0 - 3.3	GPR	Depth increasing W, drops at the bed
Benjumea et al. (2003)	Johnsons Glacier (Antarctica)	Accum.	0.6 - 2.3	GPR and seismics	Depth increasing W, drops at the bed
Hubbard et al. (2003)	Glacier de Tsanfleuron (Switzerland)	Both	$1W_0$ - $10.7W_0$	Ion concentration	Depth increasing W. Values are given relative to the water content in the upper layers W_0
Murray et al. (2007)	Glacier de Tsanfleuron (Switzerland)	Ablat.	1.18 - 3.8	GPR	Depth increasing W. Different layers than Hubbard et al. (2003)
Lüthi and Moreau (2018)	Glacier d'Argentière (France)	Ablat.	2	Calorimeter	Basal ice

Figure 1.4: Measurements of water content in temperate glaciers, with emphasis on the studied area of the glacier and the in-depth distribution. We omitted the unpublished study of Dupuy on Glacier de Saint-Sorlin, mentioned in Vallon et al. (1976), due to lack of details. This table is partly adapted from a similar review carried out in Pettersson et al. (2004). We also omit Pettersson et al. (2004) own study, for being on a polythermal glacier, although some details of it are given in the text.

Anisotropy and impurities Following Cuffey and Paterson (2010), we will concentrate the effects of variables other than temperature or water content in an enhancement factor E, that we define as

$$E = \frac{A}{A^*}, \tag{1.6}$$

where A^* is a sort of standard value of A, when the variables that modify the creep factor others than temperature and water content are not present, i.e. if we consider the effect of impurities, $A^* = A$ for clean ice.

In the case of temperate valley glaciers, it is expected that anisotropic ice is found close to the bed, due to fabric development during tertiary creep. Glen's flow law does not apply anymore, and there are several alternative constitutive laws to describe the behaviour of anisotropic ice (Gagliardini et al., 2009). The main difference, from a continuum mechanics point of view, is that since the deformation in an anisotropic material depends on the direction that we consider, the creep factor is now a tensor instead of a scalar. To compare the effect of anisotropy with respect to isotropic ice, we can compare the strain rate given by Glen's flow law $\dot{\varepsilon}_{ij}^{glen}$ and an anisotropic formulation $\dot{\varepsilon}_{ij}^{ani}$ for the same stress and creep factor (or analogous factor). In such a case, the enhancement factor due to fabric development depends on the direction that we consider, and can be defined as

$$E_{ij}^{fab} = \frac{\dot{\varepsilon}_{ij}^{ani}}{\dot{\varepsilon}_{ij}^{glen}}.$$

This depends first and foremost on the anisotropic constitutive law, and also on the stress state that we consider (Thorsteinsson, 2001). For instance, for single maximum fabrics (c axes grouped in one direction, typical of polar ice), anisotropic ice undergoing simple shear deforms much faster than isotropic ice (Mangeney et al., 1996) and we can find $E_{xy}^{fab} > 1$, although weakly anisotropic ice can display lower shearing deformation rates than isotropic ice (Thorsteinsson, 2001), and thus $E_{xy}^{fab} < 1$.

The role of impurities in controlling ice creep is difficult to quantify, and has different effects depending on the size and concentration of the impurities (Cuffey and Paterson, 2010). For microparticles and small particles, it seems that impurities soften the ice by facilitating how crystals move with respect to one another (Cuffey and Paterson, 2010). For instance, in Dye 3 (Greenland), the increased deformation in pre-Holocene ice was linked to the high amounts of dust in the ice particles, with an estimated enhancement factor of $E = 2$ to $E = 6$ (Dahl-Jensen and Gundestrup, 1987). Small rocks in the ice increase ice deformation by facilitating melt of the ice around them, while high concentrations of rocks in the ice stiffen the ice-rock mixture (Moore, 2014).

Thus, we have seen that the values of n and A can vary from glacier to glacier, and also within a given glacier. Laboratory experiments and field observations supported by numerical models allow for constraining their values, or understanding the role that environmental variables or ice fabric play on ice material parameters.

In Chapter 2 we infer the value of A at Glacier d'Argentière, a temperate alpine glacier, where we find softer ice than expected. We suggest that our observations can be explained with depth-increasing water content.

1.3.2 Hard bed friction and subglacial hydrology

In this section we review theories and observations of how glaciers slide over hard beds. Glacier - bed interactions and how the subglacial hydrology system behaves is very different between hard and soft beds, although some recent studies start to bridge the gap between them and propose general models that work well for both types of beds (Helanow et al., 2021; Maier et al., 2021a). Large-scale studies of glacier flow over hard beds require a friction law as boundary condition for properly constraining the problem. We will see that they are strongly linked to the state of the subglacial hydrology system. Several friction laws have been proposed throughout the decades, each with their own base assumptions. The choice of one law over another has a great impact in glacier velocities, and affects future estimates of glacier flow and sea level (Ritz et al., 2015; Brondex et al., 2017, 2019; Pattyn and Morlighem, 2020). Understanding the limits of these laws and, if possible, overcoming them is of great interest to glaciologists.

1.3.2.1 Theory

Classical friction laws A friction law (also known as slip law), is a mathematical relationship between glacier drag τ_b (resistance to flow) and sliding velocity u_b and other variables at the bed, i.e. a function of the form

$$\tau_b = f(u_b, \ldots). \tag{1.7}$$

A key concept is that τ_b and u_b are spatially averaged variables. At large spatial scales (hundreds and thousands of meters) τ_b is understood as a shear stress applied at the base of glaciers, and at the meso-scale (meters to tens of meters) τ_b is typically considered a result of compressive stresses around bed obstacles (Weertman, 1957). Equally, u_b refers not so much to the speed at the ice-bed interface, but to an averaged velocity a certain distance above the bed (Schoof, 2005). Despite this, τ_b is commonly called bed shear stress, and u_b is commonly called sliding velocity.

The great kick-starter of hard-bed sliding theory was Weertman (1957), who proposed the first slip law based on physical parameters. In this model, there is clean ice (i.e. with no debris) separated from the glacier bed by a thin film of water that lubricates the interface. The bed is rough, made of obstacles (cubicles in Weertman's original work, later changed to a wavy bed, e.g. Nye, 1969; Kamb, 1970; Morland, 1976a; Gudmundsson, 1997a). He envisioned that glacier slip at their base is a combination of two mechanisms. The first of them was regelation around obstacles, and the second was enhanced creep, which results from increased deformation due to stress concentration at obstacles (a result of the flow law proposed by Glen (1955)). The resultant law takes the form

$$\tau_b = A_s^{-1} u_b^{1/m}, \tag{1.8}$$

with A_s a constant that depends on the size and shape of the obstacles and creep factor A, among other variables. The original work of Weertman (1957) has been refined since (e.g. Nye, 1969; Kamb, 1970; Gudmundsson, 1997a), but it takes essentially the same form. If regelation is neglected, then $m = n$, the same exponent as in Glen's law, Eqn. (1.2). This law is represented by the dashed line in Figure 1.5 (top) and by a dash-dotted curve in Figure 1.5 (bottom). It is a monotonically increasing function: more basal speed is only possible if there is more drag at the base, which cannot explain intrannual changes in glacier speed (Lliboutry, 1968). It also underestimates glacier sliding speed for reasonable obstacle sizes (Lliboutry, 1968).

In view of these limitations, Lliboutry (1958) proposed an additional mechanism for glacier sliding that could explain intra-annual changes in glacier velocity as well as the fast glacier speeds observed in mountain glaciers. This third mechanism was called cavity opening[3]: if subglacial water becomes highly pressurized (for instance, due to an increase in water supply that cannot be evacuated by the subglacial hydrology system), it will push the overlaying ice, which will eventually detach from the bed. The opening of cavities thus will take place at the parts of the bed with the lowest pressure, typically the lee side of the obstacles (see the (a) to (d) drawings in Figure 1.5 (top)). As cavities grows they drown part of the obstacles and reduce the apparent roughness of the bed so that glaciers slide faster. The role of cavities is introduced in the friction law with a dependence on water pressure. In particular, it is common to consider the effective pressure $N = p_i - p_w$, the difference between ice pressure p_i (the weight of the ice column) and subglacial water pressure p_w, averaged over a given region. A friction law that takes into account the role of cavities through N can be found in the empirical law proposed

---

[3] Also known as cavitation. We prefer 'cavity opening' to avoid confusion with the more common cavitation considered in hydrodynamics, i.e. the phenomenon of bubble formation and bursting taking place in water flowing at high velocities.

by Budd et al. (1979),

$$\tau_b = A_B u_b^m N^p, \tag{1.9}$$

with m and p taking different values depending on the study, and A_B the corresponding sliding parameter of this law.

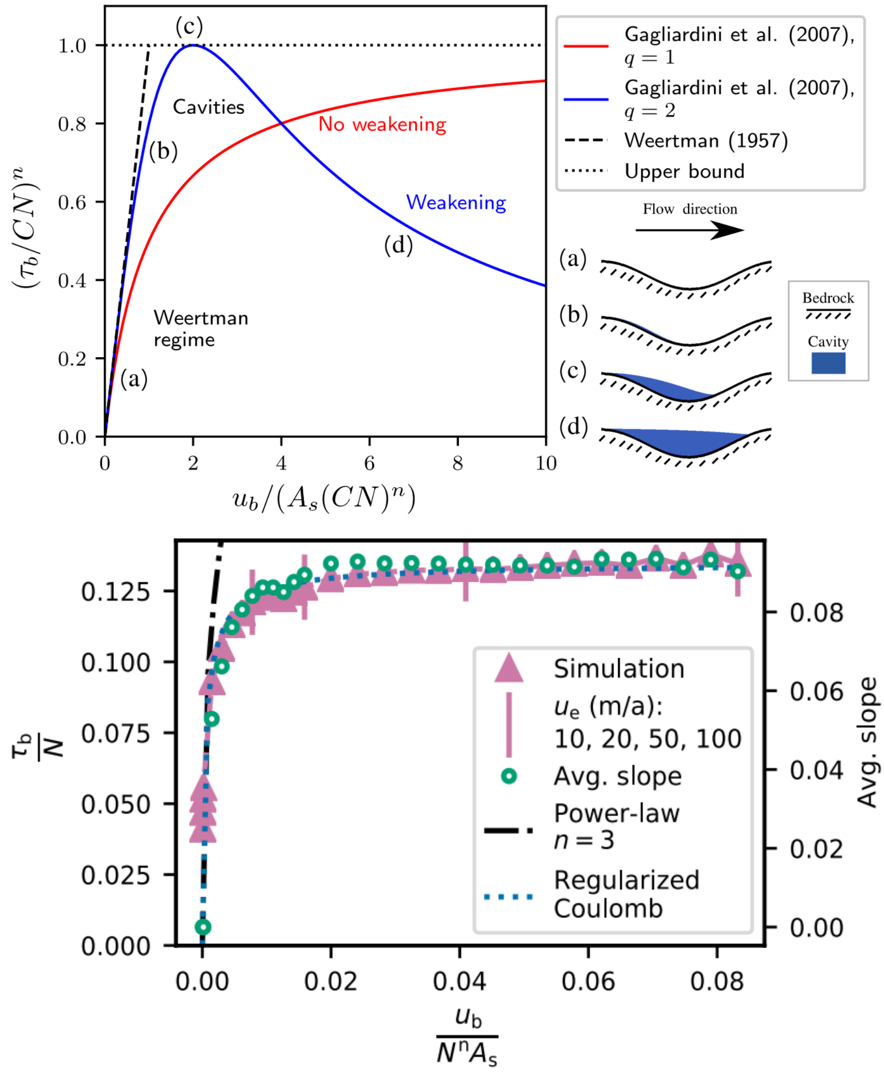

Figure 1.5: Scaled friction laws with cavities over synthetic (top) and realistic (bottom) beds. On the top we compare in the same space Weertman law (in dashed lines, Eqn. (1.8)) and the law proposed by Gagliardini et al. (2007) (Eqn. (1.10)) for $q = 1$ (red curve, monotonically increasing with asymptotic behaviour) and $q = 2$ (blue curve, multivalued). For the case $q = 2$ we provide four examples of what the cavity state looks like in subpanels (a) to (d) of the top figure, corresponding to the Weertman behaviour (a), the onset of cavities (b), the cavitation state at $\tau_b = CN$ (the cavity drowns the point at which bed slope is maximum $h' = \max(h')$) (c), and weakening range with extensive cavitation (d). On the bottom, we reproduce the friction law computed over the bed of Schwarzberggletscher (Switzerland) given in Figure 5 (A) of Helanow et al. (2021). The 'Power-law $n = 3$' curve is a Weertman law, (1.8) with $m = n = 3$. The 'Regularized Coulomb' curve, in blue dots, is an expression similar to Eqn. (1.10).

One feature of Eqn. (1.8) and Eqn. (1.9) is that they are formulated such that drag is not bounded by any physical variable, and thus τ_b can increase indefinitely. However, Iken (1981) demonstrated over a simple bed that the growth of cavities imposes an upper bound on τ_b/N, proportional to the maximum slope of the bed, later generalized by Schoof (2005) for a more general bed geometry. This upper bound stems from a force balance at the bed, therefore the friction law must respect it if we want the law to be physically consistent (Schoof, 2005).

A friction law that takes into account the role of cavities and includes the upper bound of τ_b/N is the phenomenological law proposed by Gagliardini et al. (2007) formulated after numerical experiments, and based on the developments of Fowler (1986) and Schoof (2005). Gagliardini et al. (2007) propose the following law that we reproduce in Figure 1.5 (top),

$$\frac{\tau_b}{N} = C\left(\frac{\chi}{1+\alpha\chi^q}\right)^{1/m}, \text{ with } \chi = \frac{u_b}{(CN)^m A_s},\ \alpha = \frac{(q-1)^{q-1}}{q^q}. \tag{1.10}$$

The parameter $C = \max(\tau_b/N)$ is bounded by the maximum bed slope (Iken, 1981). The exponent parameter $q \geq 1$ depends on the slope severity index, which describes the steepness of the obstacles for a given roughness (Gagliardini et al., 2007). For $q = 1$, τ_b/N increases monotonically (Fowler, 1987; Schoof, 2005) and we obtain a regularized Coulomb friction law (Joughin et al., 2019), while if $q > 1$ the law is double-valued and presents rate-weakening after the basal drag peak $\tau_b = CN$ is reached. For $u_b \ll (CN)^m A_s$, Eqn. (1.10) predicts a similar behaviour than Eqn. (1.8). Figure 1.5 (top) shows this law for $q = 1$ (red curve) and $q = 2$ (blue curve). Sustained rate-weakening is unstable and leads, in the absence of any controlling mechanism, to arbitrary high velocities. Thus, the existence of rate-weakening has been a common point in glacier friction studies (e.g. Iverson et al., 2019; Helanow et al., 2021; Gimbert et al., 2021a; De Diego et al., 2022), more so since it hasn't been observed in hard-bedded glaciers.

Subglacial hydrology We have discussed that water regulates sliding by opening cavities. The water originating from surface melting, rain, supraglacial and englacial lakes, deformation melting, etc, is routed by crevasses and moulins towards the base. If the base is temperate, the water reaches the bed and forms part of the subglacial hydrology system, otherwise it accumulates inside the glacier (as in Glacier de Tête Rousse, see Vincent et al., 2010). How water is spread along the bed depends on the subglacial water pressure, which is intrinsically coupled with water input, discharge and glacier velocities. During periods of low water discharge, typically winter, water is distributed in a network of cavities (Lliboutry, 1968). These cavities are either connected, thus allowing for water flow between them through tortuous, narrow waterways, or isolated from the main subglacial network. Flow within connected cavities is difficult, and thus the system is considered *inefficient*. Due to this inefficiency in discharging water, high water input results in increased storage, which increases subglacial water pressures. Increased water pressure in the cavity system leads to, as we discussed earlier, faster glacier flow due to reduced roughness (Lliboutry, 1968). The increase in the volume of stored water eventually connects cavities between them with large conduits, and water flow concentrates forming channels. These channels discharge water at lower pressures and higher water flux (Röthlisberger, 1972), thus the system is called *efficient*. The glacier slows down as water storage decreases, and the channel network collapses when water input eventually drops.

We illustrate this behaviour of the subglacial hydrology network with two examples in Figure 1.6. In Figure 1.6 (a) we show surface horizontal velocities, surface height and temperature (top) at a station in the Greenland Ice-Sheet and the discharge at a river 20 km downstream of the station (bottom), as discussed by Bartholomew et al. (2012). Bartholomew et al. (2012) interpret the behaviour observed in Figure 1.6 (a) as indicative of the transition from an inefficient to an efficient system. The glacier flows faster until mid July, where the surface is also higher, as a result of increased cavity size at the bed that lifts the glacier surface. The efficient system develops after mid July: glacier velocities and surface height drop while discharge is still high, indicating that cavities have emptied in favor of channels, and high pressures are no longer needed to distribute the subglacial water. In Figure 1.6 (b) we show the relationship between the depth of water in boreholes (a proxy of subglacial water pressures) and surface horizontal velocities in a nearby stake in Findelengletscher (Switzerland), a temperate alpine glacier, as studied by Iken and Bindschadler (1986). Iken and Bindschadler (1986) interpreted that the strong relationship between water pressures and velocities corresponded to a subglacial system made of connected cavities.

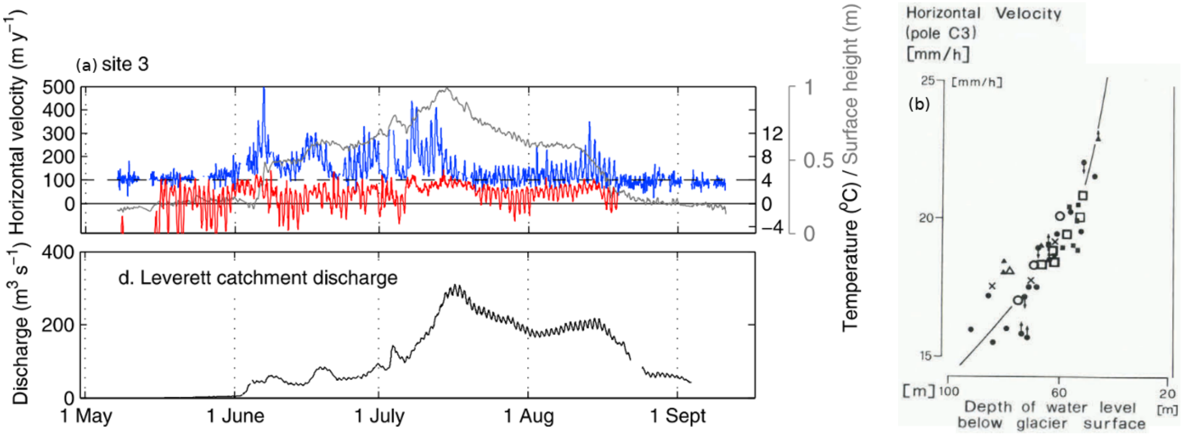

Figure 1.6: Surface velocity and other variables related to the state of the subglacial hydrology system in two different glaciers. Panels marked with (a) are taken from Bartholomew et al. (2012, Figure 6) and shows the horizontal velocity (blue), surface temperature (red) and surface elevation (grey) at a station in the Greenland Ice Sheet margin on the top, and discharge at a proglacial river 20 km downstream of the station on the bottom. Panel (b) is adapted from from Iken and Bindschadler (1986, Figure 6). It depicts the relationship between surface speed at a stake and borehole water levels (a proxy of subglacial pressures) in Findelengletscher (Switzerland), over several periods during the melt season (each symbol corresponds to a different period).

1.3.2.2 Observations and challenges

The frameworks for understanding sliding and the role of the subglacial hydrology system have been built on a combination of theoretical modeling and field observations. Here, we will discuss three limitations of the current theory that have been questioned for a long time. These three limitations are the base hypothesis followed since Weertman (1957) that at the ice-bed interface glaciers slide perfectly without friction, the role of fast changing water pressures in glacier velocity, and the scarce evidence that glacier friction laws are, indeed, representative of glacier sliding.

The role of non-zero local shear stress Most friction laws have been developed following the assumption of Weertman that a thin film of water separates the glacier from the bed at all contact areas, thus preventing any type of local shear stress at the ice - bed interface (i.e. a shear stress at a spatial scale lower than the meso-scale considered in for glacier friction laws). However, there is evidence of the presence of debris at the base of glaciers, either by direct observations of basal ice (e.g. Cohen et al., 2005, see also Figure 3.1), or by stick-slip events taking place at the ice-bed interface that can be explained by debris-bed friction (Wiens et al., 2008; Zoet and Iverson, 2015; Helmstetter et al., 2015; Roeoesli et al., 2016; Lipovsky et al., 2019; Köpfli et al., 2022). Observations show that debris-laden ice exerts additional resistance on the bed, so that it slides slower than clean ice (e.g. Cohen et al., 2005; McCarthy et al., 2017; Thompson et al., 2020). It is pertinent to consider how debris-bed interactions modify the friction laws derived assuming zero local shear stress at the ice-bed interface.

Some studies have tackled this problem. For instance, Morland (1976b) and Fowler (1979) studied how sliding with no cavities changed with non-zero local shear stress, the former for linear ice ($n = 1$) and the latter for non-linear ice and assuming low quantities of local shear stress. Schweizer and Iken (1992) studied the problem numerically for different local shear stress laws. Iverson et al. (2019) proposed a modification of Lliboutry (1968) to study how small quantities of debris affected sliding with open cavities (i.e. how it affected a law similar to Eqn. (1.10)). The results are similar among these studies, and point out that for low quantities of local shear stress we can expect the friction laws to be similar to Eqn. (1.8) and (1.10).

However, there are certain aspects missing in these studies. Firstly, they assume low quantities of local shear stress. Secondly, and by virtue of the low local shear stress assumed, they neglect the role that local shear stress plays in basal strain rates.

One of the objectives of the PhD is to study how non-zero local shear stress modifies a friction law with cavities, including the effect in ice viscosity that has been previously ignored. Chapter 3 is devoted to this work.

Unsteady water pressures and sliding Numerous studies have shown an increase in glacier speed concomitant with rising discharge and/or water pressures. Indeed, glacier accelerations typically takes place at the onset of the melt season (e.g. Iken and Bindschadler, 1986), as a result of lake drainage (e.g. Chandler et al., 2021), or after rain events (e.g. Hooke et al., 1989), all processes which increase the input of water to the bed. While the influence of unsteady water pressures on sliding has been observed for decades, glacier friction laws are formulated for the steady state, with controlling variables assumed constant in time. A few studies have recently started to consider the coupling between sliding and hydrology (e.g. Werder et al., 2013; Gilbert et al., 2022; De Diego et al., 2022). We distinguish here three types of approaches to study the interactions between the sliding and the subglacial hydrology system: i) models of either the hydrology system or glacier flow that take into account transient pressures or velocities but do not describe the other component, ii) unified models of hydrology and sliding that are not coupled, and iii) double-way coupled hydro-mechanical models.

Starting with models that describe one component, while incorporating the other, we have GlaDS (Werder et al., 2013), a 2D time-evolving model of a distributed and channelized hydrology system that can realistically reproduce the expected changes in subglacial hydrology over the course of a melt season (e.g. Schoof, 2010; Werder et al., 2013), or the more recent visco-elastic model for subglacial cavity evolution presented in Schoof (2023b) that reproduces how cavities connect to each other under unsteady water pressures. On the other hand, Gagliardini (2019) and De Diego et al. (2022) studied how steady solutions of glacier flow over a sinusoidal bed change under transient effective pressures, focusing on the friction law given in Eqn. (1.10). At slow variations of effective pressure, cavities adapt to changes in water pressure and the friction law remains overall the same; under fast changes of effective pressure, the cavity cannot adapt, and there is a lag between effective pressure and sliding speed. Both find that under fast changing effective pressures, the rate-weakening regime turns into rate-strengthening regime. The different boundary conditions that they used (fixed velocity in the case of Gagliardini (2019) and fixed drag in the case of De Diego et al. (2022)) may explain why Gagliardini (2019) results stay in the post-peak part of the friction law, while those of De Diego et al. (2022) go back to the rate-strengthening part. While this type of approaches are very valuable for understanding how water is distributed and how flow velocities change, they do not provide a unified picture. The undescribed component (i.e. sliding in Werder et al. (2013) and Schoof (2023b), pressure in Gagliardini (2019) and De Diego et al. (2022)) is treated externally to the studied system, and thus can lead to inconsistencies (Hewitt, 2013; Gagliardini and Werder, 2018).

An example of a unified model is provided in Tsai et al. (2021). In this study, water pressure regulates the extent of the bed which is drowned by the hydrology system, which in turn affects sliding. At the same time, water pressure is set by a complex, spatially variable hydrology system made of channels and cavities that change over time, thus bringing transient glacier velocities. This model, which can be seen as a one-way consistently coupled model, does not provide any control of water pressure by sliding velocity.

The third approach, and the most complete, consists in deriving intrinsically hydro-mechanical coupled models, such as the one proposed by Gilbert et al. (2022). In this case, the sliding velocity is provided by a friction law that depends on water pressures and cavity size, whereas cavity size depends on glacier sliding and water pressure, thus making a double-way coupled model. This approach was already taken by Louis Lliboutry almost 20 years ago, in an unpublished model of which only a recollection of notes is conserved.

One of the objectives of this PhD thesis is studying hydro-mechanical coupled models of sliding. We explain the unpublished hydrology - mechanical coupled model of glacier sliding presented by Lliboutry (2005) in Chapter 4, where we also compare it to the model proposed by Gilbert et al. (2022).

Validation of hard bed sliding theory So far, the presented friction laws have been derived using either analytical or numerical methods, but always over synthetic two-dimensional bed geometries, either cubic (Weertman, 1957), sinusoidal (Lliboutry, 1968; Nye, 1969; Gagliardini et al., 2007) or any irregular bed (Schoof, 2005). Several recent studies have considered the validity of these friction laws to represent sliding over more complex beds.

Zoet and Iverson (2015) ran lab experiments over sinusoidal beds (essentially, a lab adaptation of the numerical scheme studied by Gagliardini et al., 2007) and observed that a relationship such as Eqn. (1.10) was indeed representative of sliding of ice over sinusoidal beds. With this established, Helanow et al. (2020) showed that the same type of sliding law as Eqn. (1.10) can be obtained over synthetic, three dimensional beds, although the weakening range may not hold for some types of beds. Later, Helanow et al. (2021) repeated the numerical experiments over real beds belonging to deglaciated areas. They concluded that a friction law such as Eqn. (1.10) with no weakening represents well sliding over realistic bed geometries, as shown in Figure 1.5 (bottom). Meanwhile, other researchers looked for validation of friction laws at the natural scale. Gimbert et al. (2021a) showed that intra-annual variations in glacier sliding can be explained with cavity opening (Eqn. (1.10)), as shown in Figure 1.7 (a), while yearly averaged drag and sliding speeds at Glacier d'Argentière (French Alps) could be well represented by a law such as Eqn. (1.8). Maier et al. (2022) performed a similar validation over large spatial scales in Greenland, which we show in Figure 1.7 (b). They compared how differences in dynamics between the accumulation (circles) and the ablation zone (stars and squares) of the different catchments of the Greenland Ice Sheet varied spatially. Northern catchments show rate-strengthening behaviour in both accumulation and ablation zones, as seen for the squares lining up in the Weertman-like behaviour, while southern catchments differences between accumulation and ablation zones were well explained by a law such as the one given in Eqn. (1.10). These spatial differences were well correlated with the differences between the beds of northern and southern catchments.

Of the aforementioned studies, only Gimbert et al. (2021a) used direct measurements of sliding speeds, possible thanks to the subglacial cavity below the icefall at Glacier d'Argentière. However, these accessible cavities are rare, and in any case only provide the measurement of sliding at one

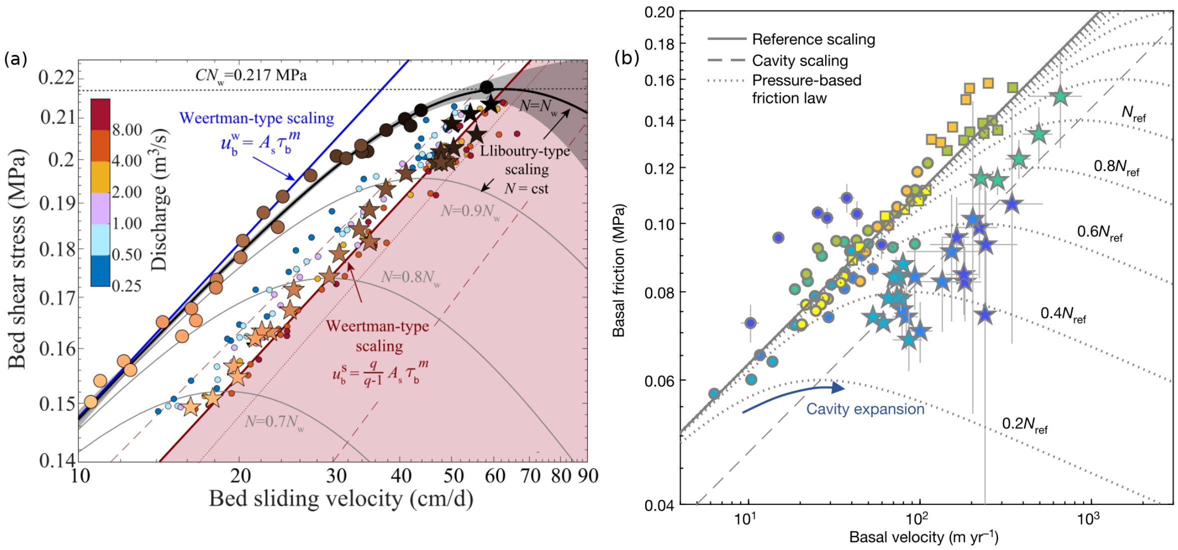

Figure 1.7: Validation of friction laws at the natural scale by Gimbert et al. (2021a) over Glacier d'Argentière (a) and by Maier et al. (2022) over Greenland (b). Panel (a) is taken from Gimbert et al. (2021a), Figure (2b), and panel (b) from Maier et al. (2022) Figure (2b).

specific point in the glacier. Fortunately, glaciologists have come up with several methods for indirectly observing sliding velocities, of which the most common is borehole inclinometry.

1.3.3 In-situ determination of ice rheology and velocity with borehole inclinometry

For more than 70 years, glaciologists have been using boreholes to observe the deformation of glaciers and measure their internal velocity. Whatever the specifics of the technique used, borehole inclinometry consists in measuring the change in inclination of a vertical borehole which is then used to infer the strain rate tensor $\dot{\varepsilon}$. With an estimation of the stress tensor τ, these measurements can be used to infer A and/or n (e.g. Perutz, 1950; Miller, 1957; Mathews, 1959). In Figure 1.8 (a) we reproduce the comparison of Nye (1953) of different stress-strain rates lines obtained from laboratory and field observations, where line number 2 corresponds to the borehole data from Jungfraufirn (Switzerland): strain rates are calculated from the deformation of a borehole, while the stress is computed assuming laminar flow. In this case, the stress - strain rates curves from the borehole data provide $n < 3$, which is not surprising since they correspond to effective deviatoric stresses lower than 0.1 MPa (10^6 dynes cm^{-2} = 0.1 MPa). Measuring internal strain rates also allow for computing the internal gradient of velocity in a glacier, which in combination with others observations such as surface velocities (e.g. with stakes, or recently with GPS networks) or subglacial water pressures, provide insights on bed processes. In Figure 1.8 (b) we show a sketch of the physical principle used to compute basal velocities directly from borehole-derived deformation velocity and surface velocity. Observations of internal velocities have allowed researchers to determine whether basal ice travels faster than overlaying ice or not (an early debated phenomenon called extrusion flow, e.g. Perutz, 1950; Sharp, 1953; Mathews, 1959; Hooke et al., 1987), to compare seasonal or intra-seasonal changes in surface, internal, and/or basal dynamics (Hooke et al., 1992; Harper et al., 1998; Amundson et al., 2006; Willis et al., 2003; Gudmundsson et al., 1999), and to constrain bed roughness (Ryser et al., 2014; Maier et al., 2019). Thus, we see that borehole inclinometry is a well known technique to understand the dynamics of glaciers.

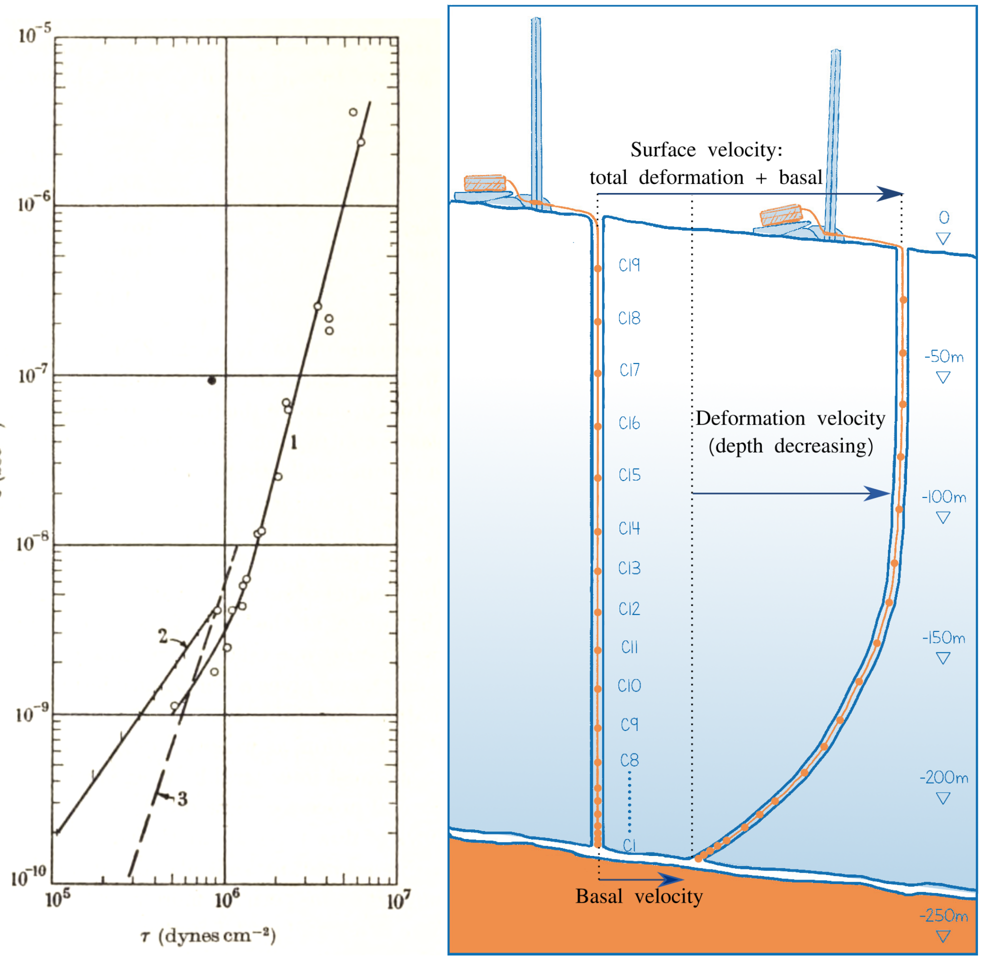

Figure 1.8: Examples of borehole inclinometry as a technique to measure ice rheological parameters (left) and basal velocities (right). On the left we reproduce the stress vs strain rates curves discussed by Nye (1953). Line 2 shows results from an inclinometry study carried out in Jungfraufirn (Switzerland) (Gerrard et al., 1952), where it was inferred that $n \leq 3$. On the right we schematize the use of borehole inclinometry to compute basal velocities. The left borehole shows the borehole after drilling with a number of deployed sensors (C19 to C1), the deformed borehole on the right shows the same borehole after some time. By measuring the change in shape over time, we can deduct the deformation velocity of the borehole. If we subtract the deformation velocity measured between the top and the bottom of the borehole to the surface velocity at the drilling site (i.e. how fast the top of the borehole has moved), we can infer the velocity at the base. Scheme adapted from Marine Jambeau's work for the SAUSSURE project: `https://saussure.osug.fr/-Drawing-78-`.

In Chapter 2, we will do a quick review on the field techniques used to measure glacier deformation with inclinometry and follow with the results from our inclinometry campaign on Glacier d'Argentière, where we used borehole inclinometry to infer the rheological parameters of the ice and compute basal velocities.

1.4 Motivation and approach of this PhD

As we have seen during this introduction, there are still many open fundamental questions regarding the flow of glaciers, all of which impact the assessment of the current and future state of the cryosphere. To answer some of these questions, the SAUSSURE project (`https://saussure.osug.fr/`) was proposed with the objectives *to evaluate, improve and validate various friction laws in a natural, geophysical scale configuration*. This project is a joint effort by several France-based geoscientists from different research institutions, to which this PhD thesis belongs.

This PhD thesis has the following objectives:

1. To analyze borehole inclinometry data in an alpine temperate glacier and use it to measure basal sliding velocities and infer ice rheological parameters.
2. To interpret those basal velocities and rheological parameters in the context of Glacier d'Argentière and explain the glacier dynamics over a melt season.
3. To develop a friction law for glacier sliding with non-zero local shear stress at the ice-bed interface, with and without open cavities, and compare it to friction laws that assume zero local shear stress.
4. To study the problem of glacier sliding with unsteady water pressures from the perspective of the last work of Louis Lliboutry, and compare it to recent approaches to the same problem.

In resume, we study in detail the problem of glacier flow over rough beds from different points of view and with different techniques, focusing on all three aspects that affect glacier sliding: ice material properties, the link between a glacier and its bed, and the role of unsteady water pressures.

1.4.1 Targeted modeling

In order to carry out this study we model the flow of glaciers at different scales and with different approaches. From larger to smaller scales, we start with the study the flow of glaciers at the large scale of hundreds to thousands of meters. At this scale, several physical processes such as ice-bed friction and the interactions with the subglacial hydrology system are represented by models. We consider this scale in the numerical simulations presented in Chapter 2 and the model described in Chapter 4. The next smaller scale that we consider in this PhD thesis is the meso-scale of meters to tens of meters. We focus on this scale to study the flow of glacier over obstacles and derive relationships between glacier velocity and basal drag in Chapters 3 and 4, and when describing the internal strain-rates of Glacier d'Argentière in Chapter 2. Micro-scale processes are not directly analyzed in this PhD thesis, although we consider several local shear stress constitutive laws that describe friction between ice and the bed at the micro-scale in Chapter 3.

The first modeling approach uses the Finite Element Method software for multi-physical problems Elmer/Ice (Gagliardini et al., 2013). This allows us to solve complex problems, and provides a more accurate result than those given by simplified analytical approaches. We use Elmer/Ice to simulate the flow of Glacier d'Argentière in Chapter 2, and to solve the flow of glaciers over rough beds in the spirit of Gagliardini et al. (2007) in Chapter 3. The Elmer/Ice model of Glacier d'Argentière has been developed by Adrien Gilbert and has been used in a variety of studies (Gimbert et al., 2021a; Gilbert et al., 2022; Vincent et al., 2022b). The second modeling approach implies the development of simplified analytical solutions of glacier flow, as we do in Chapter 2 to understand the deformation rates close to the bed, in Chapter 3 to obtain a friction law with non-zero local shear stress, and as was done by Lliboutry in the model we explain in Chapter 4. This allows us to understand the problem at hand in good detail, and establish a proper scaling analysis of the process as well as basic relationships between variables.

1.4.2 Dedicated instrumentation

The observational part of this PhD thesis makes use of an extensive network of instruments designed, installed, and maintained by project collaborators. Glacier velocities are observed with borehole inclinometry, a global navigation satellite system (GNSS) network and a subglacial wheel, which allow to partition the velocity of the glacier in surface, deformation and basal velocities, and compare them spatially and temporally. Glacier velocities are complemented with measurements of subglacial discharge at the glacier outlet and water pressure at the boreholes used to study glacier deformation. The former provides a picture of the global state of the subglacial hydrology system, while the latter provides a local snapshot of the hydrological conditions at one point in particular of the glacier.

The tools and instruments for carrying out borehole inclinometry have been designed at the Institute of Géosciences de l'Environnement (IGE, France) under the direction of Luc Piard, the GNSS network is managed by Anuar Togaibekov and Andrea Walpersdorf from the Institute de Sciences de la Terre (ISTerre, France), the subglacial wheel is maintained by Luc Moreau, associated researcher of Environnements, Dynamiques et Territoires de Montagne (EDYTEM, France), and the discharge is measured by the swiss hydroelectrical company Electricité d'Emosson SA.

1.4.3 Application to the Glacier d'Argentière, a well-documented glacier

While the aim of this PhD thesis is universal, and directed towards understanding the flow of any glacier in the world, we focus part of our investigations in one particular French alpine glacier, Glacier d'Argentière. Glacier d'Argentière (see Figure 1.1) is a temperate glacier located in the Mont Blanc range, French Alps (45°10 N, 6°10 E). The glacier rests on hard bedrock and extends for 9 km within an altitude range of 1600 m to 3400 m, separated by an icefall at an altitude of 2300 m. It has a maximum thickness of about 250 m to 230 m on the centerline of the ablation area (Vincent et al., 2009; Sergeant

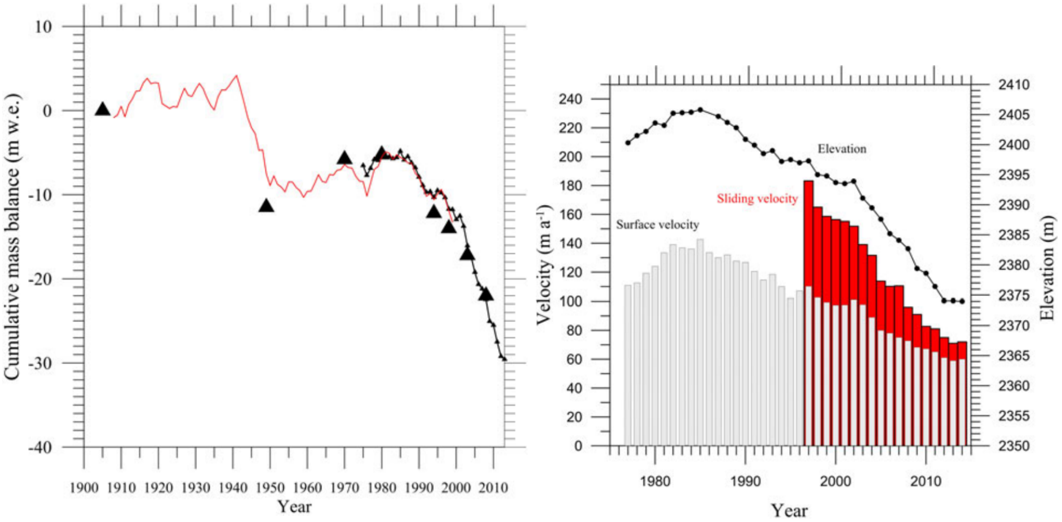

Figure 1.9: Cumulative mass balance of Glacier d'Argentière in the last century (left) and evolution of the dynamics at its ablation area (right) from 1977 to 2014, taken from Vincent and Moreau (2016). These two graphs show the clear link between glacier volume and velocities. The decline of the glacier has continued since these data were published, and surface velocities for 2020 and 2021 were lower than 50 m a^{-1} on average.

et al., 2020), flowing at an average speed of roughly 47 m a^{-1} in 2021. The proximity of the glacier to populated areas and its accessibility have allowed researchers to study Glacier d'Argentière for decades. Additional interest stems from the hydropower company Electricité d'Emosson SA, which since 1975 catches the subglacial flow of Glacier d'Argentière to fill a dam and provide electricity (see the technical sheet of Electricité d'Emosson SA, `https://emosson.ch/amenagements/prises-deau-dargentiere`). As a result, Glacier d'Argentière has a wealthy record of mass balance (one of the longest records in the world), ice cover, ice thickness, surface velocities, subglacial flow, among others (Vincent and Moreau, 2016). Sliding velocities are measured in a natural cavity close to the ice fall, a picture of which is later given in Figure 3.1. In the last years, the instrumentation network has been extended with a GNSS network (Togaibekov et al., 2022), seismometers (Helmstetter et al., 2015; Nanni et al., 2020a, 2021; Gimbert et al., 2021b), englacial tiltmeters (Roldán-Blasco et al., in preparation, see also Chapter 2) and other sensors (e.g. automatic weather stations, *smart* ablation stakes (Rabatel and Biron, 2021)), all of which allow for continuous survey of the behaviour of the glacier at short time-scales.

Glacier d'Argentière shows features typical of alpine glaciers. It has been retreating since the end of the Little Ice Age, with a marked acceleration in mass loss from early 2000's up to now, as shown in Figure 1.9 (Vincent, 2002; Vincent and Moreau, 2016). While we don't have available records of the ice fabric at Glacier d'Argentière[4], Vallon et al. (1976) observed in a nearby glacier that while ice had three to four principal directions, thereby being anisotropic, their directions were stable with respect to the stress field. As later Lliboutry and Duval (1985) discussed, 'this supports the currently held belief that glacier ice, despite producing an anisotropic fabric, behaves as an isotropic body during tertiary creep', thus we consider the ice at Glacier d'Argentière isotropic. Surface dynamics shows a seasonal pattern typical of mountain glaciers, with low surface velocity between September and April, followed by a period of sustained high velocity between May and August (Vincent and Moreau, 2016; Gimbert et al., 2021b; Vincent et al., 2022b). High subglacial runoff is observed during the summer period, and melt season acceleration as well as late summer deceleration is paired with fast increase and decrease of subglacial runoff, respectively (Vincent and Moreau, 2016; Vincent et al., 2022b). Observations of the local behaviour of the subglacial hydrology network are somewhat contradictory. Hantz and Lliboutry (1983) measured borehole water pressures at Glacier d'Argentière and determined that the drainage channel was probably located on the right margin of Glacier d'Argentière that regulated water pressure in cavities on the central part of the glacier. On a similar note, Vincent et al. (2022b) observed surface uplift during several summers, which could be explained with summer increasing cavity volume in the central part of the ablation area. On the other hand, Nanni et al. (2021) observed active subglacial flow at the onset of the 2019 melt season, and concluded that the overdeepened area drained water through a subglacial channel. The observations at Glacier d'Argentière are complemented with a three dimensional numerical model of the glacier that solves glacier flow without approximations (Gagliardini et al., 2013), and accurately represents glacier surface velocities and ice thickness (e.g. Gimbert et al., 2021a; Gilbert et al., 2022; Vincent et al., 2022b). We use this model in Chapter 2.

The combination of rich observations and numerical modeling make Glacier d'Argentière a perfect natural and numerical laboratory for studying glacier flow, and improving our understanding of it. Because the glacier displays many characteristics representative of temperate valley glaciers, the conclusions obtained regarding the behaviour of Glacier d'Argentière can be easily exported to other alpine glaciers.

---

[4] Hantz and Lliboutry (1983) indicate that such measurements were made following the 1981 field campaign, however they were never published.

1.5 Structure of the manuscript

This manuscript is made of 5 Chapters, structured thematically. Chapter 1: "Context and introduction", is the Chapter that the reader is just finishing now. Then, there is one Chapter devoted to observations and two Chapters devoted to modeling of glacier flow. In Chapter 2: "Deformation, creep enhancement and sliding in a temperate alpine glacier", we show our observations of internal deformation rates in Glacier d'Argentière, and what conclusion we draw regarding ice material parameters and the dynamics of the glacier. In Chapter 3: "The effect of local shear stress on glacier sliding", we review our work on glacier friction laws with non zero local shear stress at the base. Then, in Chapter 4: "Visiting the coupling between hydrology and friction from the perspective of the lost last paper(s) of Louis Lliboutry" we shed a light on the unpublished hydro-mechanical coupled model of glacier flow developed by Louis Lliboutry shortly before his death (Lliboutry, 2005), and compare it with a recent, similar model. We finish the manuscript with Chapter 5: "Conclusions and perspectives", which provides an overview of the PhD and the achieved goals and discusses some new questions that arise from the work done here. The contents of the PhD are supported by several annexes: Annex A includes a supplementary overview on continuum mechanics, Annex B provides an overview on methods used to infer glacier deformation rates, Annex C provides preliminary results linked to Chapter 2, Annex D provides the supplementary materials to the contents of Chapter 2, Annex E provides the supplementary materials to the contents of Chapter 3, and Annex **??** reproduces the original paper of Lliboutry (2005) studied in Chapter 4 and provide its translation to English.

Chapter 2

Deformation, creep enhancement and sliding in a temperate alpine glacier

> *I had to remain on the glacier all summer. One night, the shelter where I was sleeping was blown down by a squall: I was only slightly injured, but two weeks of records were lost*
>
> Adapted from Didier Hantz' account of a borehole campaign in 1981 on Glacier d'Argentière.

2.1 Preface

Chapter 1 introduced borehole inclinometry as a technique for measuring the internal deformation rate of a glacier and inferring rheological parameters, basal velocities and other aspects that govern basal processes and glacier dynamics. In this Chapter we describe how we applied this technique in Glacier d'Argentière and what conclusions we draw regarding the glacier rheology and annual dynamics. Sections 2.3 to 2.11 and most of Annex D are based on the paper: J.P.Roldán-Blasco, L.Piard, A.Gilbert, F.Gimbert, C.Vincent, O.Gagliardini, A.Togaibekov, A.Walpersdorf, N.Maier; "Deformation, creep enhancement and sliding in a temperate alpine glacier", undergoing the final stages of preparation before submission to *The Cryosphere*. Some changes to the text in those sections and some refinement of the results can be expected over the coming weeks, and some repetition with the text elsewhere can be found. This study has been presented at different stages of development at several conferences and meetings: 24th AGM (online), EGU 2021 (online), G2 2022 (Grenoble, France), and soon will be presented in the 26th AGM (Birmensdorf, Switzerland). After this preface, the Chapter starts with a short review on the technique of borehole inclinometry and previous results. It continues with the results of the first inclinometry campaign carried out in Glacier d'Argentière during 2019 and 2020, and includes the preliminary results of a second inclinometry campaign carried out during 2021 and 2022.

2.1.1 Setting

The borehole inclinometry campaign carried out in Glacier d'Argentière was part of the new field measurements of the SAUSSURE project. Since the project focused on basal processes and sliding, borehole inclinometry was meant to provide measurements of basal velocities in Glacier d'Argentière. As we saw in Chapter 1 and present later in this Chapter, this is something that glaciologists have been doing for decades and there are plenty observations and published studies on the subject. The only problem is that it was the first time that we carried out this type of field experience, and as such there was simply no expertise whatsoever in our lab[1]. Despite this, the researchers and engineers at IGE did a very good job designing the experiment and the instrumentation, and now this experience has been acquired. The first borehole campaign was carried out in September 2019, and for the first months the results were not very hopeful: the sensors were still not completely coupled to the ice, a few had stopped functioning and it seemed at first like not much could be done. Over time, though, the sensors started to provide good quality results and we started to get a clearer picture of the strengths and weaknesses of our study.

I volunteered to analyze the field data somewhere in 2020, as it seemed like a very interesting secondary project to do during the PhD. At the beginning I was mostly focused on developing the Python scripts and modules to automatize all the data-processing. By the time the processing pipeline was established, we started to have the first results, and we realised that the project was not going to be as straightforward as intended originally: the basal velocity at Glacier d'Argentière was not evolving through the summer as we expected, and the ice at Glacier d'Argentière seemed much softer than we had anticipated. The project eventually became a large part of this PhD. A lot of time was thus devoted to being sure that our measured deformation were correct, and that there were reasonable explanations for our observations. In the meantime, the second inclinometry campaign was originally intended to repeat the 2019 experience and validate the data, but was eventually carried out on the right margin.

2.1.2 Contributions

The work presented is a testimony to scientific collaboration. The borehole instrumentation was designed and built by the engineers of IGE under the lead of Luc Piard. Luc Piard also performed the initial analysis and regularly visited the glacier to collect the data recorded at the inclinometers. Several members of the project participated in the tiresome drilling campaigns (Bruno Jourdain, Olivier Laarman, Luc Piard, Christian Vincent, among others), with others assisting occasionally (Olivier Gagliardini, Florent Gimbert, Adrien Gilbert, Marine Jambeau, and myself among others). The data obtained from these campaigns was complemented with the GPS data provided by Anuar Togaibekov and Andrea Walpersdorf (ISTerre), who were also in charge of installing the GNSS network and ensuring with continuous field visits that it was working as intended. Finally, the work presented here uses the three-dimensional numerical model of Glacier d'Argentière developed by Adrien Gilbert, who was in charge of running the different numerical simulations presented in this Chapter, and was the one that initially proposed the role of interstitial water as a plausible explanation for our results. Finally, during most of the first part of the project Nathan Maier helped me understand what was going on inside the boreholes, and Ugo Nanni supported me with additional early analysis of the tilt.

2.2 Borehole inclinometry

2.2.1 General principles

Borehole inclinometry consists in measuring the internal deformation of a glacier through surveying the change in tilt of one or several vertical boreholes drilled, ideally, from the surface down to

---

[1] This is the first successful study of its type done in IGE. Apparently, a previous campaign was carried out in the early 80's (Hantz and Lliboutry, 1983), whose results were not published and linger somewhere in a box. In any case, all those who participated in that campaign are already retired.

the base. The amount of information that can be extracted from borehole inclinometry depends on the technique used, the density of boreholes, the quality of the instrumentation (e.g. measuring frequency, spatial density of measurements, accuracy of the instruments) and the quality of the borehole itself (verticality, borehole diameter, depth). As we will see later, different techniques can provide a series of snapshots of the internal deformation, with good spatial coverage, or on the contrary, allow for observing short term changes in deformation at the cost of lower spatial density. The information extracted also depends on the spatial arrangement of boreholes on the surface of the glacier. Boreholes close to each other (at least at distances lower than an ice-thickness) can help isolate the influence of local differences in the subglacial hydrology network (Willis et al., 2003), or in bed roughness (Maier et al., 2019), while boreholes located further from each other can provide a more general picture of the ice flow. We provide in Tables 2.1 and 2.2 a resume of inclinometry studies carried out in temperate glaciers with traditional techniques, and in temperate and polythermal glaciers with newer techniques.

Good quality drilling helps ensure that the borehole stay vertical and reach the bed more easily. In such a case, borehole inclinometry can be used to observe the complex deformation that takes place above a glacier's bed, and provide an accurate measure of basal velocity. Unfortunately there are several complications that arise when working in temperate glaciers. First and foremost, temperate glaciers do not freeze, except close to the surface if ambient temperatures are below zero. The direct consequence of these is that unless close to the surface, we will have to wait for creep to close the borehole and ensure the coupling between the sensors and the glacier provided that water does not keep it from closing. If working in a valley glacier, it is common to find rocks and stones in the ice that complicate drilling (Flusin and Bernard, 1909; Meier, 1960; Mathews, 1959; Hantz and Lliboutry, 1983; Roldán-Blasco et al., in preparation)[2]. The deeper the boreholes reach, and the longer the survey period, the stronger the strains they will be subjected to. Thus, it is not uncommon for borehole inclinometry to start failing (e.g. boreholes become obstructed or data transmission cables start to break) from the bottom up to the top (Hooke and Hanson, 1986; Doyle et al., 2018; Maier et al., 2019; Roldán-Blasco et al., in preparation). For the same reason it is particularly useful in low strains environments, such as rock glaciers (e.g. Arenson et al., 2002). We will later see the influence of these problems when we describe the field campaigns. In Annex B we provide a quick overview on methods used to infer deformation rate and velocities from borehole inclinometry analysis.

2.2.2 Techniques

2.2.2.1 Repeated inclinometry

Repeated inclinometry is the oldest technique for determining the internal deformation of a glacier. It consists in measuring the shape of a borehole during different times over the course of a field campaign. Inclinometry readings can be obtained by lowering a tiltmeter that, following the shape of the borehole, measures its inclination and orientation, i.e. the tilt and azimuth (see Figure 2.1), at a certain spatial interval. As boreholes tend to close, there are different ways of keeping it open for future surveys. The borehole can be cased in a metal tube (e.g. Miller, 1957; Mathews, 1959) for easier operation of the tiltmeter. In this case, an important source of uncertainty comes from the degree of coupling between the tube and the surrounding ice, which makes it difficult to identify whether the measured change in slope is the same as that of the glacier. Another variation of this technique can

---

[2] The case of Meier (1960) is somewhat extreme: due to several faulty components of his drilling apparatus, rocks in the ice, filtration of water, and a pipe wrench that fell into a borehole, Frank Meier reported "Three summers' work drilling with hotpoints resulted in the successful emplacement of one 150- foot pipe [... and ...] two pipes less than 300 feet long [...]. One of these latter pipes became useless when [... water froze] inside the pipe".

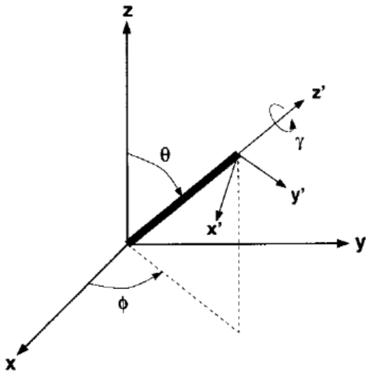

Figure 2.1: Orientation of a tiltmeter in a three-dimensional reference system. Tilt angle θ is the angle of the tiltmeter with the vertical direction, azimuth angle φ is the angle with respect to a given horizontal direction. The angle γ describes the angle with which the tiltmeter rotates around itself. The image is taken from Gudmundsson et al. (1999), Figure 1.

be found in Raymond (1971). This alternative installs a cable in an uncased borehole, which guides the tiltmeter as it moves through the borehole. Following field surveys then redrill the borehole along the cable and measure its new shape.

Since the tiltmeter has to travel the borehole twice, one descending and one ascending, repeated inclinometry provides two sets of readings per borehole per survey, which minimizes the measuring error. Copland et al. (1997) surveyed three boreholes up to 7 times, providing therefore 14 sets of measurements per borehole. Apart from the (potential) low error in the inclinometry measurement, repeated inclinometry provides observations with good in-depth spatial density, typically every one or two meters. Material wise, it can be argued that it is not an expensive technique, since except for the casing or cables, which stay trapped in the ice, the rest of the instruments are recovered after every borehole is measured. On the other hand, it is field work intensive since drilling and measuring deformation can take hours per borehole. As a result, the time interval between surveys are of the order of weeks or months. Some studies have used this technique to characterize the flow over a great portion of the glacier, installing a dense network of boreholes along and across the main flow direction to study temporal and spatial differences in internal dynamics (e.g. Raymond and Harrison, 1975; Harper et al., 1998; Willis et al., 2003).

2.2.2.2 Englacial tiltmeters

A more modern technique is the use of permanently installed sensors, called tiltmeters, that measure continuously the borehole deformation. Other sensors can be added to provide complementary information, such as piezometers to record water pressure or calorimeters to measure the temperature of the ice. Tiltmeters are usually designed *ad-hoc*, and are typically found in two versions. The most complete design measures the tilt and azimuth (see Figure 2.1), either with two orthogonal accelerometers (Ryser et al., 2014; Maier et al., 2019, 2021c), or with an accelerometer and a magnetometer (Lee et al., 2019; Roldán-Blasco et al., in preparation). The first accelerometer allows the sensor to measure its tilt, while the second one allows for computing the azimuth with respect to a machine 'zero' direction. The magnetometer allows computing the azimuth with respect to the magnetic north. The simplest design just measures the tilt using a single triaxial accelerometer, such that the direction of tilt change is typically assumed as the flow direction at the instruments location. Examples of this latter design can be found in Gudmundsson et al. (1999) and in the tiltmeters installed in 2021 on the right side of

Glacier d'Argentière, explained later in this Chapter. Special attention must be given to instrument construction and calibration, since once installed there will be no way to retrieve them and modify them.

Englacial tiltmeters can be considered complementary to repeated inclinometry. First, they record glacier deformation at high temporal frequency, of the order of hours, see Table 2.2. As long as the sensors are connected to an external power source, they operate autonomously, reducing the amount of field trips necessary. Moreover, if communication networks are available such as for our 2nd inclinometry campaign on Glacier d'Argentière, wireless data transmission reduces even further the density of field trips compared to repeated inclinometry. With respect to the spatial density of sensors, on one hand the advent of cheap microcontrollers rends the material cost down and facilitates reasonable spatial density: see in Table 2.2 how the distance between sensors has been generally decreasing with time. On the other hand, the time spent building and calibrating the sensors is pretty high, which limits the deployment of large number of boreholes.

2.2.3 Brief literature review

In this section we provide a couple of Tables that resume borehole inclinometry surveys in temperate glaciers, and surveys with englacial tiltmeters in polythermal glaciers, Tables 2.1 and 2.2. Thus, we have left out of this review those studies carried out in ice-sheets using repeated inclinometry (e.g. Dahl-Jensen and Gundestrup, 1987), or carried out in cold glaciers (e.g. Hooke, 1973; Hooke and Hanson, 1986) or rock glaciers (e.g. Arenson et al., 2002). Column *Study* shows the original paper in which the study appears. Sometimes the same inclinometry study stems several research papers, such as Harper et al. (1998, 2001) or Maier et al. (2019, 2022), in which case we show the first. Column *# BH* denotes the number of boreholes instrumented, even though some of them could not be properly studied. *Location* describes how the boreholes where arranged with respect to the main flow direction (along, or transverse to it), and where on the glacier (center means centerline, margin means at or between the center and one or both lateral margins). *Duration* reflects the duration of the survey considered in the analysis of each study, not necessarily the time during which individual boreholes were studied. Δt shows either the average time between repeated inclinometry measurements, or the frequency with which englacial tiltmeters record their tilt. Δz gives the distance between repeated inclinometry measurements or the maximum and minimum distances between consecutive tiltmeters. In *Notes* we provide accessory information.

We can extract a few conclusions from the Tables. First, we can see that in general inclinometry campaigns have become more ambitious over time as the techniques became more refined. Compare the few boreholes employed in the earlier repeated inclinometry studies on temperate glaciers with the extensive study by Harper et al. (1998) in Worthington Glacier. A similar conclusion can be drawn when comparing the ratio dz - depth of Gudmundsson et al. (1999) and Keller and Blatter (2012) with later studies. Most studies are concerned about deploying stations along a flow line and at the center of the glacier, in part probably to avoid lateral variations in the flow and facilitate the analysis. Those who drilled across the glacier main flow direction did it to look explicitly for lateral variations in the flow (Copland et al., 1997; Harper et al., 1998; Lee et al., 2019). There is a clear increase in the frequency of data-acquisition from Hooke et al. (1987) onward, with field surveys prior to 1987 measuring deformation rate over years, which after 1987 became weeks, then days, and then hours. This is probably a result of the increased interest in observing seasonal and subseasonal changes in glacier dynamics, following studies such as Iken and Bindschadler (1986).

Study	Glacier	Technique	#BH	Location	Depth m	Bed	Duration	dt	dz m	Notes
Perutz (1950)	Jungfraujoch (Switzerland)	Repeated	1	-	-	Yes	14 months	14 months	12	First study with repeated inclinometry
Sharp (1953)	Malaspina Gl. (USA)	Repeated	1	Center	305	No	1 year	3-5 weeks, 1 year	15	Only half the thickness was bored
Miller (1957)	Taku Glacier (USA)	Repeated	1	Center	75	No	38 months	4 - 15 months	1.5-6	Only 1/4 of the thickness was bored
Mathews (1959)	Salmon Glacier (USA)	Repeated	1	Center-ish	495	Yes	94 days	94 days	15-30	5 other boreholes were uninstrumented
Meier (1960)	Saskatchewan Glacier (Canada)	Repeated	1	Center	45 - 75	No	2 years	1 year	7.6	A very good example of how ungrateful borehole driling can be on temperate glaciers
Savage and Paterson (1963)	Athabasca Glacier (USA)	Repeated	4	Along 2 lines per side	314-206	Yes	3 years	1 year	15-7.5	Ice blocked three boreholes during the survey
Shreve and Sharp (1970)	Blue Glacier (USA)	Repeated	6	5 along center, 1 at margin	119-224	Yes	5 years	1 year	7.5	Only 1 borehole reached lower than 80% thickness
Hooke and Holmlund (1987)	Storglaciären (Sweden)	Repeated	1	Center	126	Yes	2 months	1 - 2 weeks	1 m	Observe extrusion flow during summer.
Hooke et al. (1992)	Storglaciären (Sweden)	Repeated	3	Center and margin	130 - 162	Yes	3 years	1 - 2 weeks	1 m	The profile of deformation changed during summer.
Copland et al (1997)	Haut Glacier d'Arolla (Switzerland)	Repeated	25	Across glacier	250 - 25	Yes	3 weeks	2 - 3 weeks	1 m	Short time between surveys yield too high uncertainties
Harper et al. (1998)	Worthington Glacier (USA)	Repeated	28	Along and across	180 - 200	Yes	60 - 70 days	1 - 30 days	2 m	Good 3D field of deformation. Most boreholes reached 10 m from the bed.

Table 2.1: A review of inclinometry surveys in temperate glaciers with any technique, and in polythermal glaciers with englacial tiltmeters. Part 1 of 2.

Study	Glacier	Technique	#BH	Location	Depth m	Bed	Duration	dt	dz m	Notes
Gudmundsson et al. (1999)	Unteraargletscher (Switzerland)	Englacial	1	Center	260	No	2 years	6 h	25 - 85 m	First study with englacial tiltmeters
Willis et al. (2003)	Haut Glacier d'Arolla (Switzerland)	Repeated and englacial	7	Along center and margin	30 - 130	Yes	15 months	15 months	1	Highly spatial variability in seasonal evolution of velocities
Keller and Blatter (2012)	Rhonegletscher (Switzerland)	Englacial	1	-	119	Yes	27 months	5 min - 8h	20	Other borehole was installed in Gornergletscher, with 1 tiltmeter
Ryser et al. (2014)	Greenland Ice Sheet	Englacial	4	Center	700 - 620	Yes	1 year	10 min	1 - 100	Kink in du/dz close to the base due to bed bumps and sticky/slippery patches
Doyle et al (2018)	Store Glacier (West Greenland)	Englacial	1	Center	611	Yes	2 months	1 h	4 - 150	Only 5 tiltmeters, most of them close to each other at the bed.
Maier et al. (2019)	Greenland Ice Sheet	Englacial	9	Margin	640 - 688	Yes	2 years	2 - 4 h	10 - 20	Kink in du/dz close to the base due to hard-bed sliding over obstacles
Lee et al. (2019)	Jarvis Gl. (USA)	Englacial	2	Margin	18 - 72	Yes	1 year	6 h	1 - 9	Found high enhancement factor (possibly anisotropy)
Roldan-Blasco et al (in prep)	Glacier d'Argentière (France)	Englacial	5	Along center	235	Yes	13 months	30 min	1 - 20	See this Chapter
Roldan-Blasco et al (in prep)	Glacier d'Argentière (France)	Englacial	4	Along margin	160-190	Yes	9 months	30 min	1 - 40	See this Chapter

Table 2.2: A review of inclinometry surveys in temperate glaciers with any technique, and in polythermal glaciers with englacial tiltmeters. Part 2 of 2.

2.3 Abstract

Glacier internal deformation is controlled by the ice rheology which is described by the Glen's law through two material parameters, the creep factor A and the flow law exponent n. There is great uncertainty in the values of these parameters as a result of scarce observations at the natural scale. One of the techniques that has been used to study ice deformation and constrain material properties is borehole inclinometry. We present here the results of an inclinometry study carried out at the ablation zone of Glacier d'Argentière, a temperate glacier in the French Alps. We monitored glacier deformation from late 2019 to late 2020 with borehole-installed tiltmeters that record tilt change every 30 minutes. We are able to reconstruct the deformation rate profile with depth and the resulting deformation velocity. Complementing our dataset with GPS-derived surface velocity, we are able to indirectly observe the basal velocity during the studied period. We infer the rheological parameters by comparing our observations with the deformation rate retrieved with a three-dimensional model solving the Stokes equation. We demonstrate that the yearly-averaged deformation rate profile has limited sensitivity to the flow law exponent n and instead mainly reflects an increase in the creep factor A with depth which could be explained with depth-increasing interstitial water content. The depth-averaged creep factor is found to be 1.5 times higher than the recommended one for temperate ice. We further show that internal ice deformation exhibits seasonal variability, such that surface velocity changes cannot be attributed solely to changes in basal conditions. At longer timescales, surface velocity variability is better explained with changes in the deformation rate, while shorter velocity variability (weeks or days) is better explained with changes in basal velocity. Summer increase in deformation velocity suggests increased drag due to ice-bed coupling during summer resulting from the development of a drainage channel in the central part of Glacier d'Argentière.

2.4 Introduction

Internal deformation of glaciers is a fundamental component of ice flow models, and for many mountain glaciers accounts for a high portion of total ice flow (e.g. Mathews, 1959; Paterson, 1970; Shreve and Sharp, 1970; Harper et al., 2001). However, ice deformation quantification at the natural scale is complicated due to the strong dependency on ice material properties and stress (Glen, 1955). The values of rheological parameters retrieved through laboratory experiments differ within different experiments (Cuffey and Paterson, 2010), and from those retrieved with large-scale observations (Cuffey and Paterson, 2010; Gillet-Chaulet et al., 2011; Millstein et al., 2022).

Borehole inclinometry provides information about the interaction between the bed topography, the stress distribution and the internal deformation rate (Raymond, 1971; Hooke and Hanson, 1986; Ryser et al., 2014; Maier et al., 2019). Several bed-reaching borehole surveys (Ryser et al., 2014; Doyle et al., 2018; Maier et al., 2019) have shown that deformation rate dependency with depth becomes increasingly complex as we approach the bed due to basal boundary effects, with deformation maxima not located at the ice-bed interface but a certain distance above it. Some of these observations can be explained either with a combination of sticky and slippery patches and bed overdeepenings (Ryser et al., 2014), or with flow over a bumpy bed (Maier et al., 2019), as expected from boundary layer theory applied to hard-bed sliding (Kamb, 1970; Gudmundsson, 1997b). Borehole surveys in temperate valley glaciers detected intra-annual changes in deformation rate patterns, generally attributed to stress redistribution resulting from changes in the subglacial hydrological network (Hooke et al., 1992; Willis et al., 2003). The extent to which the detected changes in deformation rate are spatially representative of the glacier is unclear, and observations at a borehole can be representative of only a small portion of the glacier. For instance, Willis et al. (2003) found that seasonal changes in deformation rate varied greatly at distances lower than an ice thickness, suggesting that a complex subglacial hydrology system with spatially and temporally heterogeneous water pressure distribution was the cause of the disparity in deformation rate between nearby boreholes.

With the deformation rate profile known, good constrains on the stress distribution allows to directly estimate *in-situ* material parameters, such as creep factor, creep enhancement and flow exponent (Mathews, 1959; Hooke, 1973; Dahl-Jensen and Gundestrup, 1987), or at least provide constrains on them (e.g. Maier et al., 2019). Additionally, measuring the deformation rate in a glacier provides, coupled with surface velocities, an indirect measure of the basal velocity (e.g. Harper et al., 1998; Gudmundsson et al., 1999; Ryser et al., 2014; Maier et al., 2019, 2021b). Given the scarce observations of ice rheology at the natural scale and basal velocities, ice flow models tend to use inverse methods to estimate the best material parameters that allow best matching the surface velocity (Vincent and Moreau, 2016; Zekollari et al., 2019; Millan et al., 2022). The problem is however largely undetermined due to multiple solutions leading to the same surface velocity field. Additional uncertainty arises from basal slip quantification, which is commonly inverted assuming known material parameters (Morlighem et al., 2013; Derkacheva et al., 2021; Maier et al., 2022), and sometimes inverted together with ice rheology (e.g. Hill et al., 2018).

In the following sections, we look at deformation data of Glacier d'Argentière (French Alps) to determine its internal dynamics and reconstruct the basal speed during eight months. We do so with a combination of observations, with the novelty of using several tiltmeter arrays permanently installed in boreholes drilled along the main flow line of the ablation area during late 2019 and 2020. Our dataset constitutes one of the longest continuous records of ice deformation in temperate ice, with previous studies (e.g. Willis et al., 2003; Amundson et al., 2006; Keller and Blatter, 2012) involving observations over much shorter time periods and with lower sensor density with depth, and other records of similar length and with high sensor density being obtained in polythermal glaciers (Ryser et al., 2014; Maier et al., 2019; Lee et al., 2019). We find creep enhancement at our site, which can be due to realistic water content in the ice. We also infer that seasonal changes in glacier velocity at our site is mostly due to changes in deformation velocity, with basal velocity involved only in short-term accelerations. We first describe the study site and the measurement methods. We then analyse the observation in terms of material parameters using a three dimensional ice flow model and finally provide the observed time series of both deformation and basal velocities.

2.5 Field site and instrumentation

2.5.1 Field campaign

The drilling site are located in the central part of the ablation area, between 600 and 800 m upstream of the icefall. The thickness at the center flow line of this area is about 230-250 m, see Figure 2.2 (a) and Table 2.3. The average surface speed at this location is about 47 m a^{-1} (Vincent et al., 2022b). A DEM of basal topography (black lines in Figure 2.2 (a)) is available with a mean uncertainty of ± 10 m (Vincent et al., 2009), and shows an over-deepening where most of the boreholes are located.

Drilling operations took place between the 12th and the 14th September, 2019. The boreholes were done with a custom-built hot water driller operating at 70°C, that drills a water-filled borehole with a 10 cm diameter at an average speed of 60 m/h. Insufficient weight of the driller head, fast drilling speeds, and intraglacial debris affected the verticality of the boreholes. In several occasions, probably

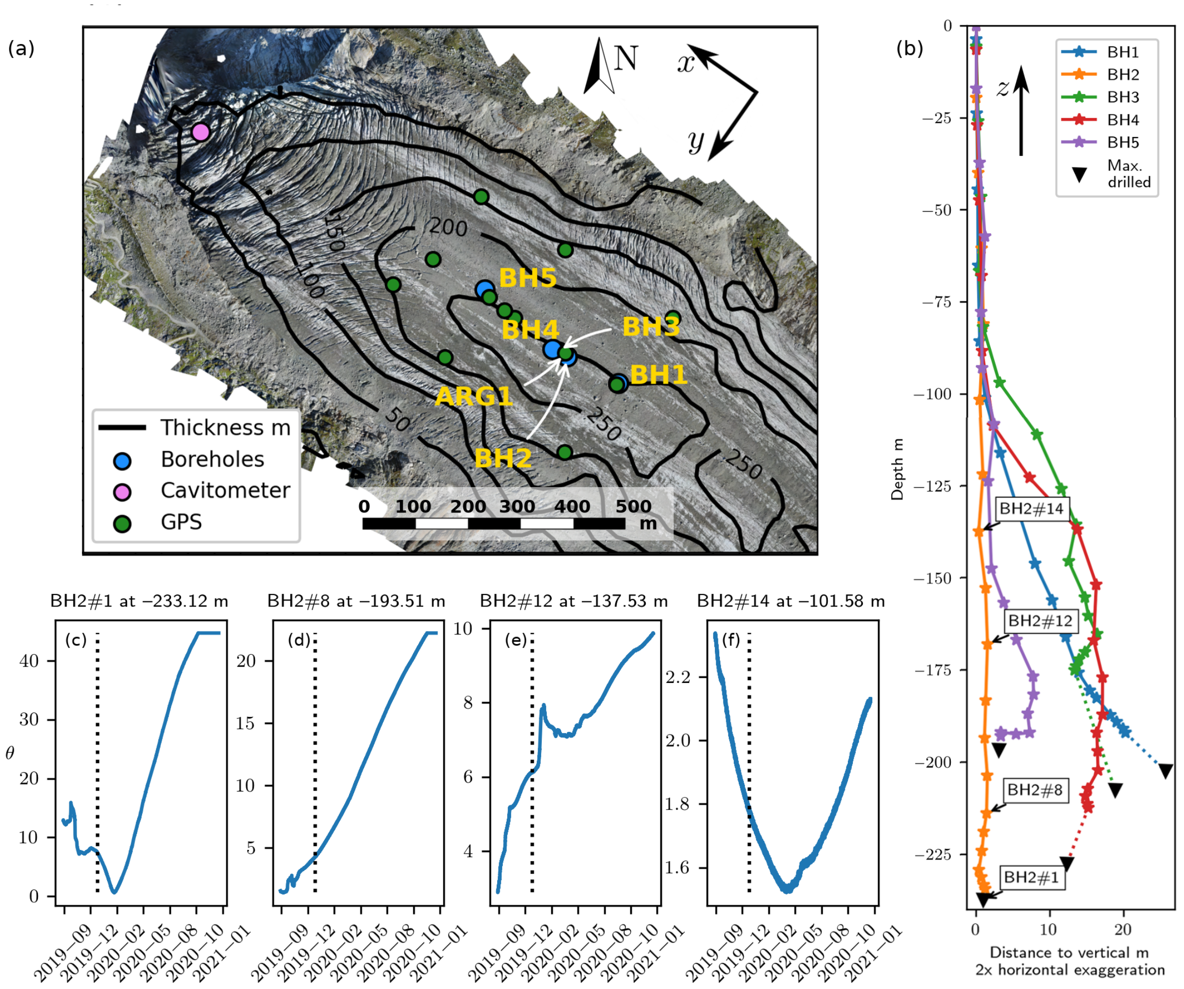

Figure 2.2: Panels showing the location of the instruments used in this study, the estimated shapes of the boreholes and some unfiltered tilt curves, and the reference system used in the study. Panel (a) shows a map of the ablation area of Glacier d'Argentière (projection EPSG:27572) with ice thickness (black contours), and instrument locations as of late September 2019. Note that 'ARG1' is a GPS station, not a borehole. Panel (b) shows the estimated initial shape, drilled depth (black triangles) and instrumented depth (every star is a tiltmeter) of the five boreholes. Panels (c) to (f) show the tilt θ (continuous lines) recorded at four example inclinometers in BH2, between installation in September 2019 and January 1st 2021. In the event of sensor failure or cable snapping the data logger records the last value, hence why the curves at the end of BH2#1 and BH2#8 are flat after November 2020. The dotted vertical lines mark January 1st 2020.

due to the presence of rocks inside the glacier (Hantz and Lliboutry, 1983), the driller head would stop advancing, enlarging the size of the borehole at the location until drilling could be resumed. On a few occasions it was not enough to resume drilling and a new location had to be chosen. There were instances of sudden borehole drainage, indicating that the borehole was connected with a water pathway or a crevasse. The position of the final completed and instrumented boreholes (BH1, BH2, BH3, BH4, BH5) are given in blue dots in Figure 2.2 (a). We give an estimate of the initial shape of the boreholes (Figure 2.2 (b)) calculated with tilt and azimuth data approximately one month after installation. The actual shapes are 3D curves, so we instead show the estimated horizontal distance between each inclinometer and a vertical line starting at the surface. Since not all boreholes could be instrumented in their entirety, we also show the estimated depth of each borehole with a black triangle.

Borehole	Tiltmeters	Depth m	Instrumented depth m	Local thickness m	Not instrumented m
BH1	18	208	194	253±10	59±10
BH2	19	238	234	237±20	3±20
BH3	17	216	174	235±20	61±20
BH4	19	237	211	234±20	23±20
BH5	17	194	190	234±10	44±10

Table 2.3: Resume of the boreholes instrumentation and depths after installation. The 'Not instrumented' column is the difference between 'Instrumented depth' and 'Local thickness', giving the estimated distance between the last tiltmeter and the bed. Local thickness for BH1 and BH5 uses GPR data (Vincent et al., 2009). Local thickness values for BH2, BH3 and BH4 are considered 20 m lower than the thickness of Vincent et al. (2009), based on the observations of Sergeant et al. (2020) in a profile close to BH4.

2.5.2 Description of the tiltmeters

The deformation rates sensors are made of a custom printed circuit board (PCB) equipped with a high end triaxial gravity sensor (Muratta SCL3000) and a triaxial magnetic sensor (ST LSM303). Sensors are respectively connected to a micro controller (Atmega 328P) through an Serial Peripheral Interface (SPI) and Inter-Integrated Circuit (I2C) bus, and then soldered to the PCB. PCB production and components soldering operation was subcontracted, and then each microcontroller was programmed and calibrated in the laboratory. To withstand the pressure exerted by moving ice and water pressure the PCB was casted with an epoxy compound inside an aluminum tube with an outside diameter of 25 mm, which we call tiltmeter. The sensors are connected to a surface unit composed of a Campbell scientific data logger (CR300), two 12V 55Ah gel batteries and a solar panel that allows for autonomous data acquisition. Communication between tiltmeters and the surface unit is done through Modbus communication protocol over half duplex RS485 serial buses. The gravity sensors are used to determine the position of the sensor with respect to its own reference system, from which we can derive the tilt θ, the angle with respect to the vertical, with an estimated accuracy of $0.01°$. Lab calibration showed that tilt readings at more than $45°$ become progressively unreliable. The magnetic sensors don't provide good absolute measures of the orientation with respect to the north as a result of being very sensitive to parasite magnetic fields. For this reason, we decide not to use them except for roughly estimating the initial shapes of the boreholes.

The tiltmeters are grouped together in chains of 20, more densely concentrated towards the bottom of the glacier, see Figure 2.2, panel (b). For any borehole i, we name each tiltmeter j as BH$i\#j$ starting at 1 for the deepest tiltmeter, i.e. BH2#5 is the fifth deepest tiltmeter installed in the second borehole. The piezometers were located in the last 15 m of the sensor chain. The sensors are connected to a surface unit composed of a Campbell scientific data logger (CR300), two 12V 55Ah gel batteries and a solar panel that allows for autonomous data acquisition. Communication between tiltmeters and the surface unit is done through Modbus communication protocol over half duplex RS485 serial buses. All sensors acquired data every 30 minutes.

The performance of the tiltmeter arrays varied between boreholes. The sensor array in BH1 stopped working after a few days and did not provide useful data. In BH2, all sensors recorded data for more than one year until late October 2020, when the cable snapped at an estimated depth of 220 meters, losing the deepest 6 tiltmeters. BH3 and BH4 were drilled close to BH2, with BH3 being the shortest borehole of the whole campaign. Both BH3 and BH4 show a very crooked shape in their deepest tiltmeters, suggesting problems during drilling that affects the quality of the measurements, either by having non-vertical tiltmeters that are then too sensitive to normal strains (Keller and Blatter, 2012), or poor sensor-ice mechanical coupling as a result of too wide borehole diameter. All sensors in BH3 and BH4 worked during 2020. The sensors in BH5 stopped functioning soon after it was installed. The number of tiltmeters installed in each borehole depends on borehole depth. We provide a resume of borehole length and instrumentation in Table 2.3. Ice thickness at BH2, BH3 and BH4 is based on Sergeant et al. (2020), which suggests that DEM derived ice thickness in the vicinity of BH4 (Vincent et al., 2009) is underestimated by about 20 m. Due to BH2 reaching the bed and showing good quality data, that we attribute to the almost vertical shape of the borehole, most of the results presented in this paper correspond to BH2.

Deformation data during the first months is compromised by insufficient mechanical coupling between the tiltmeters and the ice. We illustrate this with a few representative unfiltered tilt curves in panels (c) to (f) of Figure 2.2. The tilt is given in positive values. Most sensors show an early period of noisy and seemingly random behaviour, followed by a much longer period of steady tilt evolution. The time at which the transition between noisy and steady tilt change happens varies from sensor to sensor, but for most of the tiltmeters it happens before the 1st of January 2020, marked with the vertical dotted lines. Some sensors, like BH2#1 or BH2#14 attain their minimum tilt after September 2019, indicating they were initially tilting against the flow. Others, like BH2#8 have their minimum at, or just after, installation. Other sensors like BH2#12 show more erratic even after the January 1st 2020, possibly indicating bad mechanical coupling to the ice. Note the difference in tilt magnitude at the different depths in Figure 2.2: BH2#1 has a total change of tilt of about 60°, BH2#8 of about 25°, while BH#14 tilt change is lower than 5°. To avoid accounting for the early behaviour in some sensors, we start our analysis the first of January 2020, 15 weeks after installation. We removed high frequency noise by smoothing the tilt data using an exponential filter with a one day time constant. This filtering mostly affects short term observations, and has a negligible effect on long term (i.e. weekly or monthly averages) analysis.

2.5.3 GNSS Network and surface velocity

We used multi-frequency Leica GR25 receivers and Leica AS10 antennas that continuously registered GPS signals at a 1 s sampling interval. The GPS antennas are mounted on the aluminum masts initially anchored up to 6 m deep in the ice, their initial positions are reported in green dots in Figure 2.2. The distance between neighboring survey stations varied from 50 to 200 m. Regular (weekly to every few weeks) field visits ensure the upright position of the antenna masts and continuous power supply.

GPS phase observables were processed in kinematic mode using TRACK software (Chen, 1999) that incorporates double-differencing techniques to eliminate phase biases caused by drifts in the satellite and receiver clock oscillators (Chen, 1999; Herring et al., 2018). The position of survey sites was determined with respect to a reference station that sits on the bedrock approximately 3 km apart. In addition, Glacier d'Argentière appears to have a poor scattering environment that causes large phase residuals at elevations up to 25 °above the horizon; therefore, we used a 25 °elevation cutoff angle as opposed to commonly used 10 °(Herring et al., 2018). The average root-mean-square (RMS) residual of the position time series at each 30 s epoch is ±5 mm, and the epoch-to-epoch standard deviation of horizontal and vertical position estimates is approximately ±3 mm and ±5 mm, respectively.

We calculated horizontal velocities from the position time series smoothed using a Gaussian low-pass filter with an 18-hour sliding window. This window length was chosen by referencing to the unfiltered 4-hour static-derived velocities (King, 2004), and it appears to work best to attenuate high-frequency noise in the position time series and retrieve short-term variations in the glacier velocity. Since estimation of the actual velocity uncertainties associated with the filtered positions is impossible, we determined it empirically by deploying during two weeks another station on the moraine, approximately half a km apart from the boreholes and 3 km away from the reference station. We estimate the uncertainty in the surface velocity is ± 0.5 mm h^{-1}, equivalent to ± 4.4 m a^{-1}. The obtained surface velocities show temporal gaps and are different for each station.

2.6 Methods

2.6.1 Internal deformation rate computed from observations

We approximate the internal deformation rate du/dz from the temporal evolution of the tilt θ, (Lüthi et al., 2002; Ryser et al., 2014; Doyle et al., 2018; Maier et al., 2019),

$$\frac{du}{dz} = \frac{1}{dt}\frac{dx}{dz} \approx \frac{1}{\Delta t}\Delta \tan\theta, \tag{2.1}$$

where Δt is a given time period and $\Delta \tan\theta$ is the change in the tangent of tilt during that time period. We use a three dimensional reference system with x the main along flow direction, and z the upwards vertical with origin at the surface (see panels (a) and (b) of Figure 2.2). Velocities in x, y and z directions are denoted by u, v and w, respectively. In our particular implementation, we calculate at every Δt the least squares linear approximation of $\tan\theta(t)$, such that the slope gives directly du/dz. For this method we consider that all θ is in the direction of flow. We also consider that the only non-zero component of the velocity gradient tensor is du/dz. This hypothesis will be later tested with a three dimensional numerical model of the glacier. The estimated maximum uncertainty for the daily averaged deformation rate are, for most of the sensors lower than 0.1 a^{-1}, more details in Annex B. We test the validity of neglecting the flow gradient tensor components du/dx and dw/dz in our analysis of the tilt curves by using the analytical solution of tilt evolution given in Keller and Blatter (2012). This model provides tilt evolution under steady flow contained in a vertical plane undergoing shear du/dz and extension (or compression) in the along-flow and vertical directions, du/dx, dw/dz. To do so, we model tilt curves $\theta_K(t)$ for $du/dz \in [0.001, 1.5]$ and $dw/dz \in [-1, 1]$ from mid-February onward, and then compute the error as the L2 norm of $\theta(t) - \theta_K(t)$ at each du/dz and dw/dz combination. This method works best for tiltmeters which record a large change in tilt over the studied period.

2.6.2 Computation of surface, internal and basal velocities

To deal with the gaps in the surface velocity records we will use an approach similar to the linear model of Lliboutry, which has typically been used to reconstruct continuous surface mass balances of alpine glaciers from sparse data (Lliboutry, 1974; Vincent et al., 2017). In our case, we use it to reconstruct a continuous timeseries of the surface velocity at the GPS station close to the boreholes. The model considers that surface velocity at each GPS station i can be expressed

$$u_{s,i}(t) = \alpha_i + \beta(t), \tag{2.2}$$

with α_i the average surface velocity at the station i over 2020, and $\beta(t)$ the temporal velocity variability equal for all stations in the same glacier that satisfies $\sum \beta(t) = 0$. This base assumption is confirmed by the residuals of the reconstructed velocities following a normal distribution centered close to 0, as we show in Figure D.7. In view of the good performance of the linear model we do not consider non-linear models for reconstructing surface velocities. The model to be solved can be seen as a constrained least squares problem, i.e. find the values of α_i and $\beta(t)$ that best approximates the observations while keeping $\sum \beta(t) = 0$. We solve the system once for a temporal average of the surface velocity, compute the residuals between modeled $u_{s,i}(t)$ and the observation and compute their standard deviation s_{res}. We classify as outliers all observations whose residuals are greater than $3s_{res}$, and solve the system again without these outliers to obtain the final α_i and $\beta(t)$.

The deformation velocity at a borehole BH between two tiltmeters i and j is computed by numerically integrating the deformation rate,

$$u_{BH}(t,i,j) = \int_{z_i}^{z_j} \frac{du}{dz} dz \approx \sum_{j}^{i} \frac{1}{2\Delta t} \Big(\Delta \tan\theta(z_i) + \Delta \tan\theta(z_{i-1}) \Big)(z_i - z_{i-1}). \tag{2.3}$$

We call deformation velocity u_d the velocity computed from the lowest tiltmeter to the uppermost tiltmeter, i.e. at BH2 we have $u_d(t) = u_{BH2}(t,1,18)$.

The basal velocity is computed as the difference between the surface velocity and the integrated deformation rate u_d,

$$u_b = u_s - u_d. \tag{2.4}$$

2.6.3 Modeled deformation rate

Our observations allow us to approximate the strain-rate $\dot{\varepsilon}_{xy} = 1/2du/dz$. However, determining the rheology of the ice at Glacier d'Argentière requires constraining the stress tensor τ_{ij}. For this purpose we use a three dimensional numerical model of Glacier d'Argentière, similar to the model used by Gimbert et al. (2021a) and Vincent et al. (2022b), using the FEM Elmer/Ice (Gagliardini et al., 2013). The model solves the Stokes equation for a glacier geometry given by the measured bedrock and surface topography and is used to extract the stress and deformation rate profile along the boreholes. Ice rheology is given by the Glen's flow law:

$$\dot{\varepsilon}_{ij} = A\tau_E^{n-1}\tau_{ij}, \tag{2.5}$$

where $\dot{\varepsilon}_{ij}$ and τ_{ij} are respectively the components of the strain rate (a^{-1}) and deviatoric stress tensors (MPa), A is the creep factor (a^{-1} MPa^{-n}), $\tau_E = \sqrt{\frac{1}{2}\tau_{ij}\tau_{ij}}$ the effective stress (MPa) and n the Glen's exponent.

We assume a stress-free surface boundary condition and a basal boundary condition given by a Weertman (1957) type friction law,

$$A_s\tau_b^m = u_b, \tag{2.6}$$

where τ_b is the basal shear stress (MPa), m an exponent taken equal to 3, A_s is the friction coefficient at the bed (m a^{-1} MPa^{-m}) taken constant in time, uniform in space, and u_b the sliding velocity (m a^{-1}). We run several simulations to test the sensitivity of the deformation rate profile to different rheologies. We run a set of simulations with different Glen's flow law exponents $n = 3, 4, 5$ and constant and uniform creep factor A. The value of A is chosen such that the numerically computed total deformation velocity at the initial location of BH2 is equal to the deformation velocity u_d averaged for the 1st January to 15th October 2020 period. We run as well a simulation with $n = 3$ and depth-inverted creep factor $A = A(z)$, such that the computed deformation rate du/dz is as close to the observations as possible.

In addition, we compare the high-order Elmer/Ice model to a simplified plane-strain model, commonly referred as Shallow Ice Approximation (SIA). Assuming that all deformation is a result of linearly increasing shear stress due to gravity on an inclined valley τ_{xz}, we obtain the following deformation rate profile at the center line of the glacier (Nye, 1965),

$$\frac{du}{dz} = 2A(f\rho_i g\alpha|z|)^n. \tag{2.7}$$

Ice density is given by ρ_i, g is gravitational acceleration, α is the average slope of the glacier, and shape factor f takes into account the reduction in stress at the center line due to lateral drag. We will consider two cases, $f = 1$ (no reduction in stress at the center), and $f = 0.646$, the suitable value for a parabolic valley with a half-width to thickness ratio of 2 (Nye, 1965), a reasonable approximation of the cross section of Glacier d'Argentière at the studied site, see Figure D.1.

2.7 Results

2.7.1 Observed deformation rate profile

Deformation rate profiles at BH2, BH3 and BH4 averaged between the 1st January and the 15th October 2020, are shown in Figure 2.3. The shaded region cover the range of monthly-averaged deformation rate, computed using Eqn. (2.1). We divide our profile in three parts. The upper part, spanning the uppermost 100 m, has very noisy deformation rate (e.g. BH2#19, BH3#17 to 16, BH4#19 to 16) except at a few tiltmeters (such as BH2#18). This close to the surface we expect negligible shearing deformation rate and thus weak contribution to the internal dynamics of the glacier (e.g. Willis et al., 2003; Ryser et al., 2014; Maier et al., 2019). The middle part, which we consider from -100 m until -219 m, has much higher deformation rates, which we attribute mainly to shearing. Deformation rate increases non-linearly towards the bed, from less than 0.01 a^{-1} at -100 m to 0.64 a^{-1} at -219 m in BH2#6. The lowest part is the basal layer, which registers the highest deformation rate of each profile and extends from -219 m until -235 m (the bed). The profile at this part breaks the depth-increasing trend of the deformation rate profile. We observe a sudden decrease in deformation rate of roughly 0.25 a^{-1} between -220 and -230 m, a 40% decrease in du/dz. This decrease is followed by a more than three times increase in du/dz between -230 m and -235 m, up to almost 1.5 a^{-1}. We hypothesize that the shape of du/dz between -220 m and the bed indicates the presence of the boundary layer expected in hard bed sliding, with the maximum deformation rate being in the vicinity of BH2#1, as we show in Figure 2.7. The thickness of such boundary layer is approximately 18 m at BH2 if we consider it starts at BH2#6 (3 m between the bed and BH2#1, and 15 m between BH2#1 and BH2#6). The averaged profile in BH3 and BH4 is, in general terms, similar to that of BH2.

Some outliers and particularities of the profiles are reported in Figure 2.3. The high and noisy deformation rate recovered in a few tiltmeters of the upper part of the glacier (e.g. BH2#19, BH3#17, BH4#19) is most probably due to the tiltmeter remaining almost vertical under negligible deformation rate. As such, small changes in θ over a short period of time (due to environmental unaccounted factors such as rain entering the borehole or bad sensor-ice coupling) yield, relative to the low θ recorded by the sensor, very high deformation rate. Therefore we omit BH2#19, BH3#15 to BH3#17 and BH4#16 to BH4#19 in our analysis. In the middle part of the glacier, we find strong temporal variability in BH3#6 and BH4#8, at -160 m and -181 m respectively. These tiltmeters were located at those points where we estimated sudden changes in the direction of the borehole (see the estimated deviation with respect to the vertical in Figure 2.2 (b)) such that we can expect an enlarged borehole section and bad sensor-ice coupling. The recorded tilt at BH3#6 shows strong changes from June 2020 onward suggesting decoupling from the ice from this point. BH4#8 is always tilting at more than $45°$, which is beyond the range of tilt in which the tiltmeters provide reliable data, therefore we do not show it in Fig-

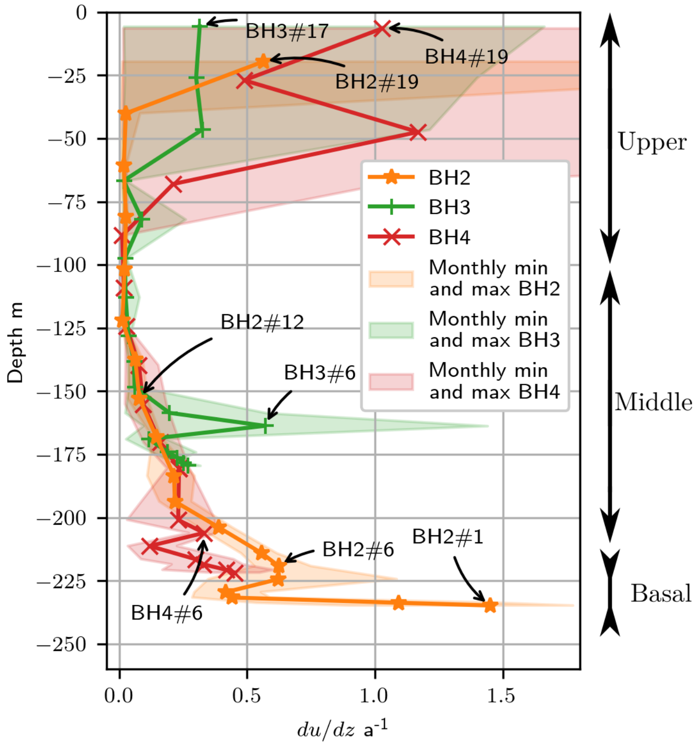

Figure 2.3: Deformation rate profiles with monthly minima and maxima at BH2, BH3 and BH4. The continuous lines show the average measured deformation rate at each borehole for the period between the 1st January and the 15th October, and the shadowed region the range between monthly averaged minima and maxima deformation rate values. Every symbol represents a tiltmeter. We point with arrows some tiltmeters to help understand the main text.

ure 2.3. In the lowest part of the glacier, the deformation rate measured at tiltmeters BH4#1 to BH4#6 is consistently lower than at BH2. However, when comparing the tilt curves provided in Figures D.2 to D.4, we observe that the tilt curves captured by BH4#1 to BH4#6 are not smooth and continuously increasing as those in BH2. Indeed, there are a few periods of several weeks over which tiltmeters BH4#1 to BH4#6 display no tilt change, resulting in very low average deformation rate. Therefore, it is unclear whether the differences in the lowermost deformation rate between BH2 and BH4 are due to differences in the strain field, or an artifact of poor drilling conditions at the bottom of BH4 (recall that the last 20 m of BH4 could not be instrumented after drilling).

The relative error between the tilt measured at BH2 and the simulated tilt curves using the model of Keller and Blatter (2012) for tiltmeters BH2#1 to BH2#9 (those that record larger changes in tilt over 2020) are shown in Figure D.5. Most of the deepest tiltmeters have the errormaps centered on $dw/dz = 0$, although they all show multiple combinations of du/dz and dw/dz that reconstruct well the observed tilt. The cases of BH2#1 and BH#2 are more clear: error maps are not centered at $dw/dz = 0$, suggesting that normal strains influence the retrieved du/dz at these locations. Both tiltmeters show an optimal value of du/dz of approximately 1.1 a^{-1}, similar to the du/dz found at BH2#2 with Eqn. (2.1) and a 25% lower than the du/dz found at BH2#1.

In resume, the retrieved deformation rate profile shows similar depth-increasing deformation rate at boreholes BH2, BH3 and BH4 with negligible near-surface deformation rate and a complicated basal pattern; differences between profiles are attributed to the drilling campaign. Normal strain rates may influence the retrieved values of du/dz close to the bed, as is probably the case for BH2#1 and BH2#2.

Given that BH2 presents the least noisy data, reached the bed, and that it is the only borehole where the whole thickness was instrumented, we focus on BH2 for the rest of the paper.

2.7.2 Comparison with modeled deformation rate profiles

We reproduce the average $du/dz(z)$ profile at BH2 with the three dimension Elmer/Ice model of Glacier d'Agentière. Simulations with constant creep factor and different values of the Glen's law exponent yield deformation rate profiles with much less curvature than observed, represented by the blue continuous curves in Figure 2.4 (a). The modeled deformation rate profiles at constant A show poor sensitivity to the flow exponent ($n = 3$, $n = 4$ and $n = 5$). In Figure 2.4 (b) we show the shear stress components (τ_{xz}, τ_{yz}, τ_{xy}) and the effective deviatoric stress (τ_E) for the simulation with depth dependent creep factor, to be compared to the SIA (Eqn. (2.7)). The full stress tensor as well as the results for the other simulations can be found in Figure D.6. We conclude that the stress tensor is rather insensitive to changes in rheological parameters. Ice flow is dominated by along flow shear in the deeper half of the glacier ($\tau_{xz} \approx \tau_E$), and by a mix of shear and extension or compression in the upper half of the glacier (τ_{xz}, τ_{yz} and τ_{xy} are clearly lower than τ_E, but non-zero). The across flow horizontal shear τ_{xy} is always lower than along flow shear, except close to the surface where they attain similar values. This distribution of stresses allows us to validate the use of Eqn. (2.1) for computing du/dz. In the middle and lower part of the ice column τ_{xz} dominates over the other shear components, and over the upper part of the ice column du/dz is negligible, such that the influence of other stress components on du/dz will be low as well in absolute terms. With regards to the stress given by the plane strain model (SIA), the dotted lines in Figure 2.4 (b), we see that despite not being able to reproduce the depth distribution of simulated stresses, the basal drag τ_b (identical to the value of τ_E at the bottom of the ice column) predicted by Eqn. (2.7) for a glacier of similar cross section as Glacier d'Argentière (blue dotted line) is almost identical to the basal drag computed by the Elmer/Ice model. If the shape factor is not accounted for (the green dotted line), τ_b is overestimated by more than 50%.

The only configuration that provides a good match between observations and the numerical results is the depth-dependent creep factor, whose deformation rate profile is plotted for the case $n = 3$ in dashed lines in panel (a) of Figure 2.4. To find the creep factor as a function of depth, we infer A by inverting Glen's law (Eqn. (2.5)) with the observed mean du/dz at BH2 and the numerical stress tensor,

$$A(z) = 2\frac{du}{dz}\tau_{E,num}^{-2}\tau_{xz,num}^{-1}. \tag{2.8}$$

We then approximate $A(z)$ by a piece wise linear function. Given that changing the creep factor slightly modifies the overall stress balance, we run the numerical model repeatedly, updating at each iteration the $A(z)$ inferred with the numerical solution of the previous iteration, until the modeled stress field converges. The results are shown in Figure 2.4: the deformation rate profile is given in dashed lines in panel (a), and the inferred creep factor is given in panel (c), stars and continuous black line, bottom horizontal axis. The deformation rate recovered in the basal layer is poorly reproduced by the numerical model. Focusing on panel (c) of Figure 2.4, we see that in the upper half of the glacier $A(z)$ is close to 78 MPa^{-3}a^{-1} (see the blue dotted line), the value proposed by Cuffey and Paterson (2010) for temperate ice and $n = 3$. From -140 m down to the bed A increases non linearly, even surpassing the value of A for $n = 3$ recommended by Paterson (1994) (green dashed line). We discuss this depth-increasing creep factor later in the Discussion.

In resume, we can only reproduce our observed du/dz profile if we consider a depth-increasing creep factor, reaching values much higher than those recommended by common literature.

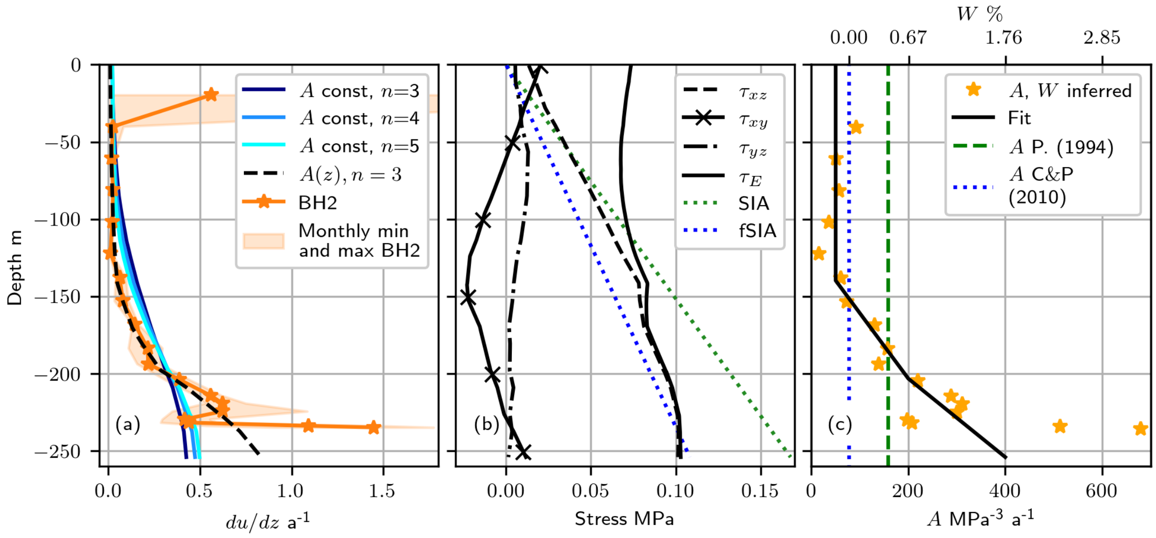

Figure 2.4: Observed and computed deformation rate profile at BH2 and other results from the numerical simulations. Panel (a) compares the observed profile at BH2 with the numerically computed deformation rate profiles. The numerical profiles are selected for four representative scenarios, with uniform creep factor $A = A_0$ and $n = 3$, $n = 4$, and $n = 5$, and with depth-variable creep factor $A = A(z)$ and $n = 3$. Panel (b) shows the vertical profile of effective and shear stress, as well as a comparison with the stress given by the SIA assuming shape factor $f = 1$ for the green dotted line, and $f = 0.646$ (Nye, 1965, parabolic channel with $W = 2$). Panel (c) shows the creep factor (bottom horizontal axis) inferred as a result of constraining the simulation with the average deformation rate profile at BH2, and the inferred water content inferred from the observed creep (top horizontal axis). The green dashed line marks the value of A for temperate ice proposed by Paterson (1994), and the blue dotted line marks the value of A proposed by Cuffey and Paterson (2010).

2.7.3 Seasonal evolution of velocity

In this section we study temporal changes in deformation at Glacier d'Argentière, the inferred basal velocity and the relationship between deformation velocity and surface velocity and water discharge.

The surface velocity u_s is obtained from reconstructing at ARG1 the linear model over one-day averages of the surface velocities. The station ARG1 is chosen since it is the closest to BH2, as depicted in Figure 2.2 (a). The residuals of the reconstructed surface velocities (shown in Figure D.7) follow a normal distribution, which validates the linear model. The deformation velocity at BH2 is computed with a time window of 1 day. The basal velocity is calculated between the reconstructed surface velocity at ARG1 and u_d. We also compute the one-day averages of the sliding velocity at the cavitometer and of the subglacial discharge captured close to the cavitometer.

Figure 2.5 (a) shows the discharge and Figure 2.5 (b) shows the timeseries of surface u_s (green), deformation u_d (blue), basal u_b (black) and cavitometer u_{cav} (red) velocities at Glacier d'Argentière, between mid February and mid October of 2020.

The surface velocities series shows a strong acceleration episode at the beginning of April, and continues to raise until May, when there is a second strong acceleration episode. Then, surface velocity remains between 50 and 60 m a^{-1} with some oscillations until September, when it starts to decline, which a couple of short-term accelerations, until it reaches almost 40 m a^{-1} in mid October. Deformation velocity increases from mid April to May, and then stays between 30 and 38 m a^{-1} until September, afterwards it declines steadily until reaching 26 m a^{-1} at mid October. A few surface speed-up events are detected simultaneously by the tiltmeters and the GPS stations: this is the case of the accelerations of the first half of April, and the two accelerations of the first half of May. In all three cases, most

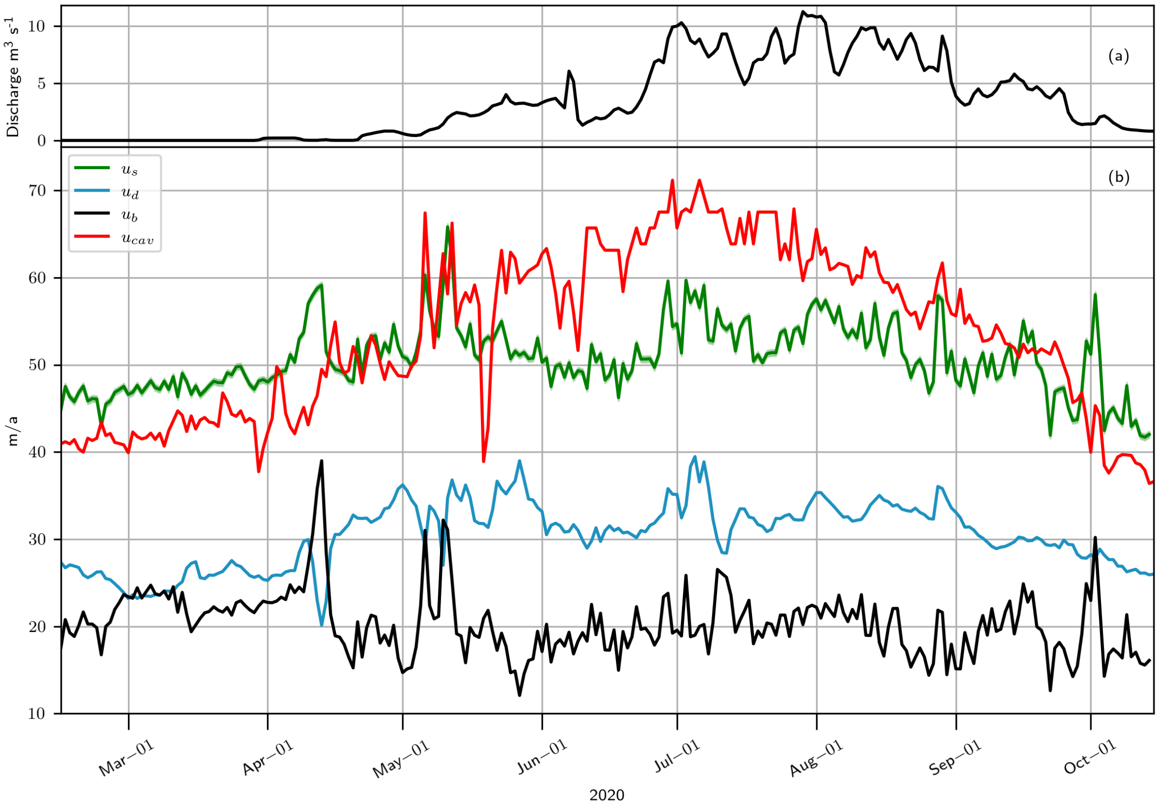

Figure 2.5: Timeseries of subglacial discharge (a) and velocities (b) at Glacier d'Argentière. The displayed velocities at panel (b) are the surface velocity computed with the linear model for the GPS station ARG1 u_s, deformation velocity at BH2 u_d, inferred basal velocity at BH2 u_b and sliding velocity at the cavitometer u_{cav}.

tiltmeters show simultaneously a sudden decrease, following by a fast increase in the deformation rate, over a few days. Basal velocities oscillate between 15 and 25 m a^{-1} for most of the period, with a few peaks over 30 m a^{-1}. No particular trend in u_b is found. The velocity at the cavitometer u_{cav} increases from the beginning of the period until July, and then decreases.

We compute the correlation between deformation rate du/dz and surface velocity u_s to study the relationship between surface and deformation velocities, using eight different averaging periods: from twelve-weeks to one-week averages. For each length of the averaging period, we perform a linear regression between du/dz and u_s and compute the correlation R^2 and the p-value. We show a resume of the regressions in Figure 2.6, where colors show the correlation coefficient (R^2, see the color bar) and the text shows the p-value. We find strong significant correlation ($R^2 > 0.5, p < 0.05$) between deformation rate and surface velocities in several of the tiltmeters below -200 m for several averaging periods, with stronger correlation for longer averaging periods. The spatial pattern of significant correlation is, for the most part, preserved, i.e. most of the tiltmeters below -200 m tend to record stronger deformation rate when surface velocities are high. Thus, we conclude that low frequency surface velocity variability can be explained with changes in the deformation velocity, which explains the increased velocity during the May - end of August period, and a few sustained peaks in the surface velocity (specially in July and August). On the other hand, high frequency surface velocity variability must be due to fast changes in the basal velocity: the fast increases in surface velocity during early April and early May, corresponding to the beginning of the melt season (see the discharge in Figure 2.5 (a)), or the two short-lived accelerations during September can't be explained by changes in deformation velocity alone.

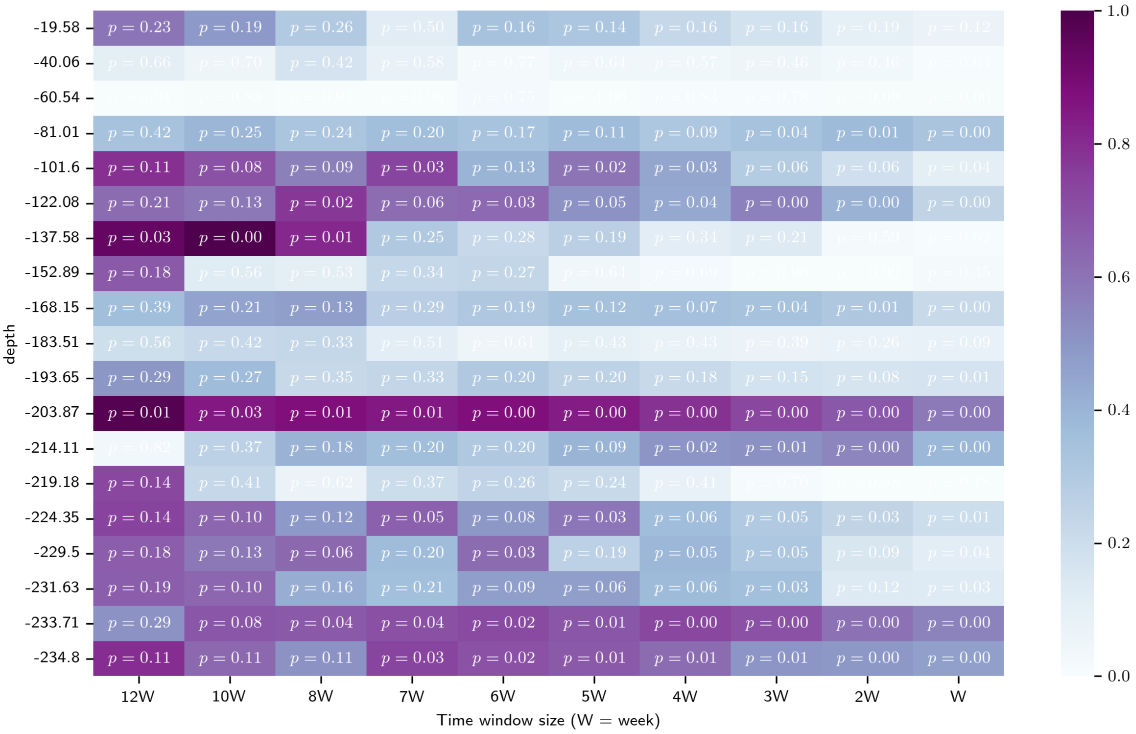

Figure 2.6: In-depth distribution of the correlations between deformation rate at BH2 du/dz with surface velocity u_s averaged at different averaging periods, computed with linear regressions. Color shows the R^2 and the text the p-value of the regressions.

2.8 Discussion

2.8.1 Evaluating the deformation profile

2.8.1.1 Implications for rheological parameters

The observed deformation could not be reproduced with the numerical model that used uniform creep factor and common values of the Glen's law exponent. Moreover, since the retrieved stress tensor was largely independent on n and A, it seems that the spatial distribution of stresses within Glacier d'Argentière is set by the glacier geometry, and not by rheological parameters.

In the case of temperate ice, this depth increasing creep factor may be due to interstitial water content W (Duval, 1977; Adams et al., 2021). We test this hypothesis with the formula proposed by Duval (1977). We adapt it considering $A = 78$ MPa^{-3}a^{-1} (Cuffey and Paterson, 2010) when $W = 0$, i.e. we assume no water content in the upper half of the glacier, obtaining

$$W = \frac{1}{2.34}\left(\frac{A}{78} - 1\right), \tag{2.9}$$

for W in % and A in MPa^{-3} a^{-1}. The inferred water content values are given in the top horizontal axis of Figure 2.4 (c). Discarding the negative values as artifacts of our chosen parameterization of Duval's model, we see that the expected water content above -219 m ranges between 0 and 1.5%, increasing down to the bed. Below this depth, the rapid increase in creep factor at the basal layers is explained with up to $W > 3\%$ at the base. These values of W, and this type of spatial distribution are comparable to those observed in temperate ice (Pettersson et al., 2004, and Table 1.4). In particular, Lüthi and Moreau (2018) found $W \approx 2\%$ at the base of Glacier d'Argentière (close to the cavitometer), which is in good agreement with our inferred values at the base at BH2. Our inversion for the water content is based on the work of Duval (1977), for shearing of temperate ice in tertiary creep with water contents up to 0.8%. However, we already commented in Chapter 1 that Adams et al. (2021) found in similar experiments that ice under secondary creep with $W > 0.6\%$ is linear viscous, which corresponds in terms of W to the ice below -200 m. However, it is unclear if the results for secondary creep apply for the case of Glacier d'Argentière which is most likely deforming under tertiary creep (Lliboutry and Duval, 1985). On a final note regarding the water content, in Annex C we explain recent efforts carried out at our laboratory to measure *in-situ* changes in W using a sonic logger installed in a borehole drilled close to the right margin of the glacier. The preliminary results are inconclusive due to insufficient constrains on the parameters required to process the measurements and do not improve our conclusions with respect to the role of interstitial water.

Other factors could explain the inferred depth-increasing creep such as depth-decreasing grain size (Cuffey and Paterson, 2010). Vallon et al. (1976) reported no discernible change in grain size except at the bed in the accumulation zone of La Mer de Glace, a glacier close to Glacier d'Argentière. If the texture of Glacier d'Argentière and la Mer de Glace are comparable, grain size does not seem to explain creep enhancement, except perhaps for the increased deformation near the base. We expect the ice at these depths to undergo tertiary creep so we discard anisotropy as an explanation for the inferred creep enhancement (Lliboutry and Duval, 1985).

2.8.1.2 Limitations of the numerical model

The results are based on the implicit assumption that the numerical stress tensor is representative of the actual stress at Glacier d'Argentière. We consider that the distribution of stresses has a few features that can be expected in a valley glacier. Firstly, the drag at the base coincides with the expected drag if we take into account the valley shape, the thickness at the studied site and the surface slope. Secondly, the numerical model provides significant extension and compression stresses in the upper part of the glacier, that then become negligible close to the base, as expected in valley glaciers (Hooke, 2005).

Since we didn't find significant changes in the stress tensor when considering different rheologies, we question the choice of the boundary conditions. The model is run in a steady state, such that using a friction law like Weertman (1957), which cannot accurately reproduce intra-annual changes in velocity (Lliboutry and Duval, 1985) is not that problematic. A more important choice is the uniform friction parameter A_s. A similar comparison between basal conditions was carried out in Vincent et al. (2022b), see Figure S3 of the supporting information (Vincent et al., 2022a). The results using uniform A_s and inverted viscosity were comparable with those presented in the main text that used inverted A_s and uniform viscosity, suggesting that the numerical results presented in this paper are not that dependent on the spatial distribution of the friction parameter, as can be expected from the stress tensor being set by the geometry of the glacier.

2.8.1.3 Identification of the boundary layer

The shape of the deformation profile and the retrieved values of du/dz close to the bed suggested a boundary layer due to sliding over a bump as explored by Maier et al. (2019). We qualitatively explored the viability of this explanation with a simulation of tilt evolution close to the bed using the deformation rate provided by Gudmundsson (1997b) and the model of tilt evolution in a given velocity field provided in Gudmundsson et al. (1999), which we use in the Appendix 2.11. As we show in Figure 2.7, important normal strain-rates developed close to the bed can cause a zig-zag shape in the du/dz profile, similar to the one observed in Figure 2.3. Thus, we conclude that it is likely that the observed profile close to the bed corresponds to the basal boundary layer (perhaps indicating that the base of the borehole is located in the lee side of a bump), and that our estimated deformation at this location is influenced by the neglected components of the velocity gradient. This should not have a strong impact on the temporal changes in deformation rate, which are similar for, at least, the tiltmeters below -150 m.

2.8.2 Temporal changes in velocity

We saw in Figure 2.5 that the deformation velocity displays seasonality, while the basal velocity does not. We interpreted with the help of Figure 2.6 that short-term surface accelerations are caused by changes in the basal speed, while surface velocity changes at longer timescales are due to changes in deformation, with a 20% increase in deformation during the melt season. To understand the origin of this increased deformation we will consider two possible origins. First we will discuss seasonal changes in stress, and then seasonal changes in the creep factor through evolving water content.

2.8.2.1 Local versus global control on ice deformation

The summer increase in deformation can originate from an increase in drag at the base (Hooke et al., 1992; Maier et al., 2021b), which, applying Glen's flow law with $n = 3$, means that we expect a change in stress of the order of $\Delta\tau = \Delta\dot{\varepsilon}^{1/3} \approx 6\%$, or 6 kPa following the numerically retrieved basal drag given in Figure 2.3 (b). We will consider two origins for this seasonally evolving stress: increased ice-bed contact area as a result of channelization (Hooke et al., 1992; Willis et al., 2003), and ice flow over increasingly steep bed bumps (Maier et al., 2021b).

On one hand, the development of a main drainage channel running very close to the position of our boreholes during the melt season has been previously identified by Nanni et al. (2021) during May 2019. These observations are confirmed with the pressure record at BH2 (see Figure D.8), which suggests a very active, well connected subglacial system between, at least, May and August, with the greatest variability during June. Another line of evidence for the presence of a drainage axis at the location of the boreholes is given in the speed up events of April and May, over which we see a fast decrease in deformation rate over a few days, similar to the observations of Mair et al. (2004) for a borehole situated just above the drainage axis of Haut Glacier d'Arolla (Switzerland). The development of a channel close to the boreholes after May means that the rise in deformation between May and September is due to increased basal coupling, in other words, the central part of the glacier becomes stickier (Willis et al., 2003).

Increased bed-coupling must not be very strong to provide an increase in drag of only 6 kPa, suggesting that cavities must survive throughout the melt season. Increased cavitation in the surrounding areas would also take up the decrease in drag at the central part of the glacier. This increased cavitation close to the central part of the glacier would be the cause of the uplift observed by Vincent et al. (2022b), and not the growth of cavities directly at the center of the glacier, as Vincent et al. (2022b) interpreted based on the sliding velocities at the cavitometer. The cavitometer velocity is perhaps more representative of the overall sliding velocity at the rest of the glacier, but not at the area inmediately above the central flow line. Spatial differences in basal velocities and in the subglacial hydrology system over short distances have been observed before (Willis et al., 2003), so finding a similar behaviour in Glacier d'Argentière is not puzzling.

Other studies linked temporal changes in deformation rate to changes in local bed topography (e.g. Maier et al., 2019). In our case, the changes in surface velocity are simultaneously seen by the ensemble of the GNSS network over hundreds of meters on the glacier surface, while the borehole is traveling a much shorter distance: with an average basal speed of 20 m a^{-1}, BH2 travels 10 m over the April - October period. The 10 m bump would have to be precisely located such that the borehole reaches and crosses over it during the extent of the melt season, which is unlikely.

In conclusion, velocity changes over the melt season and at shorter timescales can be explained with increased ice-bed coupling during the melt season following the development of a central drainage axis, although cavities must survive close to the main area of the glacier to explain other short term accelerations and previous observations. This implies that the spatial pattern of basal velocities and of the subglacial hydrology network are strongly heterogeneous at the ablation area of Glacier d'Argentière.

2.8.2.2 Change in water content

Here we test the extent with which the expected production of water from the glacier deformation is sufficient to cause seasonal changes in water content that would explain seasonal changes in internal deformation. We discarded the percolation of surface water through the ice as an origin of such changes in water content, because Glacier d'Argentière can be considered impermeable above -100 m (Hantz and Lliboutry, 1983).

Using Duval (1977) and assuming an average water content $W = 0.7\%$, roughly the average value retrieved between -150 and -235 m (see Figure 2.4), we find that water content must increase on average from $W = 0.57\%$ in winter to $W = 0.7\%$, with a seasonal difference of 0.14%. We ignore water transport through the ice and focus on water production through strain heating. We compute the maximum available water production, considering that i) the only non-zero component of the velocity gradient tensor is $du/dz = 1$ a^{-1}, the maximum value during summer at BH2#6, and ii) the only non-zero component of the stress tensor is $\sigma_{xz} = \sigma_E = 0.1$ MPa, the expected stress at the base. For a latent fusion heat of $L_f = 0.336$ MJ/kg, the water generation due to ice shearing horizontally is (Cuffey and Paterson, 2010)

$$\dot{b}_E = \frac{\sigma_{xz} du/dz}{2L_f} = 0.15 \text{ kg a}^{-1} \text{ m}^{-3}. \tag{2.10}$$

Relative to the mass of ice, this is equivalent to $W = \dot{b}_E/(\rho_i) = 0.00017$, or 0.017%. The maximum water content produced by strain heating during one season is one order of magnitude lower than required. In conclusion, the observations at the seasonal scale cannot be explained neither with the transport of surface water through the ice due to the presence of impermeable bubbly ice close to the surface, nor with strain heating due to insufficient water generation.

2.9 Conclusions

We have measured internal deformation along the central line of the ablation area of an alpine temperate glacier. Our data provided good spatial resolution at three different boreholes, which allows us to reconstruct the deformation profile and its evolution during most of 2020, including the melt season in its entirety. A complementary numerical model was used to improve our understanding of the stress conditions at our site, and an analytical model provided additional insights on the shape of our profile near the base. We identify three different behaviours along the ice thickness. The upper 100 m of ice shows negligible deformation, with the stress field being a mix of shearing and normal stresses. The deformation between -100 m and -219 m is characterized by depth-increasing deformation due to a combination of depth-increasing horizontal shearing and creep factor. Reasonable levels of depth-increasing water content can explain the inferred creep factor. Complementary evidence should clear out if the enhanced creep is a result of water content or other factor such as ice texture. The deepest part of the ice column is identified with the boundary layer expected in hard bed sliding. Our data shows seasonally evolving deformation in Glacier d'Argentière, with internal acceleration between the beginning of the melt season in May 2020 and a decrease starting in September 2020. The evolution of the deformation velocity is well correlated to the evolution of the surface velocity at multimonthly and multiweekly periods. At short timescales, surface velocity acceleration is a result of an increase in basal velocities, who otherwise stay relatively low during periods of sustained fast surface velocity. The observations reflect the seasonal evolution of a spatially heterogeneous subglacial hydrology system, which at least immediately at the location of the boreholes develops a main drainage channel after May, with cavities around it. Further analysis and field data is necessary to improve our understanding of the spatial and temporal distribution of cavities and channels in Glacier d'Argentière and confirm if our observations are representative or not of the central part of the ablation area of Glacier d'Argentière.

2.10 Contributions, acknowledgements and data

Juan Pedro Roldán-Blasco processed most of the tilt data. Luc Piard designed the tiltmeters, directed the field campaign and performed early analysis on the data. Adrien Gilbert built the numerical model. Luc Piard, Adrien Gilbert, Florent Gimbert, Christian Vincent and Olivier Gagliardini participated in the inclinometry field campaign and together with Juan Pedro Roldán-Blasco analysed the data, while Anuar Togaibekov and Andrea Walpersdorf provided the GPS measurements and velocity timeseries. Nathan Maier assisted in the modeling of deformation. All contributors participated in the discussion.

Thanks to Bruno Jourdain, Olivier Laarmann, Maël Richard, and everybody else that participated in the 2019 field campaign and the fabrication of the instruments. This work is supported by the French ANR project SAUSSURE (ANR-18- CE01-0015-01, https://saussure.osug.fr). We thank as well Luc Moreau (http://www.moreauluc.com) for providing the cavitometer measures and Electricité d'Emosson for providing the discharge measurements. Glacier surface elevation and precipitation data were acquired in the framework of the GLACIOCLIM program (https://glacioclim. osug.fr).

The data and results shown in this Chapter, and the code to process will be given in the long-term repository Zenodo of the SAUSSURE project, `https://zenodo.org/communities/saussure/`, once the corresponding article is submitted.

2.11 Appendix 1: Deformation of the basal layers

Some studies of ice flow around hard beds show that a boundary layer with important flow gradients develop around the bed bumps (Kamb, 1970; Gudmundsson, 1997a,b), with maximum deformation rate attained a certain distance above the bed, not inmediately at the ice-bed interface. Similar conclusions have been derived by Ryser et al. (2014) and Maier et al. (2019) upon analyzing deformation rate profiles. In our case, our Elmer/Ice model parameterizes this near-bed process with the friction law, and therefore it cannot be used to provide an accurate description of the flow close to Glacier d'Argentière's bed. For this purpose, we will compare our observations with an analytically derived deformation rate profile close to the bed.

We simulate the flow around bed bumps using the analytical solution for the two dimensional flow of a linear medium sliding over a sinusoidal bed of low roughness given by Gudmundsson (1997b). We compute the analytical solution for the first 10 m above the bed, using local slope $\varepsilon = 0.5$, glacier thickness $h = 250$ m, and wavenumber $k = 1$, and neglecting regelation. The obtained flow gradient are used to generate one year of synthetic tilt curves, using the forward model of tilt evolution presented in Gudmundsson et al. (1999). We then compute the corresponding averaged deformation rate using Eqn. (2.1), and compare the behaviour with our observations.

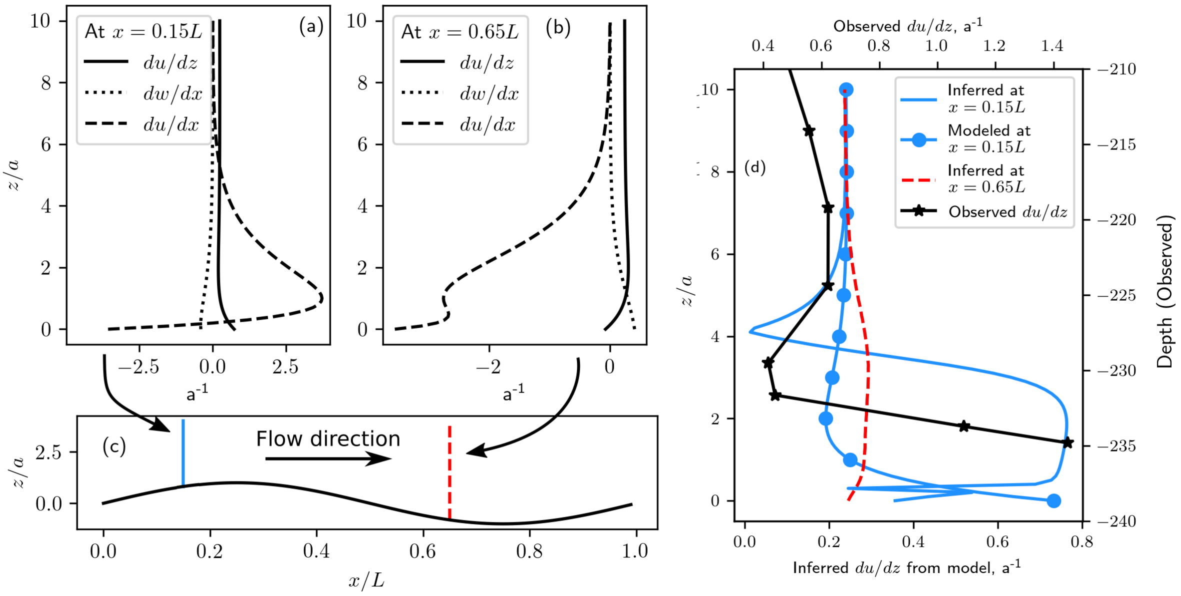

Figure 2.7: Comparison between averaged modeled du/dz curves and inferred du/dz close to the bed. z' is the vertical direction with origin at the mean bed altitude used in the modeled du/dz curves. Panels (a) and (b) show the analytical vertical profiles of the velocity gradient at two locations of a two-dimensional sinusoidal bed, their position are given in panel (c). The vertical and horizontal direction in the analytical solution, z and x, are normalized by the bed amplitude a and wavelength L, respectively. The vertical extension component dw/dz is not given, since incompressibility makes $dw/dz = -du/dx$. Panel (d) compares the inferred du/dz in continuous blue and dashed red lines, for the locations given in (c), with the actual imposed du/dz in dotted continuous blue line, and the observed deformation profile in the starred black line. The red and blue colors refer to the position at the bed in panel (c). The synthetic du/dz curves in (d) are computed after applying equation (2.1) to synthetic tilt curves built with the model of Gudmundsson et al. (1999) using the computed velocity gradient given in panels (a) and (b). More details in the text.

The components of the analytically computed averaged velocity gradient tensor over the bed at two different locations is shown in Figure 2.7 panels (a) and (b), with the location of each profile with respect to the bed given in panel (c). In panel (d) we compare the deformation profiles obtained by applying Eqn. (2.1) on the averaged synthetic tilt curves, obtained as we explained in section 2.11. The vertical direction is normalized by the bed amplitude a, and the position at the bed for each profile is indicated in panel (c), where the horizontal coordinate is normalized by the bed's wavelength L. Due to differences in magnitude, we scaled differently the synthetic 'observed' du/dz profiles in panel (d) (red continuous and red dashed lines, left and bottom axes), with the averaged du/dz retrieved at BH2 in the proximity of the bed , and the BH2 profile (black continuous line with stars, right and top axes).

The flow gradients are very different between the two locations, and we see that the extension and compression rates (the dashed lines in panels (a) and (b)) are much higher than du/dz (continuous lines) and dw/dx (dotted lines). As a result, tilt change is strongly affected by non-shearing stresses, and the inferred du/dz profiles are different than the actual profiles of du/dz shown in panels (a) and (b). The modeled profile at the upslope part of the bed is qualitatively similar to the observed one, and greatly overestimates the actual du/dz . In conclusion, the observations of tiltmeters BH2#1 to BH2#6 can reflect stress gradients due to hard bed sliding over a rough bed, as observed by Maier et al. (2019).

2.12 Appendix 2: Preliminary results on the 2021 inclinometry campaign

2.12.1 Introduction

The preliminary results of the 2019 inclinometry campaign were considered in 2020 a partial success. On the positive side, it was proven that the method for determining the internal deformation worked. The sensors were reliable, and the temporal evolution of deformation was an interesting phenomenon that deserved more attention. The basal velocity was successfully retrieved at BH2, and it showed that our initial ideas about the dynamics at Glacier d'Argentière maybe were not as accurate as we could have expected. On the negative side, it was unclear if the deformation profile and its temporal evolution were local features of the flow field, or were representative of the deformation over the ablation zone. This was in part due to having only one bed-reaching borehole, and in part due to focusing on drilling along the central flow line. Having the necessary human and economical resources at our disposal, it was decided that the campaign should be repeated again in late summer 2021. The timing was on the limit. Earlier in the year was impossible, as it takes a lot of time to properly build, assemble and calibrate the sensors. Later in 2021 was difficult, as the closer to winter, the more difficult it is to work on the glacier due to the decreasing light and deteriorating meteorology. Doing it in 2022 was unfeasible for administrative issues, and also, because then the dataset would arrive too late for my PhD. In such a case it was likely that we wouldn't be able to profit from my expertise acquired while working on the first campaign, and it could also (potentially) be too late to improve the results of the 2019 campaign. In this section we describe the changes done to the instrumentation, the location of the new boreholes and the preliminary results: the retrieved du/dz and the tilt curves.

2.12.2 Instrumentation and field campaign

2.12.2.1 Changes in the instrumentation

The field methods were improved with respect to the first campaign:

- The drilling speed was reduced by half to avoid drilling problems and ensure the verticality of the boreholes.
- The boreholes were drilled in two groups of two, so as to compare the data within each group, and between groups. If two boreholes only a few meters apart showed very similar deformation profiles, then we could be sure that the retrieved deformation was at least representative of that position.
- The boreholes would be carefully measured after drilling to ensure their verticality, and only instrumented if they did not deviate much from the vertical and reached the bed.

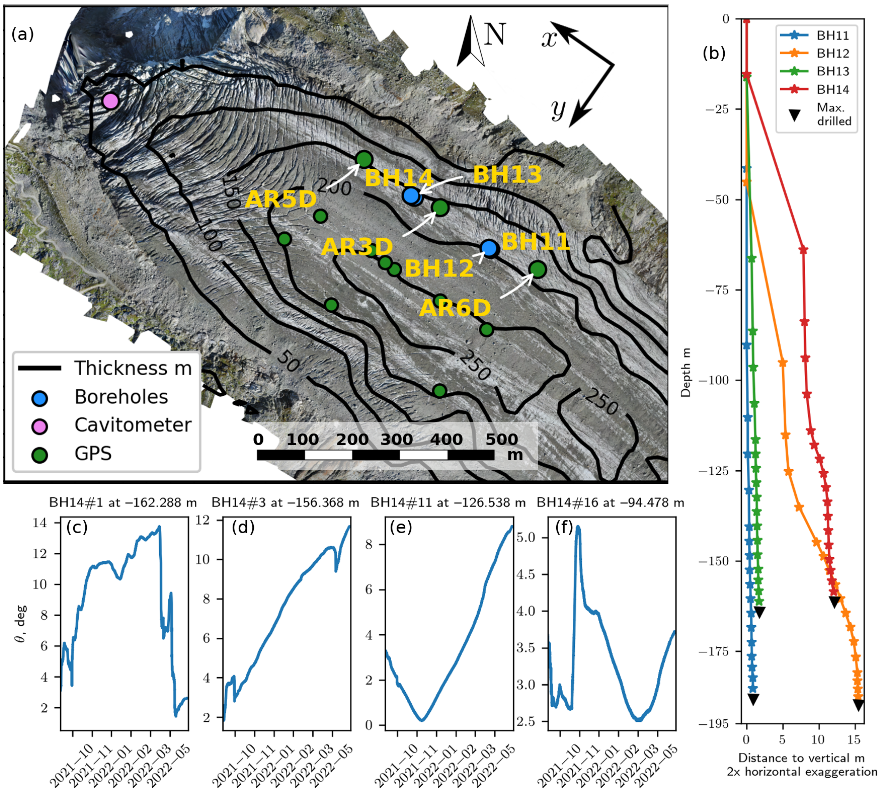

Figure 2.8: Panels showing the location of the 2021 boreholes and complementary instruments, the estimated shapes of the boreholes and some unfiltered tilt curves, and the reference system used in the study. Panel (a) shows a map of the ablation area of Glacier d'Argentière (projection EPSG:27572) with ice thickness (black contours), borehole locations during late September 2021 and instrument locations as of late September 2019. Panel (b) shows the estimated initial shape, drilled depth (black triangles) and instrumented depth (every star is a tiltmeter) of the four 2021 boreholes. Panels (c) to (f) show the tilt θ recorded at four example inclinometers in BH14, between installation in September 2021 and 1st June 2022.

- The distribution of tiltmeters was also altered. No tiltmeters were put in the uppermost 50 m of the whole array, and the density was increased towards the base.
- We discarded the use of magnetometers, given that they were considered unreliable. Five tiltmeters with magnetometers that we retrieved from the 2019 campaign were installed in BH12, named BH12#21, BH12#22, BH12#23, BH12#24 and BH12#25.
- There was one piezometer per group of boreholes, one in BH12 and one in BH14.

2.12.2.2 2021 field campaign

The field campaign started the 21st September, 2021. Drilling along the center line was much more difficult that anticipated, and no boreholes could be completed the first two days of the campaign. The boreholes were then moved to the right margin of the glacier, where ice was expected to be much cleaner of debris, but about 80 m thinner. The final positions of the boreholes are shown in Figure 2.8 (a), and a resume of the campaign is given in Table 2.4. We expect that all four boreholes reached the bed, since i) each borehole was drilled until they could not advance any more, which happened at roughly the same depth for each pair of boreholes, and ii) the drilled depth is well within the estimated ice thickness. All boreholes were much more vertical than in the 2020 campaign, as we depict in Figure 2.8 (b).

BH11 stopped working the 7th January 2022, and 1/3 of the data is compromised due to non-steady

Borehole	Tiltmeters	Piezo.	Depth m	Thickness m	Not instrumented m	Days
BH11	20	No	188	196±20	13±20	106
BH12	25	Yes	191	196±20	13±20	137
BH13	20	No	164	179±20	15±20	5
BH14	19	Yes	162	177±20	15±20	248

Table 2.4: Resume of the 2021 borehole campaign on the right side of Glacier d'Argentière. The 'Not instrumented' column is the difference between 'Borehole depth' and 'Local thickness', giving the estimated distance between the last tiltmeter and the bed. Local thickness is computed from GPS measurements of surface height at drilling and bed height measured with GPR data (Vincent et al., 2009). The 'Days' column gives number of days between installation and the first permanent tiltmeter failure recorded in the borehole, typically that of the first tiltmeter.

movement of the tiltmeters around November as seen in Figure D.9. BH12 lost tiltmeters BH12#1 through BH12#15 and BH12#21 to BH12#25, which correspond to the lower 30% of the glacier thickness, the 17 of February, 2022. BH13 had some malfunctioning component and did not work as expected, failing the 28th September 2021, only 5 days after it was drilled. BH14 tilt records have almost no gaps until the 27th May, 2022. From the 27th May 2022 onward, the data at BH14 show intermittent gaps, with permanent failure of BH14#1 to BH14#12 since the beginning of June 2022. For all these reasons, only the results at BH12 and at BH14 will be described.

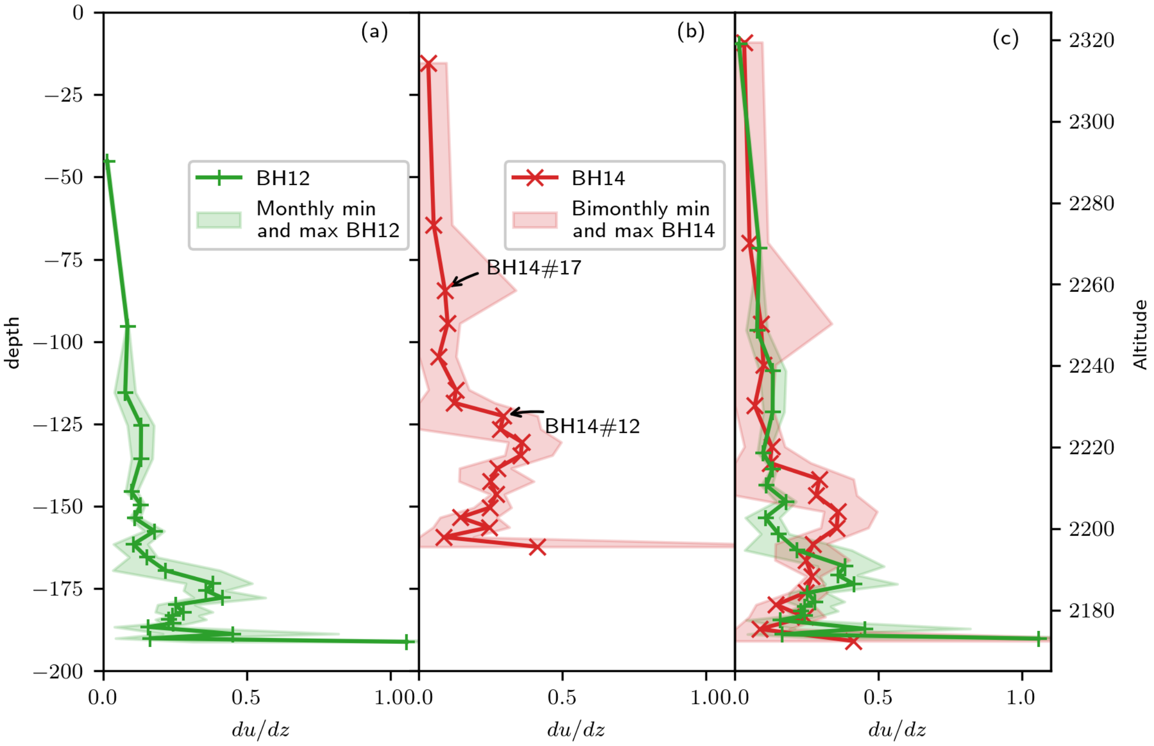

Figure 2.9: Average du/dz computed at BH12 and BH14. The profile for BH2 is computed between 1st November 2021 and 15th February 2022 and is shown vs borehole depth in (a) and vs absolute altitude in (c), while for BH14 is computed between 1st December 2021 and 1st May 2022 and shown vs depth in (b) and vs absolute altitude in (c). The monthly (a) and bimonthly (b) minima and maxima during those periods is covered by the shadowed areas. The named tiltmeters of BH14 show fast short-term changes in tilt, as depicted in the corresponding panels in Figure D.11.

2.12.3 Observed deformation rate profiles at BH12 and BH14

Figure 2.9 shows the average deformation rate du/dz in solid lines and the monthly (BH12) and bi-monthly (BH14) minima and maxima in the shadowed region for boreholes BH12 and BH14. They are computed for different periods: BH12 is computed between 1st November 2021 and 15th February 2022, and BH14 from 1st November 2021 until 1st June 2022. Therefore, they register data before the melt season. Figure 2.9 (a, b) shows the du/dz against the borehole depth, and Figure 2.9 (c) shows the du/dz at both boreholes with respect to the height, i.e. the absolute vertical position. We divide the du/dz profile in BH12 in three sections: an upper layer where we expect low shearing deformation, located between the surface until at least -45 m, followed by a middle layer between -45 m (or -95 m) and -170 m $du/dz \approx 0.15$ a^{-1}, and finally a basal layer characterized by an initial jump in du/dz to 0.38 a^{-1} at -173 m and continues decreasing almost continuously until the bed, with the final five meters showing strong changes in du/dz. The deepest tiltmeter shows the highest deformation rate with more than 1 a^{-1}. The du/dz profile in BH14 (Figure 2.9 (b)) is more difficult to interpret due to some noisy tiltmeters, and it can be at least divided in two layers. The upper layer extends between the surface and -122 m (BH14#12), and the basal layer extends between -122 m and the bed at -162 m. At the instrumented part of the upper layer of BH14, du/dz is on average 0.1 $^{-1}$, with BH14#17 showing high bi-monthly maximum and almost zero minima. The basal layer shows depth decreasing du/dz over 40 meters, at an approximate rate of -0.75 a^{-1} per each 10 m. BH14#1 delivers the highest deformation rate, with an average du/dz of 0.4 a^{-1}. Plotting the du/dz profiles at BH12 and BH14 against the absolute altitude in Figure 2.9 (c) shows that both boreholes cover almost exactly the same height and display comparable du/dz from the surface up to 2220 m. Below an altitude of 2220 m the differences are found in the thickness of the basal layer, which in BH12 is half of the thickness seen in BH14.

2.12.4 Discussion and conclusions

The internal strain-rates at the right margin of Glacier d'Argentière are much different than at the central part of the glacier. This emphasizes the strong spatial heterogeneity of the glacier flow in the transverse direction that was suggested from the results of the first inclinometry campaign. We can expect complications in the shear profiles near the margins due to the lateral components of the strain-rates and stress tensors being non-zero (Hooke, 2005). This already complicates the accuracy of the retrieved du/dz that assumes that the flow is contained in a vertical plane, a reasonable assumption taken for analyzing the deformation rate at BH2. However, the similarities in the du/dz profiles at the same height give us confidence in the retrieved deformation rate.

We need to repeat the analysis carried out with the 2020 borehole data. The stress tensor recovered from the numerical simulations used in the analysis of the 2020 borehole data will provide an estimate of the influence of lateral strain rates in the inferred du/dz at BH12 and BH14. We do not necessarily expect that we will arrive to the same conclusions regarding the water content W, as it is not clear that we should expect the same spatial distribution of water content in the margin than in the central part of the glacier. Surface velocities at the GPS stations close to the boreholes (ARG6D, AR3D and AR5D, see Figure 2.8) can be reconstructed for 2021 using the linear model. Since these stations are not as close to the boreholes as ARG1 was to BH2, we would have to spatially interpolate the velocity timeseries to approximate the surface velocities at the boreholes. Unfortunately, we have almost no data belonging to the melt season. Thus, we will not be able to study seasonal changes in deformation from this campaign alone, and determine if the seasonal changes observed at BH2 are also seen at the margin. We expect that further work will help determine why the basal layer at BH12 increases downstream until reaching double its thickness at BH14.

Chapter 3

The effect of local shear stress on glacier sliding

Except in a few cases, there doesn't seem to be any definite knowledge of just what is under these glaciers.
Johannes Weertman in Interlaken, 1985.

3.1 Preface

In Chapter 1 we presented several challenges of currently used glacier friction laws. One of such limits was the assumption that there are zero local shear stress at the bed of glaciers, in other words, there is no 'solid friction'. In this Chapter we address this issue and study how a friction law with and without cavities is modified when we include non-zero local shear stress at the ice-bed interface. The content of this Chapter is taken from the research paper : J.P. Roldán-Blasco, F.Gimbert, O.Gagliardini and A.Gilbert, "The effect of local shear stress on glacier sliding" (Roldán-Blasco et al., submitted), submitted to *Journal of Geophysical Research: Earth Surface* for review. Some background on the research and the contributions to the work presented here are given before the paper itself is reproduced as close as possible to the submitted paper. Some repetition with Chapter 1 will be found. A few adjustments to the submitted text have been done in order to be coherent to the rest of the manuscript. The supplementary materials associated with this Chapter are found in Annex E.

3.1.1 Setting

I started this work in march 2019 during a five-months MSc internship at IGE at the beginning of the SAUSSURE project. I did not know anything about glaciers before embarking on this project. The original objective was to see how glacier friction laws changed if the bed is three-dimensional and if we consider non-zero local shear stress (Roldán-Blasco, 2019) in order to prepare the terrain for the PhD. The three dimensional simulations took longer than expected, and so we focused on the role of non-zero local shear stress. At the beginning of the project, the topic of sliding with local shear stress was relatively unheard of: the observations of important local shear stresses under the bed of Engabreen (Norway) by Cohen et al. (2005) had been discussed recently in our research group, and previous theoretical models of sliding with friction (e.g. Fowler, 1979; Schweizer and Iken, 1992) were not that easy to find and understand for a neophyte in glacier sliding.

We decided to follow the work of Gagliardini et al. (2007), adding local shear stress at the base in the form of Coulomb friction. The Elmer/Ice simulations showed that there were indeed a few changes in the friction law, and while the results were generally coherent with previous literature, we wanted to go further and understand why exactly we had those changes. Shortly thereafter, Iverson et al. (2019) published a paper on the same topic with a different approach, whose results were similar to what we had seen and gave us confidence on our own results and interpretation. At the end of 2019 and early 2020, during the first year of my PhD, I started to adapt the model of Weertman (1957) to include non-zero local shear stress. We located that the source of the changes in friction came as a result of the non-linearity of the constitutive law for ice. The study was greatly improved over several review rounds: the mathematical derivations were polished, the numerical model was ran for three different local shear stress laws, and the adaptation of Weertman (1957) was expanded to the opening of cavities. The study reached its final form, the one presented here.

3.1.2 Contributions

I ran the different numerical simulations and developed the model of sliding over square obstacles with non-zero local shear stress. Olivier Gagliardini provided the original Elmer/Ice input files and the python scripts to run the simulations and do the post-processing and helped with some Elmer/Ice development. Olivier Gagliardini and Florent Gimbert designed the experiment and supervised the project. The analysis was carried out by Olivier Gagliardini, Florent Gimbert, Adrien Gilbert and myself. Andrew Fowler provided the solution for the model of Weertman (1957) with cavities and zero local shear stress. All anonymous reviewers improved the manuscript with their comments and suggestions. Nathan Maier assisted with interpretation at the early stages of the project, and Samuel Cook helped with some Elmer/Ice debugging.

3.2 Abstract

Current theories to describe drag of glaciers over hard beds are formulated on the basis that ice is free of debris and slides without friction over the glacier bed. However, debris at the basal layers and cold ice cause additional resistance to glacier flow. We provide an analytical model of glacier sliding that accounts for the effect of local shear stress at the ice-bed interface in the framework of Weertman (1957), and expand the solution to account for the opening of cavities. This additional drag slows glacier sliding but due to additional strain enhancement of the basal ice, the viscosity of the ice decreases and the basal speed is higher than expected. The inclusion of local shear stress makes the friction law implicit, complicating the identification of scaling parameters from the geometry alone. We further study this problem using a numerical finite element model of glacier sliding over a sinusoidal bed under steady-state conditions. We find that the law with non-zero local shear stress at the base retains the overall form of the friction law with zero local shear stress, such that an appropriate scaling can be obtained. The similarity between a friction law with zero and non-zero local shear stress is convenient for generalising empirical friction laws at the field scale, although it complicates the identification of the effect of local shear stress on glacier flow.

3.3 Plain Language Summary

Traditional models of glacier sliding over hard beds consider that all resistance to flow at the base of glaciers, called basal drag, originates from deformation around a rough bed. This assumption is contested by in-situ observations as well as models and laboratory experiments that show that drag between glaciers and their bed due to debris, or other factors, may represent an important portion of the total flow resistance. We provide a new model of glacier sliding that considers this new process. Our model overcomes previous limitations that simplified ice material properties or only considered a low amount of ice to bed drag. On one hand, we can expect more rapid flow, because this additional drag softens the ice. On the other hand, the mathematical problem of sliding becomes more difficult to solve. The form of the law with and without this additional drag stays relatively the same.

3.4 Introduction

Glaciers with a temperate base have their dynamics strongly controlled by basal sliding (Hooke et al., 1992; Doyle et al., 2018; Maier et al., 2019). Basal sliding speed is typically related to bed stress conditions through a friction law defined at a meso-scale of meters to several tens of meters (e.g. Weertman, 1957; Lliboutry, 1968; Budd et al., 1979; Fowler, 1986; Schoof, 2005; Gagliardini et al., 2007). At this meso-scale, bed shear stress is envisioned to be primarily set by normal stresses acting on micro-scale (decimetric to metric) obstacles (Weertman, 1957). Stress concentration on these obstacles lowers the effective ice viscosity (Weertman, 1957). For a given obstacle size and under a given stress, the shorter the distance between obstacles, the lower stress concentrations, and thus the lower the basal velocity. For a given distance between obstacles and under a given stress, the rougher the bed, i.e. the higher the obstacles' aspect ratio, the higher the resistance to flow and the lower the basal velocity. As basal water pressure increases, the ice separates from the bed at the lee side of obstacles and opens cavities (Lliboutry, 1968). The opening of these cavities reduces the contact area between the ice and the bed, which reduces the apparent roughness and increases stress concentrations, thus allowing faster basal speed (Lliboutry, 1968; Fowler, 1986; Schoof, 2005; Gagliardini et al., 2007). In the above mentioned conceptualization, perfect sliding is assumed at the ice-bed interface, i.e. local shear stress is considered negligible.

Although typically neglected in existing theories, local shear stress may in reality be non-zero due to solid-type friction acting at the ice-bed interface, for example as a result of debris-bed friction, or due to ice-bed friction if the ice locally lies below the pressure melting point. Debris carried by basal ice have long been observed below mountain glaciers. Consider for instance the deliberation about abrasion and debris-laden ice deformation in the sections *Flow law of basal ice* and *Conditions at the glacier base* of the discussion in Alean et al. (1985), or see the images recorded in a natural cavity under Glacier d'Argentière in France (Figure 3.1), or the samples taken below Engabreen (Norway) (Iverson et al., 2003; Cohen et al., 2005; Zoet et al., 2013). At the latter site, basal force records showed higher than expected levels of bed shear stress that could be due to the extra contribution of debris to bed friction (Iverson et al., 2003; Cohen et al., 2005). Laboratory tests also show that the presence of debris increases bed shear stress (Zoet et al., 2013). Moreover, sliding at subfreezing temperatures could occur in places even under generally temperate base conditions, causing additional drag as observed in laboratory experiments under conditions near the pressure-melting point (McCarthy et al., 2017). Seismic observations of basal stick-slip events emanating from the ice-bed interface provide field evidence that solid-type friction can act across large regions of the bed (Wiens et al., 2008; Zoet et al., 2012; Helmstetter et al., 2015; Roeoesli et al., 2016; Lipovsky et al., 2019) and could be an ubiquitous

Figure 3.1: Cavity under Argentière Glacier, french Alps. The debris cover visible at the base of the glacier varies in density during time. Photograph by Luc Moreau at `http://www.moreauluc.com/`

component of glacier bed friction.

Experimental investigations of the role of solid-type friction on glacier sliding have been mostly devoted to understand the micro-scale mechanisms that control debris-bed friction (e.g. Cohen et al., 2005; Hansen and Zoet, 2019; Thompson et al., 2020) or cold ice-on-rock friction (e.g. Schulson and Duval, 2009; McCarthy et al., 2017). Meanwhile, several theoretical studies considered ice as a Newtonian fluid (Morland, 1976b; Hallet, 1979, 1981), or as a non-Newtonian fluid but under low magnitudes of local shear stress with respect to total bed shear stress (Fowler, 1986; Iverson et al., 2019). Under these simplifying considerations, the ice flow field in the boundary layer above the bed has been assumed to be undisturbed by local shear stress, such that the role of non-zero local shear stress is, essentially, the reduction in basal speed via a reduction in stress concentration. This leaves the following open questions: how is the ice flow disturbed by local shear stress, and how much does that modify the description of meso-scale friction with respect to the other frictional mechanisms?

In this paper, we derive a friction law that considers non-zero local shear stress, non-Newtonian ice rheology and, we believe for the first time, that accounts for the effect local shear stress has on the ice flow field and in particular on the effective viscosity. First, we provide a short background on friction laws and constitutive relationships that may be used to describe local shear stress. Then, we analytically and numerically derive friction laws at the meso-scale that include these descriptions. We demonstrate that common friction laws developed for sliding with zero local shear stress can reasonably well be extended to sliding with non-zero local shear stress providing appropriate scaling changes. Finally, we discuss our findings in the broader context of predicting glacier basal speed.

3.5 Rationale and Methodology

3.5.1 Glacier friction laws

The first proposed and probably most widely applied friction law (e.g. Morlighem et al., 2013; Shapero et al., 2016; Larour et al., 2019), has been formulated by Weertman (1957) and takes the following form:

$$\tau_b = A_s^{-1/m} u_b^{1/m}, \tag{3.1}$$

where τ_b is the meso-scale averaged bed shear stress, u_b is the meso-scale averaged basal speed, m is a material exponent, and A_s is the sliding parameter which is dependent on ice rheology and bed geometry. If all the bed shear stress is a result of stress concentration around obstacles (i.e. other processes such as regelation are neglected), we have $m = n$, where n is the exponent of Glen's flow law, typically considered equal to 3 (Cuffey and Paterson, 2010). In the hypothesis of very low roughness r, it is found that A_s scales with $r^{-(n+1)}$ (Fowler, 1979).

Weertman law does not take into account the role of cavities, which is commonly included via the meso-scale averaged effective pressure. For a given average ice pressure $\bar{p}_i$ and subglacial water pressure at open cavities p_c, the averaged effective pressure is $N = \bar{p}_i - p_c$. In our analysis we compare our solution with the phenomenological law proposed by Gagliardini et al. (2007), which was defined based on approximating numerical results as

$$\frac{\tau_b}{N} = C\left(\frac{\chi}{1+\alpha\chi^q}\right)^{1/n}, \text{ with } \chi = \frac{u_b}{(CN)^n A_s}, \ \alpha = \frac{(q-1)^{q-1}}{q^q}. \tag{3.2}$$

The parameter $C = \max(\tau_b/N)$ is bounded by the maximum bed slope (Iken, 1981). The exponent parameter $q \geq 1$ depends on the slope severity index, which describes the steepness of the obstacles for a given roughness (Gagliardini et al., 2007). For $q = 1$, τ_b/N increases monotonically (Fowler, 1987; Schoof, 2005) and we obtain a regularized Coulomb friction law (Joughin et al., 2019), while if $q > 1$ the law is double-valued and presents velocity weakening after the basal drag peak $\tau_b = CN$ is reached. At low u_b, Eqn. (3.2) predicts a similar behaviour than Eqn. (3.1). This type of law can be applied to three dimensional sinusoidal beds, as supported by laboratory experiments (Zoet and Iverson, 2015) and numerical simulations (Helanow et al., 2020), although the rate-weakening regime may no longer hold for realistic beds (Helanow et al., 2021).

3.5.2 Strategy for testing the effect of local shear stress on meso-scale bed friction

We first use a simplified analytical model to explore the changes in meso-scale friction with non-zero local shear stress. At this stage, the constitutive law for local shear stress does not require to be described specifically. Instead, we work directly with the meso-scale averaged local shear stress, which we denote τ_f and call solid drag. This first step yields a basis to better understand our findings with more realistic models of sliding, obtained in a second step using numerical simulations. The simplified analytical model developments are presented in Section 3.6.1, and discussed in Section 3.7.

In a second step, we use a numerical model of glacier sliding with non-zero local shear stress prescribed at the micro-scale. Numerical simulations enable to do so at every point of the ice-bed boundary based on an explicit description of the stress tensor σ and its normal and tangential components σ_{nn} and σ_{nt}, respectively. The numerical results are presented in Sections 3.6.2 and 3.6.3, and discussed in Section 3.7.

For the numerical simulations, a local law giving the local shear stress needs to be defined. We will test three different laws. The first law is a simplified version of the original description of debris-bed friction provided by Hallet (1981). This framework adopts the initial hypothesis of Weertman that a water film exists and satisfies static equilibrium everywhere at the ice bed interface, i.e. water pressure at the bed p_w equals normal stress $-\sigma_{nn}$ everywhere, such that local effective pressure $N_{loc} = -\sigma_{nn} - p_w$ is zero. In this case solid-type friction at the micro-scale is due to the buoyant weight of the clast and to its velocity perpendicular to the bed, which is non-zero as a result of ice stretching around obstacles and of basal melting. Iverson et al. (2019) showed that, under constant effective pressure, the meso-scale solid drag does not vary significantly with basal speed, since an increase in velocity (and friction force) is compensated by the growth of cavities that reduces the contact area between the ice and the bed. We approximate this result by considering that Hallet (1981) meso-scale solid drag with constant effective pressure is a constant function $\tau_f = c$ and local shear stress is uniform at the ice-bed interface such that it can be described as

$$\sigma_{nt} = c/s, \tag{3.3}$$

where the value of c depends on debris concentration and size, on bed roughness characteristics and effective pressure (Iverson et al., 2019) and s is the portion of the ice in contact with the bed. Note that this is a approximation of a more complex microscopic based model. In our particular implementation, c is imposed and s is a solution of the problem. We call this approximation the Hallet-like model.

The second law that we consider was proposed by Schweizer and Iken (1992) as 'sandpaper friction'. This model was proposed for higher debris concentration than in Hallet (1981), under the assumption that a very concentrated debris cover would separate the ice from the bed, thus keeping the ice from converging towards the bed. The dependency of local shear stress to the bed normal velocity is thus negligible and local shear stress is controlled by ice pressure. Schweizer and Iken (1992) do not consider the role of water pressure, which means that water at the base must be either absent or not surrounding the clast in contact with the bed. In this case, local shear stress may be expressed through Coulomb friction at the ice-bed interface as

$$\sigma_{nt} = -\mu\sigma_{nn}. \tag{3.4}$$

We note that this Coulomb friction law is also relevant for modeling local shear stress for subtemperate ice (McCarthy et al., 2017). We later refer to this model as the sandpaper model.

In the third law, we consider the case for which the initial hypothesis of Weertman of a water film existing and satisfying static equilibrium everywhere at the ice bed interface is no longer satisfied, so that $N_{loc} = -\sigma_{nn} - p_w > 0$. This is for example expected if a nearby cavity or channel lowers the water pressure below that at static equilibrium around the debris, in which case a dependency on the local effective pressure N_{loc} must be accounted for and σ_{nt} at the ice-bed interface can be expressed as

$$\sigma_{nt} = \mu N_{loc}. \tag{3.5}$$

Later we refer to this law as the effective-pressure-driven Coulomb law, and assume a uniform water pressure everywhere equal to that in cavities.

3.5.3 Modeling setup

We consider a two-dimensional infinite glacier of average thickness $H + h_i$ and surface slope θ contained in the $x - z$ plane and flowing over a periodic bed of height $z = b(x)$ and period L (see Figure 3.2 and Table 1 for the notation definition). Normal and tangential unit vectors at the domain boundary are denoted by $\mathbf{n}$ and $\mathbf{t}$, respectively. The bottom boundary of the ice is given by the periodic function $z = h(x) \geq b(x)$. We study a subdomain of the glacier, limited in width to L and in height to H such that it defines four boundaries, the top $\partial\Omega_1$, the bottom $\partial\Omega_3$ (subdivided into the cavitated interface $\partial\Omega_{3C}$ and the uncavitated interface $\partial\Omega_{3U}$) and the left and right sides $\partial\Omega_2$ and $\partial\Omega_4$, respectively, see

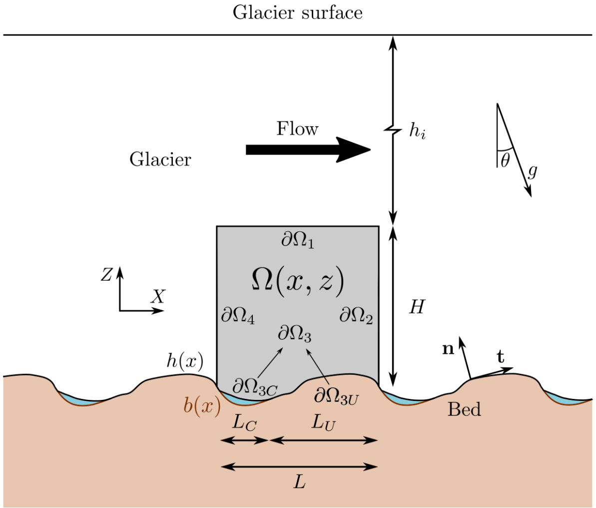

Figure 3.2: An example of a two-dimensional infinite glacier and the domain of interest Ω (in gray). The example shows a vaguely sinusoidal bed in brown with water-filled cavities in blue.

Figure 3.2. Above H, we assume that the flow field is undisturbed by the irregularities of the bed, such that at $z = H$ the stress and velocity fields are uniform. Domain length can be subdivided into two parts, $L = L_C + L_U$, each corresponding to $\partial\Omega_{3C}$ and $\partial\Omega_{3U}$ respectively. In this domain, the Stokes flow equations (momentum and mass conservation) are solved for the ice velocity $\mathbf{u}(x,z)$ and pressure $p(x,z)$:

$$\nabla \cdot \boldsymbol{\sigma} = \mathbf{0}, \nabla \cdot \mathbf{u} = 0. \tag{3.6}$$

Note that gravitational force is neglected in our domain Ω and ice is assumed incompressible. Periodic boundary conditions are applied on left and right sides, far field conditions are applied on the top boundary and correspond to overburden ice pressure of the ice column of height h_i over the modelled domain, $\sigma_{nn} = \bar{p}_i = -\rho_i g h_i \cos(\theta)$, and uniform horizontal velocity u_i. If open, the cavity is supposed to undergone a uniform water pressure p_c. At the uncavitated interface the conditions are impenetrability, $\mathbf{u} \cdot \mathbf{n} = 0$ and imposed shear stresses σ_{nt} given by either Eqn. (3.3), (3.4) or (3.5). At the cavitated interface we impose that normal stress is equal to the cavity water pressure $\sigma_{nn} = -p_c$, and tangential stress is zero $\sigma_{nt} = 0$.

We can perform the balance of vertical and horizontal forces over the bottom boundary to gain some insights about the friction law with non-zero local shear stress. We use the same procedure as that developed by Schoof (2005), considering the convention of negative stresses for compression, and normal and tangential vectors $\mathbf{n}$ and $\mathbf{t}$ with respect to the interface oriented as drawn in Figure 3.2.

Conservation of momentum dictates that basal drag and overburden pressure are balanced by reaction forces at the bottom boundary $\partial\Omega_3$

$$(-\tau_b, \bar{p}_i) = -\frac{1}{L}\int_{\partial\Omega_3} \boldsymbol{\sigma}\mathbf{n} ds. \tag{3.7}$$

Projecting into x and z, separating between horizontal and vertical directions and considering that $\sigma_{nt} = 0$ on $\partial\Omega_{3C}$ gives

$$\tau_b = \frac{1}{L}\int_L h'(-\sigma_{nn})dx + \frac{1}{L}\int_{L_U} \sigma_{nt}\ dx = \frac{1}{L}\int_L h'(-\sigma_{nn} - p_c)dx + \frac{1}{L}\int_{L_U} \sigma_{nt}\ dx \tag{3.8a}$$

$$\bar{p}_i = \frac{1}{L}\int_L -\sigma_{nn}dx - \frac{1}{L}\int_{L_U} h'\sigma_{nt}\ dx, \tag{3.8b}$$

with $h'(x)$ the local slope of the ice bottom boundary and $N = 1/L\int_L \left(-\sigma_{nn} - p_c\right)dx$. Adding p_c to the first integral will help later when studying the upper bound of the basal drag, and does not change the force balance because the integral of $h'p_c$ over the bed vanishes due to the periodicity of the bed. The first equation gives the balance of horizontal force at the bed, with basal drag divided into the viscous drag τ_u, defined as the meso-scale averaged local normal stress at the ice-bed interface, and the solid drag τ_f, defined as the meso-scale averaged local shear stress at the ice-bed interface,

$$\tau_u = \frac{1}{L}\int_L h'(-\sigma_{nn} - p_c)\ dx = \frac{1}{L}\int_L h'N dx, \text{ and } \tau_f = \frac{1}{L}\int_{L_U} \sigma_{nt}\ dx, \tag{3.9}$$

such that $\tau_b = \tau_u + \tau_f$. The horizontal force balance allows us to introduce the solid drag ratio T, a reduced variable that will be used in the following section and is defined as

$$T = \frac{\tau_f}{\tau_b},\ 0 \leq T \leq 1. \tag{3.10}$$

Note that $T = 0$ if sliding with zero local shear stress, i.e. $\tau_f = 0$.

We can also use the force balance to find the basal drag upper bound. Viscous drag is bounded by the slope and the effective pressure (Iken, 1981), so that from the first integral of Eqn. (3.8a) we can define $\tau_u \leq \sup(h')N$. This allows us to define a $C = \max(\tau_u/N) \leq \sup(h')$. Adding τ_f/N to both sides of the inequality we find a new bound in case of non-zero local shear stress, noted C_f, and defined as $C_f = \max(\tau_b/N)$ Substituting Eqn. (3.8a) into $C_f = \max(\tau_b/N)$ gives,

$$C_f \leq \sup(h'(x)) + \tau_f/N. \tag{3.11}$$

In the case of the Hallet-like model (Eqn. (3.3), note that the approach is for sliding under constant effective pressure), we have

$$C_f \leq \sup(h'(x)) + c/N. \tag{3.12}$$

For the sandpaper model, we combine Eqn. (3.4) with Eqn. (3.8a) to obtain

$$\begin{aligned}\tau_b &= \frac{1}{L}\int_L h'N dx + \frac{1}{L}\int_L -\mu(\sigma_{nn} + p_c - p_c)dx = \frac{1}{L}\int_L h'N + \mu N dx + \frac{1}{L}\int_{L_C} \mu p_c dx\\ &= \frac{1}{L}\int_L \left(h'N + \mu N\right)dx + \mu p_c s,\end{aligned}$$

with $s = L_C/L$ the portion of the bed not drowned by the cavity. If we now substitute the expression we just derived into Eqn. (3.8a), rewrite p_c as $\bar{p}_i - N$ and reorder some terms, we obtain the final expression of C_f for the sandpaper model,

$$C_f \leq \sup(h'(x)) + \mu s + \mu(1-s)\bar{p}_i/N. \tag{3.13}$$

In the case of effective-pressure-driven Coulomb law (Eqn. (3.5)) this is

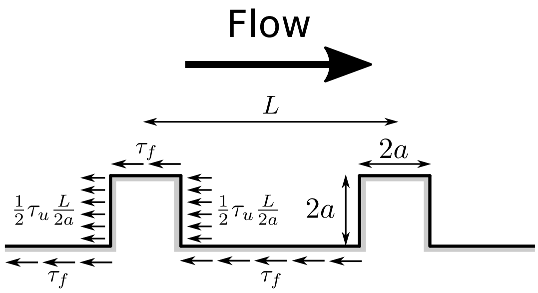

Figure 3.3: Continuous version of the tombstone model with the considered stresses, no cavity.

$$C_f \leq \sup(h'(x)) + \mu, \tag{3.14}$$

as suggested by Schoof (2005).

The presence of local shear stress strengthens the bed, as it can support higher basal stress, i.e. $C_f \geq C$. Indeed, we expect solid drag to take up some of the force that would otherwise be supported by viscous drag. For a given driving stress this would result in slower basal speed compared to the scenario with zero local shear stress. In the following section we solve the flow of ice over an undulated bedrock assuming non-zero local shear stress at the interface. We provide an analytical solution over a simplified tombstone bed and a numerical solution over a sinusoidal bed.

For the analytical solution, we consider the 'tombstone model' similar to the bed of Weertman (1957), in which the bed $b(x)$ is a rectangular function made of protuberances of side $2a$ separated between each other by a distance L, with roughness $r = a/L$ (see Figure 3.3). Considering this geometry allows only an approximate solution, albeit simplifies the problem such that it is tractable analytically. We further assume that i) viscous drag operates on the vertical sides of the bumps, and solid drag on the horizontal sides, and ii) the stress and strain rate fields are uniform over the domain of study.

To obtain the numerical solution we use the finite element model Elmer/Ice (Gagliardini et al., 2013). The numerical domain is a regular mesh of bi-linear quadrilateral elements, vertically refined towards the bottom boundary, with $L = H = 10$m. The bed height function is a single wave function with amplitude a,

$$b(x) = a \sin\left(\frac{2\pi x}{L}\right). \tag{3.15}$$

Note that since we keep the domain length fixed, we modify bed roughness by changing a. The major changes to the numerical implementation with respect to Gagliardini et al. (2007) are i) cavity opening, which now solves the corresponding contact problem between ice and bed using the residual of the Stokes equation (Gagliardini et al., 2013), ii) improved mesh resolution and iii) the already discussed local shear stress laws. Otherwise specified, the friction law is obtained by looking at steady state solutions for cavity water pressure p_c between 0 and $0.8p_i$ with increments of $0.01p_i$, with $p_i = 1.77$ MPa (the pressure of 200 m of ice) and top velocity $u_i = 150$ m a^{-1}, such that the solutions for square obstacles and for a sinusoidal bed are comparable. Spatially averaged variables u_b, τ_b, τ_f and N are then recovered from the velocity vector and the stress tensor.

3.6 Results

3.6.1 Analytical friction law

For the analytical solution, only the case without cavity is presented in the main text, the complete solution including the formation of cavities being given in 3.9. We use $u_b(T = 0)$ for basal speed in a zero local shear stress scenario and $u_b(T)$ for the basal speed when there is non-zero local shear stress at the ice-bed interface.

Assuming two-dimensional flow over square obstacles of side $2a$ and $r = a/L$, deviatoric stresses τ_{xx}, τ_{xz} and effective deviatoric stress τ_E can be approximated as (Cuffey and Paterson, 2010)

$$\begin{aligned} \tau_{xx} &= \frac{1}{2}\tau_u \frac{L}{2a},\ \tau_{zz} = -\tau_{xx},\ \tau_{yy} = 0, \\ \tau_{xy} &= 0,\ \tau_{xz} = \tau_f,\ \tau_{yz} = 0, \\ \tau_E &= (\frac{1}{16}\tau_u^2 \frac{L^2}{a^2} + \tau_f^2)^{\frac{1}{2}}. \end{aligned} \tag{3.16}$$

The constitutive law for ice is

$$\dot{\varepsilon}_{ij} = A\tau_E^{n-1}\tau_{ij}, \tag{3.17}$$

where creep parameter A is considered constant. Combining Eqn. (3.16) with Eqn. (3.17) gives the following strain rates:

$$\dot{\varepsilon}_{xx} = A\left(\frac{1}{16}\tau_u^2\frac{L^2}{a^2} + \tau_f^2\right)^{\frac{n-1}{2}} \frac{1}{4}\tau_u\frac{L}{a}, \text{ and } \dot{\varepsilon}_{xz} = A\left(\frac{1}{16}\tau_u^2\frac{L^2}{a^2} + \tau_f^2\right)^{\frac{n-1}{2}} \tau_f, \tag{3.18}$$

where $\dot{\varepsilon}_{xx}$ is the extension strain rate, and $\dot{\varepsilon}_{xz}$ the shear strain rate, both dependent on τ_u and τ_f. The basal speed is evaluated as the integral of the horizontal velocity gradient over a bump of size $2a$, at a height l from the bed. Assuming uniform strain rates, and $dw/dx = 0$, this is equivalent to

$$u_b = \int_{2a}\frac{du}{dx}dx + \int_l \frac{du}{dz}dz = \dot{\varepsilon}_{xx}2a + 2\dot{\varepsilon}_{xz}l. \tag{3.19}$$

In particular, if we take $l = 2a$ (the distance between the highest and the lowest points of the bed) and rewrite Eqn. (3.18) to include the roughness $r = a/L$ we get

$$u_b = A\left(\frac{1}{16}\tau_u^2\frac{1}{r^2} + \tau_f^2\right)^{\frac{n-1}{2}} \frac{1}{4}\tau_u\frac{1}{r}2a + A\left(\frac{1}{16}\tau_u^2\frac{1}{r^2} + \tau_f^2\right)^{\frac{n-1}{2}} 4a\tau_f. \tag{3.20}$$

Substituting solid drag ratio $T = \tau_f/\tau_b$ into Eqn. (3.20) and factoring out common terms gives the basal speed

$$u_b = A\left(\frac{1}{16}(1-T)^2\frac{1}{r^2} + T^2\right)^{\frac{n-1}{2}} \left(\frac{1}{4}(1-T)\frac{1}{r} + 2T\right)2a\tau_b^n. \tag{3.21}$$

One can note that Weertman's solution is recovered using $T = 0$, in which case we have

$$u_b(T = 0) = \frac{1}{4^n}A\left(\frac{1}{r}\right)^n 2a\tau_b^n. \tag{3.22}$$

To proceed further, we investigate the effect of solid drag on the flow speed with respect to Weertman's solution through evaluating the ratio $(u_b(T)/\tau_b^n)/(u_b(T=0)/\tau_b^n)$, equivalent to the ratio $u_b(T)/u_b(T=0)$, which takes the form

$$u_b(T)/u_b(T=0) = \underbrace{(1-T)^{\frac{2n}{n-1}}}_{\text{pure shear}} + \underbrace{16r^2(1-T)^{\frac{2}{n-1}}T^2 + 8r(1-T)^2T^{\frac{2}{n-1}}}_{\text{strain enhancement}} + \underbrace{128r^3T^{\frac{2n}{n-1}}}_{\text{simple shear}}. \tag{3.23}$$

The first term corresponds to the reduction of basal speed caused by a decrease in pure shear deformation if drag is only due to creep around obstacles. This term is a decreasing function of T, while the other terms mitigate this decrease in basal speed. The second and third terms appear due to the non-linearity of Eqn. (3.17), i.e. ice deformation depends on all stress components, such that shearing the ice will enhance ice deformation by extensional strain rates. The fourth term is the deformation of ice subjected to simple shear only.

If the roughness is very low, Eqn. (3.23) simplifies to $\lim_{r\to 0} u_b(T)/u_b(T=0) = (1-T)^{2n/(n-1)}$, as proposed by Fowler (1986). Note that, if $r = 0$, there is no resistance due to creep around bumps and we have $\tau_u = 0$, and Eqn. (3.21) does not hold. The specific form of τ_b will then be inherited from the form of the local shear stress law , i.e., if we assume that τ_f is given by effective-pressure-driven Coulomb friction, we have $\tau_b = \tau_f = \mu N$.

In the case of Newtonian ice, the flow exponent (Eqn. (3.17)) is $n = 1$, and to avoid indeterminate exponents in Eqn. (3.23) we have to derive the expression from Eqn. (3.21), obtaining

$$u_b(T)/u_b(T=0) = (1-T) + 8rT. \tag{3.24}$$

For very low roughness it simplifies to $\lim_{r\to 0} u_b(T)/u_b(T=0) = 1-T$.

Figure 3.4 (a), shows the expected decrease in basal speed when we introduce local shear stress for $n = 1$, $n = 2$, $n = 3$ and $n = 4$, when we consider the full expression (solid lines, Eqn. (3.21) and (3.24)) or the low roughness approximations of Eqn. (3.21) and (3.24), (dotted lines). On the right panel, we show the relative contribution of the terms of Eqn. (3.21) to the total decrease in basal speed for $n = 3$. Except for high values of $T = \tau_f/\tau_b$, the low roughness expression is a good approximation of the decrease in basal speed with T. For example, if $T = 0.5$, meaning half the basal drag is given by solid drag, the low roughness approximation underestimates the basal speed by 30%. Indeed, this approximation, given by the *pure shear* term of Eqn. (3.21), and represented by the solid line on Figure 3.4 (b), dominates the decrease in basal speed until roughly $T = 0.7$.

We can invert Eqn. (3.21) to obtain a friction law,

$$\tau_b = \left[A\left(\frac{1}{16}(1-T)^2\frac{1}{r^2}+T^2\right)^{\frac{n-1}{2}}\left(\frac{1}{4}(1-T)\frac{1}{r}+2T\right)2a\right]^{-1/n} u_b^{1/n}. \tag{3.25}$$

Note that this expression is non-linear, since $\tau_b = f(u_b, N, T(\tau_b))$, and solving it requires knowledge of the form of $T(\tau_b)$. Moreover, in the case of no local shear stress, Eqn. (3.1), τ_b and $u_b^{1/n}$ were linked by a sliding parameter, $A_s^{-1/n}$. This is no longer the case when local shear stress is non-zero, in which case $\tau_b/u_b^{1/n}$ is a function of $T(\tau_b)$, such that what was a constant parameter is now a variable. Moreover, the dependency in T is stronger for lower roughness, as r appears in the denominator in Eqn. (3.25). We illustrate this point in Figure E.1, where we plot the sensitivity of u_b/τ_b^n to T for several values of r, i.e. $d(u_b/\tau_b^n)/d(T)$. If $T = \tau_f/\tau_b$ is constant then we can define a scaling parameter $A_f^{\text{Tconst}} = u_b/\tau_b^n$, equivalent to

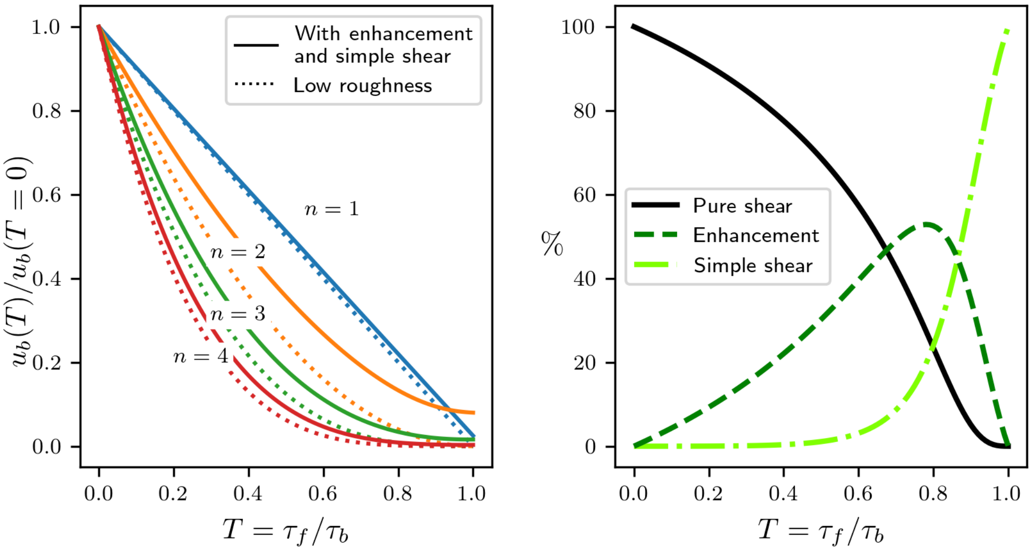

Figure 3.4: Decrease in basal speed as a function of the relative solid drag $T = \tau_f/\tau_b$ for different values of n. Panel (a) shows solutions of Eqn. (3.24) (the $n = 1$ lines) and Eqn. (3.21) ($n = 2$, $n = 3$, $n = 4$), using the full expression (continuous lines) and the low roughness approximation (dotted lines). Panel (b) shows the relative contribution of each term of Eqn. (3.21) for $n = 3$.

$$A_f^{\text{Tconst}} = A_s\left((1-T)^{\frac{2n}{n-1}} + 16r^2(1-T)^{\frac{2}{n-1}}T^2 + 8r(1-T)^2T^{\frac{2}{n-1}} + 128r^3T^{\frac{2n}{n-1}}\right). \qquad (3.26)$$

With A_s the same as in Eqn. (3.1). We show a friction law with constant $T = \tau_f/\tau_b$, scaled with A_f^{Tconst} in the examples given in 3.9.

3.6.2 Numerical friction law with effective-pressure-driven Coulomb local shear stress

Here we present the numerical simulations over sinusoidal beds and effective-pressure-driven Coulomb local shear stress at the base using the model setup presented at the end of section 3.5.3. The friction laws for $r = 0.05$, using scaling parameters C and A_s, are shown in Figure 3.5 (a, b), while the laws for $r = 0.03$ and $r = 0.08$ are given in the supporting information, Figures E.2 and E.3. C and A_s are obtained for each roughness r based on the simulation with $\mu = 0$ as explained in Gagliardini et al. (2007). The friction laws when scaled with C and A_s have the same overall shape, characterized by an initial rate-strengthening regime, with increasing curvature until a peak in $(\tau_b/CN)^3$ is reached and a transition to the rate-weakening regime. The larger the friction parameter μ, the higher the peak value and the steeper the curve in the rate-strengthening phase. The peak in bed shear stress being located higher for higher μ is a consequence of higher upper bound of τ_b, as shown in Eqn. (3.14). Likewise, the origin behind the change in the slope of the rate-strengthening regime can be found in Eqn. (3.23). Under a given basal drag, the higher T is, the slower the glacier flows and the higher the ratio τ_b/u_b, thus the slope of the curve in the rate-strengthening regime increases.

We more quantitatively investigate the extent to which the different friction laws share the same shape by scaling each of these laws with the parameters C_f^{num} and A_f^{num}, analogous to C and A_s in Eqn. (3.2), except they now account for the effect of local shear (Figure 3.5 (c, d)). To compute these parameters we impose that the peak of the laws coincide in the scaled space. C_f^{num} is calculated as $C_f^{\text{num}} = \max(\tau_b/N)$. A_f^{num} is calculated such that $u_b/(A_f^{\text{num}}(CN)^3) = \chi_M$, with χ_M a constant. We fix the value of χ_M by using as reference point the peak of the friction law in Eqn. (3.2) that matches well the friction law with zero local shear stress. We found that $\chi_M = q/(q-1)$, with $q = 1.8$ gives an appropriate collapse of all the curves. The quality of this scaling worsens for lower r, as can be seen in the $r = 0.03$ curves given in Figure E.2.

Focusing on the values of the scaling parameters, we compare C_f^{num} with a (semi)theoretical value $C_f^{\mathrm{the}} = 2k\pi r + \mu$, computed as a combination of Eqn. (3.14) with the expression $C = 0.84\ 2\pi r$ suggested by Gagliardini et al. (2007) for sinusoidal beds. We find that the value of k that best fits C_f^{num} is $k = 0.72$, 12% lower than the value 0.84 found by Gagliardini et al. (2007). The comparison between C_f^{the} and C_f^{num} is shown in the left panel of Figure E.4. While the overall shape of the friction law is conserved, as seen in panel (c) of Figure 3.5, the detailed view in panel (d) shows that the different laws do not all collide into the expected Weertman type behaviour (black line). Moreover, the higher μ, the further from the Weertman line they are. This is a direct consequence of using a constant A_f^{num} when T evolves, which limits the effectiveness of scaling the law by a constant A_f^{num}, specially for lower values of r. In the absence of an explicit theoretical expression for A_f in the case of variable T, we refrain from defining A_f^{the} for these experiments. We plot the values of the scaling parameters normalised by the parameters with no local shear stress, C_f^{num}/C and A_f^{num}/A_s, as functions of μ/r in the supporting information, Figure E.4.

3.6.3 Comparison between the three solid-type friction laws

In this section, we test whether the above presented results using the effective-pressure-driven Coulomb model also hold under other micro-scale descriptions of solid-type friction such as the Hallet-like (Eqn. (3.3)) and sandpaper (Eqn. (3.4)) models. For that, we use a sinusoidal bedrock with a given roughness $r = 0.05$. Since the Hallet-like model assumes constant effective pressure, we change the top boundary conditions from varying effective pressure and constant upper horizontal velocity to constant effective pressure at ≈ 700 kPa (40% of the initial effective pressure used in the other tests) and varying upper velocity u_i from 20 to 400 ma^{-1}. The Hallet-like model is run at fixed solid drag $\tau_f = 50$ kPa in order to lie within the range of values obtained by Iverson et al. (2019, Figure 8) for a sinusoidal bed of roughness $r = 0.05$ with debris of radius 60 mm and an effective pressure of $N = 500$ kPa (note that the roughness defined in Iverson et al. (2019) is two times the roughness defined here). The sandpaper model is implemented with a friction parameter $\mu = 0.05$, with the same top boundary conditions as the effective-pressure-driven Coulomb tests explained in section 3.5.3.

As shown in Figure 3.6, both the Hallet-like and sandpaper models yield similar predictions as those with the effective-pressure-driven Coulomb model (Eqn. 3.5) presented in the previous section. The same scaling using A_f^{num} and C_f^{num} is used here to compare the three different models of local shear stress.

The values of $C_f^{\mathrm{num}} = \max(\tau_b/N)$ are found to match quite well the theoretical values of C_f^{the}, which as in the previous section result from combining $C = k2\pi r$ proposed by Gagliardini et al. (2007) (with the $k = 0.72$ found in our study) with the different expressions for C_f given in Eqn. (3.12) to (3.14). Indeed, for the Hallet-like model with $\tau_f = 50$ kPa, the numerical value $C_f^{\mathrm{num}} = 0.320$ for $N = 700$ kPa is also not far away from the expected theoretical one $C_f^{\mathrm{the}} = 0.72 \times 2\pi r + \tau_f/N = 0.298$ obtained from Eqn. (3.12). For the sandpaper model, the numerical value $C_f^{\mathrm{num}} = 0.331$, reached for an uncavitated bed portion of $s = 0.693$ and an effective pressure $N = 634$ kPa, is very close to $C_f^{\mathrm{the}} = 0.72 \times 2\pi r + \mu s + \mu(1-s)p_i/N = 0.312$ given by Eqn. (3.13).

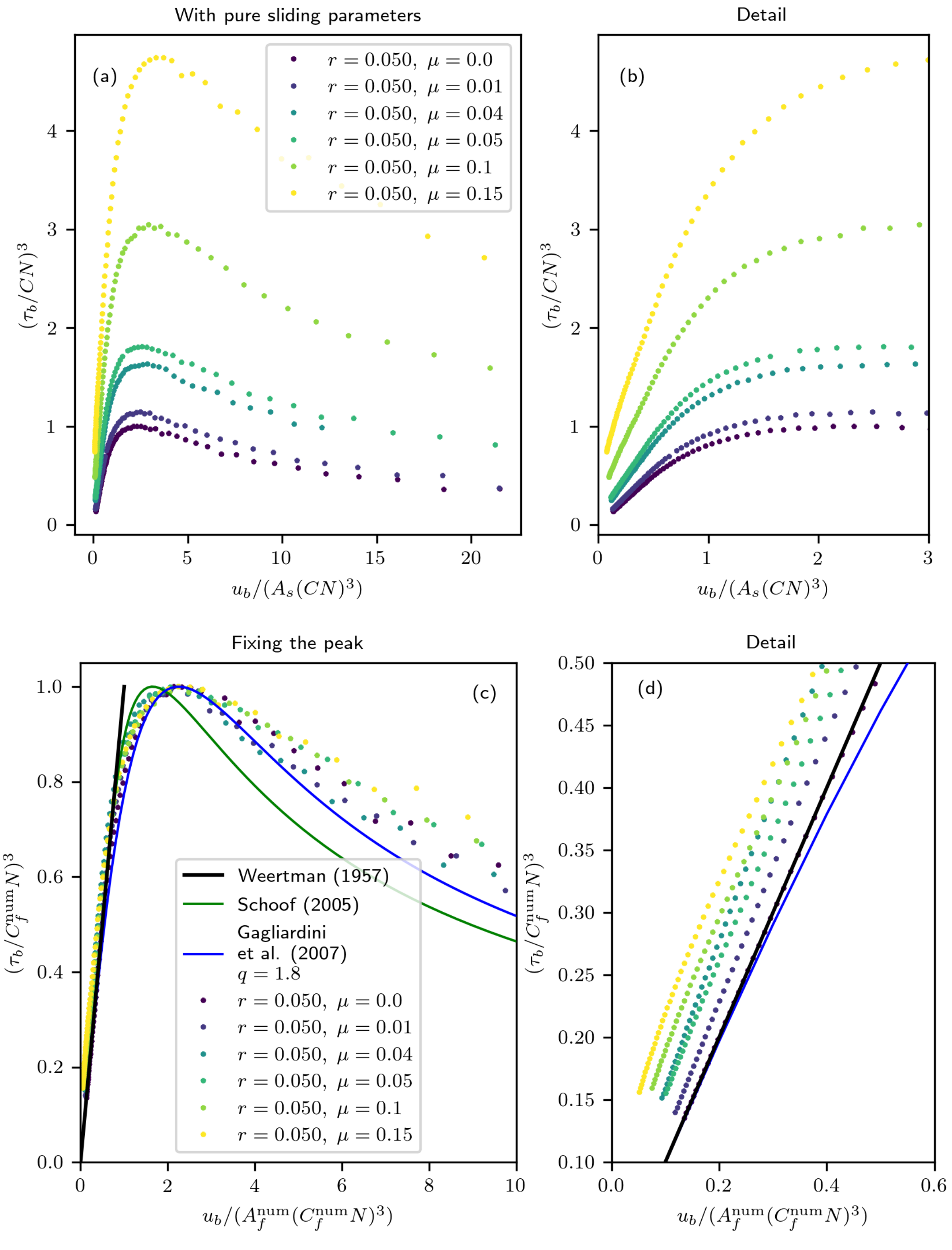

Figure 3.5: Comparison of the friction laws obtained numerically for a sinusoidal bed of roughness $r = 0.05$ and different values of μ, using ((a) and (b)) C and A_s as scaling parameters and ((c) and (d)) C_f^{num} and A_f^{num} as scaling parameters. Panels (b) and (d) are limited to the rate-strengthening part of the curves shown in (a) and (c), respectively. Symbols represent the numerical results and the curves show the Weertman (Eqn. (3.1)), Schoof (2005) and Gagliardini et al. (2007) (Eqn. (3.2)) solutions.

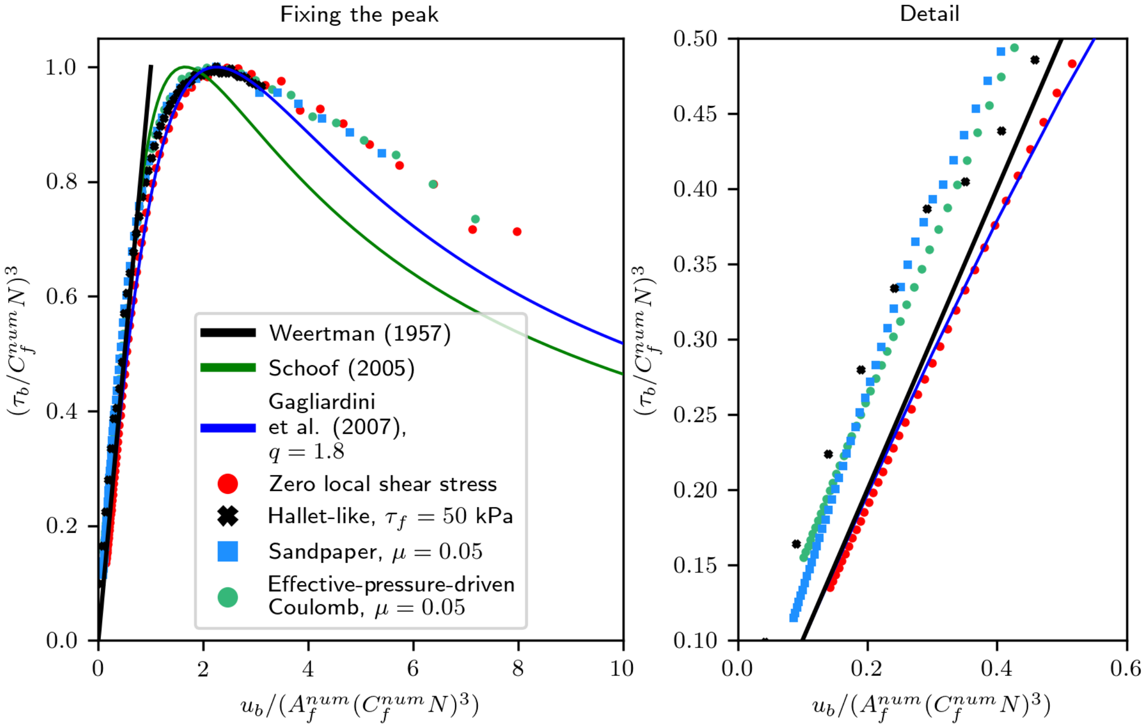

Figure 3.6: Numerical friction laws over a sinusoidal bed of $r = 0.05$ using three different local shear stress laws, constant solid drag (also called Hallet-like, Eqn. (3.3)) with $\tau_f = 50$ kPa, Sandpaper (Eqn. (3.4)) with $\mu = 0.05$, and effective-pressure-driven Coulomb (Eqn. (3.5)) with $\mu = 0.05$. Symbols represent the numerical results and the curves show the Weertman (Eqn. (3.1)), Schoof (2005) and Gagliardini et al. (2007) (Eqn. (3.2)) solutions.

3.7 Discussion

We demonstrate that meso-scale friction over sinusoidal beds under non-zero local shear stress exhibits similar characteristics to laws previously introduced with zero local shear stress, which are, mainly, softening during the rate-strengthening behavior due to the onset of cavities, a maximum attainable basal drag for a given effective pressure, and rate-weakening regime after such maximum drag is attained. The new element introduced in the friction law is the influence of local shear stress on stress concentrations and thus ice viscosity, which was ignored in previous models, although it has a relatively low impact on the overall result. Added local shear stress lowers sliding speed, although this decrease is mitigated by an increase in the effective deviatoric stress, which decreases the effective viscosity. This strain enhancement effect is represented by the T dependent terms in the (implicit) friction law given in Eqn. (3.21). This complicates the use of scaling parameters that generalize the friction law for a variety of boundary conditions. In the case of sinusoidal beds, we see that for our tested roughness and local shear stress laws, we can exploit that the form of the law is similar to sliding with no local shear stress to obtain reasonable scaling parameters by imposing that all friction laws attain the peak at the same point $(u_b/(A_f^{\mathrm{num}}(C_f^{\mathrm{num}}N)^3) = q/(q-1)$ (with $q = 1.8$) and $\tau_b/(C_f^{\mathrm{num}}N) = 1$. The quality of the scaling becomes worse for high μ and low r, as a result of the sensitivity of u_b/τ_b^n to $T = \mu N/\tau_b$ and r, see Figure E.1. Our results show that determining A_f^{num} requires solving the friction law until the peak is reached. This has several important implications. Firstly, it requires knowledge of the form of local shear stress and its relationship with other variables (e.g. glacier basal speed, effective pressure), since the friction law has to be solved. Secondly, it requires that the weakening regime is not suppressed when sliding with local shear stress, as our results show, in accordance with those of Iverson et al. (2019) which were obtained using Hallet friction and neglecting the enhancement effect. The weakening regime can only be suppressed if local shear stress increases fast enough with increasing sliding, as shown in 3.9.

How accurate is the value of the computed C_f^{num} and A_f^{num} will depend on the resolution of the friction law around the peak, i.e. on the number of points used in each numerical friction law. Since we compute C_f^{num} and A_f^{num} by looking at the point with the highest τ_b/N, too few points will mean that the numerically retrieved peak is far away from the expected position. It does not pose a problem in our case, since the relatively cheap computational cost of the numerical scheme (2D) means we compute one point of the simulation for each 1% increment of p_c, obtaining a satisfactory number of points around the peak. It could, however, pose a problem if performing a similar analysis on more complex configurations, such as three dimensional geometries.

The similarity of the friction laws with zero and with non-zero local shear stress appears to be valid regardless of the specific constitutive law used to describe local shear stress. We further explore the validity of this assumption in our comparison between models of local shear stress, as shown for different regimes of the friction law in Figures E.5, E.6 and E.7 of the supplementary material. The biggest differences in local shear stress distribution across models happens in the no-cavity regime, where the pressure-based laws vary by a factor of $\pm 100\%$ with respect to the Hallet-like implementation. However, in Hallet (1981) local shear stress comes from the weight of the particle and the stretching rate of the ice, which we can expect to concentrate at the upslope portions of glacier beds. This is already the case for a pressure based shear stress model, thus increasing even more the similarities between models for the no-cavity regime, and therefore the convenience of simple, straight-forward models of pressure-based friction for studying how τ_f affects sliding.

We have seen that the forms of a friction law with zero solid drag and a friction law with solid drag are very similar, complicating the identification of the presence or not of solid friction based on real data (e.g. Gimbert et al., 2021b). A possible solution would be the comparison of field estimates of A_s and C with those obtained with accurate flow simulation over detailed three-dimensional glacier beds (Helanow et al., 2021). Large discrepancies between them could indicate the presence of non-zero local shear stress. This comparison would require accurate knowledge of bed geometry, which is usually only possible in deglaciated areas, as well as good estimates of basal drag acting upon the studied zone, so it is not a feasible option for the large majority glaciers.

Our study has been formulated under steady-state conditions and the results may differ drastically under non-steady conditions, since solid drag likely has a shorter response time than viscous drag. Similarly, we don't expect that the presently established conclusions applies to the case of highly concentrated debris at the glacier base that would make the ice-debris mixture behave differently than a viscous fluid. The validity of our result should be also tested for other geometries, both two and three dimensionals. For three dimensional beds, we can expect that lateral variations in bed topography will restrict high stresses to a smaller bed area (Helanow et al., 2020), increasing the strain enhancement effect with respect to two dimensional beds.

3.8 Conclusions

In this study, we developed a new analytical model of glacier sliding over rough hard beds with local shear stress (such as debris-bed friction) that includes the effects of local shear stress on viscosity. The influence that non-zero local shear stress has on sliding can be included in the friction law by adding terms to the friction law based on bed geometry and average solid-type drag. We show that

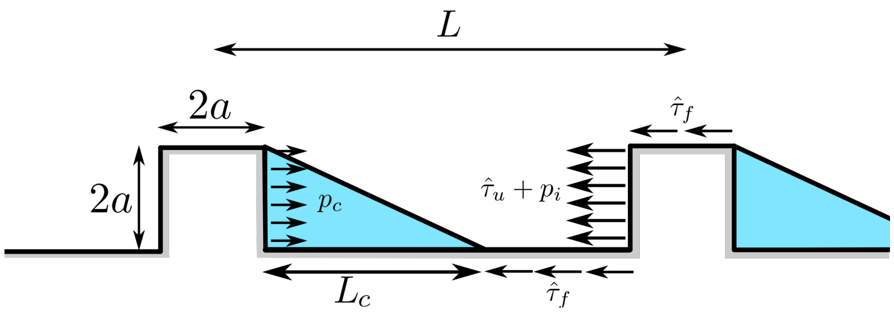

Figure 3.7: Conceptual model of cavity opening in a tombstone bed. Adapted from Andrew Fowler's solution.

additional strain enhancement will result in faster flow than could be expected, if the effects of local shear stress on friction are neglected. The effect of local shear stress on ice viscosity render the friction law implicit, further complicating the identification of scaling parameters from a purely physical point of view. Nevertheless this complication, our findings on the form of the friction law are coherent with previous studies that assumed low quantities of ice to bed friction. Ice creep around obstacles and cavities will still be representative of the sliding process, unless i) there is rate increasing solid drag and ii) it is strong enough to compensate the rate-weakening viscous drag. As a result, the friction law of glaciers sliding with non-zero local shear stress at the base will retain the same form as the law developed for sliding with no local shear stress, including the rate-weakening regime. We can exploit this fact to use laws developed for sliding with zero local shear stress to represent sliding with non-zero local shear stress, although this can fail at some circumstances, such as low roughness or high degrees of solid drag. Further work has to be carried out to confirm how the interplay between local shear stress and water pressure modifies the overall sliding dynamics, and how important the strain enhancement effect can be when sliding over realistic three-dimensional beds.

3.9 Appendix: Analytical model of sliding with non-zero local shear stress and open cavities over square obstacles

We continue in detail the analytical model developed in the main text. This solution includes the presence of cavities, and is greatly inspired by the solution for sliding over a tombstone bed with and without open cavities done by A. Fowler as part of the exercises of the Mathematical Geoscience course in Oxford University.

3.9.1 Rate-strengthening regime

We assume a cavitation state as in Figure 3.7. The spatially averaged values are lower than the actual stress applied onto the ice,

$$\begin{aligned} \tau_u L &= (\hat{\tau}_u + p_i - p_c)2a = (\hat{\tau}_u + N)2a, \\ \tau_f L &= \hat{\tau}_f (L - L_C). \end{aligned} \tag{3.27}$$

We can rewrite the equations to have the stresses as function of the spatially averaged drags. We can estimate cavity length L_C from mass continuity. In the uncavitated part, we have

$$\frac{du_b}{dx} = -\frac{dw}{dz},$$

Variable	Description	Unit
A	Creep parameter	MPa^{-n}a^{-1}
A_s	Sliding parameter if sliding with zero local shear stress	m a^{-1} MPa^{-n}
A_f	Sliding parameter if sliding with non-zero local shear stress	m a^{-1} MPa^{-n}
A_f^{Tconst}	Sliding parameter under constant T	m a^{-1} MPa^{-n}
A_f^{num}	Numerically computed A_f	m a^{-1} MPa^{-n}
a	Half bump height, sinus amplitude	m
$b(x)$	Bed height	m
c	Local shear stress in the Hallet-like model	MPa
C	Maximum attainable τ_u/N	-
C_f	Maximum attainable τ_b/N	-
C_f^{num}	Numerically computed C_f	-
C_f^{the}	C_f computed with a (semi) theoretical expression	-
H	Top boundary height	m
h_i	Height of the ice column	m
$h(x)$	Bottom of the ice	m
$h'(x)$	Slope of $h(x)$, dh/dx	-
L	Domain period length	m
L_U	Length of the uncavitated bed	m
L_C	Length of the cavity	m
$\mathbf{n}$	Normal vector	-
n	Glen's flow law exponent	-
N_{loc}	Local effective pressure	MPa
N	Mean effective pressure	MPa
p	Flow pressure	MPa
p_i	Ice column pressure	MPa
p_c	Cavity water pressure	MPa
p_w	Local subglacial water pressure	MPa
r	Bed roughness, a/L	-
s	Portion of the bed drowned by a cavity, L_C/L	-
T	Solid drag ratio, τ_f/τ_b	-
$\mathbf{t}$	Tangential vector	-
$\mathbf{u}$	Flow velocity vector	m a^{-1}
u	Horizontal component of $\mathbf{u}$	m a^{-1}
u_i	Ice velocity at top boundary	m a^{-1}
u_b	Basal slip	m a^{-1}
v	Vertical component of $\mathbf{u}$	m a^{-1}
μ	Bulk friction parameter	-
τ_b	Basal drag	MPa
τ_u	Viscous drag	MPa
τ_f	Solid drag	MPa
$\boldsymbol{\sigma}$	Cauchy stress tensor	MPa
σ_{nn}	Normal stress	MPa
σ_{nt}	Tangential stress, local shear stress	MPa

Table 3.1: Table of variables

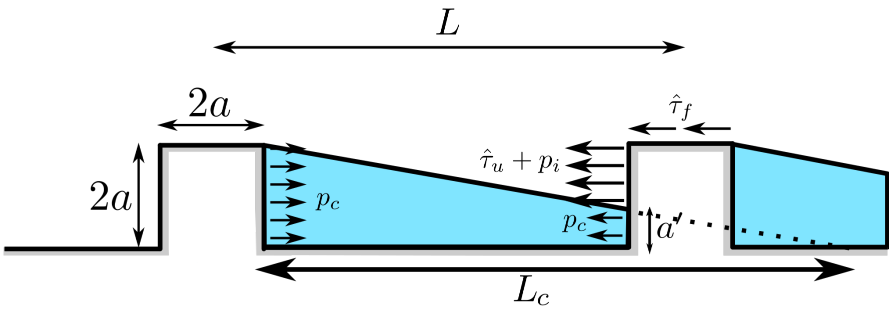

Figure 3.8: Conceptual model of square bed with open cavities that drown part of the obstacles. Adapted from Andrew Fowler's solution.

with w the vertical component of ice velocity. Now we consider that dw/dz can be approximated by the strain rate $\dot{\epsilon}_{zz} \approx AN^n$, the strain rate of the ice being compressed by the difference between the ice pressure and the water pressure. Taking $du_b/dx \approx u_b/(L - L_C - 2a)$ gives $u_b/(L - L_C - 2a) \approx AN^n$. To continue we define the roughness as $r = a/L$, the solid drag ratio $T = \tau_f/\tau_b$, and the portion of cavitated bed as

$$s = \frac{L_C}{L} \approx \frac{u_b}{LAN^n} - 2r. \tag{3.28}$$

We obtain the following expressions for the stresses at the uncavitated part of the bed,

$$\begin{aligned}
\hat{\tau}_u &= \left(\frac{1}{2r}(1 - T) - \frac{N}{\tau_b}\right)\tau_b,\\
\hat{\tau}_f &= \frac{1}{1 - s}T\tau_b.
\end{aligned}$$

Applying Glen's flow law, this gives the following strain rates around the best obstacles

$$\begin{aligned}
\dot{\epsilon}_{xx} &= \frac{1}{2}A(\hat{\tau}_u^2 + \hat{\tau}_u^2)^{\frac{n-1}{2}}\hat{\tau}_u\\
&= \frac{1}{2}A\left(\left(\frac{1}{4r^2}(1 - T) - \frac{N}{\tau_b}\right)^2 + \frac{1}{(1 - s)^2}T^2\right)^{\frac{n-1}{2}}\left(\frac{1}{2r}(1 - T) - \frac{N}{\tau_b}\right)\tau_b^n,\\
\dot{\epsilon}_{xz} &= A(\hat{\tau}_u^2 + \hat{\tau}_u^2)^{\frac{n-1}{2}}\hat{\tau}_f\\
&= A\left(\left(\frac{1}{4r^2}(1 - T) - \frac{N}{\tau_b}\right)^2 + \frac{1}{(1 - s)^2}T^2\right)^{\frac{n-1}{2}}\frac{1}{1 - s}T\tau_b^n.
\end{aligned} \tag{3.29}$$

Using the same arguments as for sliding without cavities, the basal speed is $u_b = \dot{\epsilon}_{xx}2a + 2\dot{\epsilon}_{xz}2a$.

3.9.2 Rate-weakening regime

Here we consider that cavities start to drown the vertical faces of the obstacles and the bed cannot support as much stress as before, see an example in Figure 3.8. The length of cavity is now $L_C > L - 2a$. The vertical face of the obstacles has been reduced to $2a - a'$, this area decreases with increasing cavitation. Conversely, the area where $\hat{\tau}_f$ applies is $2a$ for any degree of cavitation (a particularity of the tombstone model, in general it decreases with increasing cavitation).

The force balance gives

$$\begin{aligned} \tau_u L &= (\hat{\tau}_u + N)(2a - a'), \\ \tau_f L &= \hat{\tau}_f 2a. \end{aligned} \tag{3.30}$$

The drowned side of the obstacle, a', can be obtained by application of Thales' theorem (see Figure 3.8),

$$\frac{2a}{L_C} = \frac{a'}{L_C - L + 2a}.$$

Rewriting and multiplying by L on both sides gives

$$a' = 2a(s - 1 + 2r)/s. \tag{3.31}$$

Following the same steps as before, we have the stresses in the undrowned part of the bed,

$$\begin{aligned} \hat{\tau}_u &= \frac{1}{2r - a'/L}\left((1-T) - \frac{N}{\tau_b}\right)\tau_b, \\ \hat{\tau}_f &= \frac{1}{2r} T\tau_b. \end{aligned}$$

And applying Glen's flow law gives

$$\begin{aligned} \dot{\epsilon}_{xx} &= A(\hat{\tau}_u^2 + \hat{\tau}_f^2)^{\frac{n-1}{2}}\hat{\tau}_u \\ &= A\left(\left(\frac{1}{2r - a'/L}(1-T) - \frac{N}{\tau_b}\right)^2 + \frac{1}{4r^2}T^2\right)^{\frac{n-1}{2}}\left(\frac{1}{2r - a'/L}(1-T) - \frac{N}{\tau_b}\right)\tau_b^n, \\ \dot{\epsilon}_{xz} &= A(\hat{\tau}_u^2 + \hat{\tau}_f^2)^{\frac{n-1}{2}}\hat{\tau}_f \\ &= A\left(\left(\frac{1}{2r - a'/L}(1-T) - \frac{N}{\tau_b}\right)^2 + \frac{1}{4r^2}T^2\right)^{\frac{n-1}{2}}\frac{1}{2r}T\tau_b^n. \end{aligned} \tag{3.32}$$

The basal speed is as before, $u_b = \dot{\epsilon}_{xx}2a + 2\dot{\epsilon}_{xz}2a$.

3.9.3 Full law

We obtain a law in three parts:

1. Weertman style, as long as $N \geq (1-T)\tau_b/(4r)$
2. Rate-strengthening with cavities, from $N < (1-T)\tau_b/(4r)$ until $s = 1 - 2r$
3. Rate-weakening regime with cavities

The law is continuous with discontinuous slope. We plot in Figure 3.9 the law for $r = 0.1$, $N = 2$ MPa, and $\tau_f = T\tau_b$ with constant T, with (solid curves) and without (dotted curves) the strain enhancement effect, with no scaling variables on the top panel and with $C_f^{\mathrm{num}} = \max(\tau_b/N)$ and A_f^{Tconst} (see Eqn. (3.26)) on the bottom panel.

We see that the rate-weakening regime is not suppressed under constant T. Moreover, rate-weakening can only be suppressed if τ_f increases with sliding speed faster than τ_u decreases i.e. if the increase in τ_f is enough to overturn the weakening due to cavity growth. We compare in Figure 3.10 such a case with the friction law obtained for $T = 0.2$. The blue line corresponds to a friction law with rate increasing solid drag, such that the solid drag ratio is $T = 0.3 + 1.25 \times 10^{-4}u_b$. This expression for T was chosen just for illustration purposes of the possibility of rate-weakening suppression and it

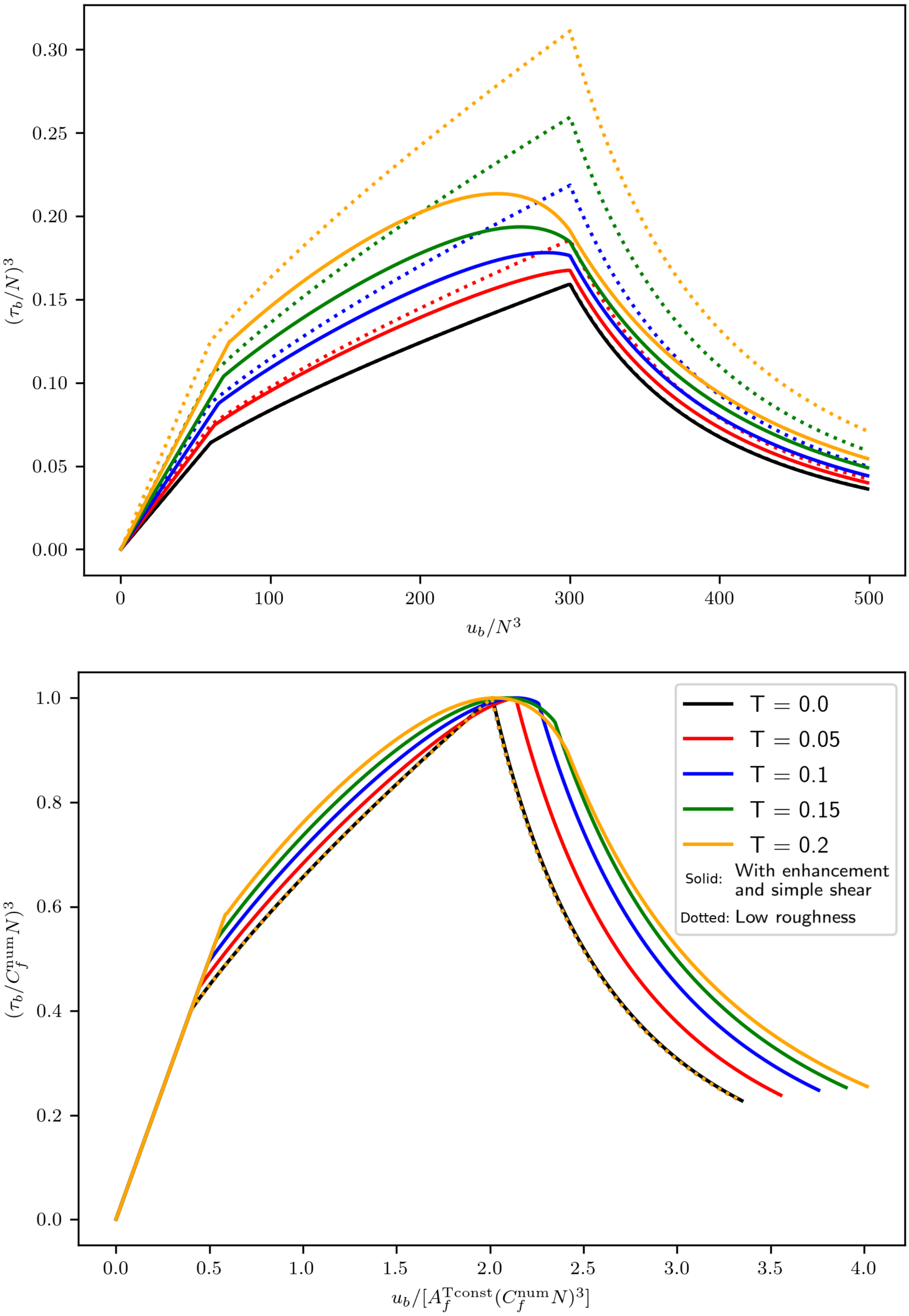

Figure 3.9: Theoretical friction laws over a tombstone bed under constant solid drag ratio, for $r = 0.1$ and $N = 2$ MPa. We show the solutions with (solid curves) and without (dotted curves) the strain enhancement effect, in their unscaled (top panel) and scaled (bottom panel) version. We can see in the top panel that at equal basal drag, ignoring the influence of τ_f in ice viscosity results in an underestimation of sliding velocity. Once properly scaled, the friction laws converge approximately into the same shape.

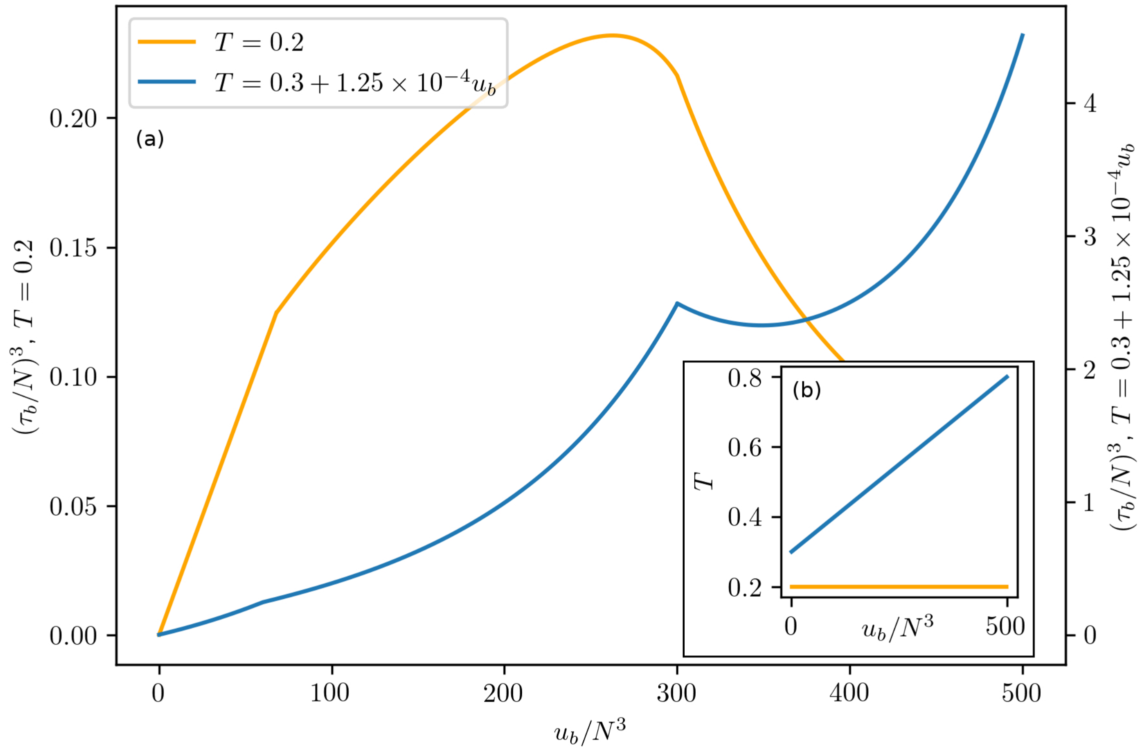

Figure 3.10: Theoretical frictions laws over a tombstone bed with constant $T = 0.2$ and linear $T = 0.3 + 1.25 \times 10^{-4} u_b$. We show the laws in the main panel (a), and the values of T in subpanel (b). Comparing the shapes of the orange and and blue curves we see that under very high and rate increasing solid drag ratio T, the friction law has no weakening, except for just after the bumps start to be drowned (u_b/N^3 between 300 and 400 m a^{-1} MPa^{-3} in this particular example). The linear expression of T of the no-weakening example (blue line) is chosen for illustration purposes only.

does not intend to represent a realistic expression of solid drag ratio.

3.10 Acknowledgements and data

This work was supported by the French National Research Agency project SAUSSURE (ANR-18-CE01-0015-01). The authors would like to thank Andrew Fowler for his solution of sliding with cavity over a tombstone bed, as well as Nathan Maier and Christian Vincent for their useful comments and help. The authors are indebted as well to all reviewers, whose accurate comments greatly improved the original manuscript.

The numerical output and the scripts used process the data and generate the plots are accessible in the Zenodo repository of the SAUSSURE project, `https://doi.org/10.5281/zenodo.5046764` (Roldán-Blasco et al., 2022).

Chapter 4

Visiting the coupling between hydrology and friction from the perspective of the lost last paper(s) of Louis Lliboutry

> *On en est resté aux théories grossières, incomplètes et erronées émises dans les années 60 par Weertman, moi-même, Nye, Röthlisberger et Budd,qui n'ont plus q'un intêret historique.*[1]
>
> Louis Lliboutry, 2005.

4.1 Preface

In Chapter 1, we saw that most friction laws are built under the assumption that water pressure is independent of sliding and that cavities are instantaneously at equilibrium with sliding speed and water pressure, i.e. the friction laws are formulated for the steady state. In this Chapter we investigate hydro-mechanical coupled models of glacier flow under unsteady water pressures, in a manner slightly different than presented in the two previous Chapters: I present a model of which I am not the author, and I have almost no results to show. The goal of this Chapter is to i) write down the story and make public the last model of Louis Lliboutry, ii) provide an explanation of such model, and iii) set some comparison between his work and current models of unsteady sliding. To do so, we start with the historical background of "Glissement et hydraulique sous-glaciares", an unpublished conferece paper that develops a model presented by Louis Lliboutry in 2005, which we include and translate as part of this PhD in Annex **??**. We continue with our interpretation of the model. Then we compare the results of Lliboutry's model with those of Gilbert et al. (2022) and establish their similarities and differences. This paper is being prepared for an eventual submission to *Journal of Glaciology*, as Lliboutry originally intended.

---

[1] Translation: We remain captive to the crude, incomplete, and erroneous theories developed in the 60s by Weertman, myself, Nye, Röthlisberger, and Budd, which should only be of a historical interest today.

4.1.1 Setting

During one meeting held at the beginning of this PhD, Olivier Gagliardini told a story about a paper that had been presented by Louis Lliboutry in a conference many years ago and that he had recently found. In the conference paper, Louis Lliboutry developed a coupled model of glacier sliding under unsteady water pressures, and according to its grandiose wording it was worth a reading. Olivier Gagliardini promptly shared it with a few collaborators of the SAUSSURE project, and while we realised that there was potential behind it, its lack of details and insufficient explanations meant that the amount of effort needed to unravel the work of Lliboutry was perhaps too much for what we could get out of it. The idea kept wandering around our heads while we were busy with our everyday research, and we never really got to take a further look. It wasn't until the end of 2021 that, dreading to perform yet another correction on "The effect of local shear on glacier sliding", I started to work on Lliboutry's last paper to procrastinate a little bit. What started as an intellectual exercise eventually became a project in itself and the more I worked on it, the more interest I had on understanding his work. The experience gained during my PhD had led me in a pretty good position to reverse engineer the models presented by Lliboutry and provide a reasonable explanation of the model. Working on analytical friction laws, and having passed time with Lliboutry's first (english written) paper on glacier friction laws (Lliboutry, 1968) helped me understand his geometrical reasoning, which was key to unravel the equations proposed. The experience dealing with the actual dynamics of mountain glaciers, and their complex mechanical behaviour (e.g. effect of valley sides, distribution of subglacial channels, opening and closing of cavities) helped interpret the physical, non-equations based, aspect of the paper. A few dedicated weeks during spring and summer 2022 helped me iron most of the details of the paper that were still around[2], and thus this account became possible.

4.1.2 Contributions

The main contributor to this Chapter is of course, Louis Lliboutry, who wrote the original paper which is now reproduced and translated in Annex **??**. I am responsible for working most of the aspects of Lliboutry's original model. I'd like to thank Facu Sapienza, who assisted with a few details regarding the friction law just after the 2022 Karthaus Summer School, and Adrien Gilbert, who discussed with me his recent work (Gilbert et al., 2022) and gave a thorough review to the original version of this Chapter. Olivier Gagliardini provided the original document, and with Florent Gimbert and Christian Vincent corrected a few errors and suggested changes to improve the text, and pushed for making this Chapter something more than just a nice story to be told.

4.2 The lost paper(s) of Louis Lliboutry

Louis Lliboutry's contribution to glaciology is vast, covering a wide array of topics (e.g. glacier friction laws, ice creep, ice texture, glacial geomorphology, surface mass balance, numerical modeling of glacier flow, theoretical fluid dynamics, subglacial hydrology)[3]. The most notorious of them all is, most probably, glacier friction laws, to which he dedicated more than 20 papers. It occupied a great portion of his scientific production from the late 50's through the 60's, up to the point that the correctness of his own theories, and the incorrect theories of his peers, most notably Johaness Weertman, became a personal issue. As stated by Fowler (2011), "[Weertman and Lliboutry] bickered with one another

---

[2] I have not been able to solve it, though, see section 4.3.4.

[3] This introduction is partly based on the recollection of this story written by Olivier Gagliardini for Louis Lliboutry's biography, (Turrel, 2017), translated into english for the introduction of the SAUSSURE project, https://saussure.osug.fr/-History-.

through a number of publications, variously adapting or improving (largely in cosmetic ways) their two theories. The course of this tussle was finally charted in exasperation by Lliboutry (1968), following which the eruptive phase entered a period of dormancy". What Andrew Fowler probably didn't know, nor many researchers at the LGGE (the Laboratory of Glaciology and Geophysics of the Environment of Grenoble, now part of IGE), is that Louis Lliboutry continued to think about the problem long after he retired. Let's put things in perspective.

On Thursday 10th March 2005, the glaciology and snow sciences section of the SHF (Hydrotechnical French Society, or Societé Hydrotechnique Française in the original french) organised their annual meeting in Grenoble. Among the speakers there was the already retired Prof. Louis Lliboutry, and attending the presentation there was Olivier Gagliardini. In fifteen minutes, Liboutry presented a conference paper of six pages titled "Glissement et hydraulique sous-glaciares" ("Sliding and subglacial hydraulics"), wich we reproduce in Annex **??**. Its first paragraph stated:

"During the last three years, my intellectual activity has focused on the sliding of temperate glaciers and the subglacial flow of water. I have developed a theory of which I cannot but give here a brief and incomplete sketch. It is explained in three articles that I am finishing, and that I will submit to *Journal of Glaciology*".

In this conference paper of six pages, he develops a new conceptual hydro-mechanical coupled model of glacier flow, including a new friction law, temporal changes in cavity volume due to transversal water flow across the glacier and a spatially variable water pressure. Of the three announced papers, the first one would (probably) be the model of temperate valley glaciers, the second one would treat surging glaciers, and the third one would deal with sub-daily unsteady water pressures.

The conference paper of Lliboutry has several methodology sections, all following the same logic. Lliboutry introduces a physical process (say, the friction law), describes the idea behind his model (sliding past bumps with connected and unconnected cavities), gives some assumptions (hemispherical bumps of same radius, no regelation), continues with the resulting equation (in this case, Eqn. (4.11)) and adds an interpretation of it (we can expect non-negligible drag due to isolated cavities) and a motivation (this new law allows for explaining the fast sliding velocities in some glaciers). He repeats this cycle for several parts of the hydro-mechanical coupled model: the friction law, subglacial flow, the temporal evolution of the subglacial hydrology system, and the steps to solve the mathematical problem. After presenting the model, he proposes an example for a valley glacier, "solves" it, discusses that it yields reasonable results, and closes the paper saying

"In conclusion, this study shows that

- A realistic model, taking into account the laws of Mechanics and Physics can be established. Glaciologists should not try to just look for simple correlations.
- There is a considerable amount of numerical calculations to be done. I leave it for the younger researchers, not taken back for the fact that the topic is not fashionable anymore."

The presentation and the accompanying document were regarded by the public as incomprehensible, and it was quickly forgotten. In its defence, the model was quite complex to be explained in such a short time, and it can be said that since the model and its applications were going to be published in three articles, the details could be worked out later.

Unfortunately, that never happened. When Louis Lliboutry died two years later, the articles hadn't been published. Years later, and asked to write some words for Lliboutry's biography (Turrel, 2017), Olivier Gagliardini looked for them in Lliboutry's personal notes and computer, but neither he, nor Lliboutry's family, could find anything. Likewise, the editorial board at *Journal of Glaciology* confirmed

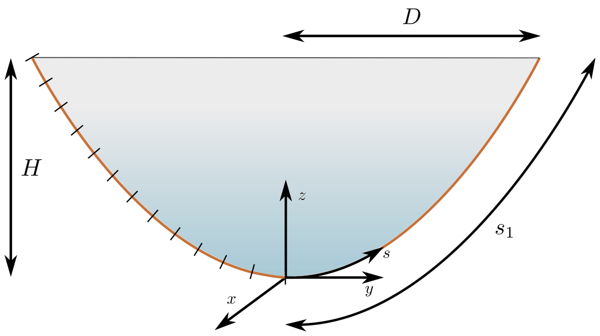

Figure 4.1: Cross section of a parabolic glacier valley of depth H and half-width D. The left half of the bed is discretized in 12 elements, as considered by Lliboutry for his example.

that they had never received any finished paper, nor any draft whatsoever. The only thing that was left were the few copies that had been distributed (physically, not numerically) to the audience, in the shape of a short, convoluted document written in french that juxtaposed assumptions with results and conclusions, with only seven equations and one single figure providing part of the initial conditions needed to run the model.

Fortunately, after carefully studying the original document, we have been able to reconstruct and interpret most of what is presented in Lliboutry (2005). The model presented below is an intrinsically hydro-mechanical coupled model, the third approach discussed in Chapter 1 (section 1.3.2.2). In the particular framework of Lliboutry (2005), sliding velocities are controlled by water pressure and cavity size, water pressure depends on changes in cavity size, and the evolution of cavities is set by sliding velocities and subglacial water pressures. This interdependence between sliding and hydrology is very similar to the model proposed by Gilbert et al. (2022), which so far is the only framework that consistently treats these variables together. For this reason, we will compare the model of Lliboutry (2005) to that of Gilbert et al. (2022).

The original structure of Lliboutry (2005) has been changed to make this Chapter more understandable, and all the diagrams except for Figure 4.3 are new. We provide more equations than the original paper, in order to clarify the original model, extend it and compare it with Gilbert et al. (2022). For internal consistency we rename all variables with the nomenclature already used in this dissertation (i.e. basal speed will be called u_b, not U as in the original), and we try to keep the definition of new variables to a minimum. When the text says 'Lliboutry considers', 'He proposed' and similar expressions we mean that such idea was explicitly given in Lliboutry (2005). When we use 'we', it means an assumption based on what is written.

The work will be presented in the following way. First, we will provide the set up and main hypothesis. Then, we will treat the friction law (slip law, actually), and the treatment of cavities. Later, we will continue with changes due to subglacial flow, including the permeability and the temporal evolution of cavities. We will follow with some words about the spatial distribution of stress. Finally, we will provide the comparison with the model developed by Gilbert et al. (2022).

4.3 The model

4.3.1 Preliminary considerations

Lliboutry considers an infinitely long glacier flowing down a parabolic-shaped valley, of maximum height H and half-width D, as shown in Figure 4.1. The three dimensional reference system consists

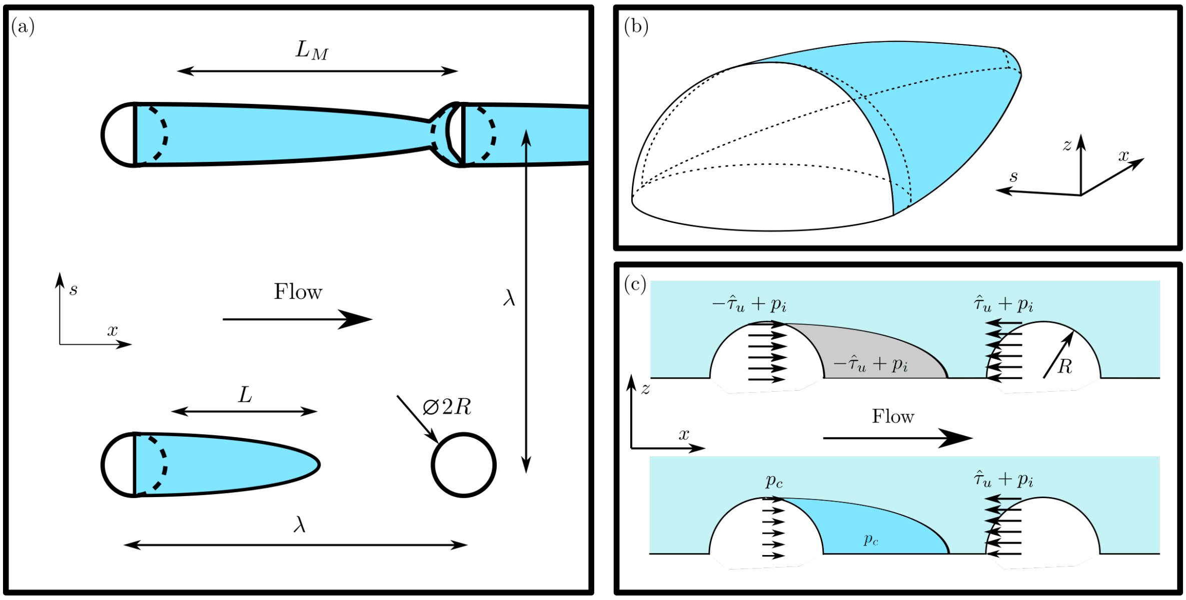

Figure 4.2: Meso scale description of the bed envisioned by Lliboutry. We give a top view in panel (a). The shape of the cavity behind the top left bump is drawn so as to have the cavity go around the bump and connect with the downstream cavity, which should happen for $L = L_M$. In panel (b) we draw a perspective of the spheroidal cavities behind a bump. Panel (c), similar to Figure 3.3 shows the distribution of stresses needed for the friction law described by Lliboutry.

in the along flow direction x, the upwards vertical direction z and the across flow direction along the bed profile, s, different from the horizontal direction y, with origin at the mid point of the bed. The bed height is given by $b(y) = (H/D^2)y^2$, and the thickness is simply $h(y) = H - b(y)$. The conversion from y to s is

$$s(y) = \frac{1}{2}y\sqrt{4\frac{H^2}{D^4}y^2 + 1} + \left(\frac{D^2}{4H}\right)\operatorname{asinh}\left(2\frac{H}{D^2}y\right). \tag{4.1}$$

With s Lliboutry defines the reduced coordinate $S = s/s_1$, where $s_1 = s(D)$ is the length of half the profile. Ice creep follows Glen's flow law, with creep parameter A and Glen's law exponent $n = 3$. Regelation and local shear stress at the ice - bed interface are neglected.

Focusing on the bed at the local scale, Lliboutry models the bed as a flat plane with hemispherical bumps of radius R, see Figure 4.2, separated by a distance λ from each other (or, conversely, there is one bump per every λ^2). The roughness r is defined as the frontal section of the bumps that the glacier must overcome per unit area, therefore

$$r = \frac{\pi}{2}R^2\frac{1}{\lambda^2}. \tag{4.2}$$

If the subglacial water pressure at the lee side of the bumps is high enough, cavities will open. The cavities are approximately modeled as spheroids (as depicted in panel (b) of Figure 4.2), with principal axes R (along z), R (along s), and L (along x), where L is called the cavity length and is computed from the last point of the bump on which they open till the tip of the cavity, as depicted in Figure 4.2 (a,c). The volume of the cavity is thus the quarter of an spheroid, yielding

$$V_c = \pi R^2 L/3. \tag{4.3}$$

Lliboutry considers that cavity length attains a maximum $L_M = \lambda - R$ when the cavity connects with the downstream cavity as depicted in the top left bump in Figure 4.2. This allows Lliboutry to define a reduced cavity length l, such that

$$l = \frac{L}{L_M} = \frac{L}{\lambda - R}, \tag{4.4}$$

$l = 0$ when there is no cavity, and $l = 1$ when there is hypercavitation, i.e. all bumps are connected with downstream bumps. Each cavity is at a pressure p_c, such that the effective pressure of the ice around the cavity is $N = p_i - p_c$. We define ice pressure as the weight of the ice column, $p_i = \rho_i g h(y(s)) \cos\alpha_s$, with ρ_i the ice density, g the gravitational acceleration and α_s the surface slope. In the case of cavities at the atmospheric pressure (i.e. empty of water) this is simply $N = p_i$, while in the case of unconnected cavities we assume that they stay at equilibrium with the surrounding ice, and thus at the cavity $N = 0$. At any point at the bed, the hydraulic head Z, taking as reference the origin, is the sum of the cavity pressure head and the height of the bed (related to the potential gravitational energy). Therefore, we can write

$$Z(s) = \frac{p_c}{\rho_w g} + b(y(s)) = \frac{-N + \rho_i g h(y(s)) \cos\alpha_s}{\rho_w g} + b(y(s)), \tag{4.5}$$

where ρ_w denotes water density.

Lliboutry considers that the subglacial hydrology network is not uniform, and is composed of a mix of isolated and connected cavities. This network is spatially heterogeneous, such that we can consider, for example, a series of isolated cavities of different lengths on the margins, a partially connected system of cavities towards the center, and a subglacial channel with fully connected cavities on the central part of the bed. In order to account for that, Lliboutry defines a connection ratio c, where $c = 0$ means all bumps are unconnected, the water pressure must be in equilibrium with the surrounding ice at every cavity, and $c = 1$ means intense cavitation, and all bumps and their cavities are freely connected between them. In other words, c defines the portion of cavities that are connected between them. Lliboutry notes that even in the absence of water filled cavities, there must be some bumps hydraulically connected to each other, such that sliding is favored at these bumps. On the other hand, if cavities grow, more bumps become connected and at the same pressure. In order to reconcile these two assumptions Lliboutry consider the following connection ratio c (Eqn. (2) in the original),

$$c = c_0 + (1 - c_0)l. \tag{4.6}$$

We call c_0 the background connection ratio. If all cavities are connected, $l = 1$ and then $c = 1$.

4.3.2 Friction law

Since we saw earlier in Chapter 3 how to obtain a simple friction law, we will go over the details here. For those bumps that don't have open cavities or whose cavities are unconnected such that the water pressure within the cavity is in equilibrium with the surrounding ice, we have a Weertman type friction law (see section 3.6.1),

$$\tau_n = \left(\frac{u_b}{AR}\right)^{1/3} 2r. \tag{4.7}$$

In the case of connected cavities, we have (see section 3.9.1)

$$\tau_c = \left[\left(\frac{u_b}{AR}\right)^{1/3} + N\right] r. \tag{4.8}$$

Now, considering that both not connected bumps (ratio $1-c$) and connected bumps (ratio c) contribute proportionally to the basal drag, we have that at equal basal speed

$$\tau_b = (1-c)\tau_n + c\tau_c = (1-c)\left(\frac{u_b}{AR}\right)^{1/3} 2r + c\left(\frac{u_b}{AR}\right)^{1/3} r + cNr = (2-c)\left(\frac{u_b}{AR}\right)^{1/3} r + cNr. \tag{4.9}$$

The friction law is not anymore a function of the type $\tau_b = f(u_b, N)$, but $\tau_b = f(u_b, N, c)$. A more compact form, similar to the friction law developed in Chapter 3 is

$$\frac{\tau_b}{N} = \left[(2-c)\left(\frac{u_b}{1N^3R}\right)^{1/3} + c\right] r. \tag{4.10}$$

We can rewrite the friction law to make it a slip law, obtaining the same equation as Lliboutry (Eqn. (1) in the original),

$$u_b = AR\left(\frac{\tau_b/r - cN}{2-c}\right)^3. \tag{4.11}$$

4.3.3 Subglacial permeability

The spatially and temporal variable hydraulic conditions require water transport through the subglacial network. Lliboutry considers that the hydraulic gradient can be modeled as continuous at the local scale, such that Darcy's law can be applied for modeling the subglacial water discharge parallel to the main flow axis (along x) $\varphi_{||}$ and perpendicular to the main flow axis (along s) $\varphi_{\perp}$, we have

$$\varphi_{||} = -K_{||}\frac{\partial Z}{\partial x};\ \varphi_{\perp} = -K\perp\frac{\partial Z}{\partial s}. \tag{4.12}$$

With cavity volume known and some rewriting Lliboutry obtains the amount of water per unit area stored in connected cavities C_{vol},

$$C_{vol} = \frac{2}{3}crL = \frac{2}{3}rmR\left[c_0 l + (1-c_0)l^2\right], \tag{4.13}$$

we call $m = L_M/R$ the shadow slope, since it is the approximated slope between the highest and the lowest point of the cavity. With the water discharge and the stored volume of water established, Lliboutry now introduces the conservation of mass for water within the subglacial hydrology system. Assuming that C_{vol} stays relatively uniform in x, but varies along s, he derives that any temporal changes in the stocked water volume is due to lateral flow,

$$\frac{\partial C_{vol}}{\partial t} + \frac{\partial \varphi_{\perp}}{\partial s} = 0. \tag{4.14}$$

Rewriting to use S, provides an equation that expresses $Z(S)$ as a function of the temporal evolution of cavity length (Eqn. (6) in the original),

$$\frac{\partial^2 Z}{\partial S^2} = \frac{1}{K_{\perp}}\frac{\partial C_{vol}}{\partial t} = E\left[c_0 + 2(1-c_0)l\right]\frac{\partial l}{\partial t}, \tag{4.15}$$

with $E = 2rmRs_1^2(3K_{\perp})^{-1}$. It is important to note that Lliboutry assumed that subglacial permeability in the across-flow direction $K_{\perp}$ is constant. Note that the subglacial flow affects only C_{vol}, which is the volume in connected cavities, as by definition disconnected cavities (the $1-c$ portion of cavities) cannot transfer water to the hydrology network. This model of water transfer applies only for water filled cavities. Lliboutry deals with empty (air filled) cavities through the boundary conditions.

4.3.4 Closing the system

So far, there are four independent variables, $u_b(S,t)$, $\tau_b(S,t)$, $l(S,t)$ and $Z(S,t)$. In order to solve the system, we have equations (4.11) and (4.15), such that we need to provide two more. This section is perhaps the most complex to understand of the original document, since it has almost no hints. I will therefore present what Lliboutry wrote, and my interpretation of it based on physical reasoning.

The third equation required to solve the system is given by the change in cavity size, a balance of two competing processes, the cavity opening due to sliding v_o, and cavity closing due to creep v_c (e.g. Werder et al., 2013; Gilbert et al., 2022), such that

$$\frac{\partial L}{\partial t} = v_o(u_b) - v_c(1, N^3). \tag{4.16}$$

Let's take a cavity at time t with volume $V_c = 1/3\pi R^2 L$, as discussed earlier. If we consider only cavity opening due to sliding (ice is turned into a solid), in a time dt the ice advances $u_b dt$, leading to a volume change of $dV_c = 1/2\pi R^2 u_b dt$. To accommodate the new volume $V_c^* = V_c + dV_c$, the cavity will have a new length L^*, such that we have

$$1/3\pi R^2 L^* = V_c + dV_c = 1/3\pi R^2 L + 1/2\pi R^2 u_b dt. \tag{4.17}$$

Rewriting the terms, and considering $dL/dt = (L^* - L)/dt$, we have

$$\frac{dL}{dt} = \frac{3}{2} u_b. \tag{4.18}$$

Focusing on cavity closing, Lliboutry considers only closure by ice creep (Werder et al., 2013), ignoring other processes such as friction melting (Hewitt, 2011). Standard models of creep closure (e.g. Röthlisberger, 1972; Hewitt, 2011; Werder et al., 2013; Gilbert et al., 2022) give a relationship of the type

$$\frac{dL}{dt} = AKN^n, \tag{4.19}$$

with K a geometrical factor. In the case of Lliboutry, this value is $K = 3/2(L + R)$. Adding together the opening and closure rates and rewriting to include the dimensionless variables l and m, gives the total dl/dt, Eqn. (7) in the original,

$$\frac{\partial l}{\partial t} = \frac{3}{2mR}\left[u_b - AR(1 + ml)N^3\right], \tag{4.20}$$

valid for $0 \leq l \leq 1$.

The fourth equation is the Stokes equation. However, solving the system as he did is not really needed, since solving the mechanical equilibrium of the glacier can be done with any finite element software such as Elmer/Ice. Nevertheless, we continue with his proposed method for solving the flow. Lliboutry claims that "the fourth relationship comes from the fact that τ_b and u_b are components of the stress and velocity tensors on the whole glacier.[...] Fortunately, we can find good approximations of $\tau_b(S)$ and $u_b(S)$ using 4th degree polynomials, only dependant on $\tau_b(S = 0) = \tau_0$ and $\tau_b(S = 1) = \tau_1$, provided we consider a cylindrical glacier with parallel flow. Explaining how to determine them would be too long to be done here. Let's only say that if we know l and Z on 5 *control points*, regularly spread over the semi-transverse profile of the glacier, there is one unique solution to this mathematical problem".

What are those polynomials? We have no more information on how to obtain them, only that

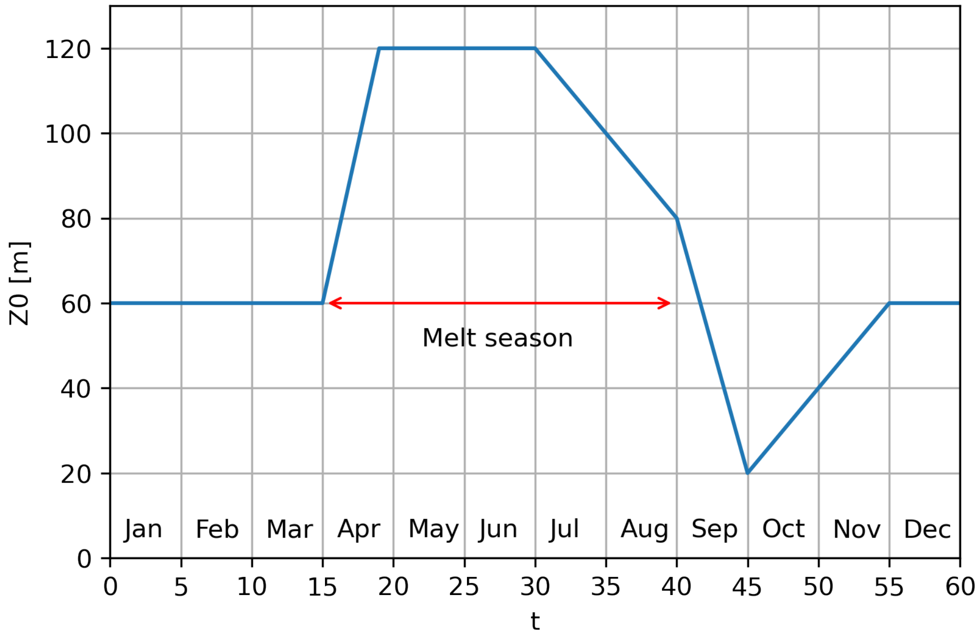

Figure 4.3: Evolution of Z at the central part of the glacier.

they must depend on five constants, so as to need five points to determine them. Thus, we look for polynomials of the form

$$\tau_b(S) = a_\tau S^4 + b_\tau S^3 + c_\tau S^2 + d_\tau S + \tau_0,\; u_b(S) = a_u S^4 + b_u S^3 + c_u S^2 + d_u S + u_{b0} \tag{4.21}$$

If we dig deep in Lliboutry's works, we find that in Lliboutry (1969), through successive approximations and 84 equations over 21 pages, Lliboutry derives this type of equations for τ_b and u_b for plane and cylindrical glaciers. The results of such paper are not directly applicable to this case, though, since he did not derive fourth order polynomials. If Lliboutry derived similar relationships for the model that we present here, arriving to the same result as he intended would be practically impossible.

4.3.5 Boundary conditions

Lliboutry proposes two boundary conditions to solve the problem. The first one is the hydraulic head at the central flow line over time, $Z(0,t)$. We reproduce his proposed value in Figure 4.3. The other boundary condition is the lateral position s at which there is no stored water at the bed. Lliboutry (2005) is probably inspired by his observations at Glacier d'Argentiere (Hantz and Lliboutry, 1983), where he expects a lateral channel that controls subglacial pressures. During the melt season (April to September), the boundary condition to impose at that point is simply $Z(s) = b(s)$. During the rest of the year, the condition at this limit must be changed to $\partial Z/\partial S = 0$ to ensure that there is no lateral water flow, $\phi_\perp = -k_\perp \partial Z/\partial s = 0$. Lliboutry continues discussing the numerical scheme to solve the problem. Since we could not solve it the same way he did, we will not describe it. Those interested can find the details in the original document and its translation in Annex **??**.

Variable/Equation	Lliboutry (2005)	This PhD	Gilbert et al. (2022)
Basal speed	U	u_b	u_b
Basal drag	T	τ_b	τ_b
Bump height	R	R	h_r
Creep factor	B_1	1	A
Cavity state variable	c	c	θ
Cavity state variable for steady state	Undefined	c^*	θ^*
Cavity volume	W	C_{vol}	Undefined
Distance between obstacles	L_M	L_M	l_r
Hydraulic head	Z	Z	Φ
Friction law	Eqn. (1)	Eqn. (4.11)	Eqn. (1)
Cavity state	Eqn. (2)	Eqn. (4.6)	In text (θ)
Discharge	Eqn. (3)	Eqn. (4.12)	Eqn. (11)
Stocked water volume	Eqn. (4)	Eqn. (4.13)	Eqn. (8)
Mass conservation (water)	Eqn. (5)	Eqn. (4.14)	Eqn. (9) from Werder et al. (2013)
Hydropotential gradient	Eqn. (6)	Eqn. (4.15)	Eqn. (24) from Werder et al. (2013)
Cavity evolution	Eqn. (7)	Eqn. (4.20)	Eqn. (7)

Table 4.1: Comparison of variables used in Lliboutry (2005), this PhD and Gilbert et al. (2022) model. See subsection 4.4 for more details.

4.4 Comparison with Gilbert et al. (2022)

The unsteady friction law proposed by Gilbert et al. (2022) is very similar in some aspects to the Lliboutry model, as we can see for the equation by equation comparison that we provide in Table 4.1. Mind that not all equations and variables in Lliboutry (2005) describe exactly the same physical concept in Gilbert et al. (2022). Gilbert et al. (2022) propose a friction law of the form $\tau_b = f(u_b, \theta)$,

$$\tau_b^m = (1-\theta)\frac{u_b}{A_s}, \tag{4.22}$$

with $0 \leq \theta \leq 1$ a dimensionless variable that represents the cavitation state, akin to l. Subglacial water pressure is linked to changes in cavity volume with Eqn. (24) from Werder et al. (2013)

$$\frac{e_v}{\rho_w g}\frac{\partial \phi}{\partial t} + \nabla \cdot \mathbf{q} + \frac{\partial h}{\partial t} - m_i = 0, \tag{4.23}$$

with e_v a parameter that relates water storage to water pressure, ϕ the hydropotential gradient, $\mathbf{q}$ the water discharge, h a measure of the size of the subglacial water sheet, a similar parameter to cavity height, and m_i is surface water input and basal melt. This equation stems from mass conservation and is therefore analogous to Eqn. (4.15). Indeed, for $e_v = 0$ and $m_i = 0$, it gives

$$\nabla \cdot \mathbf{q} + \frac{\partial h}{\partial t} = 0, \tag{4.24}$$

which is virtually identical to Eqn. (4.14) and thus to Eqn. (4.15). Cavity opening and closing in Gilbert et al. (2022) is also controlled via sliding and creep,

$$\frac{d\theta}{dt} = \frac{1}{l_r}\left(u_b(1-\theta)^{\frac{1}{q}} - A_s C^m |N|^{m-1} N \frac{\theta}{\alpha}^{\frac{1}{q}}\right), \tag{4.25}$$

Parameter	Value	Unit
R	1.5	m
r	1/15	-
A	5.5	MPa^{-3}a^{-1}
L_M	3.854 R	m
c_0	0.5	-

Table 4.2: Variables used by Louis Lliboutry in his example, and followed here for the friction laws shown in Figures 4.4 and 4.5.

with l_r equivalent to L_M, q and α as given by Gagliardini et al. (2007) (see Eqn. (1.10)) and $m = n$, the Glen's Law exponent. This expression is the equivalent to Eqn. (4.20). Mechanical equilibrium (the fourth equation that Lliboutry (2005) requires to solve the system) is obtained by solving a three-dimensional numerical model of Glacier d'Argentière using Elmer/Ice. Thus, both models propose a friction law, a link between water pressure and cavity size (or stored water), and an equation that regulates changes in cavity size to sliding speed. The key differences between the models of Lliboutry and Gilbert et al. (2022) are the double control on friction given simultaneously by N and c in the model proposed by Lliboutry, and the explicit dependence of τ_b on N in the proposed friction law. In the case of Gilbert et al. (2022), the control on friction is only through θ, which is somewhat problematic, since the force balance at the bed dictates that the friction law should have an explicit dependence on N (Schoof, 2005). Gilbert et al. (2022) choose to neglect this aspect as they focus on a timescale where friction is mainly controlled by cavity size variability. In order to further study the similarities between Lliboutry (2005) and Gilbert et al. (2022), we will compare the steady-state solution of both models. The model of Gilbert et al. (2022) is built to be equivalent to the friction law proposed by Gagliardini et al. (2007) and that has been presented earlier in Chapters 1 and 3. In the Lliboutry model, we first find l such that the cavities do not evolve over time, i.e. $l = l^*$ that makes $\partial l/\partial t = 0$. Using Eqn. (4.20) and substituting into $m = L_M/R$ gives

$$l^* = \frac{1}{L_M}\frac{u_b - ARN^3}{ARN^3}. \tag{4.26}$$

Now we can substitute l by l^* in Eqn. (4.6)) to obtain c^*. Then, plugging c^* in the friction law given by Eqn. (4.11) gives

$$\frac{\tau_b}{N} = \left[(2-c^*)\left(\frac{u_b}{AN^3R}\right)^{1/3} + c^*\right]r, \text{with } c^* = c_0 + (1-c_0)\frac{1}{L_M}\frac{u_b - ARN^3}{ARN^3}. \tag{4.27}$$

We show two alternative depictions of this law in Figures 4.4 and 4.5, with c^* considered outside of the range $[c_0, 1]$ considered by Lliboutry (2005). Figure 4.4 (a,b) shows a solution of Eqn. (4.27) solved for $N = 1$ MPa, u_b from 0 to 100 m a^{-1}, and all the model parameters as given in the original model of Lliboutry, see Table 4.2. Figure. 4.4 (a) shows the solution with unscaled variables and Figure. 4.4 (b) shows the solution scaled with a variable space similar to Figure 1.5. We compute the upper limit with $C = \max \tau_b/N$. The sliding parameter is computed as $A_s = \overline{u_b/\tau_b^n}$, with u_b/τ_b averaged over the portion of the friction law with $c^* < c_0$. The friction law in Figure. 4.4 is shown in blue, with the range comprised between $c = c_0$ (red start) and $c = 1$ (yellow start) given with a continuous curve, while the part of the friction law outside this range is represented by a discontinuous curve. We compare the law, as we did in Chapter 3, with the formulations of Weertman (1957) and Gagliardini et al. (2007). In this case we show the law of Gagliardini et al. (2007) with $q = 1.35$ for aesthetic purposes, mind that $q > 1$ is necessary to show rate-weakening. The steady state friction law under fixed N is strikingly similar to a friction law with cavities: at low sliding velocities (and low c^*) it has a strengthening regime similar to Weertman behaviour, then as cavities open (and they connect to each other, $c \geq c_0$) the law departs more from the Weertman behaviour, until a peak at the maximum length of the cavity is reached ($c^* = 1$). A weakening regime follows with increased cavity size, such that the drag cannot be supported by the bumps in the region with cavity size larger than the upper limit considered by Lliboutry ($c^* > 1$). We show a solution of Eqn. (4.27) under an imposed $\tau_b = 0.15$ MPa in Figure 4.5 (a),

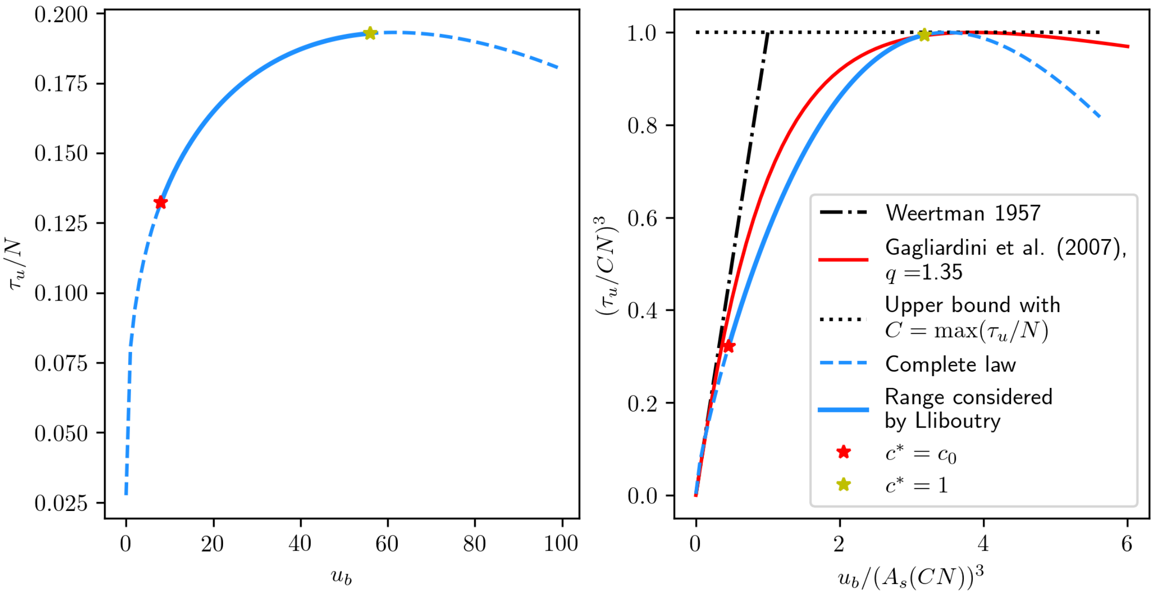

Figure 4.4: Steady state friction law built using Eqn. (4.27) for fixed $N = 1$ MPa, varying u_b between 0 and 100 m a^{-1} and the parameters given by Lliboutry, see Table 4.2. Panel (a) shows the friction law without any scaling paramters. Panel (b) uses sliding parameters C and A_s and considers the $n-th$ power of τ_b and N.

and a similar solution provided by Gilbert et al. (2022) for the same τ_b in Figure 4.5 (b). The friction law is given in a black line in both panels, in panel (a) we show it in a continuous line for $c_0 \leq c^* \leq 1$ and discontinuous elsewhere, with the two limit values of c^* are given in green and red. The background colors show proxies of the cavitation state in both models: c^* in panel (a) and h/h_r in panel (b), the latter being a function of θ. The red star in panel (b) depicts the transition between rate-strengthening and weakening, which in panel (a) corresponds roughly to the intersection between the black and the red curves. They provide qualitatively the same result, with the same behaviour as observed under fixed N in Figure 4.4.

4.5 Conclusion

Louis Lliboutry presented in 2005 a hydro-mechanical coupled model of glacier sliding under unsteady water pressure that was between 15 and 18 years ahead of its time (if we take as reference Gilbert et al. (2022) or Thøgersen et al. (2019), a previous step in Gilbert et al. (2022) model). Lliboutry proposed a friction law that depends on cavity size, and then introduced a series of physical based equations to relate the size of the cavity with distribution of water in the subglacial hydrology network. By relating the temporal evolution of the cavity to both sliding and subglacial pressures, the system becomes completely coupled. There are a few ideas in Lliboutry's paper that merit more attention, such as the role of unconnected cavities in regulating bed friction or the explicit inclusion of effective pressures in the friction law. We have shown that the model of Lliboutry (2005) shares many similarities with the model

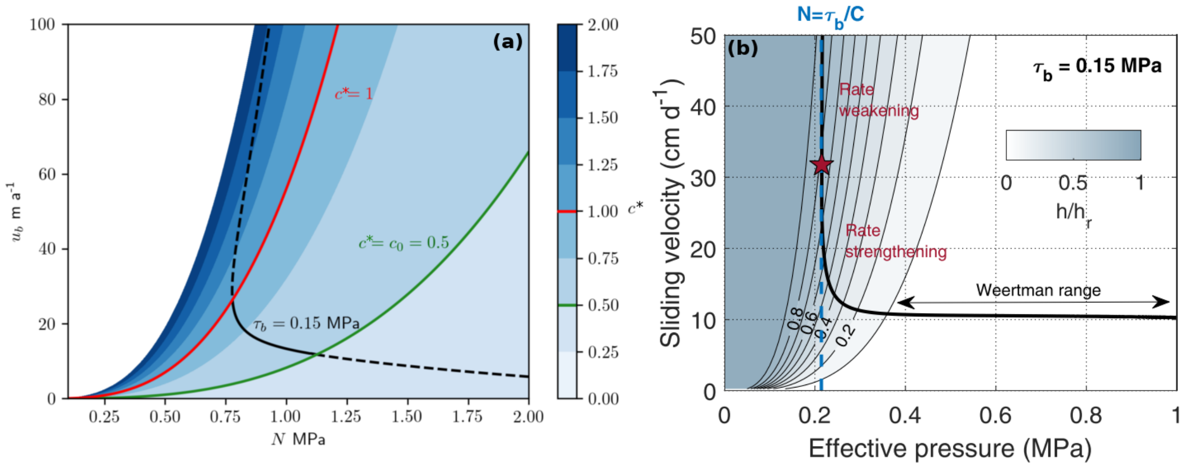

Figure 4.5: Comparison between the steady friction law that results from Lliboutry (2005) (Eqn. (4.27), panel (a)) and the steady friction law given by Gilbert et al. (2022) (panel (b)), both computed for a fixed $\tau_b = 0.15$ MPa. The scale of the axes is different to suit the different parameters used to build each model. The background color in both panels depict a variable related to the cavitation state. Panel (b) is extracted from Gilbert et al. (2022), Figure (1a).

recently developed by Gilbert et al. (2022). In its steady-state version, Lliboutry's friction law is physics based and considers rate-strengthening, the opening of cavities and rate-weakening. Although not explored in this Chapter, it is worth mentioning here that a friction law that takes into account the role of unconnected cavities has been just recently considered by Christian Schoof (Schoof, 2023a,b). Therefore, the interest in the ideas presented in Lliboutry's model is not only historical, and the model has the potential to inspire future models of sliding under unsteady water pressure and with unconnected cavities. We would like to remind that we cannot be sure if our interpretation of Lliboutry's model is as he intended. Solving Lliboutry's model will confirm whether or not it can realistically model glacier flow and demonstrate that "a realistic model, taking into account the laws of Mechanics and Physics can be established". Lliboutry was surely wrong when he stated that sliding was not a fashionable topic anymore, as has been recently proven during the last years through the works of Schoof (2005, 2023a,b), Gagliardini et al. (2007); Gagliardini (2019), Zoet and Iverson (2015); Zoet et al. (2021), Helanow et al. (2020, 2021), Gilbert et al. (2022) and with this manuscript, among others. We can only lament that such a hydro-mechanical coupled model couldn't be published by his original author, and hope that our review will do it justice.

Chapter 5

Conclusions and perspectives

Perge, vox?
'Forward, no?', ancient Tamidian proverb.

5.1 Conclusions

I have started discussing the results of this PhD with Chapter 2, where I have shown the deformation rates in the interior of the ablation area of Glacier d'Argentière, an alpine temperate glacier, observed with borehole inclinometry during most of 2020. I have shown that we need to consider creep enhancement at our site to correctly reproduce our observations. This creep enhancement could be due to depth-increasing water content of the order of 0 to 2%. Both this spatial distribution and retrieved values of the water content are strikingly similar to those previously observed in temperate glaciers. Combined with high-frequency measurements of surface velocity at out study site, I was able to partition the velocity of the glacier in surface, deformation and basal velocities. I have shown that the seasonal evolution of glacier surface velocities is well correlated to changes in ice deformation, while short term changes in surface velocities must be due to fast accelerations at the bed. When compared to seismic measurements during the melt season of 2019 and uplift observations during 2019 and 2020 at our study site, I have discussed that the subglacial hydrology system most likely displays strong spatial heterogeneity, with a central drainage channel and cavities at the sides of it. The preliminary results of another inclinometry campaign on the margin point out to the strong heterogeneity in the transverse direction. All these observations point out that simplified assumptions regarding glacier flow, such as uniform creep factor and changes in velocity due solely to changes in sliding can fail a close scrutiny when confronted with detailed observations. Accurate modeling of glacier velocities and their intra-annual variations thus require accurate measurements of the glacier internal flow.

Next, I have developed a friction law under non-zero local shear stress including its effect on ice viscosity, which I presented in Chapter 3. For that, I developed a simplified friction law over square obstacles, building on the models of Weertman (1957) and a posterior solution with cavities done by A. Fowler. My formulation improved previous efforts by including the role of local shear stress in ice viscosity, an aspect previously neglected due to its potential low impact on the overall solution. Numerical modeling allowed me to expand my simplified solution to sliding with non-zero local shear stress over a more complex bed and with more complex local shear stress laws. I have shown that with this improved formulation, the friction law still retains the overall form of a friction law developed under the assumption of zero local shear stress. This work suggests that identifying the magnitude of local shear stress in a glacier is complicated without access to the bed.

Finally, I have studied how friction laws change under unsteady water pressures in Chapter 4. I started this study by understanding and explaining an unpublished model of glacier sliding under unsteady water pressures developed by Louis Lliboutry shortly before his death. The model links friction and sliding to effective pressure and cavity size. Cavity size evolution and effective pressures are linked to one another, and to the sliding speed as well, thus providing a two-way hydro-mechanical coupled model of glacier flow. This model was ahead of its time, and if published it would have arrived between 15 and 18 years earlier than similar studies (Thøgersen et al., 2019; Tsai et al., 2021; Gilbert et al., 2022). I have demonstrated that the model of Lliboutry has more than a historical interest, since it provides for the first time hydro-mechanical coupling with an explicit dependence of the friction law on effective pressure. Future application of the model is required to fully understand the potential of Lliboutry's model.

Altogether, the results of this PhD point out that glacier flow is more complex than typically assumed, that it can be understood with simple models, and that numerical modeling is key to exploit the insights obtained with these simple models and to use them to explain our observations. Our measurements of ice deformation rates could not be properly interpreted without high order simulations of glacier flow. Glacier flow models are, on the other hand, limited by the assumptions they are built onto. Some of these assumptions seem to be strong, such as neglecting the role of local shear stress which does not change the overall model of glacier friction, while other assumptions such as the steady state mean that we are limited in simulating the flow of glaciers at seasonal and subseasonal timescales. In the next section I explain how to exploit the friction laws developed here, and a few ideas on how to validate our observations regarding the behaviour observed at Glacier d'Argentière at long and short timescales.

5.2 Perspectives

5.2.1 Improving models of glacier flow

We have focused most of this PhD on basal processes, and have provided two different friction laws to overcome two common limits that classical friction laws include: non-zero local shear stress and the unsteady evolution of subglacial water pressures. What we have not provided is an application of our results, in other words, we have not put our results to use in a real problem. We will start discussing when it is reasonable to use our parameterisation of sliding with local shear stress, and continue with the necessary steps to use the model proposed by Lliboutry (2005).

Large-scale models of glacier flow that simulate the evolution of glaciers over large spatiotemporal scales can probably ignore the effect of local shear stress, as long as they are not focused on accurately modeling small scale processes such as local shear stress. This applies to such studies that focus on the ice-sheet scale (e.g. Larour et al., 2019), those that aim at reconstructing glaciers and ice-sheets during past glaciations (e.g. Seguinot et al., 2018; Gowan et al., 2021) or those that study the evolution of many glaciers at once (such as done for alpine glaciers, see Zekollari et al., 2019; Bolibar et al., 2022). These tend to consider Weertman (1957) as friction law, adjusting the value of the sliding parameter to a set of observations, usually related to surface velocities and ice thickness. Given that the focus is not put in modeling basal processes, if would not make much sense to use a friction law that i) requires more parameters to be fit thus complicating the already computationally expensive study, and ii) can be reasonably well represented by Weertman (1957) if the parameters are carefully chosen. This is not to say that this studies should completely forego the notion that non-zero local shear stress has an impact on glacier dynamics. In the context of non-zero local shear stress, the sliding parameter inverted in the aforementioned studies stops having a fully traceable physical meaning: it is not anymore a parameter that results from ice flowing past obstacles of a certain size, but a parameter that represents 'well enough' the combined effects of deformation around obstacles and friction between debris laden ice and the bed.

Detailed studies of glacier-bed interactions, however, can benefit from our proposed friction law. In particular, those that are interested in basal melting (such as done for the Greenland Ice Sheet in Karlsson et al., 2019) or in erosion and landscape evolution (e.g. Herman et al., 2015). In the former case, including a friction law that accounts for τ_f allows for direct computation of basal melting, since the product $\tau_f u_b$ directly provides the power dissipated to melt ice due to local shear stress per unit area. In the latter case, the erosion rate of the bed is typically linked to a power of u_b using a model based on the local shear constitutive law proposed by Hallet (1979), in other words, the parameterisation of the erosion rate is already, implicitly, accounting for τ_f. Therefore, models of erosion rates already consider one of the most important elements that are needed in order to use a friction law with non-zero local shear stress at the base of glaciers. They can almost automatically benefit from such a law as developed in Chapter 3.

Concerning the model of Lliboutry (2005), we must first solve it in order to fully understand its potential, as has been done in the models proposed by Tsai et al. (2021); Gilbert et al. (2022) and Schoof (2023b). We can start by solving the same problem as Lliboutry: a parabolic channel with the same size, variable values and boundary condition given in Lliboutry (2005). The values of basal speed and cavity size provided by Lliboutry at some mesh points for some particular timesteps can be used to further check the solution. Once this is validated, we can continue testing the model in a a more realistic setting, repeating the numerical experiment carried out by Gilbert et al. (2022), i.e. applying the unsteady friction law to the numerical model of Glacier d'Argentière and comparing the modeled basal speed at the subglacial wheel with the historical records.

5.2.2 Multi-instrument monitoring of short term velocity changes in a temperate glacier

In Chapter 2 we studied the evolution of surface, internal and basal velocities at Glacier d'Argentière focusing on their average values as well as seasonal changes. However, as we described in the same Chapter, our instrumentation recorded surface motion and internal deformation rates at sub daily frequencies, allowing for observations at much shorter timescales. This allowed us to capture several short term acceleration episodes during 2019 and 2020, which were detected simultaneously by the GNSS network deployed at the surface and by the tiltmeters installed in its interior.

The acceleration events are shown in Figure 5.1, on the left for the late 2019 events, and on the right for the 2020 melt season events. Deformation velocity is computed at BH2 in both panels. There are several differences between these events. In the late 2019 speed-ups, surface accelerations are followed by three peaks in subglacial pressures. Likewise, the speed-ups are accompanied by an increase in tiltmeter-derived internal deformation. These events are happening during the period in which we do not expect good coupling between the instruments and the glacier, so it is not sure if the tiltmeters are merely recording free movement of the sensors as the glacier accelerates, or a real increase in

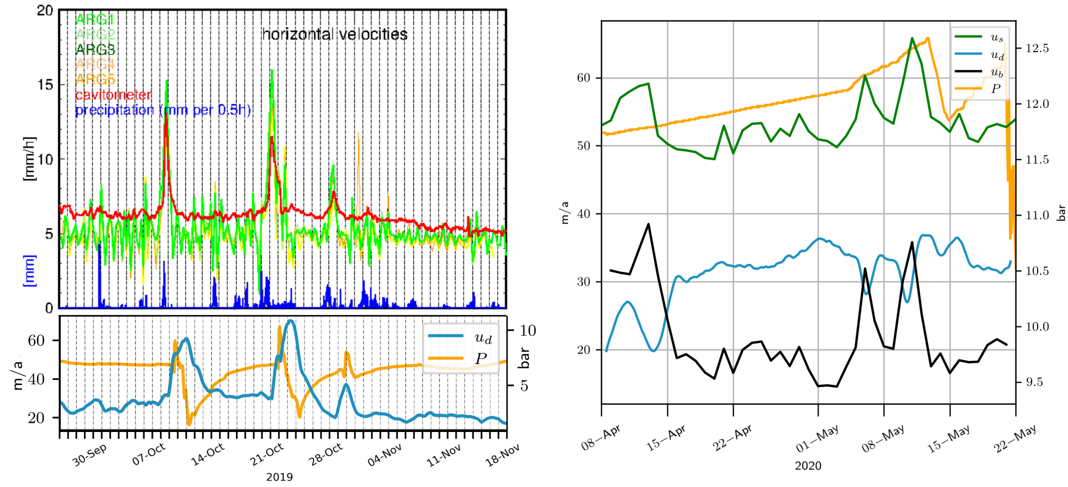

Figure 5.1: Glacier velocities and subglacial water pressures over a few speed-up events registered in Glacier d'Argentière during late 2019 (left) and at the beginning of the 2020 melt season (right). On the left, glacier velocities correspond to several GPS stations deployed on the ablation area, and the deformation velocity as well as the subglacial water pressures correspond to BH2. The instrumentation is described in more detail in Chapter 2.

internal deformation. These accelerations are being studied in more detail by Anuar Togaibekov, as part of his PhD, supervised by Florent Gimbert and Andrea Walpersdorf. On the other hand, during the 2020 events, water pressure at BH2 is almost unrelated to the dynamical changes in the glacier until after the third event depicted on the right panel of Figure 5.1. This suggest that unlike in late 2019, the borehole is not connected to the main subglacial hydrology network during most of the early melt season. The tiltmeters in this case are expected to be coupled to the surrounding ice, and they record a reduction in deformation velocity u_d concomitant to surface acceleration, as depicted in blue on the right panel. The inferred basal velocity u_b, in black on the right panel, shows strong accelerations during these events.

In Chapter 2, we briefly considered the 2020 speed-up events to argue that indeed there was a drainage channel developing at the beginning of the melt season. Therefore, we can replicate that kind of approach to study the 2019 speed up events and infer the state of the subglacial hydrology system close to BH2 after the end of the melt season.

5.2.3 Validation of friction laws with simulations of ice flow over realistic beds

Several results presented in this PhD are hindered by the fact that we cannot observe in good detail glacial bed processes. The corollary of the main result of Chapter 3 is the difficulty to discern the magnitude of local shear stress on a glacier without access to the bed, despite the indirect evidence of the presence of local shear stress at the base of glaciers (Lipovsky et al., 2019; Köpfli et al., 2022), including Glacier d'Argentière (Helmstetter et al., 2015). Likewise, in Chapter 2 we concluded that seasonal changes in glacier velocity during 2020 were linked to changes in deformation velocity at seasonal timescales and basal velocity at shorter timescales. These results were in conflict with the increasing cavity size proposed by Vincent et al. (2022b) to explain the summer uplift and suggested that the hydrology network must be strongly heterogeneous at our study site.

The idea to follow would be to replicate the work of Helanow et al. (2021) and simulate the flow over real beds at Glacier d'Argentière. If they used DEMs from several deglaciated areas around the world, in our case we have a high resolution (5 cm) DEM of a deglaciated area of Glacier d'Argentière, just by the icefall (close to the cavitometer). The steps to follow would be: i) Divide the DEM is smaller areas and select a few of them, ii) identify the mean flow direction in each area, iii) extend each subarea to make them periodic, and iv) run Elmer/Ice simulations over these areas for various velocities and subglacial water pressures.

The results of these simulations can be used to, in first place, infer if the bed can sustain the expected basal drag without the need to consider an additional source of drag (given by local shear stress). In second place, to infer a few characteristics from the friction law and compare with the law considered by Gimbert et al. (2021a). Are the values of A_s and C found by direct computation of ice flow over real beds comparable to those retrieved with a glacier-wide analysis over several decades? Even though there are several processes that can explain why rate-weakening is not observed in hard bedded glaciers (Gimbert et al., 2021a; De Diego et al., 2022; Gilbert et al., 2022), does the bed of Glacier d'Argentière allow the development of rate-weakening? In third place, this study can be used to study how cavities connect to each other, and how easily they communicate water. This would help improve our understanding of the evolution of sliding during summer: we could see is glacier uplift is possible without great changes in sliding velocity, perhaps validating the observations of Vincent et al. (2022b) against our observations in Chapter 2; we could also study how rapidly the permeability between cavities evolve from low to high, and better constrain the model of subglacial permeability consider in studies such as Gilbert et al. (2022).

Using a realistic model to infer realistic conditions at a glacier is not without pitfalls, given that increasing the resolution of our modeling is usually paired with increased model complexity. For example, I showed in Chapter 2 that we expect a depth-increasing creep factor in Glacier d'Argentière. Must we, therefore, include depth-increasing A if we simulate sliding over the deglaciated bed of Glacier d'Argentière? Can we realistically consider that the ice some distance above the bed (e.g. 15 m as in Helanow et al., 2021) has uniform creep factor? And what value do we give to A to be sure that we achieve realistic results?

Bibliography

Electricité d'Emosson SA: Fiche technique prises d'eau d'Argentière, retrieved on 02/11/2022. From `https://emosson.ch/amenagements/prises-deau-dargentiere`.

Adams, C. J., Iverson, N. R., Helanow, C., Zoet, L. K., and Bate, C. E.: Softening of Temperate Ice by Interstitial Water, Frontiers in Earth Science, 9, 1–11, doi: 10.3389/feart.2021.702761, 2021.

Advanced Logic Technology sa: User Guide QL40 FWSS - Full Waveform Sonic.

Alean, P., Braun, S., Iken, A., Schram, K., and Zwosta, G.: Hydraulic Effects at the Glacier Bed and Related Phenomena, 90, 1985.

Allison, E. A.: The spiritual significance of glaciers in an age of climate change, Wiley Interdisciplinary Reviews: Climate Change, 6, 493–508, doi: 10.1002/wcc.354, 2015.

Amundson, J. M., Truffer, M., and Lüthi, M. P.: Time-dependent basal stress conditions beneath Black Rapids Glacier, Alaska, USA, inferred from measurements of ice deformation and surface motion, Journal of Glaciology, 52, 347–357, doi: 10.3189/172756506781828593, 2006.

Arenson, L., Hoelzle, M., and Springman, S.: Borehole deformation measurements and internal structure of some rock glaciers in Switzerland, Permafrost and Periglacial Processes, 13, 117–135, doi: 10.1002/ppp.414, 2002.

Bartholomew, I., Nienow, P., Sole, A., Mair, D., Cowton, T., and King, M. A.: Short-term variability in Greenland Ice Sheet motion forced by time-varying meltwater drainage: Implications for the relationship between subglacial drainage system behavior and ice velocity, Journal of Geophysical Research: Earth Surface, 117, 1–17, doi: 10.1029/2011JF002220, 2012.

Benjumea, B., Macheret, Y. Y., Navarro, F. J., and Teixidó, T.: Estimation of water content in a temperate glacier from radar and seismic sounding data, Annals of Glaciology, 37, 317–324, doi: 10.3189/172756403781815924, 2003.

Biemans, H., Siderius, C., Lutz, A. F., Nepal, S., Ahmad, B., Hassan, T., von Bloh, W., Wijngaard, R. R., Wester, P., Shrestha, A. B., and Immerzeel, W. W.: Importance of snow and glacier meltwater for agriculture on the Indo-Gangetic Plain, Nature Sustainability, 2, 594–601, doi: 10.1038/s41893-019-0305-3, URL `http://dx.doi.org/10.1038/s41893-019-0305-3`, 2019.

Bolibar, J., Rabatel, A., Gouttevin, I., Zekollari, H., and Galiez, C.: Nonlinear sensitivity of glacier mass balance to future climate change unveiled by deep learning, Nature Communications, 13, 1–11, doi: 10.1038/s41467-022-28033-0, 2022.

Bouhassira, E.: Clark Glacier Commemorated at Funeral in Oregon, retrieved on 18/10/2022. From Columbia Climate School - GlacierHub Blog, `https://news.climate.columbia.edu/2020/10/27/clark-glacier-funeral-oregon/`, 2020.

Brondex, J., Gagliardini, O., Gillet-Chaulet, F., and Durand, G.: Sensitivity of grounding line dynamics to the choice of the friction law, Journal of Glaciology, 63, 854–866, doi: 10.1017/jog.2017.51, 2017.

Brondex, J., Gillet-Chaulet, F., and Gagliardini, O.: Sensitivity of centennial mass loss projections of the Amundsen basin to the friction law, Cryosphere, 13, 177–195, doi: 10.5194/tc-13-177-2019, 2019.

Budd, W. and Jacka, T.: A review of ice rheology for ice sheet modelling, Cold Regions Science and Technology, 16, 107–144, doi: 10.1016/0165-232X(89)90014-1, URL `https://linkinghub.elsevier.com/retrieve/pii/0165232X89900141`, 1989.

Budd, W. F., Keage, P. L., and Blundy, N. A.: Empirical studies of ice sliding., Journal of Glaciology, doi: 10.1017/S0022143000029804, 1979.

Carey, M., Jackson, M., Antonello, A., and Rushing, J.: Glaciers, gender, and science: A feminist glaciology framework for global environmental change research, Progress in Human Geography, 40, 770–793, doi: 10.1177/0309132515623368, 2016.

Cerdan, A., Humbert, G., Noyon, R., and Ranc, A.: Avant-Après: L'âge sans glace, L'obs, https://www.nouvelobs.com/planete/20190628.OBS3872/avant-apres-regardez-comme-les-glaciers-francais-ont-fondu-en-150-ans.html, accessed: 18/10/2022, 2019.

Chandler, D., Hubbard, B., Hubbard, A., Murray, T., and Rippin, D.: Optimising ice flow law parameters using borehole deformation measurements and numerical modelling, Geophysical Research Letters, 35, 3–7, doi: 10.1029/2008GL033801, 2008.

Chandler, D. M., Wadham, J. L., Nienow, P., Doyle, S. H., Tedstone, A. J., Telling, J., Hawkings, J., Alcock, J. D., Linhoff, B., and Hubbard, A.: Rapid development and persistence of efficient subglacial drainage under 900 m-thick ice in Greenland, Earth and Planetary Science Letters, 566, 116 982, doi: 10.1016/j.epsl.2021.116982, URL https://doi.org/10.1016/j.epsl.2021.116982, 2021.

Chen, G.: GPS kinematic positioning for the airborne laser altimetry at Long Valley, California, Phd, Massachusetts Insitute of Technology, 1999.

Clarke, G. K.: A short history of scientific investigations on glaciers, Journal of Glaciology, 33, 4–24, doi: 10.3189/S0022143000215785, URL https://www.cambridge.org/core/product/identifier/S0022143000215785/type/journal_articlehttp://doi.wiley.com/10.1029/JZ068i015p04513, 1987.

Cohen, D.: Rheology of ice at the bed of engabreen, Norway, Journal of Glaciology, 46, 611–621, doi: 10.3189/172756500781832620, 2000.

Cohen, D., Iverson, N. R., Hooyer, T. S., Fischer, U. H., Jackson, M., and Moore, P. L.: Debris-bed friction of hard-bedded glaciers, Journal of Geophysical Research: Earth Surface, 110, doi: 10.1029/2004JF000228, 2005.

Compagno, L., Jouvet, G., Bauder, A., Funk, M., Church, G., Leinss, S., and Lüthi, M. P.: Modeling the re-appearance of a crashed airplane on gauligletscher, Switzerland, Frontiers in Earth Science, 7, 1–8, doi: 10.3389/feart.2019.00170, 2019.

Copland, L., Harbor, J., Minner, M., and Sharp, M.: The use of borehole inclinometry in determining basal sliding and internal deformation at Haut Glacier d'Arolla, Switzerland, Annals of Glaciology, 24, 331–337, doi: 10.3189/S0260305500012404, URL https://www.cambridge.org/core/product/identifier/S0260305500012404/type/journal_article, 1997.

Cuffey, K. and Paterson, W.: The Physics of Glaciers, June 2006, 2010.

Dahl-Jensen, D.: Steady thermomechanical flow along two-dimensional flow lines in large grounded ice sheets, Journal of Geophysical Research: Solid Earth, 94, 10 355–10 362, doi: 10.1029/JB094iB08p10355, URL http://doi.wiley.com/10.1029/JB094iB08p10355, 1989.

Dahl-Jensen, D. and Gundestrup, N. S.: Constitutive properties of ice at Dye 3, Greenland, International Association of Hydrological Sciences Publication, pp. 31–43, URL http://hydrologie.org/redbooks/a170/iahs_170_0031.pdf, 1987.

De Diego, G. G., Farrell, P. E., and Hewitt, I. J.: Numerical approximation of viscous contact problems applied to glacial sliding, Journal of Fluid Mechanics, 938, 1–24, doi: 10.1017/jfm.2022.178, 2022.

Derkacheva, A., Gillet-Chaulet, F., Mouginot, J., Jager, E., Maier, N., and Cook, S.: Seasonal evolution of basal environment conditions of Russell sector, West Greenland, inverted from satellite observation of surface flow, Cryosphere, 15, 5675–5704, doi: 10.5194/tc-15-5675-2021, 2021.

Doyle, S. H., Hubbard, B., Christoffersen, P., Young, T. J., Hofstede, C., Bougamont, M., Box, J. E., and Hubbard, A.: Physical Conditions of Fast Glacier Flow: 1. Measurements From Boreholes Drilled to the Bed of Store Glacier, West Greenland, Journal of Geophysical Research: Earth Surface, 123, 324–348, doi: 10.1002/2017JF004529, 2018.

Duval, P.: The role of the water content on the creep rate of polycrystalline ice, IAHS Publ, 118, 29–33, 1977.

Eis, J., van der Laan, L., Maussion, F., and Marzeion, B.: Reconstruction of Past Glacier Changes with an Ice-Flow Glacier Model: Proof of Concept and Validation, Frontiers in Earth Science, 9, 1–16, doi: 10.3389/feart.2021.595755, URL https://www.frontiersin.org/articles/10.3389/feart.2021.595755/full, 2021.

Flusin, G. and Bernard, M.: Forages glaciaires à grande profondeur (Appareil et Méthode de MM . Blumcke et Hess). Rapport de la mission scientifique envoyée en 1906 sur le Hintereisferner (Oetztai), Tech. rep., Études Glaciologiques, tome 1, Tirol autrichien. Massif des Grandes Rousses, 1909.

Forbes, J. D.: Occasional papers on glaciers, Edinburgh Simpkin, pp. https://news.ge/anakliis–porti–aris–qveynis–momava, 1859.

Fountain, A. G.: Borehole water-level variations and implications for the subglacial hydraulics of South Cascade Glacier, Washington State, USA, Journal of Glaciology, 40, 293–304, doi: 10.1017/S0022143000007383, 1994.

Fowler, A. C.: A Theoretical Treatment of the Sliding of Glaciers in the Absence of Cavitation, 298, 32 117, URL https://doi.org/10.1098/rspa.1986.0090, 1979.

Fowler, A. C.: Sub-Temperate Basal Sliding, Journal of Glaciology, 32, 3–5, doi: 10.3189/S0022143000006808, URL https://www.cambridge.org/core/product/identifier/S0022143000006808/type/journal_article, 1986.

Fowler, A. C.: Sliding with Cavity Formation, Journal of Glaciology, 33, 255–267, doi: 10.3189/s0022143000008820, 1987.

Fowler, A. C.: Weertman, Lliboutry and the development of sliding theory, Journal of Glaciology, 56, 965–972, doi: 10.3189/002214311796406112, 2011.

Francou, B. and Vincent, C.: Les glaciers à l'epreuve du climat, IRD Éditions, 2010 edn., 2010.

Fu, P., Harbor, J. M., Stroeven, A. P., Hättestrand, C., Heyman, J., and Zhou, L.: Glacial geomorphology and paleoglaciation patterns in Shaluli Shan, The southeastern Tibetan Plateau - Evidence for polythermal ice cap glaciation, Geomorphology, 182, 66–78, doi: 10.1016/j.geomorph.2012.10.030, URL http://dx.doi.org/10.1016/j.geomorph.2012.10.030, 2013.

Gagliardini, O.: Accounting for transient effects in water pressure in friction law, in: Geophysical Research Abstracts, edited by 2019, E. G. A., vol. 21, from https://meetingorganizer.copernicus.org/EGU2019/EGU2019-4019.pdf, 2019.

Gagliardini, O. and Werder, M. A.: Influence of increasing surface melt over decadal timescales on land-terminating Greenland-type outlet glaciers, Journal of Glaciology, 64, 700–710, doi: 10.1017/jog.2018.59, 2018.

Gagliardini, O., Cohen, D., Råback, P., and Zwinger, T.: Finite-element modeling of subglacial cavities and related friction law, Journal of Geophysical Research: Earth Surface, 112, doi: 10.1029/2006JF000576, 2007.

Gagliardini, O., Gillet-Chaulet, F., and Montagnat, M.: A review of anisotropic polar ice models: from crystal to ice-sheet flow models, Low Temperature Science, 68, 149–166, URL http://citeseerx.ist.psu.edu/viewdoc/download?doi=10.1.1.496.2886&rep=rep1&type=pdf, 2009.

Gagliardini, O., Zwinger, T., Gillet-Chaulet, F., Durand, G., Favier, L., de Fleurian, B., Greve, R., Malinen, M., Martín, C., Råback, P., Ruokolainen, J., Sacchettini, M., Schäfer, M., Seddik, H., and Thies, J.: Capabilities and performance of Elmer/Ice, a new-generation ice sheet model, Geoscientific Model Development, 6, 1299–1318, doi: 10.5194/gmd-6-1299-2013, URL https://www.geosci-model-dev.net/6/1299/2013/, 2013.

Gerrard, J., Perutz, M. F., and Roch, A.: Measurement of the velocity distribution along a vertical line through a glacier, Proceedings of the Royal Society of London. Series A. Mathematical and Physical Sciences, 213, 546–558, doi: 10.1098/rspa.1952.0144, URL https://royalsocietypublishing.org/doi/10.1098/rspa.1952.0144, 1952.

Gilbert, A., Gimbert, F., Thøgersen, K., Schuler, T. V., and Kääb, A.: A Consistent Framework for Coupling Basal Friction With Subglacial Hydrology on Hard-Bedded Glaciers, Geophysical Research Letters, 49, 1–10, doi: 10.1029/2021GL097507, 2022.

Gillet-Chaulet, F., Hindmarsh, R. C., Corr, H. F., King, E. C., and Jenkins, A.: In-situ quantification of ice rheology and direct measurement of the Raymond Effect at Summit, Greenland using a phase-sensitive radar, Geophysical Research Letters, 38, 1–6, doi: 10.1029/2011GL049843, 2011.

Gimbert, F., Gilbert, A., Gagliardini, O., Vincent, C., and Moreau, L.: Do Existing Theories Explain Seasonal to Multi-Decadal Changes in Glacier Basal Sliding Speed?, Geophysical Research Letters, 48, 1–10, doi: 10.1029/2021GL092858, 2021a.

Gimbert, F., Nanni, U., Roux, P., Helmstetter, A., Garambois, S., Lecointre, A., Walpersdorf, A., Jourdain, B., Langlais, M., Laarman, O., Lindner, F., Sergeant, A., Vincent, C., and Walter, F.: A multi-physics experiment with a temporary dense seismic array on the argentière Glacier, French Alps: The RESOLVE project, Seismological Research Letters, 92, 1185–1201, doi: 10.1785/0220200280, 2021b.

Glen, J. W.: The creep of polycrystalline ice, Proceedings of the Royal Society of London. Series A. Mathematical and Physical Sciences, 228, 519–538, doi: 10.1098/rspa.1955.0066, 1955.

Gowan, E. J., Zhang, X., Khosravi, S., Rovere, A., Stocchi, P., Hughes, A. L., Gyllencreutz, R., Mangerud, J., Svendsen, J. I., and Lohmann, G.: A new global ice sheet reconstruction for the past 80 000 years, Nature Communications, 12, 1–9, doi: 10.1038/s41467-021-21469-w, URL http://dx.doi.org/10.1038/s41467-021-21469-w, 2021.

Gudmundsson, G. H.: Basal-flow characteristics of a non-linear flow sliding frictionless over strongly undulating bedrock, Journal of Glaciology, 43, 80–89, doi: 10.1017/s0022143000002835, 1997a.

Gudmundsson, G. H.: Basal-flow characteristics of a linear medium sliding frictionless over small bedrock undulations, Journal of Glaciology, 43, 71–79, doi: 10.1017/s0022143000002823, 1997b.

Gudmundsson, G. H., Bauder, A., Lüthi, M., Fischer, U. H., and Funk, M.: Estimating rates of basal motion and internal ice deformation from continuous tilt measurements, Annals of Glaciology, 28, 247–252, doi: 10.3189/172756499781821751, 1999.

Hallet, B.: A Theoretical Model of Glacial Abrasion, Journal of Glaciology, 23, 39–50, doi: 10.3189/S0022143000029725, URL https://www.cambridge.org/core/product/identifier/S0022143000029725/type/journal_article, 1979.

Hallet, B.: Glacial Abrasion and Sliding: their Dependence on the Debris Concentration in Basal Ice, Annals of Glaciology, 2, 23–28, doi: 10.3189/172756481794352487, 1981.

Hansen, D. D. and Zoet, L. K.: Experimental constraints on subglacial rock friction, Annals of Glaciology, 60, 37–48, doi: 10.1017/aog.2019.47, 2019.

Hantz, D. and Lliboutry, L.: Waterways, Ice Permeability at Depth, and Water Pressures at Glacier D'Argentière, French Alps, Journal of Glaciology, 29, 227–239, doi: 10.3189/S0022143000008285, 1983.

Harper, J. T., Humphrey, N. F., and Pfeffer, W. T.: Three-dimensional deformation measured in an Alaskan glacier, Science, 281, 1340–1342, doi: 10.1126/science.281.5381.1340, 1998.

Harper, J. T., Humphrey, N. F., Pfeffer, W. T., Huzurbazar, S. V., Bahr, D. B., and Welch, B. C.: Spatial variability in the flow of a valley glacier: Deformation of a large array of boreholes, Journal of Geophysical Research: Solid Earth, 106, 8547–8562, doi: 10.1029/2000jb900440, 2001.

Helanow, C., Iverson, N. R., Zoet, L. K., and Gagliardini, O.: Sliding Relations for Glacier Slip With Cavities Over Three-Dimensional Beds, Geophysical Research Letters, 47, doi: 10.1029/2019GL084924, 2020.

Helanow, C., Iverson, N. R., Woodard, J. B., and Zoet, L. K.: Slip laws for bed-bedded glaciers derived from actual bed topography, Science Advances, pp. 2–10, 2021.

Helmstetter, A., Nicolas, B., Comon, P., and Gay, M.: Basal icequakes recorded beneath an alpine glacier (Glacier d'Argentière, Mont Blanc, France): Evidence for stick-slip motion?, Journal of Geophysical Research: Earth Surface, 120, 379–401, doi: 10.1002/2014JF003288, 2015.

Herman, F., Beyssac, O., Brughelli, M., Lane, S. N., Leprince, S., Adatte, T., Lin, J. Y., Avouac, J. P., and Cox, S. C.: Erosion by an Alpine glacier, Science, 350, doi: 10.1126/science.aab2386, 2015.

Herring, T. A., King, R. W., Floyd, M. A., Mcclusky, S. C., and Sciences, P.: GAMIT Reference manual 10.6, June, Department of Earth, Atmospheric, and Planetary Sciences, Massachusetts Institute of Technology, URL http://geoweb.mit.edu/gg/docs/GAMIT_Ref.pdf, 2018.

Hewitt, I. J.: Modelling distributed and channelized subglacial drainage: The spacing of channels, Journal of Glaciology, 57, 302–314, doi: 10.3189/002214311796405951, 2011.

Hewitt, I. J.: Seasonal changes in ice sheet motion due to melt water lubrication, Earth and Planetary Science Letters, 371-372, 16–25, doi: 10.1016/j.epsl.2013.04.022, URL http://dx.doi.org/10.1016/j.epsl.2013.04.022, 2013.

Hill, E. A., Hilmar Gudmundsson, G., Rachel Carr, J., and Stokes, C. R.: Velocity response of Petermann Glacier, northwest Greenland, to past and future calving events, Cryosphere, 12, 3907–3921, doi: 10.5194/tc-12-3907-2018, 2018.

Hooke, R. L.: Structure and Flow in the Margin of the Barnes Ice Cap, Baffin Island, N.W.T., Canada, Journal of Glaciology, 12, 423–438, doi: 10.3189/s0022143000031841, 1973.

Hooke, R. L.: Principles of Glacier Mechanics, Cambridge University Press, 2 edn., doi: 10.1017/CBO9780511614231, 2005.

Hooke, R. L., Holmlund, P., and Iverson, N. R.: Extrusion Flow Demonstrated by Bore-Hole Deformation Measurements Over a Riegel, Storglaciären, sweden, Journal of Glaciology, 33, 72–78, doi: 10.3189/S0022143000005372, URL https://www.cambridge.org/core/product/identifier/S0022143000005372/type/journal_article, 1987.

Hooke, R. L., Calla, P., Holmlund, P., Nilsson, M., and Stroeven, A.: A 3 year record of seasonal variations in surface velocity, Storglaciaren, Sweden, Journal of Glaciology, 35, 235–247, doi: 10.3189/s0022143000004561, 1989.

Hooke, R. L., Pohjola, V. A., Jansson, P., and Kohler, J.: Intra-seasonal changes in deformation profiles revealed by borehole studies, Storglaciaren, Sweden, Journal of Glaciology, 38, 348–358, doi: 10.1017/S0022143000002239, 1992.

Hooke, R. L. B. and Hanson, B.: Borehole deformation experiments, Barnes Ice Cap, Canada, Cold Regions Science and Technology, 12, 261–276, doi: 10.1016/0165-232X(86)90039-X, 1986.

Hubbard, B. P., Hubbard, A., Mader, H. M., Tison, J. L., Grust, K., and Nienow, P. W.: Spatial variability in the water content and rheology of temperate glaciers: Glacier de Tsanfleuron, Switzerland, Annals of Glaciology, 37, 1–6, doi: 10.3189/172756403781815474, 2003.

Iken, A.: The Effect of the Subglacial Water Pressure on the Sliding Velocity of a Glacier in an Idealized Numerical Model, Journal of Glaciology, 27, 407–421, doi: 10.3189/S0022143000011448, URL https://www.cambridge.org/core/product/identifier/S0022143000011448/type/journal_article, 1981.

Iken, A. and Bindschadler, R. A.: Combined measurements of Subglacial Water Pressure and Surface Velocity of Findelengletscher, Switzerland: Conclusions about Drainage System and Sliding Mechanism, Journal of Glaciology, 32, 101–119, doi: 10.3189/S0022143000006936, URL https://www.cambridge.org/core/product/identifier/S0022143000006936/type/journal_article, 1986.

Intergovernmental Panel on Climate Change, I.: Sea Level Rise and Implications for Low-Lying Islands, Coasts and Communities, p. 321–446, Cambridge University Press, doi: 10.1017/9781009157964.006, 2022.

Iverson, N. R., Cohen, D., Hooyer, T. S., Fischer, U. H., Jackson, H., Moore, P. L., Lappegard, G., and Kohler, J.: Effects of basal debris on glacier flow, Science, 301, 81–84, doi: 10.1126/science.1083086, 2003.

Iverson, N. R., Helanow, C., and Zoet, L. K.: Debris-bed friction during glacier sliding with ice-bed separation, Annals of Glaciology, 60, 30–36, doi: 10.1017/aog.2019.46, 2019.

Jaquet, S. and l'afp: Des funérailles en montagne pour le Pizol, un glacier suisse disparu, retrieved on 18/10/2022. From RTS, https://www.rts.ch/info/sciences-tech/environnement/10727637-des-funerailles-en-montagne-pour-le-pizol-un-glacier-suisse-disparu.html, 2019.

Joughin, I., Smith, B. E., and Schoof, C. G.: Regularized Coulomb Friction Laws for Ice Sheet Sliding: Application to Pine Island Glacier, Antarctica, Geophysical Research Letters, 46, 4764–4771, doi: 10.1029/2019GL082526, 2019.

Jouvet, G. and Funk, M.: Modelling the trajectory of the corpses of mountaineers who disappeared in 1926 on Aletschgletscher, Switzerland, Journal of Glaciology, 60, 255–261, doi: 10.3189/2014JoG13J156, 2014.

Jouzel, J., Masson-Delmotte, V., Cattani, O., Dreyfus, G., Falourd, S., Hoffmann, G., Minster, B., Nouet, J., Barnola, J. M., Chappellaz, J., Fischer, H., Gallet, J. C., Johnsen, S., Leuenberger, M., Loulergue, L., Luethi, D., Oerter, H., Parrenin, F., Raisbeck, G., Raynaud, D., Schilt, A., Schwander, J., Selmo, E., Souchez, R., Spahni, R., Stauffer, B., Steffensen, J. P., Stenni, B., Stocker, T. F., Tison, J. L., Werner, M., and Wolff, E. W.: Orbital and millennial antarctic climate variability over the past 800,000 years, Science, 317, 793–796, doi: 10.1126/science.1141038, 2007.

Kääb, A., Leinss, S., Gilbert, A., Bühler, Y., Gascoin, S., Evans, S. G., Bartelt, P., Berthier, E., Brun, F., Chao, W. A., Farinotti, D., Gimbert, F., Guo, W., Huggel, C., Kargel, J. S., Leonard, G. J., Tian, L., Treichler, D., and Yao, T.: Massive collapse of two glaciers in western Tibet in 2016 after surge-like instability, Nature Geoscience, 11, 114–120, doi: 10.1038/s41561-017-0039-7, 2018.

Kamb, B.: Sliding motion of glaciers: Theory and observation, Reviews of Geophysics, 8, 673–728, doi: 10.1029/RG008i004p00673, 1970.

Karlsson, N. B., Colgan, W. T., Binder, D., Machguth, H., Abermann, J., Hansen, K., and Pedersen, A.: Ice-penetrating radar survey of the subsurface debris field at Camp Century, Greenland, Cold Regions Science and Technology, 165, 102 788, doi: 10.1016/j.coldregions.2019.102788, URL https://doi.org/10.1016/j.coldregions.2019.102788, 2019.

Keller, A. and Blatter, H.: Measurement of strain-rate components in a glacier with embedded inclinometers, Journal of Glaciology, 58, 692–698, doi: 10.3189/2012JoG11J234, 2012.

King, M.: Rigorous GPS data-processing strategies for glaciological applications, Journal of Glaciology, 50, 601–607, doi: 10.3189/172756504781829747, 2004.

Kluskiewicz, D., Waddington, E. D., Anandakrishnan, S., Voigt, D. E., Matsuoka, K., and McCarthy, M. P.: Sonic methods for measuring crystal orientation fabric in ice, and results from the West Antarctic ice sheet (WAIS) Divide, Journal of Glaciology, 63, 603–617, doi: 10.1017/jog.2017.20, 2017.

Köpfli, M., Gräff, D., Lipovsky, B. P., Selvadurai, P. A., Farinotti, D., and Walter, F.: Hydraulic Conditions for Stick-Slip Tremor Beneath an Alpine Glacier, Geophysical Research Letters, 49, 1–11, doi: 10.1029/2022gl100286, 2022.

Larour, E., Seroussi, H., Adhikari, S., Ivins, E., Caron, L., Morlighem, M., and Schlegel, N.: Slowdown in Antarctic mass loss from solid Earth and sea-level feedbacks, Science, 364, doi: 10.1126/science.aav7908, 2019.

Lee, I. R., Hawley, R. L., Bernsen, S., Campbell, S. W., Clemens-Sewall, D., Gerbi, C. C., and Hruby, K.: A novel tilt sensor for studying ice deformation: Application to streaming ice on Jarvis Glacier, Alaska, Journal of Glaciology, 66, 74–82, doi: 10.1017/jog.2019.84, 2019.

Lipovsky, B. P., Meyer, C. R., Zoet, L. K., McCarthy, C., Hansen, D. D., Rempel, A. W., and Gimbert, F.: Glacier sliding, seismicity and sediment entrainment, Annals of Glaciology, 60, 182–192, doi: 10.1017/aog.2019.24, 2019.

Lliboutry, L.: Contribution à la théorie du frottement du glacier sur son lit., C. R. Hebd. Se´ances Acad. Sci., 247, 318–320, 1958.

Lliboutry, L.: General Theory of Subglacial Cavitation and Sliding of Temperate Glaciers, Journal of Glaciology, 7, 21–58, doi: 10.3189/S0022143000020396, URL https://www.cambridge.org/core/product/identifier/S0022143000020396/type/journal_article, 1968.

Lliboutry, L.: The Dynamics of Temperate Glaciers from the Detailed Viewpoint, Journal of Glaciology, 8, 185–205, doi: 10.3189/S002214300003118X, URL https://www.cambridge.org/core/product/identifier/S002214300003118X/type/journal_article, 1969.

Lliboutry, L.: Permeability, Brine Content and Temperature of Temperate Ice, Journal of Glaciology, 10, 15–29, doi: 10.3189/s002214300001296x, 1971.

Lliboutry, L.: Multivariate Statistical Analysis of Glacier Annual Balances, Journal of Glaciology, 13, 371–392, doi: 10.3189/s0022143000023169, 1974.

Lliboutry, L.: Glissement et hydraulique sous-glaciares, S.H.F. Section de Glaciologie-Nivologie. Réunion du 10 Mars 2005., 2005.

Lliboutry, L. and Duval, P.: Various isotropic and anisotropic ices found in glaciers and polar ice caps and their corresponding rheologies, International Journal of Rock Mechanics and Mining Sciences Geomechanics Abstracts, 22, 198, doi: 10.1016/0148-9062(85)90267-0, URL https://linkinghub.elsevier.com/retrieve/pii/0148906285902670, 1985.

Luckhurst, T.: Iceland's Okjokull glacier commemorated with plaque, retrieved on 18/10/2022. From BBC, https://www.bbc.com/news/world-europe-49345912, 2019.

Lüthi, M., Funk, M., Iken, A., Gogineni, S., and Truffer, M.: Mechanisms of fast flow in Jakobshavn Isbræ, West Greenland: Part III. Measurements of ice deformation, temperature and cross-borehole conductivity in boreholes to the bedrock, Journal of Glaciology, 48, 369–385, doi: 10.3189/172756502781831322, 2002.

Lüthi, M. P. and Moreau, L.: Calorimetric in-situ determination of the unfrozen water content in glacier ice, 2018.

Maier, N., Humphrey, N., Harper, J., and Meierbachtol, T.: Sliding dominates slow-flowing margin regions, Greenland Ice Sheet, Science Advances, 5, eaaw5406, doi: 10.1126/sciadv.aaw5406, URL https://advances.sciencemag.org/lookup/doi/10.1126/sciadv.aaw5406, 2019.

Maier, N., Gimbert, F., Gillet-Chaulet, F., and Gilbert, A.: Basal traction mainly dictated by hard-bed physics over grounded regions of Greenland, Cryosphere, 15, 1435–1451, doi: 10.5194/tc-15-1435-2021, 2021a.

Maier, N., Humphrey, N., Meierbachtol, T., and Harper, J.: Deformation motion tracks sliding changes through summer, western Greenland, Journal of Glaciology, pp. 1–10, doi: 10.1017/jog.2021.87, URL https://www.cambridge.org/core/product/identifier/S0022143021000873/type/journal_article, 2021b.

Maier, N., Humphrey, N., Meierbachtol, T., and Harper, J.: Deformation motion tracks sliding changes through summer, western Greenland, Journal of Glaciology, pp. 1–10, doi: 10.1017/jog.2021.87, URL https://www.cambridge.org/core/product/identifier/S0022143021000873/type/journal_article, 2021c.

Maier, N., Gimbert, F., and Gillet-Chaulet, F.: Threshold response to melt drives large-scale bed weakening in Greenland, Nature, 607, 714–720, doi: 10.1038/s41586-022-04927-3, URL https://www.nature.com/articles/s41586-022-04927-3, 2022.

Mair, D., Willis, I., Fischer, U. H., Hubbard, B., Nienow, P., and Hubbard, A.: Hydrological controls on patterns of surface, internal and basal motion during three "spring events": Haut Glacier d'Arolla, Switzerland, Journal of Glaciology, 49, 555–567, doi: 10.3189/172756503781830467, 2004.

Mangeney, A., Califano, F., and Castelnau, O.: Isothermal flow of an anisotropic ice sheet in the vicinity of an ice divide, Journal of Geophysical Research: Solid Earth, 101, 28 189–28 204, doi: 10.1029/96JB01924, URL http://doi.wiley.com/10.1029/96JB01924, 1996.

Marshall, H. P., Harper, J. T., Pfeffer, W. T., and Humphrey, N. F.: Depth-varying constitutive properties observed in an isothermal glacier, Geophysical Research Letters, 29, 2–5, doi: 10.1029/2002GL015412, 2002.

Mathews, W. H.: Vertical Distribution of Velocity in Salmon Glacier, British Columbia, Journal of Glaciology, 3, 448–454, doi: 10.3189/S0022143000017184, URL https://www.cambridge.org/core/product/identifier/S0022143000017184/type/journal_article, 1959.

Maurel, A., Lund, F., and Montagnat, M.: Propagation of elastic waves through textured polycrystals: Application to ice, Proceedings of the Royal Society A: Mathematical, Physical and Engineering Sciences, 471, doi: 10.1098/rspa.2014.0988, 2015.

McCarthy, C., Savage, H., and Nettles, M.: Temperature dependence of ice-on-rock friction at realistic glacier conditions, Philosophical Transactions of the Royal Society A: Mathematical, Physical and Engineering Sciences, 375, doi: 10.1098/rsta.2015.0348, 2017.

McConnell, J. R., Wilson, A. I., Stohl, A., Arienzo, M. M., Chellman, N. J., Eckhardt, S., Thompson, E. M., Pollard, A. M., and Steffensen, J. P.: Lead pollution recorded in Greenland ice indicates European emissions tracked plagues, wars, and imperial expansion during antiquity, Proceedings of the National Academy of Sciences of the United States of America, 115, 5726–5731, doi: 10.1073/pnas.1721818115, 2018.

Meier, M. F.: Mode of flow of Saskatchewan Glacier, Alberta, Canada, Geological Survey Professional Paper, 351, 70, URL https://pubs.er.usgs.gov/publication/pp351, 1960.

Millan, R., Mouginot, J., Rabatel, A., and Morlighem, M.: Ice velocity and thickness of the world's glaciers, Nature Geoscience, 15, 124–129, doi: 10.1038/s41561-021-00885-z, URL https://www.nature.com/articles/s41561-021-00885-z, 2022.

Miller, M.: Phenomena associated with the deformation of a glacier bore-hole, Extrait Des Comptes Rendus Et Rapports- Assemblée Générale de Toronto, URL http://ks360352.kimsufi.com/redbooks/a046/04641.pdf, 1957.

Millstein, J. D., Minchew, B. M., and Pegler, S. S.: Ice viscosity is more sensitive to stress than commonly assumed, Communications Earth Environment, 3, 1–7, doi: 10.1038/s43247-022-00385-x, 2022.

Moore, P. L.: Deformation of Debris-Ice Mixtures Reviews of Geophysics, pp. 435–467, doi: 10.1002/2014RG000453.Received, 2014.

Morland, L. W.: Glacier Sliding Down an Inclined Wavy Bed, Journal of Glaciology, 17, 447–462, doi: 10.1017/S0022143000013733, URL https://www.cambridge.org/core/product/identifier/S0022143000013733/type/journal_article, 1976a.

Morland, L. W.: Glacier Sliding Down an Inclined Wavy Bed With Friction, Journal of Glaciology, 17, 463–477, doi: 10.3189/S0022143000013745, URL https://www.cambridge.org/core/product/identifier/S0022143000013745/type/journal_article, 1976b.

Morlighem, M., Seroussi, H., Larour, E., and Rignot, E.: Inversion of basal friction in Antarctica using exact and incomplete adjoints of a higher-order model, Journal of Geophysical Research: Earth Surface, 118, 1746–1753, doi: 10.1002/jgrf.20125, 2013.

Murray, T., Stuart, G. W., Fry, M., Gamble, N. H., and Crabtree, M. D.: Englacial water distribution in a temperate glacier from surface and borehole radar velocity analysis, Journal of Glaciology, 46, 389–398, doi: 10.3189/172756500781833188, 2000.

Murray, T., Booth, A., and Rippin, D. M.: Water-content of Glacier-ice: Limitations on estimates from velocity analysis of surface ground-penetrating radar surveys, Journal of Environmental and Engineering Geophysics, 12, 87–99, doi: 10.2113/JEEG12.1.87, 2007.

Nanni, U., Gimbert, F., Vincent, C., Gräff, D., Walter, F., Piard, L., and Moreau, L.: Quantification of seasonal and diurnal dynamics of subglacial channels using seismic observations on an Alpine glacier, Cryosphere, 14, 1475–1496, doi: 10.5194/tc-14-1475-2020, 2020a.

Nanni, U., Gimbert, F., Roux, P., and Lecointre, A.: Observing the subglacial hydrology network and its dynamics with a dense seismic array, Proceedings of the National Academy of Sciences of the United States of America, 118, 1–7, doi: 10.1073/pnas.2023757118, 2021.

Nye, J. F.: The flow law of ice from measurements in glacier tunnels, laboratory experiments and the Jungfraufirn borehole experiment, Proceedings of the Royal Society of London. Series A. Mathematical and Physical Sciences, 219, 477–489, doi: 10.1098/rspa.1953.0161, URL `https://royalsocietypublishing.org/doi/10.1098/rspa.1953.0161`, 1953.

Nye, J. F.: The Flow of a Glacier in a Channel of Rectangular, Elliptic or Parabolic Cross-Section, Journal of Glaciology, 5, 661–690, doi: 10.3189/s0022143000018670, 1965.

Nye, J. F.: A Calculation on the Sliding of Ice Over a Wavy Surface Using a Newtonian Viscous Approximation, Proceedings of the Royal Society A: Mathematical, Physical and Engineering Sciences, 311, 445–467, doi: 10.1098/rspa.1969.0127, URL `http://rspa.royalsocietypublishing.org/cgi/doi/10.1098/rspa.1969.0127`, 1969.

OGGM - edu (web resource): European Alps: Future glacier evolution, `https://edu.oggm.org/en/latest/alps_future.html`, accessed: 06/01/2023.

Paterson, W. S. B.: The Sliding Velocity of Athabasca Glacier, Canada, Journal of Glaciology, 9, 55–63, doi: 10.3189/S0022143000026794, URL `https://www.cambridge.org/core/product/identifier/S0022143000026794/type/journal_article`, 1970.

Paterson, W. S. B.: The physics of glaciers, Pergamon Oxford, OX, England ; Tarrytown, N.Y., U.S.A, 3rd ed. edn., 1994.

Pattyn, F.: Antarctic subglacial conditions inferred from a hybrid ice sheet/ice stream model, Earth and Planetary Science Letters, 295, 451–461, doi: 10.1016/j.epsl.2010.04.025, 2010.

Pattyn, F. and Morlighem, M.: The uncertain future of the Antarctic Ice Sheet, Science, 367, 1331–1335, doi: 10.1126/science.aaz5487, URL `https://science.sciencemag.org/content/367/6484/1331`, 2020.

Perutz, M. F.: Report on Problems Relating to the Flow of Glaciers, Journal of Glaciology, 1, 47–51, doi: 10.3189/s0022143000007541, 1947.

Perutz, M. F.: Direct Measurement of the Velocity Distribution in a Vertical Profile Through a Glacier, Journal of Glaciology, 1, 382–383, doi: 10.3189/s0022143000012594, 1949.

Perutz, M. F.: Direct Measurement of the Velocity Distribution in a Vertical Profile Through a Glacier, Journal of Glaciology, 1, 382–383, doi: 10.3189/S0022143000012594, URL `https://www.cambridge.org/core/product/identifier/S0022143000012594/type/journal_article`, 1950.

Pettersson, R., Jansson, P., and Blatter, H.: Spatial variability in water content at the cold-temperate transition surface of the polythermal Storglaciären, Sweden, Journal of Geophysical Research: Earth Surface, 109, n/a–n/a, doi: 10.1029/2003jf000110, 2004.

Preunkert, S., McConnell, J. R., Hoffmann, H., Legrand, M., Wilson, A. I., Eckhardt, S., Stohl, A., Chellman, N. J., Arienzo, M. M., and Friedrich, R.: Lead and Antimony in Basal Ice From Col du Dome (French Alps) Dated With Radiocarbon: A Record of Pollution During Antiquity, Geophysical Research Letters, 46, 4953–4961, doi: 10.1029/2019GL082641, 2019.

Rabatel, A. and Biron, R.: SmartStake: an autonomous measurement station for high resolution glacier ablation monitoring, retrieved on 09/11/2022. From `https://a2photonicsensors.com/smartstake-monitor-glacier-ablation/`, 2021.

Raymond, C.: Flow in a Transverse Section of Athabasca Glacier, Alberta, Canada, Journal of Glaciology, 10, 55–84, doi: 10.3189/s0022143000012995, 1971.

Raymond, C. F. and Harrison, W. D.: Some Observations on the Behavior of the Liquid and Gas Phases in Temperate Glacier Ice, Journal of Glaciology, 14, 213–233, doi: 10.3189/s0022143000021717, 1975.

Rémy, F. and Testut, L.: Mais comment s'écoule donc un glacier ? Aperçu historique, Comptes Rendus - Geoscience, 338, 368–385, doi: 10.1016/j.crte.2006.02.004, 2006.

Ritz, C., Edwards, T. L., Durand, G., Payne, A. J., Peyaud, V., and Hindmarsh, R. C.: Potential sea-level rise from Antarctic ice-sheet instability constrained by observations, Nature, 528, 115–118, doi: 10.1038/nature16147, URL `http://dx.doi.org/10.1038/nature16147`, 2015.

Roeoesli, C., Helmstetter, A., Walter, F., and Kissling, E.: Meltwater influences on deep stick-slip icequakes near the base of the Greenland Ice Sheet, Journal of Geophysical Research: Earth Surface, 121, 223–240, doi: 10.1002/2015JF003601, 2016.

Roldán-Blasco, J., Gimbert., F., Gagliardini, O., and Gilbert, A.: Pre and post- processing files and scripts for the paper 'The effect of local shear stress on glacier sliding', doi: 10.5281/zenodo.5046764, URL https://doi.org/10.5281/zenodo.5046764, 2022.

Roldán-Blasco, J. P.: Modelling of friction at the base of glaciers, Msc thesis, École Centrale de Nantes, International Center for Numerical Methods in Engineering, 2019.

Roldán-Blasco, J. P., Piard, L., Gilbert, A., F., G., Vincent, C., Gagliardini, O., Togaibekov, A., and Walpersdorf, A.: Deformation, creep enhancement and sliding in a temperate alpine glacier, in preparation.

Roldán-Blasco, J. P., Gimbert, F., Gagliardini, O., and Gilbert, A.: The effect of local shear stress on glacier sliding, submitted.

Röthlisberger, H.: Water Pressure in Intra- and Subglacial Channels, Journal of Glaciology, 11, 177–203, doi: 10.3189/s0022143000022188, 1972.

Ryser, C., Lüthi, M. P., Andrews, L. C., Hoffman, M. J., Catania, G. A., Hawley, R. L., Neumann, T. A., and Kristensen, S. S.: Sustained high basal motion of the Greenland ice sheet revealed by borehole deformation, Journal of Glaciology, 60, 647–660, doi: 10.3189/2014JoG13J196, URL https://www.cambridge.org/core/product/identifier/S0022143000203018/type/journal_article, 2014.

Schaer, J.-P.: Le rôle d 'Agassiz en glaciologie ou la réussite d 'un entrepreneur scientifique ambitieux, Comité Français d'Histoire de la Géologie - Troisième série, 2001.

Schoof, C.: The effect of cavitation on glacier sliding, Proceedings of the Royal Society A: Mathematical, Physical and Engineering Sciences, 461, 609–627, doi: 10.1098/rspa.2004.1350, 2005.

Schoof, C.: Ice-sheet acceleration driven by melt supply variability, Nature, 468, 803–806, doi: 10.1038/nature09618, URL http://www.nature.com/articles/nature09618, 2010.

Schoof, C.: The evolution of isolated cavities and hydraulic connection at the glacier bed . Part 1 : steady states and friction laws, EGUsphere, pp. 1–27, doi: 10.5194/egusphere-2022-1380, 2023a.

Schoof, C.: The evolution of isolated cavities and hydraulic connection at the glacier bed . Part 2 : a dynamic viscoelastic model, EGUsphere, doi: https://doi.org/10.5194/egusphere-2022-1400, 2023b.

Schulson, E. M. and Duval, P.: Creep and Fracture of Ice, Cambridge University Press, doi: 10.1017/CBO9780511581397, 2009.

Schweizer, J. and Iken, A.: The role of bed separation and friction in sliding over an undeformable bed, Journal of Glaciology, 38, 77–92, doi: 10.1017/S0022143000009618, 1992.

Seguinot, J., Ivy-Ochs, S., Jouvet, G., Huss, M., Funk, M., and Preusser, F.: Modelling last glacial cycle ice dynamics in the Alps, Cryosphere, 12, 3265–3285, doi: 10.5194/tc-12-3265-2018, 2018.

Seligman, R.: Joint Meeting of the British Glaciological Society, the British Rheologists' Club and the Institute of Metals, Journal of Glaciology, 1, 231–240, doi: 10.3189/002214349793702827, URL https://www.cambridge.org/core/product/identifier/S0022143000009795/type/journal_article, 1949.

Sergeant, A., Chmiel, M., Lindner, F., Walter, F., Roux, P., Chaput, J., Gimbert, F., and Mordret, A.: On the Green's function emergence from interferometry of seismic wave fields generated in high-melt glaciers: Implications for passive imaging and monitoring, Cryosphere, 14, 1139–1171, doi: 10.5194/tc-14-1139-2020, 2020.

Shapero, D. R., Joughin, I. R., Poinar, K., Morlighem, M., and Gillet-Chaulet, F.: Basal resistance for three of the largest Greenland outlet glaciers, Journal of Geophysical Research F: Earth Surface, doi: 10.1002/2015JF003643, 2016.

Sharp, R. P.: Deformation of a Vertical Bore Hole in a Piedmont Glacier, Journal of Glaciology, 2, 182–184, doi: 10.3189/S0022143000025685, URL https://www.cambridge.org/core/product/identifier/S0022143000025685/type/journal_article, 1953.

Shreve, R. and Sharp, R.: Internal Deformation and Thermal Anomalies in Lower Blue Glacier, Mount Olympus, Washington, U.S.A., Journal of Glaciology, 9, 65–86, doi: 10.3189/S0022143000026800, URL https://www.cambridge.org/core/product/identifier/S0022143000026800/type/journal_article, 1970.

Solomina, O. N., Bradley, R. S., Jomelli, V., Geirsdottir, A., Kaufman, D. S., Koch, J., McKay, N. P., Masiokas, M., Miller, G., Nesje, A., Nicolussi, K., Owen, L. A., Putnam, A. E., Wanner, H., Wiles, G., and Yang, B.: Glacier fluctuations during the past 2000 years, Quaternary Science Reviews, 149, 61–90, doi: 10.1016/j.quascirev.2016.04.008, 2016.

Thøgersen, K., Gilbert, A., Schuler, T. V., and Malthe-Sørenssen, A.: Rate-and-state friction explains glacier surge propagation, Nature Communications, 10, 1–8, doi: 10.1038/s41467-019-10506-4, URL http://dx.doi.org/10.1038/s41467-019-10506-4, 2019.

Thompson, A. C., Iverson, N. R., and Zoet, L. K.: Controls on Subglacial Rock Friction: Experiments With Debris in Temperate Ice, Journal of Geophysical Research: Earth Surface, 125, 1–18, doi: 10.1029/2020JF005718, 2020.

Thorsteinsson, T.: An analytical approach to deformation of anisotropic ice-crystal aggregates, Journal of Glaciology, 47, 507–516, doi: 10.3189/172756501781832124, 2001.

Togaibekov, A., Walpersdorf, A., and Gimbert, F.: Short-term surface velocity variations of the Argentière glacier monitored with a high-resolution continuous GNSS network, i, 5194, 2022.

Trnkoczy, A.: Understanding and parameter setting of STA/LTA trigger algorithm, in: New Manual of Seismological Observatory Practice (NMSOP), Potsdam : Deutsches GeoForschungsZentrum GFZ, 1-20, edited by Bormann, P., vol. 14, pp. 27–35, 1999 edn., doi: https://doi.org/10.2312/GFZ.NMSOP_r1_IS_8.1, 2015.

Tsai, V. C., Smith, L. C., Gardner, A. S., and Seroussi, H.: A unified model for transient subglacial water pressure and basal sliding, Journal of Glaciology, pp. 1–11, doi: 10.1017/jog.2021.103, 2021.

Turrel, M.: Louis Lliboutry, le champollion des glaces, UGA editions, 2017.

Vallon, M., Petit, J.-R., and Fabre, B.: Study of an Ice Core to the Bedrock in the Accumulation zone of an Alpine Glacier, Journal of Glaciology, 17, 13–28, doi: 10.3189/s0022143000030677, 1976.

Vincent, C.: Influence of climate change over the 20th Century on four French glacier mass balances, Journal of Geophysical Research Atmospheres, 107, ACL 4–1–ACL 4–12, doi: 10.1029/2001JD000832, 2002.

Vincent, C. and Moreau, L.: Sliding velocity fluctuations and subglacial hydrology over the last two decades on Argentière glacier, Mont Blanc area, Journal of Glaciology, 62, 805–815, doi: 10.1017/jog.2016.35, 2016.

Vincent, C., Soruco, A., Six, D., and Meur, E. L.: Glacier thickening and decay analysis from 50 years of glaciological observations performed on Glacier d'Argentière, Mont Blanc area, France, Annals of Glaciology, 50, 73–79, doi: 10.3189/172756409787769500, 2009.

Vincent, C., Garambois, S., Thibert, E., Lefèbvre, E., Le Meur, E., and Six, D.: Origin of the outburst flood from Glacier de Tête Rousse in 1892 (Mont Blanc area, France), Journal of Glaciology, 56, 688–698, doi: 10.3189/002214310793146188, 2010.

Vincent, C., Fischer, A., Mayer, C., Bauder, A., Galos, S. P., Funk, M., Thibert, E., Six, D., Braun, L., and Huss, M.: Common climatic signal from glaciers in the European Alps over the last 50 years, Geophysical Research Letters, 44, 1376–1383, doi: 10.1002/2016GL072094, 2017.

Vincent, C., Gilbert, A., Walpersdorf, A., Gimbert, F., Gagliardini, O., Jourdain, B., Juan Pedro, R.-B., Laarman, O., Piard, L., Six, D., Moreau, L., Cusicanqui, D., Thibert, E., and Al, V. E. T.: Supporting Information for Evidence of seasonal uplift in the Argentière glacier (Mont Blanc area, France), 2022a.

Vincent, C., Gilbert, A., Walpersdorf, A., Gimbert, F., Gagliardini, O., Jourdain, B., Pedro, J., Blasco, R., Laarman, O., Piard, L., Six, D., Moreau, L., Cusicanqui, D., Thibert, E., and Al, V. E. T.: Evidence of Seasonal Uplift in the Argentière Glacier (Mont Blanc Area , France) Journal of Geophysical Research : Earth Surface, doi: 10.1029/2021JF006454, 2022b.

Weertman, J.: On the Sliding of Glaciers, Journal of Glaciology, 3, 33–38, doi: 10.3189/S0022143000024709, 1957.

Weertman, J.: General theory of water flow at the base of a glacier or ice sheet, Reviews of Geophysics, 10, 287–333, doi: 10.1029/RG010i001p00287, 1972.

Werder, M. A., Hewitt, I. J., Schoof, C. G., and Flowers, G. E.: Modeling channelized and distributed subglacial drainage in two dimensions, Journal of Geophysical Research: Earth Surface, 118, 2140–2158, doi: 10.1002/jgrf.20146, 2013.

WGMS: Fluctuations of Glaciers Database, Zurich, Switzerland, data retrieved from World Glacier Monitoring Service (WGMS), https://doi.org/10.5904/wgms-fog-2022-09, 2022.

Wiens, D. A., Anandakrishnan, S., Winberry, J. P., and King, M. A.: Simultaneous teleseismic and geodetic observations of the stick-slip motion of an Antarctic ice stream, Nature, 453, 770–774, doi: 10.1038/nature06990, 2008.

Willis, I., Mair, D., Hubbard, B., Nienow, P., Fischer, U. H., and Hubbard, A.: Seasonal variations in ice deformation and basal motion across the tongue of Haut Glacier d'Arolla, Switzerland, Annals of Glaciology, 36, 157–167, doi: 10.3189/172756403781816455, 2003.

Zeitz, M., Levermann, A., and Winkelmann, R.: Sensitivity of ice loss to uncertainty in flow law parameters in an idealized one-dimensional geometry, Cryosphere, 14, 3537–3550, doi: 10.5194/tc-14-3537-2020, 2020.

Zekollari, H., Huss, M., and Farinotti, D.: Modelling the future evolution of glaciers in the European Alps under the EURO-CORDEX RCM ensemble, Cryosphere, doi: 10.5194/tc-13-1125-2019, 2019.

Zoet, L. K. and Iverson, N. R.: Experimental determination of a double-valued drag relationship for glacier sliding, Journal of Glaciology, 61, 1–7, doi: 10.3189/2015JoG14J174, URL `https://www.cambridge.org/core/product/identifier/S0022143000203535/type/journal_article`, 2015.

Zoet, L. K., Anandakrishnan, S., Alley, R. B., Nyblade, A. A., and Wiens, D. A.: Motion of an Antarctic glacier by repeated tidally modulated earthquakes, Nature Geoscience, 5, 623–626, doi: 10.1038/ngeo1555, 2012.

Zoet, L. K., Carpenter, B., Scuderi, M., Alley, R. B., Anandakrishnan, S., Marone, C., and Jackson, M.: The effects of entrained debris on the basal sliding stability of a glacier, Journal of Geophysical Research: Earth Surface, 118, 656–666, doi: 10.1002/jgrf.20052, 2013.

Zoet, L. K., Iverson, N. R., Andrews, L., and Helanow, C.: Transient evolution of basal drag during glacier slip, Journal of Glaciology, pp. 1–10, doi: 10.1017/jog.2021.131, URL `https://www.cambridge.org/core/product/identifier/S0022143021001313/type/journal_article`, 2021.

ANNEX A

An introduction to continuum mechanics

A.1 Introduction

In this Annex we will introduce basic concepts of continuum mechanics, and its applications to modeling ice dynamics. Many of the concepts are, for brevity, explained in less details in the rest of the thesis, so we will use this section to lay them out with a little bit more of detail.

Continuum mechanics deals with the movement and deformation of continuous media. It is a very powerful tool to model the behaviour of solid and fluids, yet not an easy one to work with, since its mathematical representation can oftentimes become cumbersome (hence the opening quote). An assessment of such power is found in the amount of accurate mechanical analysis of glacier and ice-sheet flow performed prior to the advent of large-scale remote sensing techniques and numerical modeling techniques, Glen (e.g. 1955); Weertman (e.g. 1957); Nye (e.g. 1965); Lliboutry (e.g. 1968); Raymond (e.g. 1971); Hooke (e.g. 1973).

We will start the chapter with a short description of stress, strain rate, and the constitutive relation commonly used for ice. We will continue with a few notes on commonly assumed ice mechanical properties that will later be considered in this thesis. We will finish with a simplified view of the form of the vertical distribution of the stress and strain rate that can be reasonably expected in a glacier.

A.2 Stress and strain rate

A.2.1 General description

In a continuum mechanics framework objects deform when subjected to stress. In Figure A.2 we schematize how a square volume deforms under compression, tractions, and shearing stress. Stress is a measure of force by unit area, therefore it represents a distributed force acting on a surface. strain rate is the rate (i.e. speed) of deformation, and measures how fast a medium, typically a fluid, is deforming under continuously applied stress. Ice is a mechanically complex material whose response to stress depends on the applied stress and the strain rates at which it is deforming.

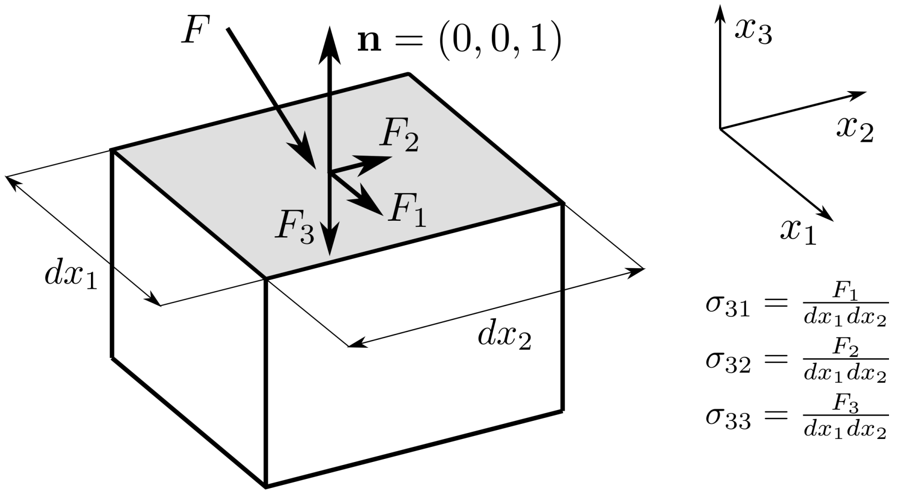

Figure A.1: Scheme of forces and the derived Cauchy stress acting at a point over a horizontal plane.

A.2.2 Mathematical representation of vectors and tensors

We will start by assuming that we are working with a three dimensional ortonormal reference system, of directions x_1, x_2, and x_3, which we will also call x, y, and z respectively. We will identify x_1 (or x) with the along flow horizontal direction, and x_3 (or z) with the upwards vertical direction. Vectors, or first order tensors, such as velocity, will therefore have three components, one per direction. For a given vector $\mathbf{a}$, its components will be a_1, a_2 and a_3, equivalent to a_x, a_y, and a_z. Second order tensors (abbreviated to just tensors, most of the time) have nine components, one per each unique combination of two directions. For a given tensor $\mathbf{A}$, the nine components will be A_{11}, A_{12}, A_{13}, A_{21}, A_{22}, A_{23}, A_{31}, A_{32}, and A_{33}. A typical example of second-order tensor that will appear often in this PhD is the velocity gradient tensor $\mathbf{L}$, represented by

$$\mathbf{L} = \nabla \mathbf{u} = \begin{pmatrix} L_{11} & L_{12} & L_{13} \\ L_{21} & L_{22} & L_{23} \\ L_{31} & L_{32} & L_{33} \end{pmatrix} = \begin{pmatrix} \frac{du}{dx} & \frac{du}{dy} & \frac{du}{dz} \\ \frac{dv}{dx} & \frac{dv}{dy} & \frac{dv}{dz} \\ \frac{dw}{dx} & \frac{dw}{dy} & \frac{dw}{dz} \end{pmatrix},$$

with $\mathbf{u} = (u, v, w) = (u_1, u_2, u_3)$ the velocity vector. In this case, any component L_{ij} refers to the derivative of the u_i component with respect to the direction x_j. Thus, L_{11} is equivalent to du/dx, L_{12} is equivalent to du/dy, L_{13} is equivalent to du/dz, and so on. The gradient can also be written with the gradient operator $\nabla = \partial/\partial x_j$ We will further develop this tensor in chapter 1.3.3.

Stress and strain rate are represented with second-order tensors $\boldsymbol{\sigma}$ and $\dot{\boldsymbol{\epsilon}}$, called the Cauchy stress tensor and the strain rate tensor, respectively. At any given point of space, the term σ_{ij} represents the j component of the force per unit area acting on a plane with normal x_i. Figure A.1 illustrates an example of how to translate forces into stress. Let's consider a force $\mathbf{F} = (F_1, F_2, F_3)$ acting on a point P, and a horizontal plane with normal vector $n = (0,0,1)$ passing through P, such that we can define the force per unit area $\mathbf{F_{surf}} = (F_1, F_2, F_3)/(dx_1 dx_2)$ for an infinitesimal surface of area $dx_1 dx_2$. This allows us to obtain already three components of the Cauchy stress tensor $\boldsymbol{\sigma}$. The first component is $\sigma_{31} = \sigma_{13} = F_1/(dx_1 dx_2)$, which over this plane is a shearing stress, as F_1 is parallel to the plane. The second component is $\sigma_{32} = \sigma_{23} = F_2/(dx_1 dx_2)$, which is also a shearing stress. The third component is $\sigma_{33} = F_3/(dx_1 dx_2)$, which is a normal compressive stress, since it is normal to the surface, and in this example F_3 is towards the surface.

In glaciology, we usually consider the stress tensor $\boldsymbol{\tau} = \boldsymbol{\sigma} - 1/3tr(\boldsymbol{\sigma})\boldsymbol{I}$, which is the deviatoric part

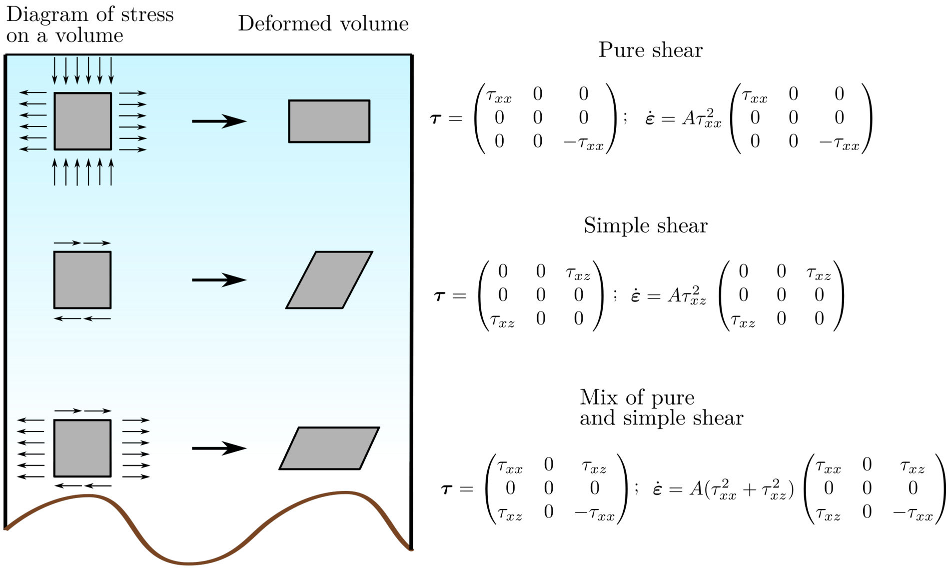

Figure A.2: Simplified two-dimensional stress states with depth in a glacier. Based on Hooke (2005) for the surface and middle parts of the glacier and in Gudmundsson (1997a) for the basal part. Our observations in Glacier d'Argentière agree with this scheme. More details in the text.

of the Cauchy stress tensor. The reason behind this is that the isotropic pressure $\mathbf{p} = 1/3tr(\boldsymbol{\sigma})\boldsymbol{I}$, called the spherical part of $\boldsymbol{\sigma}$, has no effect on the deformation of incompressible media such as ice. Due to equilibrium conditions, it can be proven that $\boldsymbol{\sigma}$ and therefore $\boldsymbol{\tau}$ are symmetric. Conversely for the strain rate, $\dot{\boldsymbol{\varepsilon}}$ is defined as the symmetric component of $\mathbf{L}$, therefore $\dot{\boldsymbol{\varepsilon}} = 1/2(\mathbf{L} + \mathbf{L}^T)$, with $\mathbf{L}^T$ the transpose of $\mathbf{L}$. Because they are symmetric, $\boldsymbol{\tau}$ and $\dot{\boldsymbol{\varepsilon}}$ only have six independent components:

$$\boldsymbol{\tau} = \begin{pmatrix} \tau_{11} & \tau_{12} & \tau_{13} \\ \tau_{12} & \tau_{22} & \tau_{23} \\ \tau_{13} & \tau_{23} & \tau_{33} \end{pmatrix}; \ \dot{\boldsymbol{\varepsilon}} = \begin{pmatrix} \dot{\varepsilon}_{11} & \dot{\varepsilon}_{12} & \dot{\varepsilon}_{13} \\ \dot{\varepsilon}_{12} & \dot{\varepsilon}_{22} & \dot{\varepsilon}_{23} \\ \dot{\varepsilon}_{13} & \dot{\varepsilon}_{23} & \dot{\varepsilon}_{33} \end{pmatrix} = \frac{1}{2} \begin{pmatrix} 2\frac{du}{dx} & \frac{du}{dy} + \frac{dv}{dx} & \frac{du}{dz} + \frac{dw}{dx} \\ \frac{dv}{dx} + \frac{du}{dy} & 2\frac{dv}{dy} & \frac{dv}{dz} + \frac{dw}{dy} \\ \frac{dw}{dx} + \frac{du}{dz} & \frac{dw}{dy} + \frac{dv}{dz} & 2\frac{dw}{dz} \end{pmatrix}. \tag{A.1}$$

A.3 Simplified stress and strain rate in a valley glacier

We illustrate three typical stress states found in glaciers in Figure A.2, where we also show the type of deviatoric stress tensors that describe those states. The shown example is done for two-dimensional flow, such that $\tau_{yy}, \tau_{xy}, \tau_{yz}$, which relate to the horizontal direction transverse to the flow, are zero. This assumption is typically valid for the center line of symmetric glaciers, and is a reasonable approximation for the stress regime in ice-sheets (Hooke, 2005).

Starting from the top, we show that close to the surface the glacier is subjected to a pure-shear state, this is, the deviatoric stress is characterized by compression and extension in the horizontal and vertical directions. For example, if the glacier is close to an icefall we expect strong tractions at the surface (typically indicated by the presence of crevasses, as in Glacier d'Argentière), such that $\tau_{zz} < 0$ and $\tau_{xx} > 0$ (Figure A.2 shows this case). As we go towards the base, τ_{xx} and τ_{zz} decrease (Hooke, 2005), but ice pressure increases, creating a horizontal pressure gradient between the upstream and downstream parts of the glacier, stronger the steeper the surface slope. This depth-increasing horizontal stress causes the stress state to be dominated by pure-shear, thus stress tensor components other than τ_{xz} can be neglected. In Chapter 2 we consider this stress state for computing the internal deformation of the glacier. Finally, immediately close to the bed, there are important stress gradients that develop as the ice deforms around the bed's ostacles, so that the stress state becomes a mix of extension, compression, and shear (Gudmundsson, 1997a), as indicated in Figure A.2. Large scale models of ice flow tend to abstract this complex near-bed stress state into a large-scaled shear stress τ_b called basal drag. In chapter 3, we give more details about basal processes and how to compute the basal drag τ_b from micro-scale stress at the bed.

ANNEX B

Tilt data analysis

B.1 Models of deformation

The goal of inclinometry is, ultimately, the determination of the velocity gradient tensor $\mathbf{L}$. As mentioned in Annex 1, $\mathbf{L}$ has nine independent components, one for the derivative of each component of the velocity vector with respect to each direction in a three dimensional space. However, borehole inclinometry only constrains, at maximum, three of such components (one per direction), with an additional constrain given by mass conservation. Thus, the rest of the components must be either ignored (the most common method), obtained with a different technique such as numerical modeling (see Chapter 2) or interpolated from surface strains (Hooke, 1973; Hooke and Hanson, 1986). We will briefly review different methods found in glaciological literature to retrieve the internal deformation. We will assume the orthonormal reference system indicated in Annex 1 with x the main flow direction and z the vertical upwards, and velocity vector $\mathbf{u} = (u, v, w)$.

The simplest of these methods neglects all components other than horizontal shear in the flow direction, du/dz. We can relate the temporal change in tilt with du/dz (Lüthi et al., 2002; Ryser et al., 2014; Doyle et al., 2018; Maier et al., 2019) as,

$$\frac{du}{dz} = \frac{1}{dt}\frac{dx}{dz} \approx \frac{1}{\Delta t}\Delta \tan\theta, \tag{B.1}$$

where Δt is a given time period and $\Delta \tan\theta$ is the change in the tangent of tilt during that time period. If the tilt is obtained with repeated inclinometry, Δt is typically the time difference between measurements. In the case of englacial tiltmeters, the higher frequency of data acquisition allows for using smaller Δt for seasonal and sub-seasonal studies of deformation (see Ryser et al., 2014; Maier et al., 2021b, and Chapter 2). If tilt can be decomposed into tilt in the $X-Z$ and $Y-Z$ planes, this equation is usually applied separately to compute du/dz and dv/dz, respectively (Maier et al., 2019). Otherwise, all tilt is assumed to be contained in the $X-Z$ plane (Gudmundsson et al., 1999, and Chapter 2), a reasonable approximation if we expect symmetric flow.

In case of non-zero along-flow extension or compression, the tilt of the borehole will be affected: along-flow extension will increase the tilt, while compression will dampen it (Nye, 1953; Shreve and Sharp, 1970; Hooke, 2005; Keller and Blatter, 2012). Similarly, if there is significant vertical flow the shape of the borehole will change, and so it must be taken into account. If we assume two-dimensional

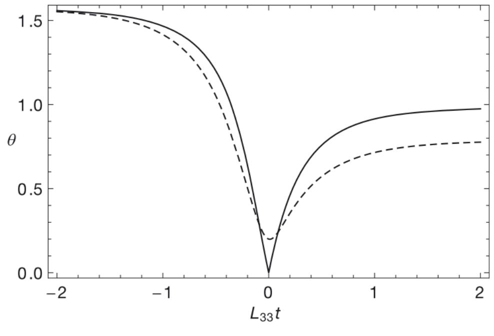

Figure B.1: Temporal change in tilt θ (in rad) under two different conditions. The solid curve has $du/dz = 3dw/dz$, and $\theta_0 = 0$ (tiltmeter contained in the X - Z plane). The dashed line has $du/dz = 2dw/dz$, and is initially off the vertical plane, such that its minimum tilt is $\theta_0 = 0.2$ rad. Extracted from Keller and Blatter (2012).

steady flow, the deformation can be computed as (Hooke, 2005)

$$\frac{du}{dz} = \frac{d}{dt}\tan\theta - 2\frac{du}{dx} + w\frac{d}{dz}\tan\theta. \tag{B.2}$$

The first term on the right hand side is the same as in Eqn. (B.1), the second represents the effect of du/dx and dw/dx, and the latter term is the advection term, as differential vertical flow will also change the shape of the borehole. Note that the total derivative of the velocity are now partial derivatives. Eqn. (B.2) requires *a priori* knowledge of the du/dx and w, which are usually unknown. A more complex expression is given by Keller and Blatter (2012), who provide an analytical solution of tilt evolution intended for englacial tiltmeter analysis. If we neglect the change in shape due to vertical movement (last term in Eqn. (B.2)), we have

$$\begin{aligned} \theta(t) &= \arctan\sqrt{\zeta(t)}, \\ \text{with } \zeta(t) &= e^{-2tL_{33}}\left(\frac{L_{13}}{L_{33}}\tan\theta_0\cos\phi_0 - \frac{L_{13}^2}{2L_{33}} + \tan^2\theta_0\sin^2\phi_0\right) \\ &\quad + e^{-4tL_{33}}\left(\tan\theta_0\cos\phi_0 - \frac{L_{13}}{2L_{33}}\right)^2 + \frac{L_{13}^2}{4L_{33}^2}. \end{aligned} \tag{B.3}$$

We keep the original notation for simplicity, and remind that $L_{13} = du/dz$ and $L_{33} = dw/dz$.

Since englacial tiltmeters provide accurate tilt curves, this solution can be easily inverted to estimate best fitting du/dz, du/dx and dw/dz (Keller and Blatter, 2012; Ryser et al., 2014; Maier et al., 2019, and Chapter 2). Under the same du/dx, the deformation of the borehole will increase if $du/dx > 0 > dw/dz$, and it will be dampened if $du/dx < 0 < dw/dz$. An advantage of Keller and Blatter (2012) solution over Eqn. (B.2) is that Eqn. (B.3) also takes into account out-of-plane tilting, which happens in two-dimensional flow when the tiltmeters are not installed in the $X - Z$ plane.

To finish this section we will mention the numerical scheme used in Gudmundsson et al. (1999). In their analysis of deformation in Unteraargletscher (Switzerland), Gudmundsson et al. (1999) proposed an algorithm that traced the movement of a lagrangian vector (representing the tiltmeter) subjected to a known flow field. Thus, we can represent any velocity gradient tensor and observe how the tilt and azimuth of a tiltmeter evolves with time. Conversely, we can explore a variety of flow conditions (tune the parameters of the model) to find the best fitting combination and obtain reasonable estimates of deformation (Gudmundsson et al., 1999).

B.2 Computation of internal and basal velocity

The deformation velocity $u_d(z)$ is typically computed by integration of du/dz between the bed and a depth z. If we have a series of N observations of du/dz, we can use the trapezoidal rule to obtain the deformation velocity between the deepest measurement ($k = 1$) and the uppermost measurement ($k = N$) as

$$u_d(z_N) \approx \sum_{k=1}^{N-1} \frac{du/dz_{k-1} + du/dz_k}{2} (z_k - z_{k-1}). \tag{B.4}$$

Where sub-index k indicates the observation number. In case of insufficient vertical resolution the velocity computed with this method will have high uncertainties (Gudmundsson et al., 1999; Doyle et al., 2018).

Provided that surface velocity u_s is measured, the basal speed u_b can be computed as the residual component of u_s,

$$u_b = u_s - u_d(z_N). \tag{B.5}$$

By virtue of this definition, u_b combines sliding (i.e. the basal speed at the ice-bed interface) with the deformation velocity between the bed and the deepest measurement of du/dz. If the borehole does not reach the bed, some assumptions can be made to estimate the basal velocity. For instance, we can fit a polynomial function to $u_d(z)$ and extrapolate the values up to the base to obtain the deformation velocity through the whole ice thickness, and then inferr the basal velocity like Hooke and Hanson (1986) did. Another option is given in Gudmundsson et al. (1999), who instead of computing the velocity in Unteraargletscher (Switzerland) from inclinometry, assumed the distribution of horizontal and vertical velocities (based on observations and reasonable assumptions), and tuned the values of $u(x,z)$, and $w(x,z)$ until the synthetic tilt curves matched the observed ones. Finally, we can solve this problem by ignoring it and accepting that the retrieved basal velocity is a mix of sliding and deformation above the bed as done by Hooke et al. (1992).

B.3 Estimating the uncertainty in deformation derived with englacial tiltmeter

In this section we use uncertainty propagation to estimate the uncertainty in du/dz and u_d computed from englacial tiltmeters and Eqn. (B.1), as we use in Chapter 2. Starting from Eqn. (B.1), we can estimate the error in the deformation,

$$\epsilon_{du/dz} = \frac{1}{\Delta t} \frac{d \tan\theta}{d\theta} \epsilon_\theta = \frac{1}{\Delta t}(1 + \tan^2\theta)\epsilon_\theta. \tag{B.6}$$

Where ϵ_θ is the maximum error we can expect in the tilt, and the other variables are as defined in Eqn. (B.1). We bound the computation of the error to the values as $\theta = 0$ and $\theta = \pi/4$ (i.e. we study the error for vertical tiltmeters, and tiltmeters at 45°),

$$\epsilon_0 = \frac{1}{\Delta t}\epsilon_\theta, \; \epsilon_{\pi/4} = 2\epsilon_0. \tag{B.7}$$

The error in the velocity can be roughly estimated as just the product of the deformation error with the thickness h over which we integrate the tilt data,

$$\epsilon_{ud} = \epsilon_{du/dz} h. \tag{B.8}$$

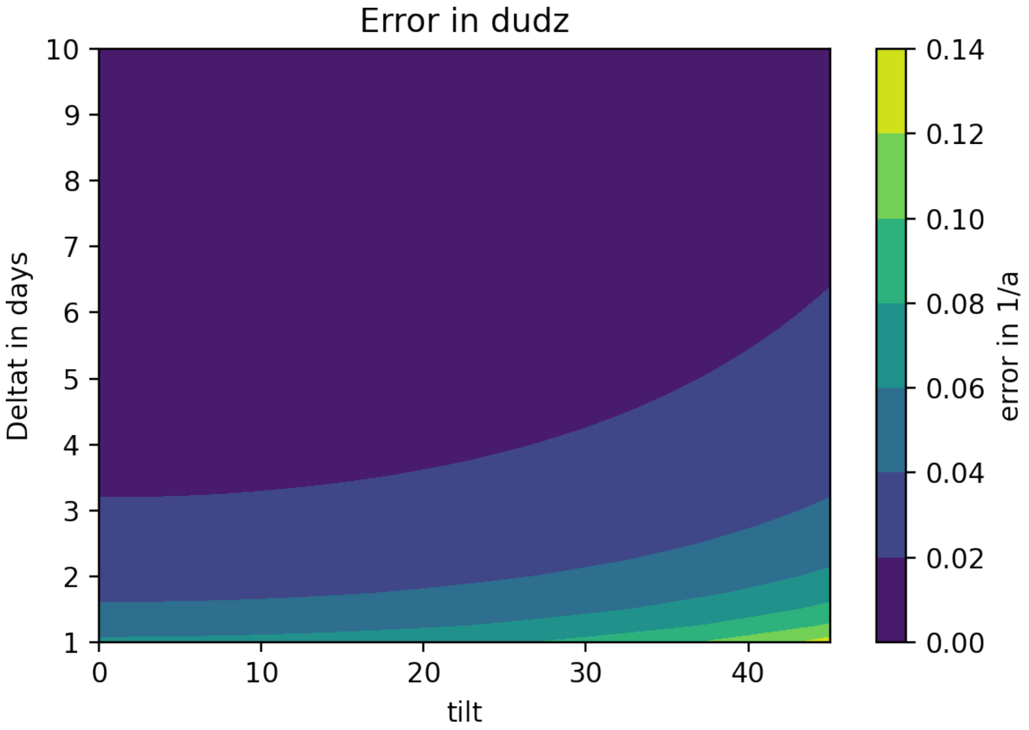

Figure B.2: Error in the deformation from Eqn. (B.6).

We show the ϵ_0 and $\epsilon_{\pi/4}$ curves for $\epsilon_\theta = 0.01° = 0.00017$ rad in Figure B.2. An estimation of the error in the deformation velocity for the two extreme cases considered is shown in Figure B.3. Since not all tiltmeters are at either 0 or $45°$, the real line should be in between the two. However, it must be remarked that these error bounds are unrealistically high, since it is unlikely that the worst case scenario of maximum error in the tilt data is always applicable.

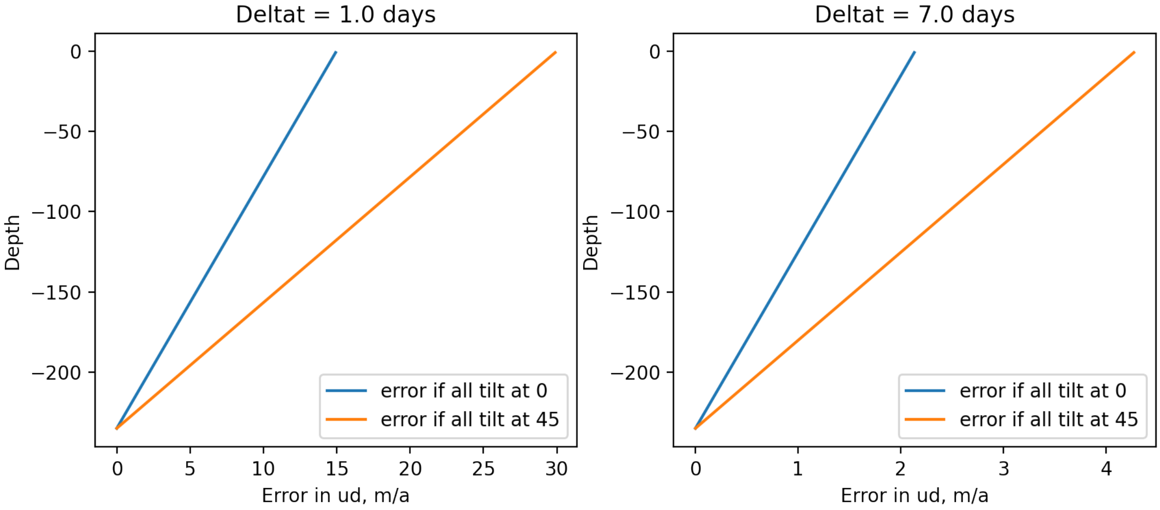

Figure B.3: Cumulative machine error in the velocity, which is basically multiplying the dudz error by the thickness. The real value will be in between the two lines, since for half the thickness of the glacier, the tilt is almost at zero, therefore the error is minimized.

ANNEX C

In-situ measurements of water content in Glacier d'Argentière using a sonic logger

This Annex presents the preliminary results obtained from the sonic-logger measurements mentioned in Chapter 2, Section 2.8.2.2.

C.1 Introduction

The creep enhancement found in Glacier d'Argentière with the inclinometry measurements can have a variety of origins. In Chapter 2 we theorized that depth-increasing water content could realistically explain the increase in creep parameter. The retrieved values of W, and its spatial distribution were comparable to previous studies carried out in temperate glaciers. Another possibility that we cannot discard is ice anisotropy, although *a priori* we don't expect a strong influence in ice deformation.

In order to explore this question in more detail, a preliminary campaign of *in situ* measurements of water content and ice texture using a sonic logger was carried out in June 2022 close to BH12 (see the location of BH12 in Figure 2.8). The field campaign was carried out by researchers and engineers of IGE, including but not limited to Thomas Chauve, Florent Gimbert, Maurine Montagnat and Luc Piard. The preliminary study,including the computation of wave speeds was mainly done by Thomas Chauve with the assistance of Maurine Montagnat. I have interpreted the computed P-wave speeds in terms of water content.

C.2 Method

The method exploits the dependence of the velocity of sonic waves (P and S waves) on the media they travel through. On one hand, it has been shown both theoretically (Maurel et al., 2015) and experimentally (Kluskiewicz et al., 2017) that the velocity of wave propagation depends on ice texture, thus we can use sonic methods to infer the degree of anisotropy in a glacier. On the other hand, wave speed through a solid-water mixture depends as well on the amount of water in the mixture: more water means slower wave propagation (Benjumea et al., 2003). In this Annex we focus on the latter

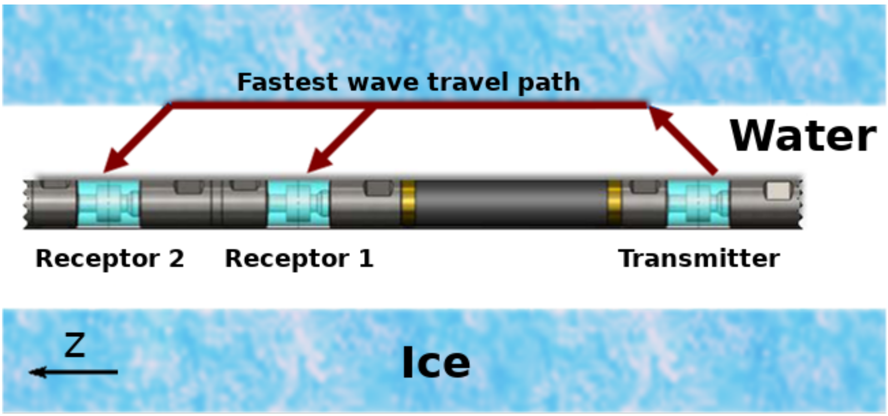

Figure C.1: Typical wave path considered in sonic logging. Adapted from the user guide of the QL40 FWSS sonic logger provided by Advanced Logic Technology sa.

case. The P-wave speed V_P in an ice-water mix can be expressed as (Benjumea et al., 2003):

$$V_P = V_W\left(1+\frac{100-W}{W}\right)\left[\left(1+\frac{(100-W)\rho_i}{W\rho_w}\right)\left(1+\frac{(100-W)\rho_W V_W^2}{W\rho_i V_i^2}\right)\right]^{-1/2}, \tag{C.1}$$

with $V_W = 1500$ m s^{-1} and $V_i = 3800$ m s^{-1} the propagation velocities in water and ice, and $\rho_w = 1000$ kg m^{-3} and $\rho_i = 911$ kg m^{-3} the densities of water and ice at 0°C, respectively.

The instrumentation consisted in a QL40 FWSS sonic logger, which we schematize in Figure C.1. The sonic logger consists in a signal transmitter and four regularly spaced receptors. As the sonic logger descends the borehole, the transmitter sends a sonic signal. Since wave velocities are slowest through air, the signal first received by the receptors are those that travel directly through the borehole to the surrounding ice, then through the ice, and then directly back at the receiver. Sampling frequency is 250 KHz.

In order to compute wave velocities, we must accurately detect the signals detected at each receptor to identify the arrival time of each wave. Once this arrival time is obtained, wave velocity is given by simply dividing the arrival time by the distance between the transmitter and the receptor. In this case, the chosen algorithm to detect the arrival of each wave is called STA/LTA, which detects typical seismic signals based on four given parameters (Trnkoczy, 2015): length of short time average window (STA), length of long time average window (LTA), and the lower and upper thresholds for detecting when a event is triggered (t_{on} and t_{off}). STA measures the instant value of a seismic signal, while LTA allows for measuring the average amplitude of the background noise (Trnkoczy, 2015): too low STA means that environmental noise can be mistaken for real signals, while if STA is too high some events will not be detected; low LTA reduces the sensitivity of event detection. The thresholds are based on the ratio between STA and LTA: if the STA/LTA ratio is higher than t_{on} the algorithm detects an event (the arrival of the seismic signal), and when STA/LTA falls lower than t_{off}, the algorithm detects that the event has finished. The values of STA, LTA, t_{on} and t_{off} are strongly dependant on the application, thus requiring careful tuning to correctly measure the arrival time of the waves and infer wave speed. Multiple receptors improve the reliability of the measured wave velocities.

C.3 Preliminary results and discussion

We show two preliminary results of this study in Figure C.2, with each set of results obtained with different pre-processing parameters, indicated over each panel of Figure C.2. P-wave speeds and water content are shown with running averages over 3 meters, the same used by Kluskiewicz et al. (2017). The values of W reported in Figure C.2 (a) are somewhat reasonable, while Figure C.2 (b) shows $W > 5\%$ in most of the profile, which is much more than expected in temperate glaciers (see Table 1.4). Both profiles show strong variations in the wave speeds, and therefore in the retrieved water content, over a few meters. These strong changes in V_P can be caused by several reasons, and is not necessarily due to changes in water content. For instance, localised increases in P-wave speed could be due to the presence of debris at a particular depth, which will provide stiffer ice. In such a case we cannot discard that enhanced melting around the debris will increase interstitial water (Moore, 2014) and thus produce the opposite effect, marking a decrease in P-wave speed.

Without clearer guidelines as to what values select for the parameters STA, LTA, t_{on} and t_{off} we do not have many more arguments to discard one set of values over the other, or evaluate the retrieved changes in W. Further work has to be carried out to choose the correct pre-processing algorithm for trigger detection and set its parameters to their right values, thus obtaining meaningful distributions of P-wave speed and water content. The analysis can be extended to study S waves, or to use wave speed to infer possible changes in ice texture at our site, following Maurel et al. (2015) and Kluskiewicz et al. (2017).

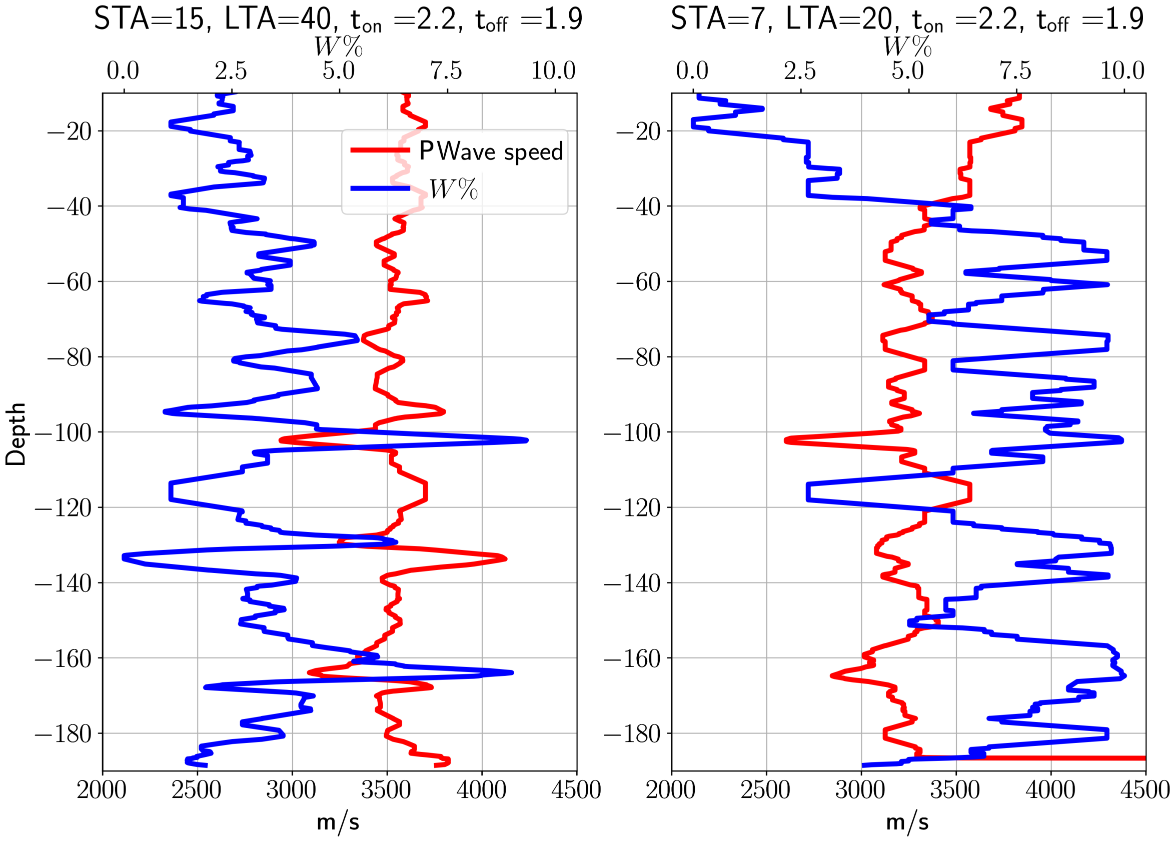

Figure C.2: Two preliminary profiles of P-wave and water content W in a borehole at Glacier d'Argentière. The two sets of profiles are obtained from the same dataset, and their differences are due to the different pre-processing parameters indicated over each panel. Water content is computed from P-wave speed using Eqn. (C.1).

ANNEX D

Supplementary Materials of Chapter 2

These materials contain:

1. The cross section of Glacier d'Argentière at profile 4, Figure D.1.
2. The tilt curves at BH2, BH3 and BH4, Figures D.2 to D.4.
3. Error between measured tilt curves at BH2 and the tilt-curves reproduced by Keller and Blatter (2012) for several combinations of du/dz and du/dx, tiltmeters BH2#1 to BH2#9 Figure D.5.
4. Numerical stress tensors for the simulations with constant A, Figure D.6.
5. Residuals of the linear model applies to the reconstruction of surface velocities at the ablation zone of Glacier d'Argentière over 2020, Figure D.7.
6. Pressure at BH2 from September 2019 to the end of 2020, Figure D.8.
7. Tilt curves at BH12 and BH14, Figures D.10 and D.11.

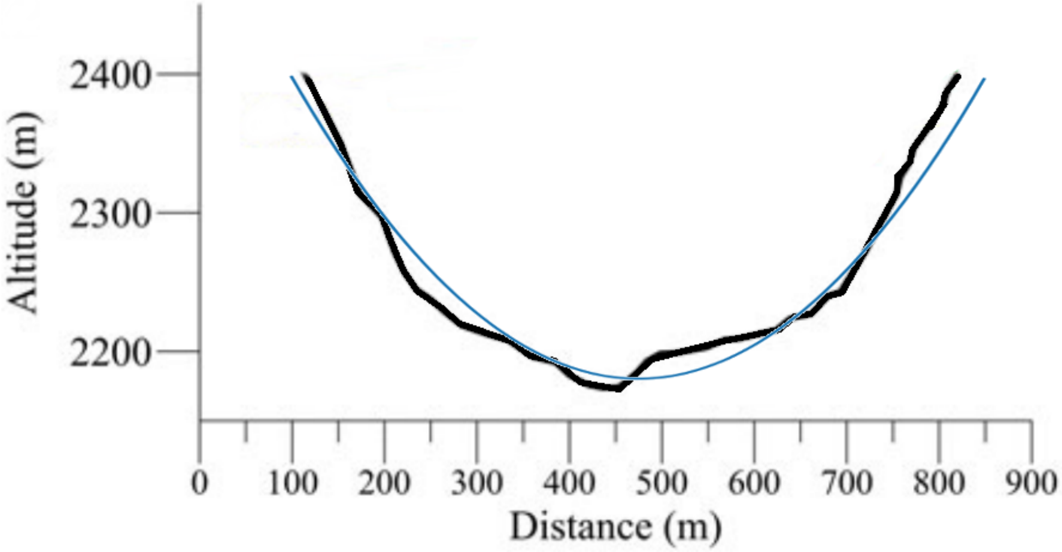

Figure D.1: Cross section of profile 4 of Glacier d'Argentière (Vincent et al., 2009) and parabolic approximation of the valley with a half-width to height ratio of 2. Note that the 'Distance' and 'Altitude' axis are not at the same scale.

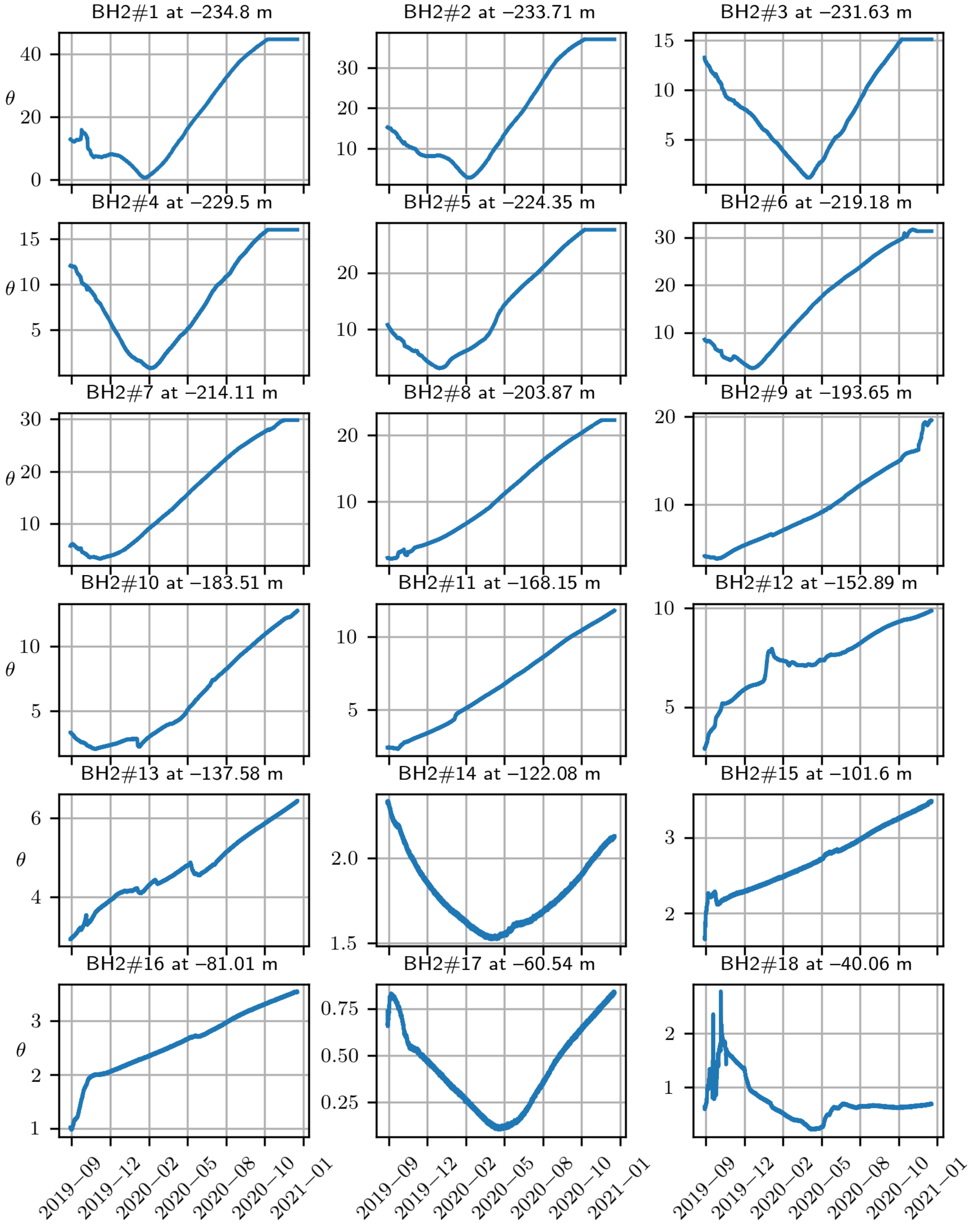
BH2#1 at −234.8 m

BH2#2 at −233.71 m

BH2#3 at −231.63 m

BH2#4 at −229.5 m

BH2#5 at −224.35 m

BH2#6 at −219.18 m

BH2#7 at −214.11 m

BH2#8 at −203.87 m

BH2#9 at −193.65 m

BH2#10 at −183.51 m

BH2#11 at −168.15 m

BH2#12 at −152.89 m

BH2#13 at −137.58 m

BH2#14 at −122.08 m

BH2#15 at −101.6 m

BH2#16 at −81.01 m

BH2#17 at −60.54 m

BH2#18 at −40.06 m

Figure D.2: Tilt curves at BH2.

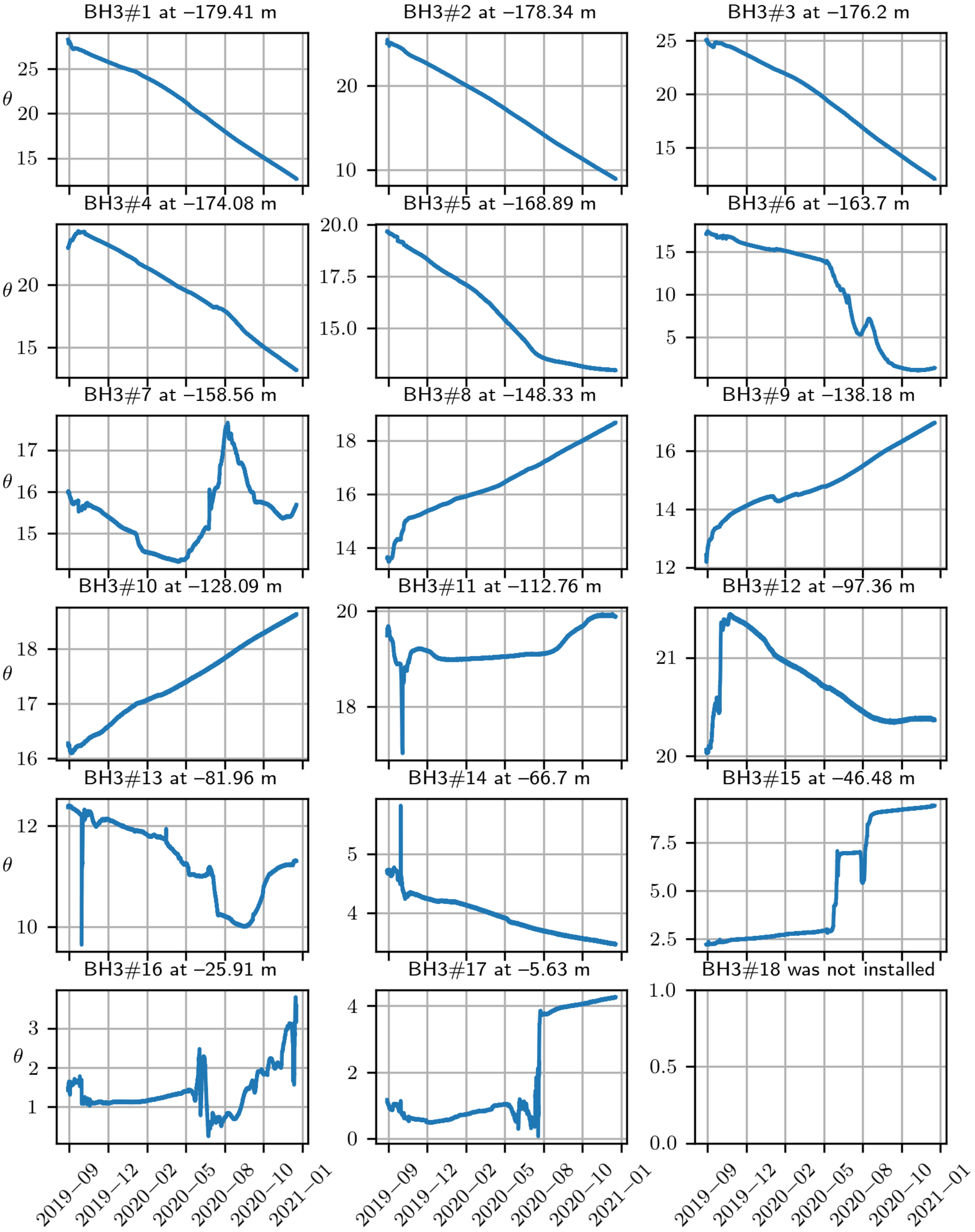

Figure D.3: Tilt curves at BH3.

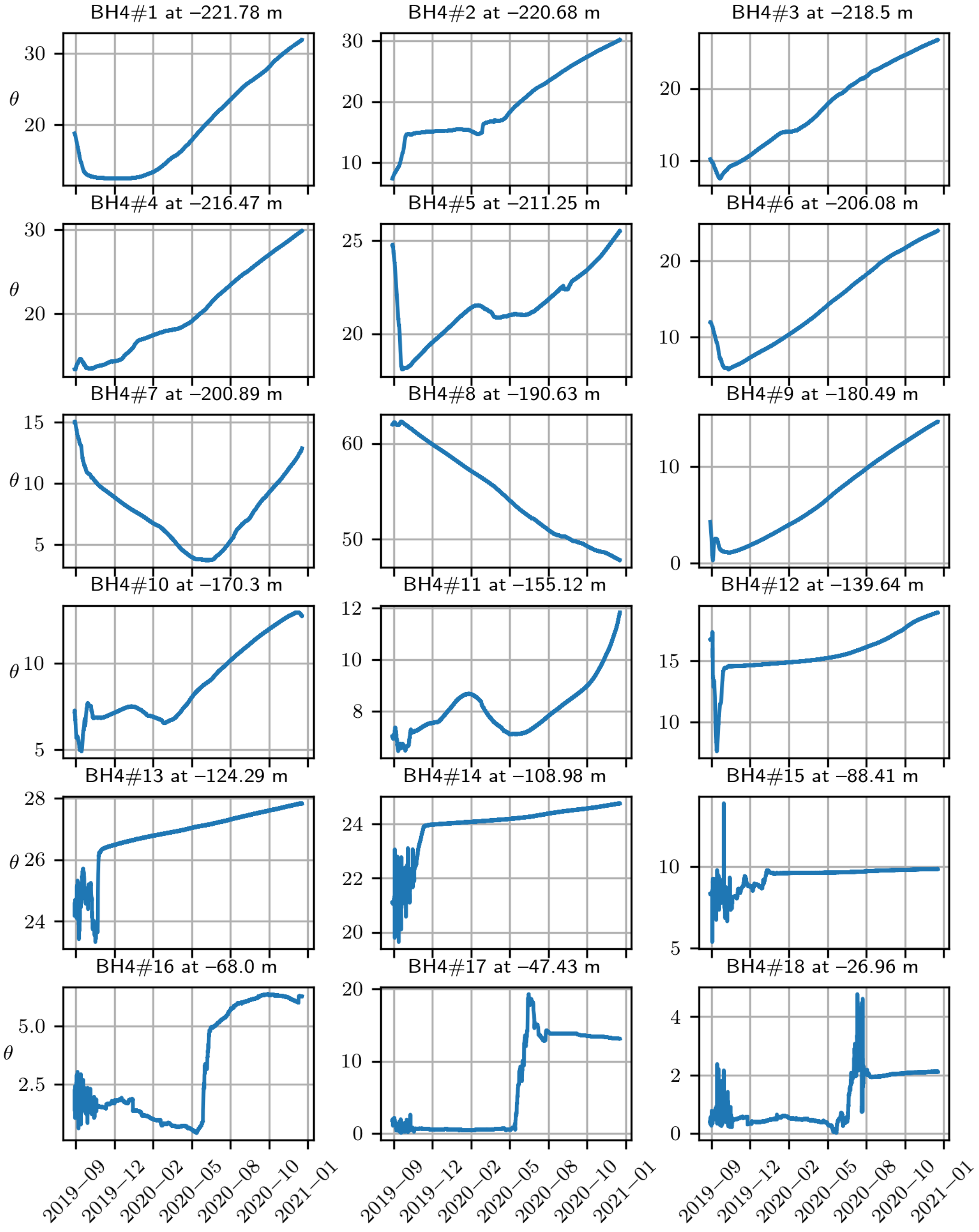

Figure D.4: Tilt curves at BH4.

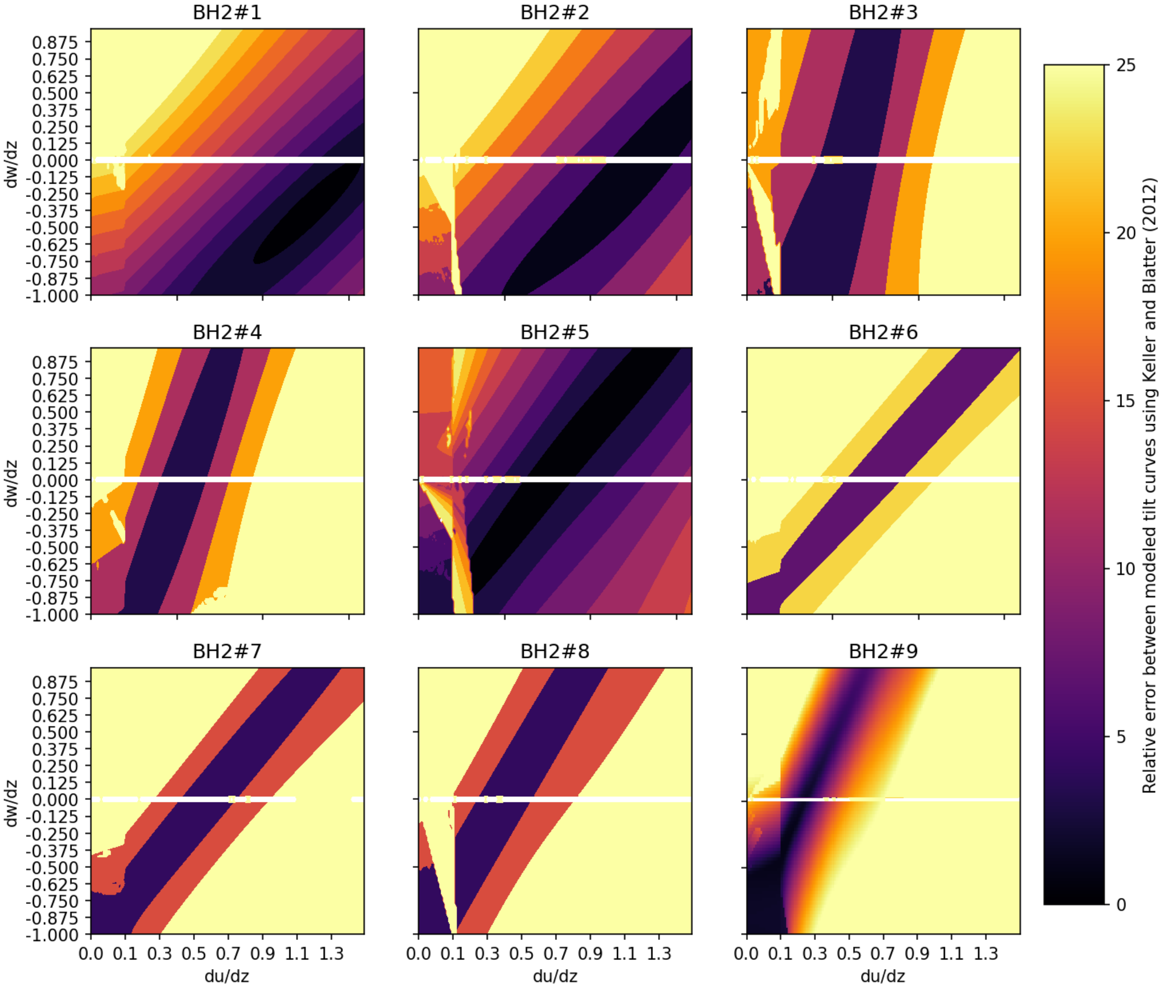

Figure D.5: Relative error of the reproduced tilt curves using Keller and Blatter (2012) for different du/dz and dw/dz on the BH2#1 to BH2#9 tilt curves.

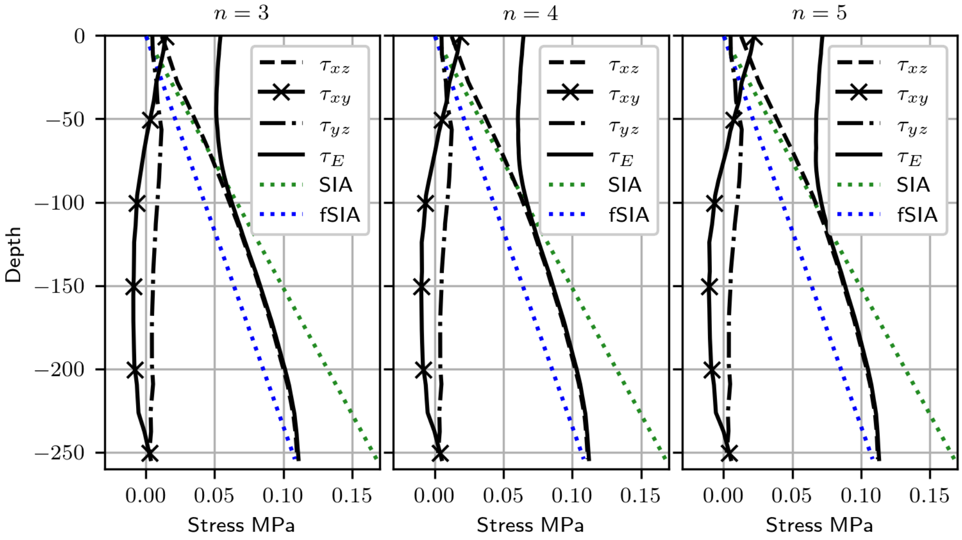

Figure D.6: Stress plots for the constant A simulations.

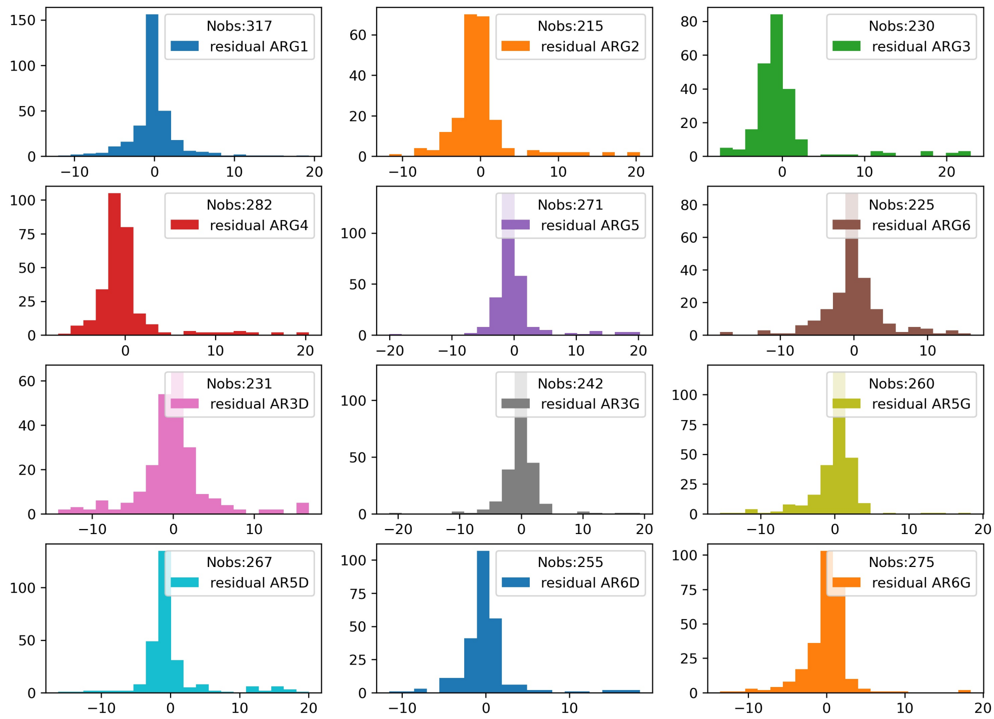

Figure D.7: Residuals between daily measured and reconstructed surface velocities at Glacier d'Argentière over 2020, once outliers (points with residuals greater than 3 standard deviations of the residuals) have been removed.

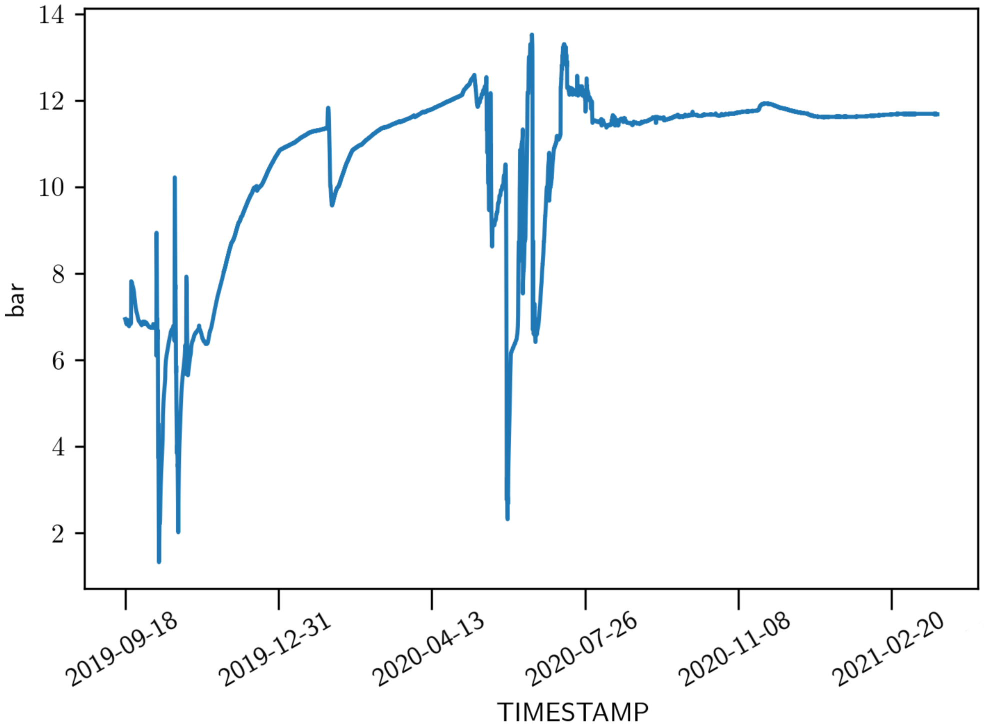

Figure D.8: Pressure recorded at the piezometer installed in BH2, approximately 15 m from the bed.

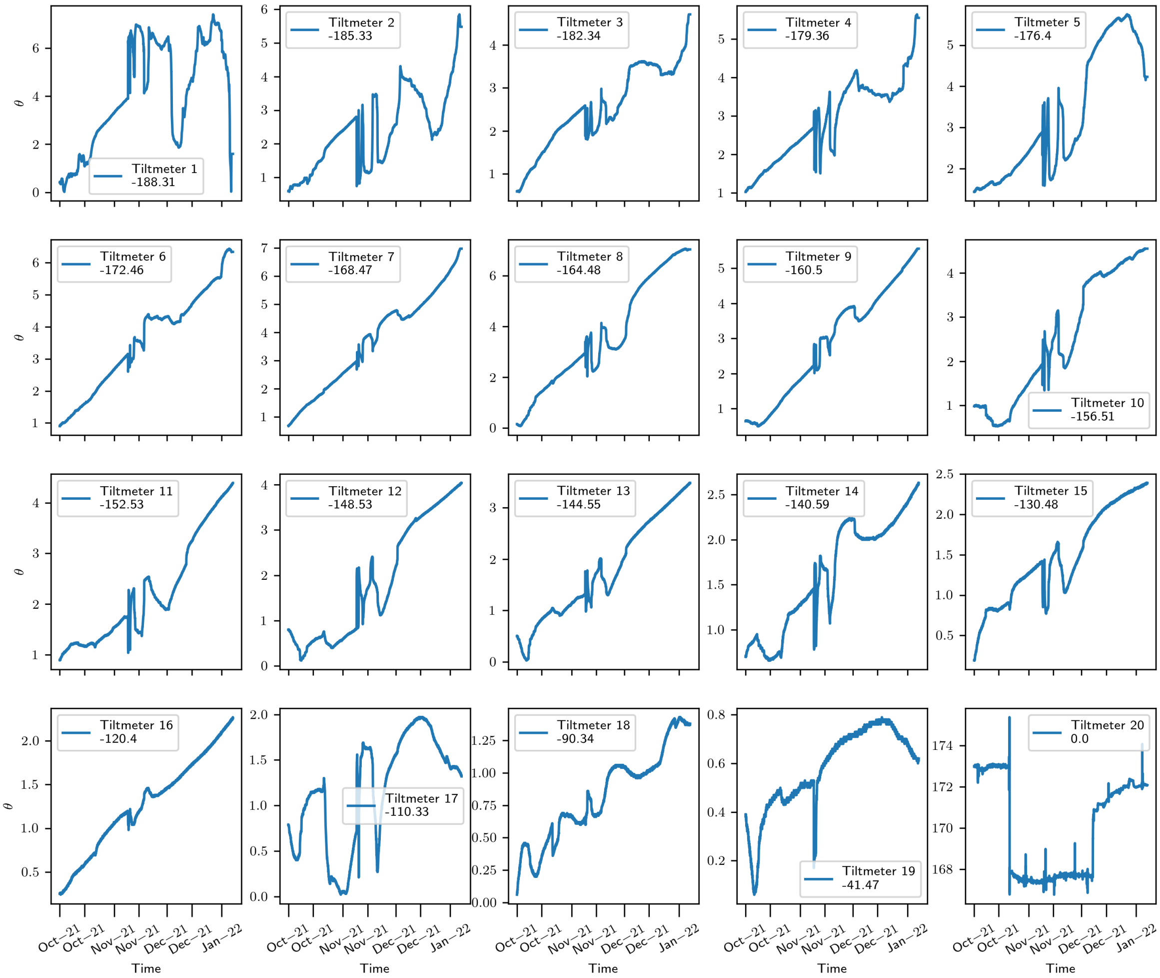

Figure D.9: Tilt curves at BH11. Note that the timeseries ends in January 2022.

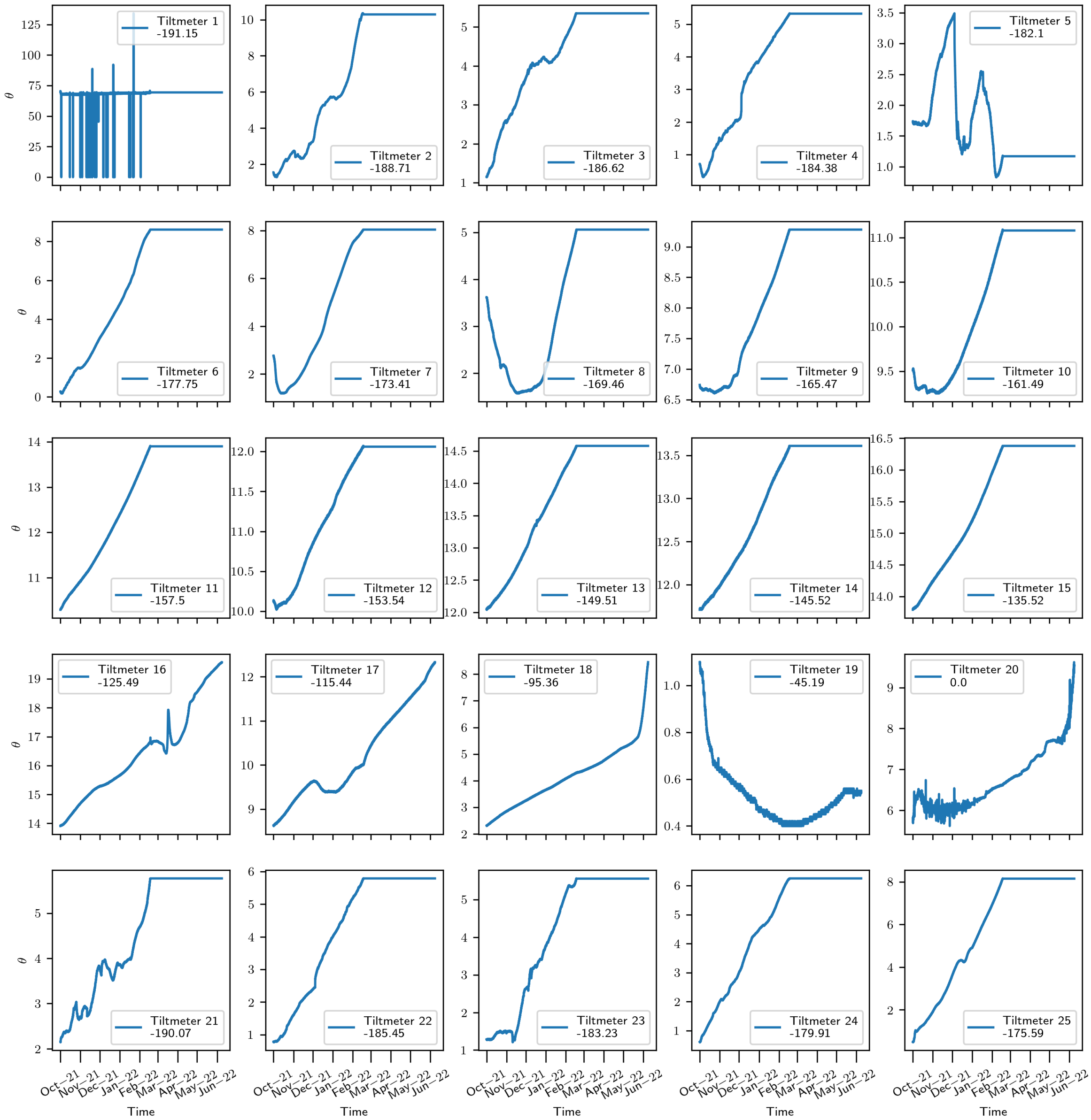

Figure D.10: Tilt curves at BH12. Note that tiltmeters BH12#21 to BH12#25 are located between BH12#1 and BH12#7.

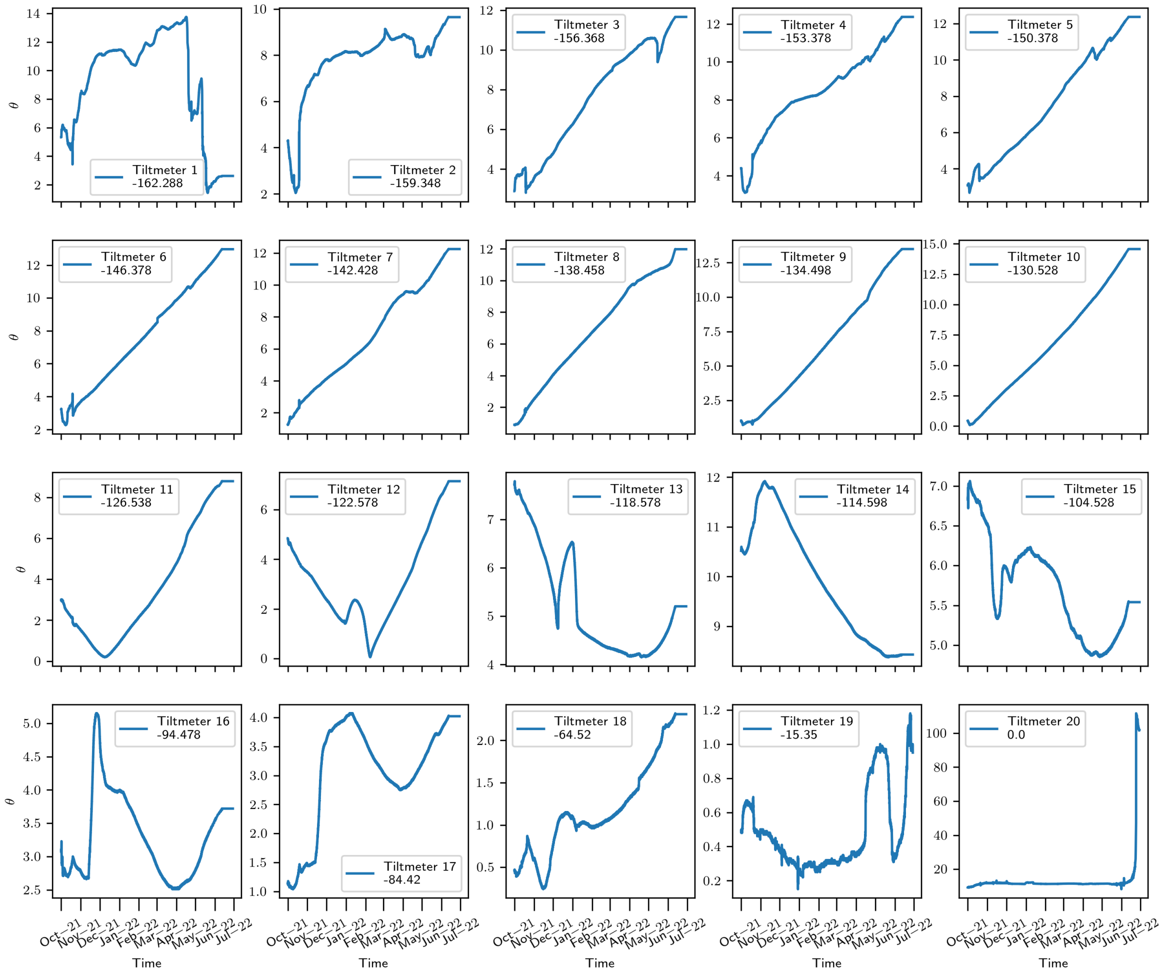

Figure D.11: Tilt curves at BH14.

ANNEX E

Supplementary Materials of Chapter 3

This supporting information contains

1. A plot of the sensitivity of ub/τ_b^n given in Eqn. (3.25) to T for several roughness, Figure E.1.
2. The numerical friction laws for $r = 0.03$ and $r = 0.08$, Figures E.2 and E.3.
3. The plots of the normalized scaling parameters $C_f^{\mathrm{num}}/C^{\mathrm{num}}$ and $A_f^{\mathrm{num}}/A^{\mathrm{num}_s}$, Figure E.4.
4. Plots of the normalized shear stress at the base ($\sigma_{nt}(x)/\tau_f$) for the three sets of simulations presented in section 3.3, Figures E.5 to E.7.

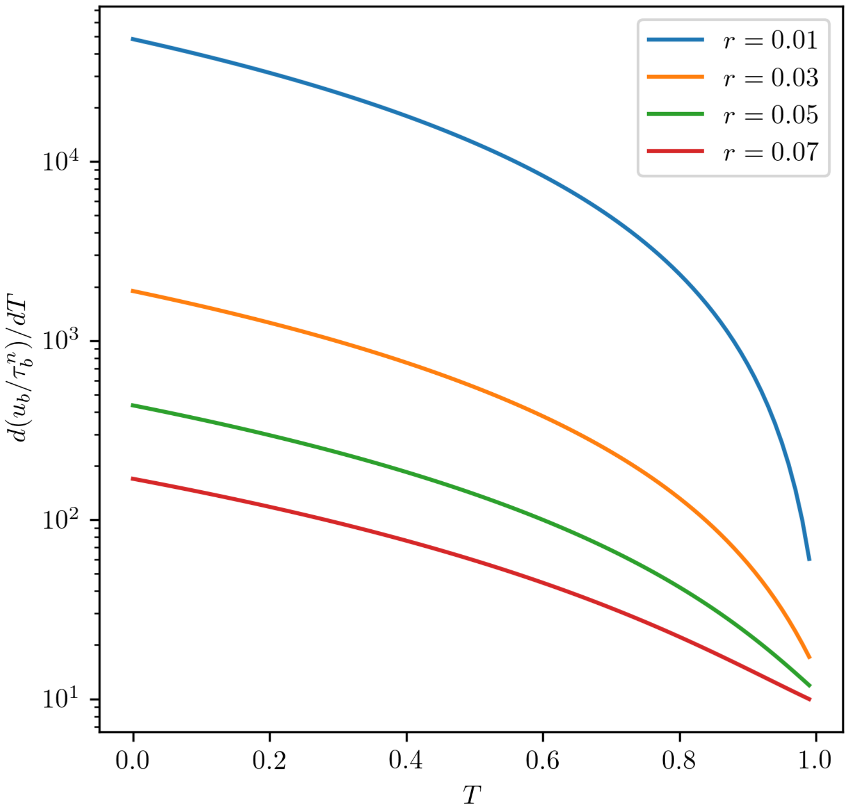

Figure E.1: Sensitivity of u_b/τ_b^n to T for several values of r for $n = 3$. The sensitivity is computed as $d(u_b/\tau_b^n)/d(T)$, starting from Eqn. (27), with $A = 1$ and the roughness values as given in the legend.

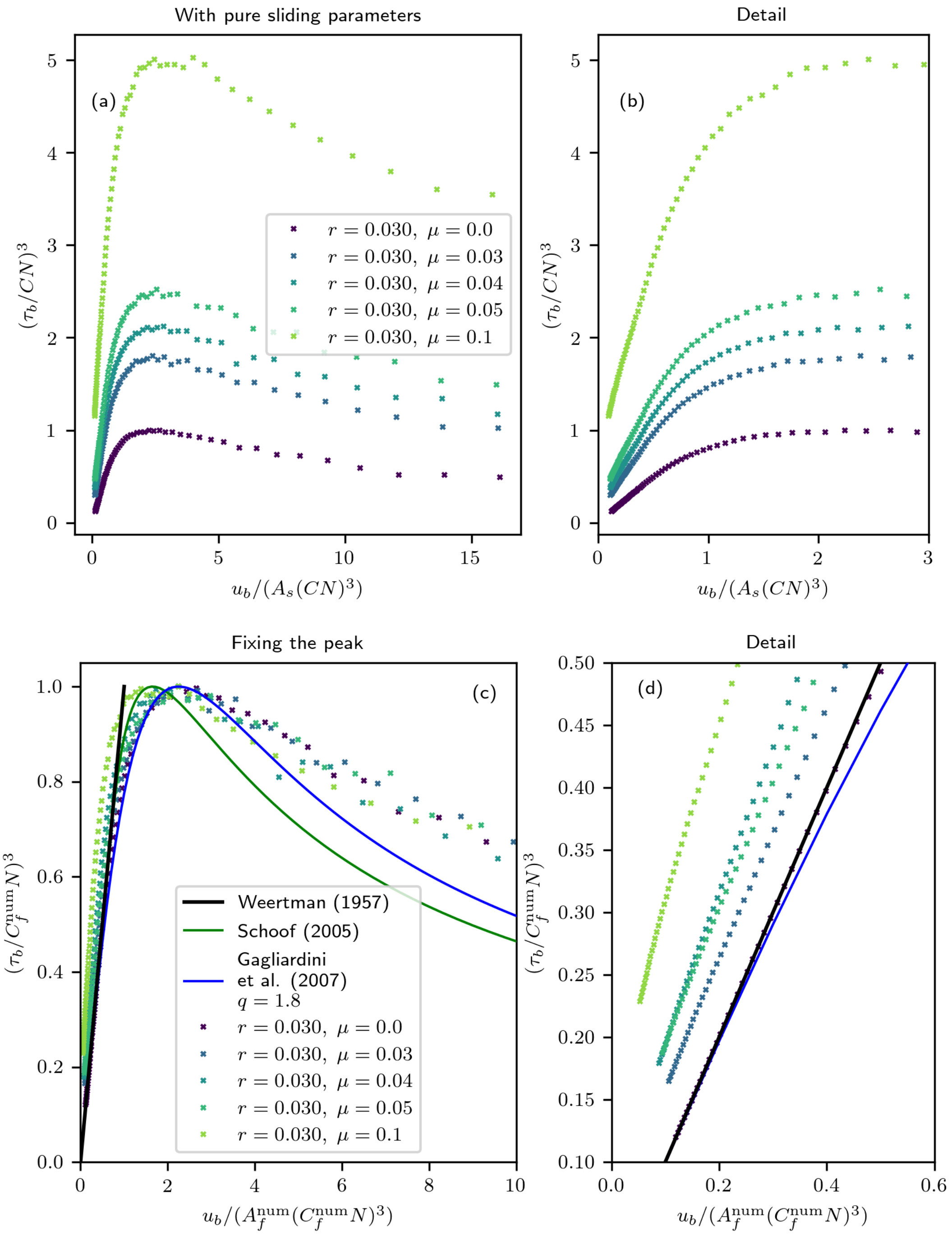
With pure sliding parameters

Detail

Fixing the peak

Detail

Figure E.2: Comparison of the friction laws obtained numerically for a sinusoidal bed of roughness $r = 0.03$ and different values of μ, using ((a) and (b)) C and A_s as scaling parameters and ((c) and (d)) C_f^{num} and A_f^{num} as scaling parameters. Panels (b) and (d) are limited to the rate-strengthening part of the curves shown in (a) and (c), respectively. Symbols represent the numerical results and the curves show the Weertman (Eqn. (1)), Schoof (2005) and Gagliardini et al. (2007) (Eqn. (2)) solutions.

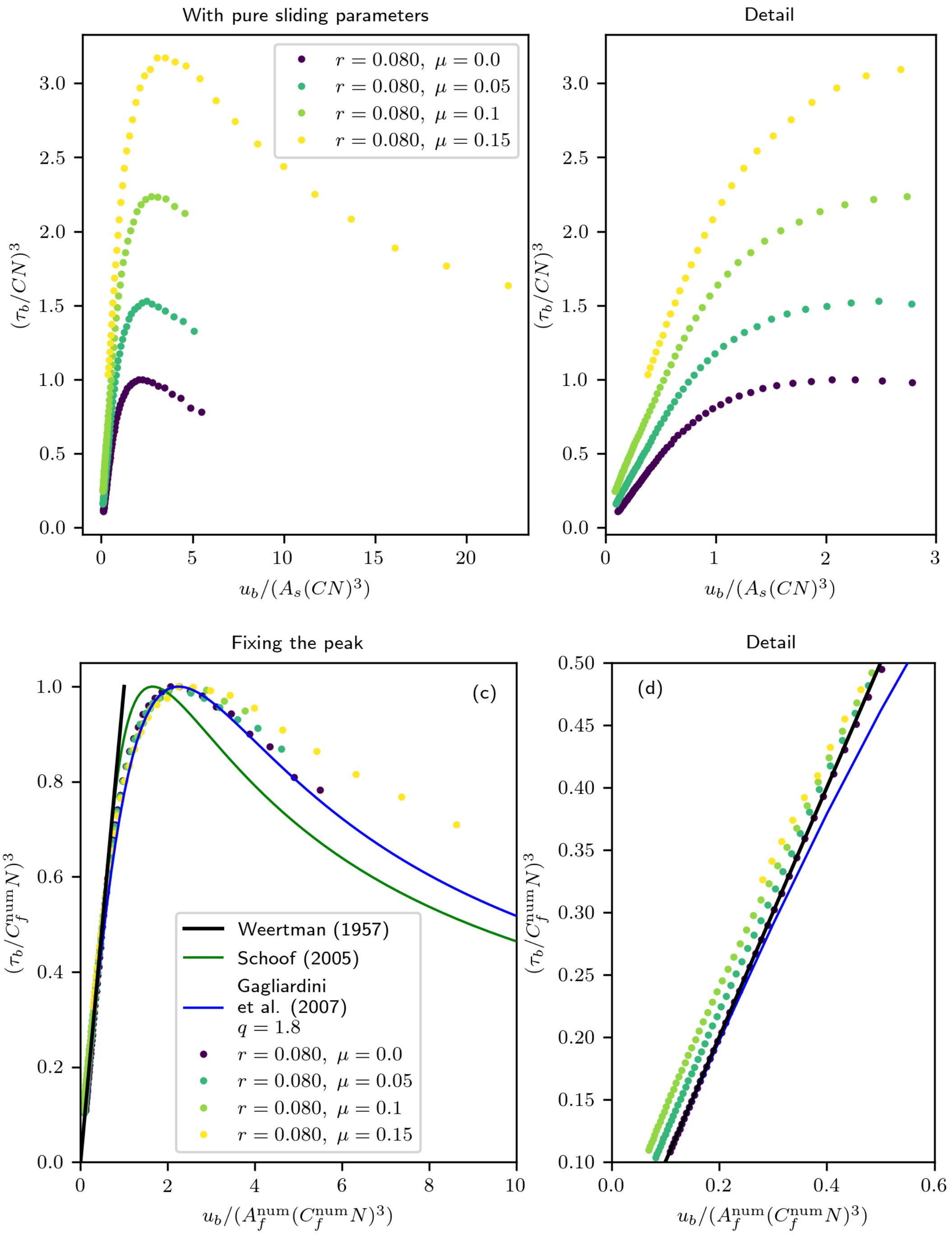

Figure E.3: Comparison of the friction laws obtained numerically for a sinusoidal bed of roughness $r = 0.08$ and different values of μ, using ((a) and (b)) C and A_s as scaling parameters and ((c) and (d)) C_f^{num} and A_f^{num} as scaling parameters. Panels (b) and (d) are limited to the rate-strengthening part of the curves shown in (a) and (c), respectively. Symbols represent the numerical results and the curves show the Weertman (Eqn. (1)), Schoof (2005) and Gagliardini et al. (2007) (Eqn. (2)) solutions.

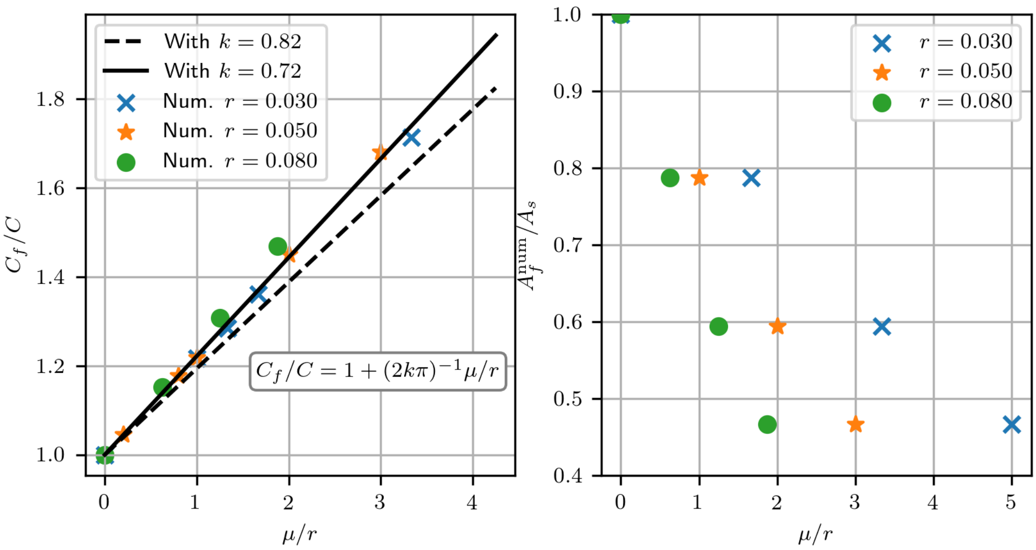

Figure E.4: Normalized scaling parameters $C_f^{\mathrm{num}}/C^{\mathrm{num}}$ and A_f^{num}/A_s, from the numerical simulations with Coulomb shear stress at the bed.

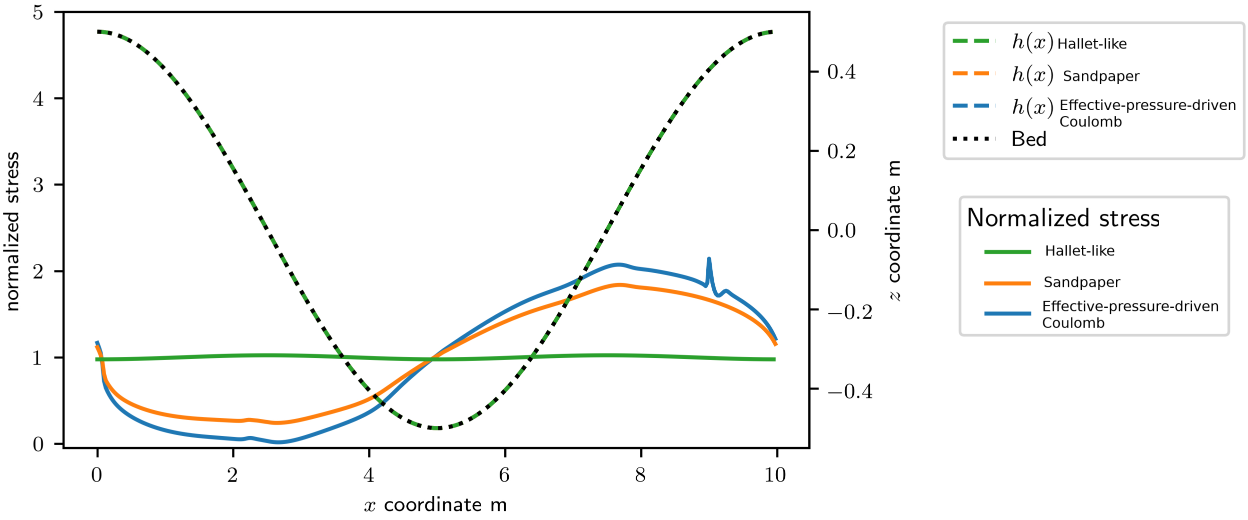

Figure E.5: Normalized shear stress $\sigma_{nt}(x)/\tau_f$ (solid lines), cavity roof height $h(x)$ (i.e. ice-bed-cavity interface, dashed lines), and bed (black dotted curve) for the three different local shear stress models discussed, corresponding to the rate strengthening regime with no cavity.

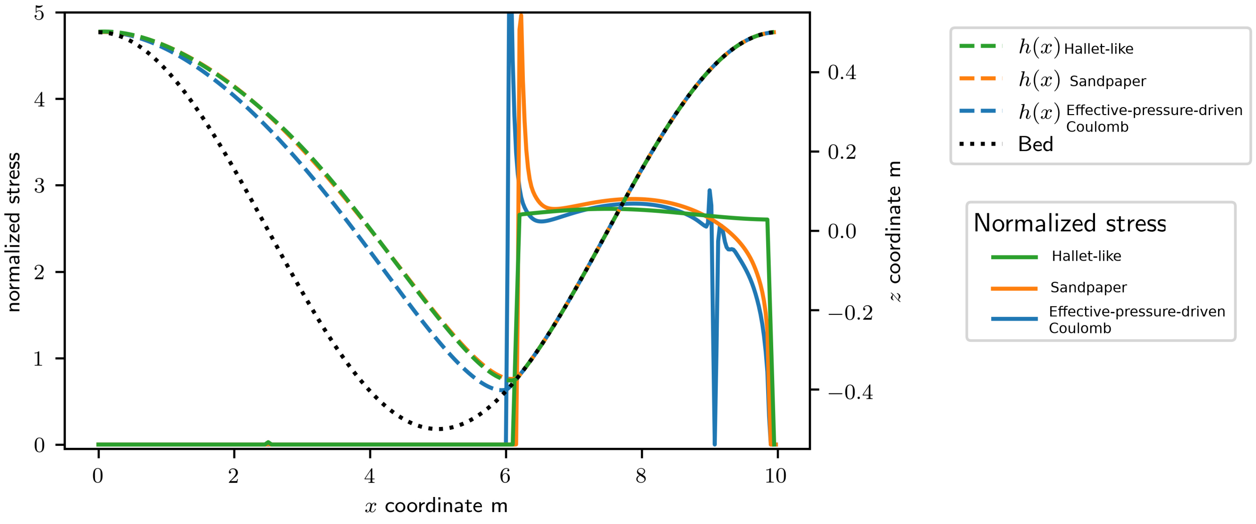

Figure E.6: Normalized shear stress $\sigma_{nt}(x)/\tau_f$ (solid lines), cavity roof height $h(x)$ (i.e. ice-bed-cavity interface, dashed lines), and bed (black dotted curve) for the three different local shear stress models discussed, corresponding to the rate strengthening regime with cavity. There is an open cavity in those points where $h(x)$ is different than the bed. The space between them is the cavity size.

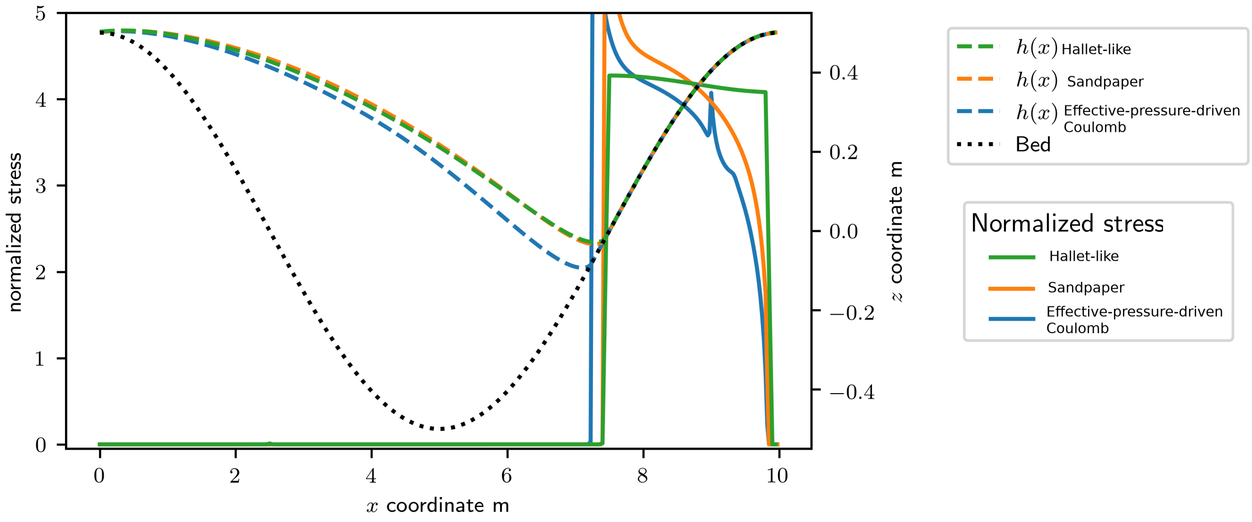

Figure E.7: Normalized shear stress $\sigma_{nt}(x)/\tau_f$ (solid lines), cavity roof height $h(x)$ (i.e. ice-bed-cavity interface, dashed lines), and bed (black dotted line) for the three different local shear stress models discussed, corresponding to the rate weakening regime. There is an open cavity in those points where $h(x)$ is different than the bed. The space between them is the cavity size.

ANNEX F

Original and English translation of ’Glissement et hydraulique sousglaciares’ by Louis Lliboutry

This Annex presents the original version of ’Glissement et hydraulique sousglaciares’ by Louis Lliboutry in 2005, later scanned by Olivier Gagliardini, and presented in Chapter 4. We add the english translation later.

dernière publi 2002

S.H.F. Section de Glacologie-Nivologie. Réunion du 10 Mars 2005

Glissement et hydraulique sous-glaciaires

Louis LLIBOUTRY
3, Av. de la Foy, Corenc, 38700 La Tronche

Ces trois dernières années mon activité intellectuelle a concerné le glissement des glaciers tempérés et l'écoulement sous-glaciaire de l'eau. J'ai élaboré une théorie dont je ne peux donner ici qu'un aperçu bref et incomplet. Elle est exposée dans trois articles que je suis en train de terminer et que je soumettrai au *Journal of Glaciology.*

La théorie est nécessaire pour guider les mesures sur le terrain et les interpréter. Mais, bien que dans ce domaine les observations, mesures et enregistrements se soient multiplié depuis 30 ans, surtout sur les glaciers à surges, on en est resté aux théories grossières, incomplètes et erronées émises dans les années 60 par Weertman, moi-même, Nye, Röthlisberger et Budd, qui n'ont plus qu'in intérêt historique. Elles ignorent en particulier que la pression de l'eau sous-glaciaire varie continuellement et n'est pas uniforme sous tout le glacier.

1. Loi de frottement

Je ne considère pas les lits constitués entèrement de sédiments, qui sont parfaitement aplanis. Les obstacles causant un frottement sont schématisés par de grosses bosses hémisphériques toutes de même taille (rayon)R (dans mes calculs $R = 1{,}5$ m), parfaitement lisses ainsi que la surface les supportant. Cela évite de considérer la microrugosié, et les phénomènes complexes de fonte et regel à la base (Lliboutry, *J. Glaciol.* n° 131, 1993). La surface supportant les bosses étant concave, au centre le lit peut être *inondé, swamped*, (l'eau ne baignant que le bas des bosses), ou *noyé, drowned*, (les bosses étant entièrement recouvertes d'eau et le frottement nul). Seul ce dernier cas rend compte du grand stockage temporaire d'eau souvent observé.

On considère le frottement à une *échelle locale*, intermédiaire entre l'*échelle globale* utilisée pour traiter la mécanique du glacier et l'*échelle du microrelief* utilisée pour l'étude des cavités sur les faces aval des bosses. Contrairement à mon idée ancienne, adoptée par tous aujourd'hui, le frottement dû aux bosses avec cavités "autonomes", non connectées entre elles, n'est pas négligeable. On peut définir une fraction de bosses connectées c (*connection ratio*), qui croît avec la longueur des cavités, mais n'est pas nulle en l'absence de cavités connectées (lit *moist, humide*, si les connexions sont à une pression supérieure à l'atmosphérique, lit *sec*, *dry*, si les connexions sont vides d'eau et à la pression atmosphérique).

J'appelle *rugosité* $r = (\pi R^2/2) \times$ (nombre d'hémisphères par unité d'aire) (dans mes calculs $r = 1/15$), et *pression effective* N = (pression de l'eau dans les cavités connectées) – (pression de la glace, à l'échelle locale). Avec une solution approchée pour les contraintes à l'échelle du microrelief, on obtient comme loi de frottement à l'échelle locale, pour *tout lit non inondé* :

$$U = B_1 R \left(\frac{T/r - cN}{2 - c} \right)^3 \tag{1}$$

U = vitesse de glissement ; T = frottement ; $B_1 = B/80$, la loi relation liant le taux de déformation efficace $\gamma = 2\varepsilon$ à la cission efficace τ étant pour la glace $\gamma = B\,\tau^3$. Dans mes calculs $B = 0{,}44$ bar^{-3} an^{-1}.

2. Hypercavitation

Soit L la longueur d'une cavité aval (distance du pôle aval de la bosse au point le plus éloigné de sa cavité aval). Lorsque la cavitation est intense, toutes les cavités communiquent entre elles librement, et il n'y a plus de cavités autonomes. J'appelle cet état *hypercavitation.* On schématise en admettant que l'hypercavitation apparaît pour une longueur L_M bien nette (dans mes calculs, $L_M = 3{,}854\, R$). Cela permet de définir une longueur réduite $l = L/L_M$. J'admets, à l'échelle locale, la loi :

$$c = c_0 + (1 - c_0)\,l \tag{2}$$

(Pour les calculs j'ai pris $c_0 = 0{,}5$). La loi de frottement locale devient $U = U(T,l,N)$ et non pas $U(T,N)$ comme admis jusqu'ici. On peut expliquer les très grandes vitesses observées en haut des Séracs du Géant et lieux similaires avec T de l'ordre de 2 bars, un lit hypercavitant et sec, bien que N soit loin d'être nul.

Dans un glacier de vallée N s'annule aux bords, et il y a donc toujours le long de chaque rive une bande hypercavitante sèche. En période de fonte courent à leur limite inférieure, à l'air libre, deux *torrents sous-glaciaire marginaux.* C'est vers eux que s'écoulent dans un premier temps l'eau s'engouffrant dans les moulins. Les torrents marginaux sont aussi alimentés par la fonte de neige hivernale subsistant hors du glacier. Le torrent sous-glaciaire central, celui capturé pour l'hydro-électricité, ne doit pas exister en zone d'accumulation.

Il y a aussi, mais pas toujours, ou au moins pas de façon permanente, hypercavitation dans une bande centrale inondée ou noyée, pas à la pression atmosphérique. Le torrent central sous-glaciaire s'écoule par toute cette bande. On est très loin du conduit à section transversale plus ou moins semi-circulaire type glacier du Gorner étudié par Röthlisberger et appelé de ce fait R-channel. La loi semi-empirique liant le débit du torrent sous-glaciaire à l'aire de la section transversale du conduit doit être modifiée.

3. Perméabilité sous-glaciaire

L'interface glacier-lit n'est ni parfaitement étanche comme l'a affirmé Weertman, ni, comme je l'ai supposé dans le temps, suffisamment pourvue de connections pour donner, en l'absence d'hypercavitation, libre passage à l'eau. Lorsque l'eau n'est pas à la pression atmosphérique, bien que son gradient hydraulique soit discontinu à l'échelle du microrelief, on peut le considérer comme continu à l'échelle locale et admettre une loi de type Darcy : les flux d'eau parallèle ($\varphi_{\parallel}$) et perpendiculaire ($\varphi_{\perp}$) à l'axe du glacier sont proportionnels aux dérivées de la charge hydraulique Z. En appelant s la coordonnée transversale le long du lit (pas la coordonnée cartésienne) :

$$\varphi_{\parallel} = -K_{\parallel}\frac{\partial Z}{\partial x}, \qquad \varphi_{\perp} = -K_{\perp}\frac{\partial Z}{\partial s} \tag{3}$$

Les perméabilités sous-glaciaires $\kappa_{\parallel}$ et $\kappa_{\perp}$ sont différentes et inconnues. Dans les calculs j'ai pris $\kappa_{\perp} = 1{,}1 \times 10^{-5}$ m^2 s^{-1} = 347 m^2 an^{-1}, ce qui est 0,275 fois celle donnée par Fountain (1994) pour le South Cascade Glacier où il y a une couche sédimentaire continue. Le volume d'eau stockée dans une cavité étant à peu près $\pi R^2 L/3$, la quantité d'eau stockée par unité d'aire de lit est :

$$W = \frac{2}{3} c r L = \frac{2}{3} r m R \left[c_0 l + (1-c_0) l^2\right] \tag{4}$$

Elle varie peu avec x, et l'on peut écrire la conservation de l'eau pour le flux sous-glaciaire transversal :

$$\frac{\partial W}{\partial t} + \frac{\partial \varphi_{\perp}}{\partial s} = 0 \tag{5}$$

En introduisant la coordonnée réduite $S = s/s_1$ (s_1 étant la demi-longueur du lit du glacier dans une section transversale) on aboutit à :

$$\frac{\partial^2 Z}{\partial s^2} = E\left[c_0 + 2(1-c_0) l\right]\frac{\partial l}{\partial t}$$

$$E = \frac{2 r m R s_1^2}{3 K_{\perp}} \quad = 100 \text{ m an dans mes calculs} \tag{6}$$

4. Problème mathématique déduit du modèle physique

Comme c se déduit directement de l par (2) et N de Z, il y a 4 variables principales dont il faut étudier la répartition selon S et l'évolution au cours du temps : U, T, l, Z. Or nous ne disposons que des deux équations (1) et (6). Une troisième équation résulte de la déformation plastique de la cavité, qui s'oppse à son ouverture causée par le glissement. Avec une solution approchée on trouve :

$$\frac{\partial l}{\partial t} = \frac{3}{2mR}\left[U - B_1 R\,(1+ml)\,N^3\right] \tag{7}$$

équation valable si $0 < l < 1$: lit cavitant sec, ou avec cavités connectées pleines d'eau, appelé lit *mouillé (wet).*

La quatrième relation provient du fait que T et U sont des composantes des champs de contraintes et de vitesses dans tout le corps du glacier. Il n'est donc pas possible de scinder le problème de l'écoulement d'un glacier tempéré en deux problèmes indépendants, (1) loi de frottement établie à l'échelle locale, (2) déformation du glacier à l'échelle globale, avec cette loi de frottement comme condition à la limite inférieure. (Jusqu'ici c'est ce qu'on fait tous les théoriciens). Calculer ces champs à chaque pas de temps et, pour un pas de temps, à chaque approximation successive de l et Z serait d'une longueur prohibitive. Heureusement pour un glacier cylindrique avec toutes les vitesses parallèles (seul cas étudié), on peut trouver de bonnes approximations de $T(|S|)$ et de $U(|S|)$ sous forme de polynômes du 4e degré, ne dépendant que de deux paramètres : $T(0) = T_0$ et $T(1) = T_1$. Expliquer comment on les détermine serait trop long pour être fait ici. Disons seulement que pour l et Z connus en 5 *points d'ajustement* régulièrement répartis sur le demi-profil transversal du lit, il y a toujours une solution et une seule à ce problème mathématique.

Lorsque l et $\partial l/\partial t$ à chaque S sont connus, (6) donne $Z(S)$ par deux ingégrations successives, si l'on a des conditions aux limites. On admet que $Z(0)$, la charge hydraulique dans le torrent sous-glacaire central, est une fonction donnée du temps, à périodicité annuelle (la périodicité diurne n'est introduite que dans mon 3e article, dont je ne parlerai pas ici). En période de fonte, l'autre limite $(S_{w/hc})$ est là où coule le torrent marginal, qui alimente en eau les cavités sous-glaciaires (surtout au début de la fonte). Sa position peut être calculée directement à partir de $T(S)$ .et d'une approximation antérieure de $Z(S)$. La condition à cette limite est alors Z = altitude du lit, connue. Sans fonte, cette limite est toujours là où Z atteint l'altitude du lit et la pression de l'eau connectée devient atmosphérique, mais, aucune eau ne pouvant parvenir de plus haut et de la bande cavitante sèche, la condition à cette limite $(S_{w/c})$ est alors $\partial Z/\partial S = 0$.

Le fait que $Z(0)$ ait une périodicité annuelle n'entraîne pas obligatoirement que les autres variables sous-glaciaires aient une périodicité annuelle, même en supposant que les épaissurs du glacier ne varient pas. En particulier il peut exister une bande centrale inondée dont la largeur maximale annuelle croît d'année en année jusqu'à provoquer un *surge*. Cette voie de recherche prometteuse na pas été explorée. Je n'ai traité dans le 2e article qu'un exemple où il n'y a jamais de bande centrale inondée.

Probablement en cas de périodicité annuelle, en adoptant au départ des valeurs cohérentes entre elles mais arbitraires, et en simulant l'évolution pour un grand nombre d'années successives, on finirait par atteindre ce régime périodique. Mais ce serait extrêmement long, et il est préférable de procéder par essais et erreurs.

5. Solution numérique du problème mathématique

J'ai adopté un pas de temps de 1/60 d'année et un pas en S de 1/12. Un pas en S plus fin, pour des variables locales, n'aurait guère de sens physique. Toutefois $S_{w/hc}$ ou $S_{w/c}$, auxquels la solution est très sensible, on été calculés avec bien plus de précision, et les valeurs en ces points obtenues par interpolation. Un nœud du réseau est défini par i (temps, avec $i = 0$ le 1er Janvier), et $j = 12 \;|S|$. Le calcul est fait pour des i successifs, à partir de $i = 15$ où commence la fonte. En $i = 15$ comme en $i = 40$ (fin de la fonte), les 2_{ij} et T_{ij} ont des changements brusques par suite du changement dans la condition à une limite signalé, alors que les l_{ij} sont continus. A chaque i donné on améliore successivement :

—T, avec les approximations polynomiales, et, en période de fonte, $S_{w/hc}$;

— l , avec (7), et lorsqu'il y a une bande humide centrale, sa limite $S_{m/w}$:

— Z, avec (6), et en période sans fonte $S_{w/c}$.

On recommence plusieurs fois cette boucle, jusqu'à ce que les changements soient insignifiants. Toutefois en période sans fonte, la condition $\partial Z/\partial S = 0$ rend l'algorithme divergent. On obtient la convergence en moyennant les nouvelles valeurs de T et de $\partial^2 Z/\partial S^2$ avec les valeurs respectives précédentes.

Le modèle de glacier adopté est cylindrique. Sa section transversale a un profil du lit parabolique, une surface horizontale large de 640 m, une épaissur maximale, au centre, de 160 m. La pente longitudinale de la surface est telle que le frottement moyen soit 0,8 bar.Z_{i0}, une donnée, est représenté ci-dessous.

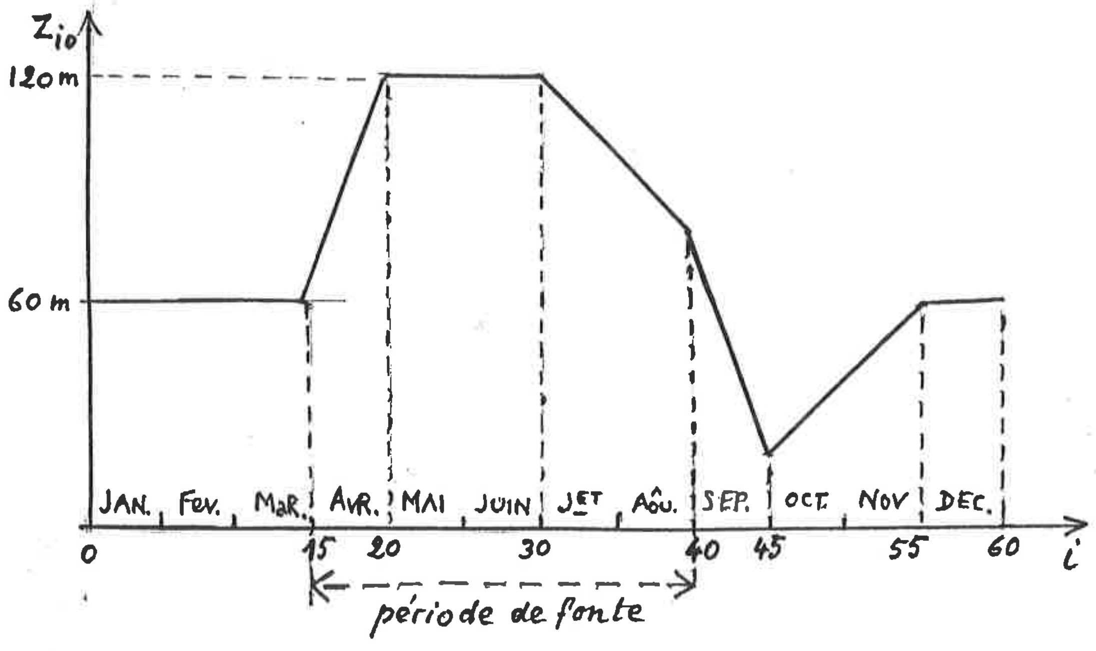

Vers la fin de la longue saison sans fonte tout lit mouillé, à cavités connectées pleines d'eau, à eu le temps de disparaître. Le lit est humide jusqu'en $j = 6$, et sec, sans cavités connectées en $j = 7$ et 8. Mais des cavités vides continuent à se refermer lentement en $j = 9$ et 10. On passe de $l_{40,9} = 0{,}29$ et $l_{40,10} = 0{,}69$ au début de la période sans fonte à $l_{15,9} = 0{,}13$ et $l_{15,10} = 0{,}64$ à sa fin. A noter que si l'on admettait $\partial l / / \partial t = 0$, on trouverait $l_{15,9} = 0$ et $l_{15,10} = 0{,}133$, ce qui montre l'erreur commise en supposant un régime hydraulique stationnaire pour calculer des moyennes annuelles.

Dans le modèle traité, sans bande inondée et avec un frottement modéré, les vitesses de glissement sont faibles. Dans la région centrale environ 0,74 cm par jour en hiver et 1,95 cm par jour, le maximum, au début de Juillet, lorsque N est le plus faible et l encore très petit. Si l'on veut étudier les fluctuations saisonnières de vitesse sur un tel glacier sans pouvoir accéder au lit, il faut relever les positions de balises à deux semaines d'intervalle tout au début de l'été.

En conclusion, cette étude montre que :
— Un modèle réaliste, tenant compte de toutes les lois de la Mécanique et de la Physique, peut être établi. Les glaciologues ne doivent pas se contenter de chercher de simples corrélations.
— Il reste un travail de calcul numérique considérable à faire. Je le laisse à de plus jeunes chercheurs, non rebutés par le fait que le thème ne soit pas à la mode.

F.2 Subglacial sliding and hydraulics

S.H.F. Section de Glaciologie-Nivologie meeting. 10th March 2005.

Subglacial sliding and hydraulics

Louis LLIBOUTRY

During the last three years, my intellectual activity has concerned the sliding of temperate glaciers and the flow of subglacial water. I have developed a theory of which I can but give here a brief and incomplete sketch. It will be explained in three articles that I am finishing and that I will submit to *Journal of Glaciology*.

Theory is necessary in order to guide and interpret field measurements. However, while in our domain observations, measurements and registers have multiplied for the last 30 years, specially regarding glacier surges, we remain captive to the crude, incomplete, and erroneous theories developed in the 60s by Weertman, myself, Nye, Röthlisberger, and Budd, which should only be of a historical interest today. They ignore, in particular, that subglacial water pressure varies continuously and is not uniform underneath the glacier.

F.2.1 Friction law

I do not consider the beds made completely off sediments, which are perfectly flat. The obstacles that create friction are schematized by big semispherical bumps of the same size (radius) R (in my calculations, $R = 1.5$ m), perfectly smooth like the surface that supports them. This keeps us from considering microroughness, and the complex phenomena of melting and refreezing at the base (Lliboutry, J. Glaciol. n°131, 1993)[1]. The surface that supports the bumps is concave, at its center the bed can be *swamped*[2] (water touches the lower part of the bumps), or *drowned*[1], (the bumps are completely underwater and there is no drag). Only this last case explains the great temporal water storage that is often observed.

We consider friction at a *local scale*, in between the *global scale* used for treating glacier mechanics and the *microroughness scale* used for studying cavities at the lee side of the bumps. Contrary to my old idea, adopted by everybody nowadays, drag due to "autonomous" cavities, not connected between them, is not negligible. We can define a fraction of connected cavities c (*connection ratio*[1]), that grows with cavity length, but is not zero in the absence of connected cavities (*moist*[1] bed, if all connexions are at higher-than-atmospheric pressure, *dry*[1] bed if cavities are free of water and at atmospheric pressure).

I call *roughness* $r = (\pi R^2/2)\times$ (number of semispheres per unit area) (in my calculations, $r = 1/15$), and *effective pressure* $N =$(water pressure inside connected cavities) - (ice pressure, at local scale). With an approximation of the stress at the microroughness scale, we obtain as friction law at the local scale, for *every not swamped bed*:

$$U = B_1 R\left(\frac{T/r - cN}{2 - c}\right)^3 \tag{F.1}$$

$U =$ sliding speed; $T =$ drag; $B_1 = B/80$, with the relation linking effective deformation rates $\dot{\gamma} = 2\dot{\varepsilon}$ to effective shear τ being for ice $\dot{\gamma} = B\tau^3$(see footnote [3]). In my calculations, $B = 0.44$ $\text{bar}^{-3}\text{a}^{-1.}$

---

[1] TN: Lliboutry, L. (1993). Internal melting and ice accretion at the bottom of temperate glaciers. Journal of Glaciology, 39(131), 50-64, doi:`https://doi.org/10.3189/S0022143000015719`

[2] TN: this and all terms in italics marked with a [1] appear in english in the original text.

[3] TN: the dot over $\dot{\gamma}$ and $\dot{\varepsilon}$ is missing in the original text.

F.2.2 Hypercavitation

Given L the length of a cavity dowstream (distance from the downstream pole of the bump to the farthest point of the cavity at its downstream point). Once cavitation is intense, all cavities freely communicate with each other and there are no more autonomous cavities. I call this state *hypercavitation*. We simplify assuming that hypercavitation appears for a very specific length L_M (in my calculations, $L_M = 3.854R$). This allows to define a reduced length $l = L/L_M$. I admit, at the local scale, the law:

$$c = c_0 + (1 - c_0)l \tag{F.2}$$

(For the calculations I took $c_0 = 0.5$). The local friction law becomes $U = U(T, l, N)$ and not $U(T, N)$ as considered until now. We can explain the very high speeds observed in the high parts of the Séracs du Géant and similar places with T of the order of 2 bars, a dry and hypercavitating bed, with N being far from zero.

In a valley glacier N becomes zero at the sides, and there is always a dry hypercavitant band at each side. During the melt season, two *subglacial marginal streams* run freely at their lower limit. Initially, the water inside the moulins drain towards them. The marginal streams are also fed by the melt of winter snow that survives outside of the glacier. The central subglacial stream, captured for hydro-electrical power, must not exist in the accumulation zone.

There is also, but not always, or at least not permanently, hypercavitation in a central, swamped or drowned band, not at atmospheric pressure. The subglacial central stream flows along this band. It is very far from the channel with an almost semicircular cross-section like the Gorner glacier studied by Röthlisberger and called R-channel after him. The semi-empirical law that links subglacial discharge to the channel's cross-section must be modified.

F.2.3 Subglacial permeability

The glacier-bed interface is not neither perfectly impervious as claimed by Weertman, nor, as I supposed over time, made of enough connections so as to freely allow, in the absence of hypercavitation, the passage of water. While water is not at the atmospheric pressure, and its hydraulic gradient is discontinuous at the microroughness scale, we can consider it continuous at the local scale and assume a Darcy type law: the flow of water parallel ($\varphi_{\|}$) and perpendicular ($\varphi_{\perp}$) to the glacier's axes are proportional to the derivative of the hydraulic charge Z. Calling s the transversal coordinate along the bed (not the cartesian coordinate):

$$\varphi_{\|} = -K_{\|}\frac{\partial Z}{\partial x}, \quad \varphi = -K_{\perp}\frac{\partial Z}{\partial s} \tag{F.3}$$

Subglacial permeabilities $K_{\|}$ and $K_{\perp}$ are different and unknown. In the calculations I have taken $K_{\perp} = 1.1 \times 10^{-5}$ m^{-2} s^{-1} $= 347$ m^2 a^{-1}, which is 0.275 times the one given by Fountain (1994) for the South Cascade Glacier where there is a continuous sedimentary layer. The volume of stored water in a cavity being approximately $\pi R^2 L/3$, the amount of water stored per unit area is

$$W = \frac{2}{3}crL = \frac{2}{3}rmR\left[c_0 l + (1 - c_0)l^2\right] \tag{F.4}$$

It varies little with x, and we can write the conservation of water for the transverse subglacial flux

$$\frac{\partial W}{\partial t} + \frac{\partial \varphi_{\perp}}{\partial s} = 0 \tag{F.5}$$

Introducing the reduced coordinate $S = s/s_1$ (s_1 being the half-length of the glacier bed over a transverse section) we arrive to:

$$\begin{aligned} \frac{\partial^2 Z}{\partial s^2} &= E\left[c_0 + 2(1-c_0)l\right]\frac{\partial l}{\partial t} \\ E &= \frac{2rmRs_1^2}{3K_\perp} = 100 \text{ m a in my calculations} \end{aligned} \tag{F.6}$$

F.2.4 Mathematical problem deduced from the physical model

Since c is directly found from l by (2) and N from Z, there are 4 main variables of which we have to study the distribution along S and the evolution over time: U, T, l, Z. We only have two equations available, (1) and (6). A third equation results from the plastic deformation of the cavity, which opposes its opening by sliding. With an approximated solution we find:

$$\frac{\partial l}{\partial t} = \frac{3}{2mR}\left[U - B_1 R(1+ml)N^3\right] \tag{F.7}$$

valid as long as $0 < l < 1$: dry bed with cavities, or with water-filled connected cavities, called *wet*[1] bed.

The fourth relationship comes from the fact that T and U are components of the stress and velocity fields over the whole glacier. It is not thus possible to cut the problem of sliding of temperate glaciers in two independent problems, (1) friction law established at the local scale, (2) deformation of the glacier at the lobal scale, with this friction law as a bottom boundary condition. (Until here, what all theoretical studies have done). Computing these fields at every timestep and, for every timestep, at every successive approximation of l and Z would be of prohibitive length. Fortunately for a cylindrical glacier with parallel velocities (only studied case), we can find good approximations of $T(|S|)$ and $U(|S|)$ of the form of 4th degree polynomials, that depend only on two parameters: $T(0) = T_0$ and $T(1) = T_1$. Explaining how we determine them would be too long to be done here. Let's only say that for l and Z known in 5 *adjustment points* regularly distributed along half a cross-section of the bed, there is always one single solution to this mathematical problem.

Whilst l and $\partial l/\partial t$ are known at every S, (6) gives $Z(S)$ after two sucessive integrations, if we give two boundary conditions. We assume that $Z(0)$, the hydraulic charge at the central subglacial stream, is a function of time, with annual periodicity (journal periodicity is introduced only in my 3rd article, of which I will not talk here). During the melt season, the other limit ($S_{w/hc}$) is there where a marginal stream flows, feeding with water the subglacial cavities (specially at the beginning of the melt season). Its position can be directly computed from $T(S)$ and from a previous approximation of $Z(S)$. The condition at this limit is thus $Z =$ bed altitude, known. Without melt, this limit is always there where Z reaches bed altitude and the pressure of the connected water becomes atmospheric, but, since no water can come from above and from the dry cavitating band, the condition at this limit ($S_{w/c}$) is then $\partial Z/\partial S = 0$.

The fact that $Z(0)$ has an annual periodicity does not necesserily mean that the other subglacial variables have an annual periodicity, even under the assumption that glacier thickness does not change. In particular there can be a central swamped band whose maximum length grows year after year until provoking a *surge*[1]. This promising research line has not been explored. I only treated in my 2nd article an example where there is never a central swamped band.

In the case of annual periodicity, starting from arbitrary but coherent initial conditions, and simulating the evolution over a great number of years, we would probably arrive to this periodic regime.

But this would be extremely long, and it is preferable to proceed by trial and error.

F.2.5 Numerical solution of the mathematical problem

I have adopted a timestep of $1/60$ a year and a step in S of $1/12$. A smaller step in S, for local variables, would not have much physical sense. In any case, $S_{w/hc}$ or $S_{w/c}$, to which the solution is very sensitive, have been calculated with much more accuracy, and the values at these points are obtained from interpolation. A node of the mesh is defined by i (time, with $i = 0$ the 1st January), and $j = 12|S|$. The computation is done for successive i, from $i = 15$ when melting starts. At $i = 15$ and $i = 40$ (end of melting season), the Z_{ij}(see footnote[4]) and T_{ij} have sudden changes following changes in the condition at one of the aforementioned limits, even though l_{ij} are continuous. At each given i we iteratively improve:

- T, with the polynomial approximations, and, during the melt season, $S_{w/hc}$;
- l, with (7), and while there is a central wet band, its limit $S_{m/w}$
- Z, with (6), and outside the melt season $S_{w/c}$.

We restart several times this loop, until the changes are insignificant. In any case during the period with no melting, the condition $\partial Z/\partial S = 0$ makes the algorithm divergent. We reach convergence by averaging the new values of T and $\partial^2 Z/\partial S^2$ with their previous respective values.

The glacier model considered is cylindrical. Its cross section has parabolic shape, a horizontal surface of 640 m, a maximum thickness, at the center, of 160 m. Its longitudinal surface slope is such that average drag is 0.8 bar. Z_{i0}, given, is represented here below.

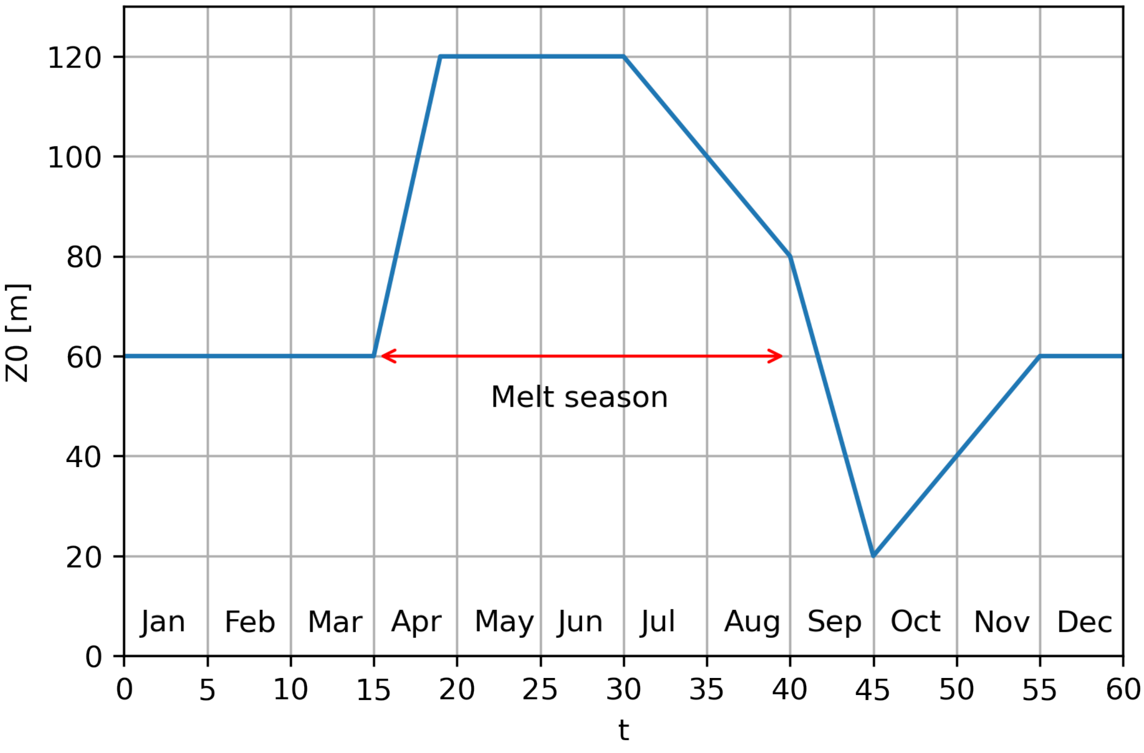

Towards the end of the long season with no melting every drowned bed, with water-filled connected cavities, has had the time to disappear. The bed is wet until $j = 6$, and dry, with no connected cavities in $j = 7$ and 8. But empty cavities continue to slowly close in $j = 9$ and 10. We go from $l_{40,9} = 0.29$

---

[4] TN: The original text says 2_{ij}. It must be a typo, assuming that Lliboutry used an AZERTY keyboard and pressed the key above Z, writing 2 instead.

and $l_{40,10} = 0.69$ at the beginning of the season with no melting to $l_{15,9} = 0.13$ and $l_{15,10} = 0.64$ at its end. Note that if we assumed $\partial l/\partial t = 0$, we would find $l_{15,9} = 0$ and $l_{15,10} = 0.133$, which shows the error that would have been made if we computed yearly averages assuming a steady hydraulic regime.

In the treated model, with no swamped central band and with moderate drag, the sliding speeds are weak. In the central region, approximately 0.74 cm per day in winter and 1.95 cm per day, the maximum, at the beginning of July, while N is at its lowest and l is still very small. If we want to study seasonal fluctuations of velocity over such a glacier without being able to reach the bed, we would have to change the positions of the stakes every two weeks at the beginning of summer.

In conclusion, this study shows that:

- A realistic model, taking into account the laws of Mechanics and Physics, can be established. Glaciologists must not look for simple correlations.
- There is still a considerable amount of numerical computations to be made. I leave that for the younger researchers, not taken back by the fact that this topic is not fashionable anymore.